



Poznan University of Technology
Faculty of Control, Robotics and Electrical Engineering
Institute of Automatic Control and Robotics
Division of Electronic Systems and Signal Processing

Integration of vision and sensory data in monitoring of measurement vehicle environment

Kacper Podbucki

Ph.D. dissertation

Supervisor:
Prof. Adam Dąbrowski, Ph.D., D.Sc.

Auxiliary Supervisor:
Tomasz Marciniak, Ph.D.

Poznań 2025

*First, I would like to thank my supervisor
prof. Adam Dąbrowski, Ph.D., D.Sc.,
for his guidance and invaluable advice
throughout this thesis work.*

*I would like to thank my auxiliary supervisor
Tomasz Marciniak, Ph.D.,
for his continuous support, insightful comments, advice,
patience, and inspiring ideas.*

*I would like to express my deepest gratitude to
Mr. Bogusław Marciniak, manager of Energetics
Department at Poznań–Ławica Airport, for enabling the
implementation of research and scientific work.*

*I would also like to express my deepest gratitude to my
family and friends,
for their understanding,
constant encouragement,
and contribution that they are.*

Abstract

The emerging regulations related to the control of industrial processes according to the idea of Industry 4.0 or monitoring the status of individual system elements in reference to standards require the usage of different methods for carrying out these activities. These requirements are met by solutions provided by broadly understood automation and robotics, which enable partial or complete replacement of humans in order to ensure repeatability, acceleration of performed activities and increase the frequency of measurements that are not achievable for them, but for a robot or computer including scientific areas of automation, electronic, and electrical engineering. One example of such issues, analyzed during the doctoral thesis research, is the testing the operation quality of airfield ground lighting (AGL). In this case, very fast control is required in a short period of time due to the conducted flight operations and short slots between them. Furthermore, the process of measuring the photometric parameters of AGL must result in a report that refers to strictly defined standards issued by the International Civil Aviation Organization (ICAO) and the European Aviation Safety Agency (EASA). Mobile measuring devices are designed for such measurements, which is the subject of the analysis in the doctoral dissertation.

This thesis presents the results of research on the integration of vision and sensory data in the monitoring of measurement vehicles. The presented solutions were examined using a measurement platform for AGL quality testing. To perform the most accurate measurement of the photometric characteristics of the airport navigation system lamps, it is necessary to precisely position the vehicle relative to the incident light beam. The algorithms and methods known in the literature in the aspect of vehicle localization, mainly cars and autonomous vehicles, are not directly reflected in the specifics of the airport environment, among others due to its size and the nature of the characteristic points constituting a reference. The use of multi-sensor measurements and methods of processing vision and sensory data enables precise localization of the measuring vehicle in the work environment in order to perform an accurate measurement of the given object - the airport navigation system lamps.

The following scientific thesis was formulated in the doctoral dissertation: The proposed integrated vision and sensory data processing allows for the vehicle monitoring environment to precisely determine localization of the object for the measurement assessment.

The analysis of multi-sensor solutions for monitoring the vehicle environment allowed for the selection of the following types of measurement sensors for locating the measuring device: satellite navigation sensors, Light Detection and Ranging (LiDAR), vision cameras, and electronic photosensitive modules. The dissertation presents their operating principles, applications, data processing methods, environment features data acquisition modules, and criteria for assessing the measurement accuracy. An analysis was also carried out regarding the embedded system enabling multi-sensor data processing. The dissertation contains a description of the types of AGL, as well as the requirements set by the EASA and ICAO in the scope of standards for individual luminaires. Concepts related to photometric characteristics such as light distribution, light beam intensity, and luminous intensity,

were also described. A comparison of methods and solutions of performing quality control of AGL was made.

As part of the conducted research, methods of processing sensory and vision data were proposed in order to increase the precision of measuring the photometric characteristics of AGL. Data from the satellite navigation system are filtered on the basis of the horizontal dilution of precision (HDOP) parameter and number of visible satellites to reduce the impact of their constellation distribution error on the position determination. The point cloud obtained from the LiDAR sensors is processed using the random sample consensus (RANSAC) algorithm, which allows distinguishing the points of objects that constitute reference points from the points that compose the background. The video sequences presenting the image of the airport areas were processed by threshold processing, the use of dilation operations, and histogram analysis to detect light points in the form of lamps, so that their position relative to the axis of the measuring vehicle could be determined. The dissertation presents research on multi-point measurement of photometric characteristics of AGL. The commercial sensors way of work was analyzed and the concept of an original solution of a module using a photodiode to measure light intensity was proposed. The concept of measurement matrices for testing the quality of airport navigation lighting operation based on a matrix with regular and irregular sensor distribution was also described. The scientific research presented in the doctoral thesis was carried out thanks to the formal cooperation between the Division of Signal Processing and Electronic Systems at the Poznań University of Technology and the Energetics Department of Poznań–Ławica Airport.

Streszczenie

Pojawiające się regulacje związane z przeprowadzaniem kontroli procesów przemysłowych zgodnie z ideą Przemysłu 4.0 czy monitorowaniem stanu poszczególnych elementów systemów w odniesieniu do norm, wymagają zastosowania różnych metod przeprowadzania tych działań. Naprzeciw tym wymaganiom wychodzą rozwiązania dostarczane przez szeroko pojętą automatykę i robotykę, która umożliwia częściowe lub całkowite zastąpienie człowieka w celu zapewnienia powtarzalności, przyspieszenia wykonywanych czynności oraz zwiększenia częstotliwości wykonywania pomiarów, które nie są osiągalne dla ludzi, ale dla robota czy komputera już tak, łącząc tym samym obszary naukowe z zakresu automatyki, elektroniki i elektrotechniki. Jednym z przykładów tego typu zagadnień, przeanalizowanych w czasie badań w ramach rozprawy doktorskiej, jest badanie jakości działania lamp oświetlenia lotnisk (AGL). W tym przypadku wymagana jest bardzo szybka kontrola w krótkim przedziale czasu ze względu na przeprowadzane operacje lotnicze i krótkie sloty pomiędzy nimi. Ponadto, proces pomiaru parametrów fotometrycznych lamp oświetlenia nawigacyjnego lotnisk musi skutkować raportem, który odnosi się do ściśle określonych norm wydanych przez Organizację Międzynarodowego Lotnictwa Cywilnego (ICAO) i Europejską Agencję Bezpieczeństwa Lotniczego (EASA). Do takich pomiarów konstruuje się mobilne urządzenia pomiarowe, co jest przedmiotem analizy doktoratu.

W pracy przedstawiono wyniki badań dotyczące integracji danych wizyjnych i sensorycznych w monitorowaniu pojazdu pomiarowego. Prezentowane rozwiązania zostały przetestowane z wykorzystaniem platformy pomiarowej do badania jakości działania oświetlenia nawigacyjnego lotnisk. W celu przeprowadzenia możliwie dokładnego pomiaru charakterystyki fotometrycznej lotniskowych lamp systemu oświetlenia nawigacyjnego niezbędne jest precyzyjne ustawienie pojazdu względem padającej wiązki światła. Algorytmy i metody znane w literaturze w aspekcie lokalizowania pojazdów, głównie samochodów oraz pojazdów autonomicznych, nie mają bezpośredniego odzwierciedlenia w przypadku specyfiki środowiska portu lotniczego między innymi ze względu na jego rozmiar oraz charakter punktów charakterystycznych stanowiących odniesienie. Zastosowanie pomiarów wieloczuJNIKOWYCH oraz metod przetwarzania danych wizyjnych i sensorycznych umożliwia precyzyjne zlokalizowanie pojazdu pomiarowego w środowisku pracy w celu przeprowadzenia dokładnego pomiaru zadanego obiektu - lamp lotniskowego systemu nawigacyjnego.

W rozprawie doktorskiej sformułowana została następująca teza naukowa: Zaproponowane przetwarzanie zintegrowanych danych wizyjnych i sensorycznych umożliwia monitorowanie otoczenia pojazdu w celu precyzyjnego określenia lokalizacji obiektu do oceny pomiarowej.

Analiza rozwiązań wieloczuJNIKOWYCH służących do monitorowania otoczenia pojazdów pozwoliła dokonać selekcji następujących typów czujników pomiarowych służących do lokalizacji urządzenia pomiarowego: czujników nawigacji satelitarnej, LiDARu (ang. Light Detection and Ranging), kamer wizyjnych oraz elektronicznych modułów światłoczułych. W rozprawie przedstawiono ich zasady działania, zastosowania, metody przetwarzania danych, przykładowe moduły oraz kryteria oceny dokładności pomiarowej. Przeprowadzono także analizę dotyczącą systemu wbudowanego

umożliwiającego wieloczułnikowe przetwarzanie danych. W rozprawie zawarto opis typów lamp oświetlenia nawigacyjnego lotnisk, jak również wymagania stawiane przez EASA oraz ICAO w zakresie norm dla poszczególnych opraw. Opisano również pojęcia związane z charakterystykami fotometrycznymi takimi jak rozsył światłości, natężenie wiązki światła oraz światłość. Dokonano zestawienia metod oraz sposobów dokonywania kontroli jakości AGL.

W ramach przeprowadzonych badań zaproponowano metody przetwarzania danych sensorycznych i wizyjnych w celu zwiększenia precyzji dokonywania pomiaru charakterystyki fotometrycznej lotniskowych lamp oświetlenia nawigacyjnego. Dane pochodzące z systemu nawigacji satelitarnej są filtrowane w oparciu o parametr HDOP (ang. horizontal dilution of precision) oraz liczbę widocznych satelitów, aby ograniczyć wpływ błędu rozkładu konstelacji satelitów na określenie położenia. Chmura punktów otrzymywana z czujników typu LiDAR jest przetwarzana za pomocą algorytmu RANSAC (ang. random sample consensus), który umożliwia odróżnienie punktów obiektów stanowiących punkty odniesienia od punktów stanowiących tło. Sekwencje wizyjne przedstawiające obraz płaszczyzn lotniskowych zostały przetworzone poprzez progowanie, zastosowanie operacji dylatacji oraz analizy histogramów w celu detekcji punktów świetlnych w postaci lamp, aby możliwe było określenie ich pozycji względem osi pojazdu pomiarowego. W rozprawie przedstawiono badania dotyczące wielopunktowego pomiaru charakterystyk fotometrycznych lamp lotniskowego oświetlenia nawigacyjnego. Przeanalizowano sposób działania czujników komercyjnych oraz zaproponowano koncepcję autorskiego rozwiązania modułu wykorzystującego fotodiodę do pomiaru natężenia światła. Opisano również koncepcję matryc pomiarowych do badania jakości działania lamp lotniskowych oświetlenia nawigacyjnego lotnisk w oparciu o matrycę o równomiernym i nierównomiernym rozkładzie czujników. Badania naukowe przedstawione w rozprawie doktorskiej zostały przeprowadzone dzięki formalnej współpracy pomiędzy Zakładem Układów Elektronicznych i Przetwarzania Sygnałów Politechniki Poznańskiej z Zespołem Energetycznym Portu Lotniczego Poznań–Ławica.

List of Abbreviations

2D – two-dimensional
3D – three-dimensional
AC – Alternating Current
ACC – Accuracy
AD – Automated Driving
ADC – Analogue-Digital Converter
AGL – Airfield Ground Lighting
AI – Artificial Intelligence
APP – Approach system lamp
ASCII – American Standard Code for Information Interchange
AV – Autonomous vehicle
BGR – Blue, Green, Red
C/C – Clear/Clear
C/R – Clear/Red
CAA – Civil Aviation Authority
CAV – Connected autonomous vehicles
CCD – Charge-coupled device
CIE – Commission Internationale de L'éclairage
CL – Camera LiDAR
CMOS – Complementary metal-oxide semiconductor
CMY – Cyan, Magenta, Yellow
CMYK – Cyan, Magenta, Yellow, Black
CNN – Convolutional Neural Network
CPS – Cyber-Physical Systems
CSI – Camera Serial Interface
DC – Direct Current
DFE – Decision Feedback Equalizer
DGNSS – Differential Global Navigation Satellite Systems
DOP – Dilution of Precision
EASA – European Aviation Safety Agency
ECEF – Earth Centered Earth Fixed
FAA – Federal Aviation Administration
FN – False negative
FNR – False negative rate
FoV – Field of View
FP – False positive

FPR – False positive rate
FPS – Frames per second
G/Y – Green/Yellow
GDOP – Geometric Dilution of Precision
GLONASS – Global'naya Navigatsionnaya Sputnikovaya Sistema
GMT – Greenwich Mean Time
GNSS – Global Navigation Satellite System
GPS – Global Positioning System
GUI – Graphical user interface
HDOP – Horizontal Dilution of Precision
HLF – High-level fusion
HSI – Hue Saturation Intensity
HSV – Hue Saturation Value
I²C – Inter-Integrated Circuit
ICAO – International Civil Aviation Organization
IEEE – Institute of Electrical and Electronics Engineers
IMU – Inertial measurement unit
IoT – Internet of Things
IR – Infrared
ISP – Image Signal Processor
ITS – Intelligent Transportation System
LED – Light-emitting diode
LiDAR – Light Detection and Ranging
LLF – Low-level fusion
mAP – mean Average Precision
MLF – Mid-level fusion
MSHIF – Multi-source and heterogenous information fusion
N – Negative
NCAP – New Car Assessment Programs
NEU – North-East-Up
NMEA – National Marine Electronics Association
NPV – Negative predictive value
P – Positive
PANSA – Polish Air Navigation Services Agency
PC – Personal computer
PCB – Printed circuit board
PCD – Point cloud data
PDOP – Position Dilution of Precision
PMTK – MediaTek proprietary data transfer protocol
PN – Predicted negative

PP – Predicted positive
PPV – Positive predictive value
PWM – Pulse-width modulation
QZSS – Quasi-Zenith Satellite System
RANSAC – Random sample consensus
RC – Radar camera
RCLi – Radar camera LiDAR
RCL – Runway centre line lamp
RGB – Red, Green, Blue
RMS – Root mean square
RMSE – Root mean square error
RNN – Recursive neural network
ROI – Region of interest
RTCM – Radio Technical Commission for Maritime Services
RTK – Real-time kinematic
RX – Receiver
SCL – Serial Clock
SDA – Serial Data
SLAM – Simultaneous localization and mapping
SLD – Spot light detection
SNR – Signal-to-noise ratio
SPI – Serial Peripheral Interface
SSE – Sum squared error
SSL – Solid State LiDAR
SSR – State space representation
TAXI – Taxiway centre line lamp
TDOP – Time dilution of precision
TDZ – Touchdown zone lamp
TN – True negative
TNR – True negative rate
TOF – Time-of-Flight
TP – True positive
TPR – True positive rate
TTA – Time to alert
TX – Transmitter
UART – Universal Asynchronous Receiver-Transmitter
UAV – Unmanned aerial vehicle
UTC – Coordinated Universal Time
VDOP – Vertical dilution of precision
WiFi – Wireless fidelity

Contents

Abstract	v
Streszczenie	vii
List of Abbreviations	ix
1 Introduction	1
1.1 Research area	1
1.2 Aim of work and scientific thesis	5
1.3 Main scientific achievements	11
1.4 Organization of the thesis	16
2 Current methods and solutions in sensorial measurements	18
2.1 Multi-sensors localization measurement	18
2.2 Localization using electronic measurement sensors	24
2.2.1 Global Navigation Satellite System	27
2.2.2 Light Detection and Ranging sensor	34
2.2.3 Analysis of vision sequences in video monitoring	41
2.2.4 Photosensitive elements for light measuring	52
2.3 Methods and devices for AGL lamps testing	59
2.3.1 Requirements of in-pavement AGL lamps system	59
2.3.2 In-pavement AGL system assessment methods	65
3 Proposed improvement of multi-sensor localization techniques	71
3.1 Concept of multi-sensor system for monitoring measurement vehicle	71
3.2 Filtering of positioning data of GNSS measurement	72
3.2.1 Static localization error measurement using GNSS	78
3.2.2 Dynamic localization measurement using GNSS	86
3.3 Correction of distance estimation using LiDAR	91
3.3.1 Preliminary experiments	91
3.3.2 Elevated airport edge lamps detection using LiDAR	93
3.3.3 LiDAR point cloud data classification	95

3.4	Detection of characteristic points on video sequences.....	98
3.4.1	Proposed modified light spots detection algorithm.....	100
3.4.2	Analysis of the impact of lighting conditions on the algorithm's performance.....	107
4	Proposal of light sensors integration for AGL evaluation.....	111
4.1	Analysis of in-pavement AGL luminous intensity distribution	111
4.1.1	The influence of the AGL power supply type on the measurement using illuminance sensors.....	112
4.1.2	Laboratory assessment of AGL photometric characteristics	116
4.1.3	Proposed polynomial correction for AGL assessment using illuminance sensors.....	120
4.1.4	Evaluation of photometric parameters of selected used and refurbished AGL using illuminance sensor.....	127
4.2	Design of matrix with regular arrangement of photodiodes.....	131
4.2.1	Analysis of the measurement acquisition time using illuminance sensors.....	132
4.2.2	Design of photodiode based illuminance sensor	137
4.2.3	Proposed algorithm of measurement using matrix of illuminance sensors.....	144
4.3	Proposed matrix design with irregular arrangement of photodiodes.....	145
4.3.1	Evaluation of the performance of the proposed measurement matrix in AGL measurements	149
4.3.2	Comparison of proposed solution with reference measurements	154
4.4	Proposed AGL measurement platform with environment monitoring	155
5	Conclusions	159
	Bibliography	163
	List of Figures.....	175
	List of Tables.....	179

Chapter 1

Introduction

1.1 Research area

The changing regulations for controlling industrial processes and monitoring individual system elements in line with standards call for the implementation of various approaches to achieve these objectives. Measuring devices and vehicles in specialized applications require appropriate positioning to obtain reliable and accurate results [1], [2], [3]. Therefore, a thorough analysis of the work environment area is essential. Such automated monitoring can be implemented using a multi-channel measurement system consisting of both measurement sensors and camera images [4], [5], [6], [7]. The scientific research includes combined areas of automation, electronic and electrical engineering (Figure 1).

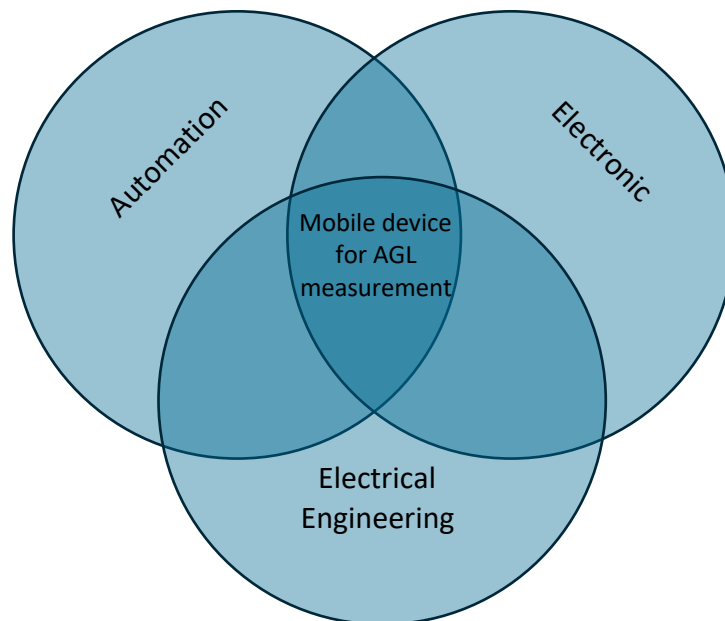


Figure 1 Scientific research in aspects of PhD application area

Multi-sensor measurement systems are widely used in vehicle environment monitoring e.g. in the automotive industry (Figure 2). Modern vehicles are equipped with many systems responsible for travel safety and comfort [8], [9], [10]. Their use is possible due to the appropriate analysis of not only the vehicle parameters itself, but also information from its surroundings. Monitoring the area around the vehicle requires the use of measurement sensors and vision systems, which enable multi-channel data analysis and integration in order to obtain coherent information about the measurement environment [11], [12], [13]. Specialized measuring devices can be considered a special case of vehicles, the correct

operation of which is possible thanks to a thorough analysis of the environment in which they move and the determination of their location.

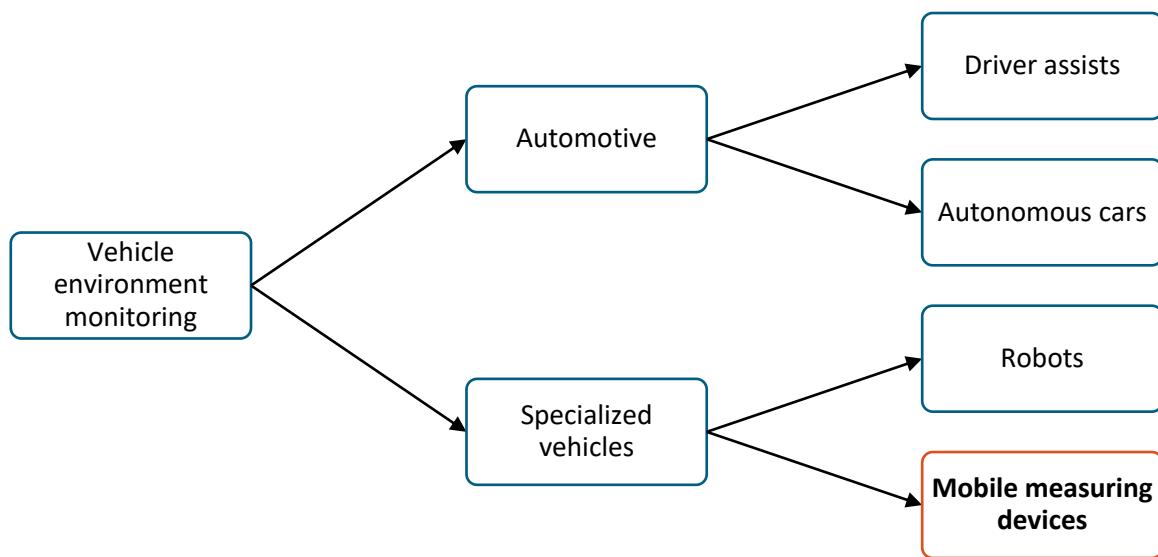


Figure 2 Example areas of vehicle environment monitoring

Measuring devices may require manual control by the operator, equipped with a support system, automated or autonomous. The required precision of measurement is therefore possible to achieve through control by the operator based on his own observations, measurement readings from the support system, instructions from an automated system or an integrated autonomous measuring device. In the case of measuring devices and vehicles, it is crucial to orient the measuring equipment, i.e. the head or measuring matrix, in such a way that the test is carried out with the greatest possible precision [14], [15], [16], [17]. Achieving such an effect involves many factors, starting from the appropriate calibration of devices in relation to each other, checking measurement errors resulting from the properties and imperfections of the sensors themselves. Another aspect that must be considered at the design stage of the device and its location support system is the working environment conditions. On the basis of its specificity, the appropriate types of sensors and their parameters are selected [12].

The localization process and monitoring of the surroundings of the measuring devices require, first of all, a thorough analysis of the sensor data. Appropriate selection of useful data is possible by selecting sensors for individual tasks in such a way that they focus on detecting characteristic features of the environment that are key to obtaining detailed information about the area and, further, characteristic features. Correct calibration and mutual spatial arrangement of the sensors determine whether further data processing will be carried out optimally and as effectively as possible [18], [19], [20]. To obtain accurate and useful measurement data while maintaining the ability to operate in real time, the preprocessing

stage of the received data is also a very important aspect. The processing of information from sensors may take place at various stages of the algorithm, i.e. before or after data fusion, which also affects the final result, including accuracy. The last stage, closely related to monitoring the environment of the measurement vehicles using integrated sensory and vision data, is to define the evaluation criteria and the output data of the system (Figure 3) [21], [22].

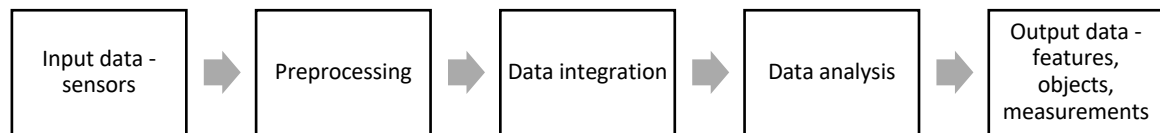


Figure 3 Stages of data processing in vehicle integrated monitoring

Annex 14 to the Convention on International Civil Aviation Organization specifies technical requirements for various types of lighting, including their photometric parameters [23]. These requirements mandate continuous monitoring of airport navigation lighting systems to ensure compliance with maintenance standards for lamps parameters. Fundamental maintenance guidelines for lighting systems include the following instructions and criteria for quantitative and qualitative assessment:

- airports must develop a maintenance program for the lighting system
- a light point is deemed non-operational if the average luminous intensity of its main beam is less than 50% of the required value
- the frequency of light measurements for approach lighting systems and runway lights must be at least twice a year for in-pavement lights and once a year for other lights
- maintenance and inspection frequencies should increase with higher airport traffic and in adverse environmental or climatic conditions.

Airports are required to submit reports on compliance with navigation lighting standards to the Civil Aviation Authority (CAA) and the Polish Air Navigation Services Agency (PANS), which then forward them to EUROCONTROL (ICAO).

Operational services at airports perform periodic inspections, maintenance, and repairs on navigation lighting components based on manufacturer recommendations. These tasks typically involve simplified measurements of lighting parameters, routine maintenance, and the replacement of damaged components, including bulbs. Given the stringent photometric requirements for lighting systems, visual assessments and routine maintenance alone are insufficient.

The time factor in inspection, maintenance, and repair is also critical, especially with the rapid increase in air traffic, which limits the ability of technical teams to introduce extended operational downtimes at airports.

Since the current method for assessing navigation lighting functionality is primarily visual and lacks comprehensive measurements of light point performance, there is a pressing need to implement precise photometric measurement techniques as part of inspection, maintenance, and repair services. Introducing innovative photometric measurement technology with superior functionality compared to traditional methods can reduce service time and costs.

To ensure the proper operation of the airport navigation lighting system, ICAO requires monitoring in the following areas:

- functionality of light points — assessable visually
- performance of light points — requires measurement (a light point is considered non-operational if the average intensity of its main beam is less than 50% of the value specified for each lamp group at the airport)
- light intensity distribution and levels of light points — requires measurement (at the boundary and within the ellipse or rectangle defining the main beam, the light intensity distribution must meet precise requirements).

Currently, periodic checks of lighting fixture parameters in airport navigation systems are conducted under field conditions using mobile units for assessing and recording photometric values. Mobile lighting intensity measurement systems are used to establish the relationship between illuminance and directional luminous intensity, forming the basis for inspection reports.

The view of the runway at Poznań - Ławica Airport presented in Figure 4 shows the research environment of the measuring platform for testing the quality of the AGL. The lamps are built into the runway surface and in this case emit white light. The runway centre line lighting, edge lamps and the touchdown zone are visible. In comparison to the entire width of the runway, they constitute only a small point, which requires very high precision when measuring the photometric characteristics of individual lamps.



Figure 4 View of the runway with AGL lamps turned on at Poznań – Ławica Airport runway 28

The airport environment is somewhat reminiscent of roads on which cars drive, with the difference that everything here is on a larger scale and there are no elements that could constitute reference points due to the open space. Therefore, directly using methods known from the automotive industry allowing for monitoring the environment using integrated sensory and vision data is impossible and requires their adaptation. Some aspects also require the use of specific hardware and software solutions to enable the best possible location of the device in order to achieve appropriate measurement precision.

1.2 Aim of work and scientific thesis

The investigated solution (Figure 5) described in this thesis is focused on four different sensor sources of data: GNSS, LiDAR, camera and illuminance sensors. For each of them processing methods and algorithms are proposed and implemented, which are necessary to extract features of environment of measuring platform for quality testing of in-pavement AGL to precise detect each investigated lamp.

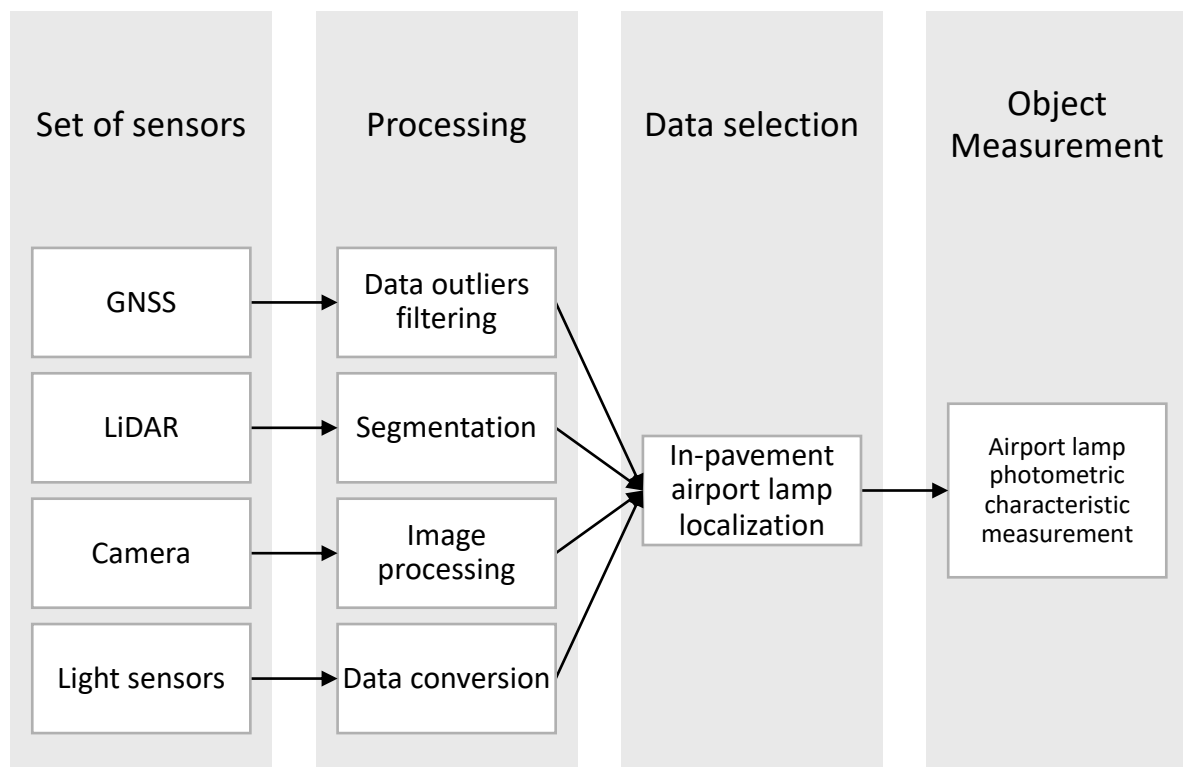


Figure 5 Investigated research aspects

With the development of technology, including the automation of processes, e.g. measurements, there is parallel progress in various areas of production and control. Following this trend, the European Union Aviation Safety Agency (EASA) also anticipates the development and use of new technologies, including artificial intelligence (AI), presenting various concepts and areas requiring their implementation [24]. The device for testing the quality of photometric parameters of AGL is intended for operation on runways and taxiways.

Its task is to check the luminous intensity value in the angular distribution of the light spectrum. Its use requires precise guidance over the tested lamp embedded in the road surface. The conceptual measurement platform for the quality testing of AGL equipped with an environment monitoring system is presented in Figure 6.

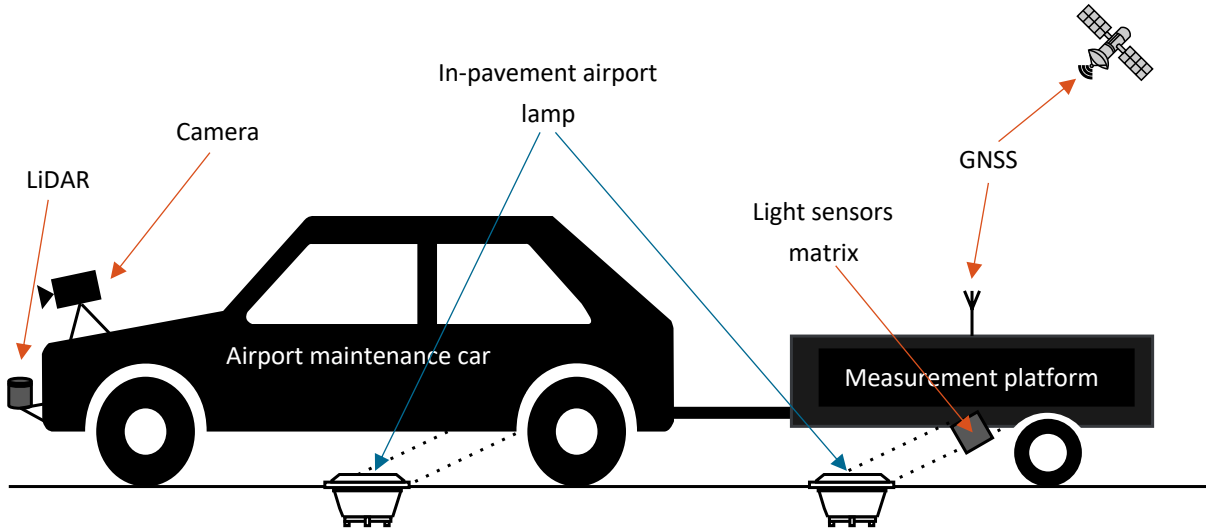


Figure 6 Measurement platform for testing in-pavement AGL with environment monitoring system

The proposed final measurement algorithm includes the following data processing scheme (Figure 7): the GNSS module is used for rough localization, the position is refined thanks to LiDAR data, the airport navigation lighting is aligned after analyzing the camera image, and the detailing and final correction of the approach over the tested lamp is made thanks to the illuminance sensor measurement matrix. The system allows for receiving feedback on the correction of the driving path, conducting the correct measurement and then comparing the measurement results with the standards.

The combination of all the above systems consisting of sensors allows for accurate and precise monitoring of the measuring vehicle's surroundings, and thus its location. With this information, it is possible to send instructions to the operator of the measuring system for testing AGL to drive over the tested lamp as precisely as possible.

The issues described in Chapter 1.1 focus on the use of multisensory observation of the environment and the integration of collected measurement data to increase the precision of vehicle localization. In the case of specialized measuring devices, the specificity of the task performed by the device and the environment in which it operates play a key role.

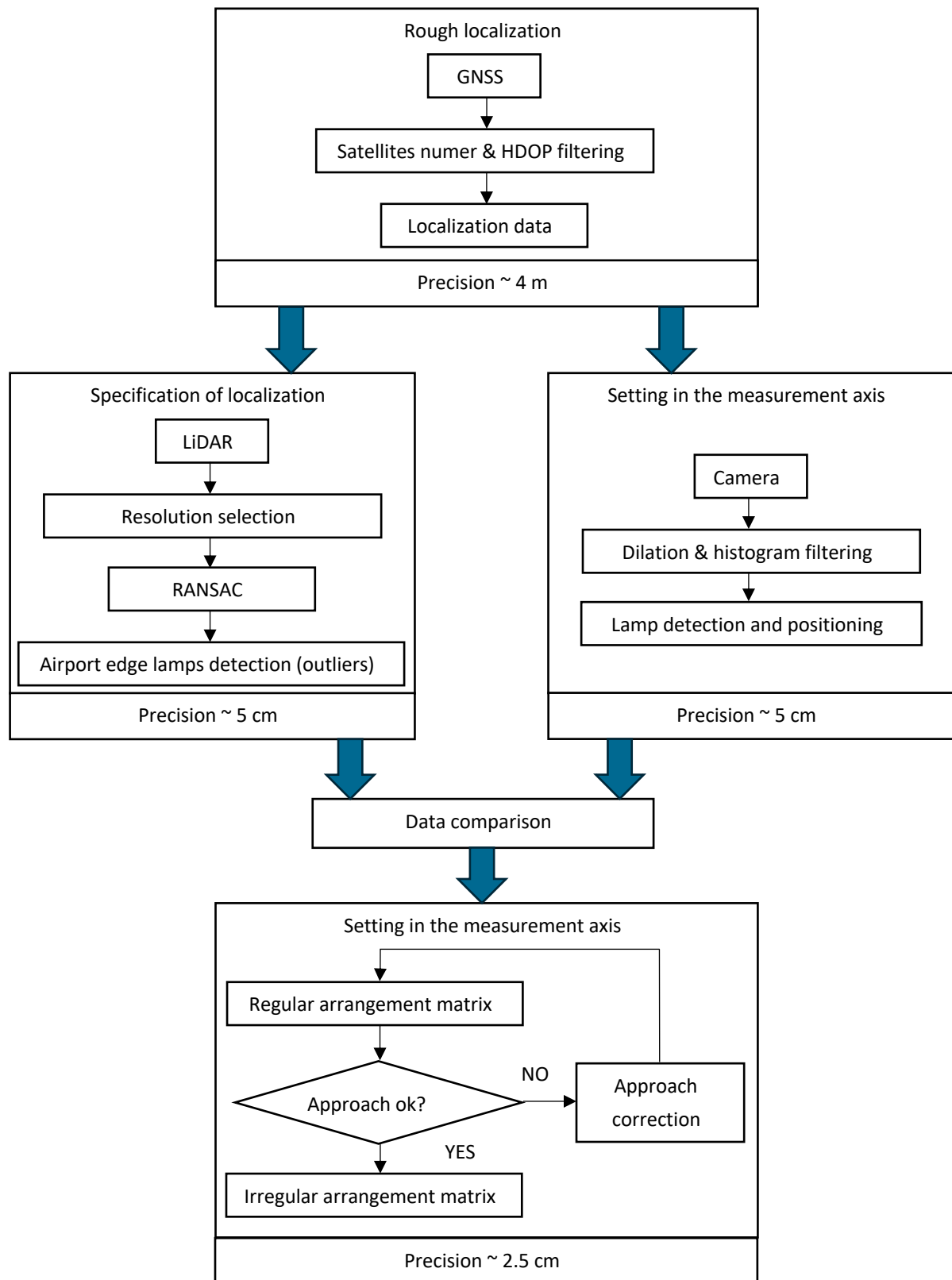


Figure 7 Final proposed algorithm of measuring device environment monitoring

The aim of this PhD thesis is to propose data processing methods that allow effective monitoring of the measurement vehicle environment using integrated vision and sensory data.

This data is aimed at improving the functioning and precision of systems responsible for measuring photometric parameters of in-pavement AGL.

The values received from sensors and video cameras require processing in order to extract data, which then can provide details about localization of measurement vehicle as well as the measurement parameters themselves. Hardware tests and experiments were performed in laboratory and real conditions. The datasets obtained during research were analyzed in terms of the selection of appropriate algorithms for data processing. The end result is an algorithm that allows for effective monitoring of the measurement vehicle environment.

The **detailed objectives** of the thesis can be divided into five items:

- collection of measurement datasets for electronic sensors measurement datasets during laboratory and real conditions tests
- hardware experiments for choosing the optimum solution for monitoring the measurement vehicle environment
- analysis of data processing methods from GNSS sensors, LiDAR, vision cameras and illuminance sensors
- proposal of the solution for multi-point testing of the light beam emitted by airport lamps in order to assess their photometric parameters
- development of effective methods to analyze the measurement vehicle environment based on integrated vision and sensory data.

Scientific thesis

Based on the research conducted, the following scientific thesis can be formulated: *The proposed integrated vision and sensory data processing allows for the vehicle monitoring environment to precisely determine localization of the object for the measurement assessment.*

In order to verify the proposed solutions for data processing and their integration for precise monitoring of the measuring vehicle's surroundings, it was necessary to collect measurement data. This data was collected from various types of GNSS modules, including unique data from the restricted airport area while moving on the runway and taxiways, as well as data from static measurement of location coordinates. Measurement data of point clouds from LiDAR were also prepared independently and compiled into a dataset predicting different environmental conditions. A video dataset with a total size of over 98 GB was prepared. It contains recordings from runs on the runway and taxiways in different directions, at different times of day and in different weather conditions. About 500 lamps were tested using light intensity sensors, including luminaires with a light source on two sides. These were airport lamps from use and new or refurbished, so it was possible to compare their characteristics. This set of data is unique because there are no available public datasets regarding photometric parameters of AGL.

The presented research results were possible to implement thanks to the research & development cooperation with Poznań-Ławica Airport, with which an agreement was concluded in documents (PP)RU00021806 and 45/2022/RK. It allowed for the support of knowledge and consultation of ideas and solutions from specialists dealing with AGL as well as maintenance - testing the correct operation of airport lighting. Substantive support helped to develop algorithms and measurement concepts in such a way that they were carried out in accordance with the regulations of national and international aviation safety agencies. Poznań-Ławica Airport allowed access to the runway and taxiways to collect a dataset for analysis and test the proposed solutions. In addition, during the 3-month internship at Poznań-Ławica Airport, it was possible to examine all installed worn-out in-pavement AGL from the runway centre line and touchdown zone, and then, after their maintenance, to re-verify the measurements. Details regarding the cooperation between the Poznan University of Technology Division of Signal Processing and Electronic Systems and Poznań-Ławica Airport are presented in Figure 8.

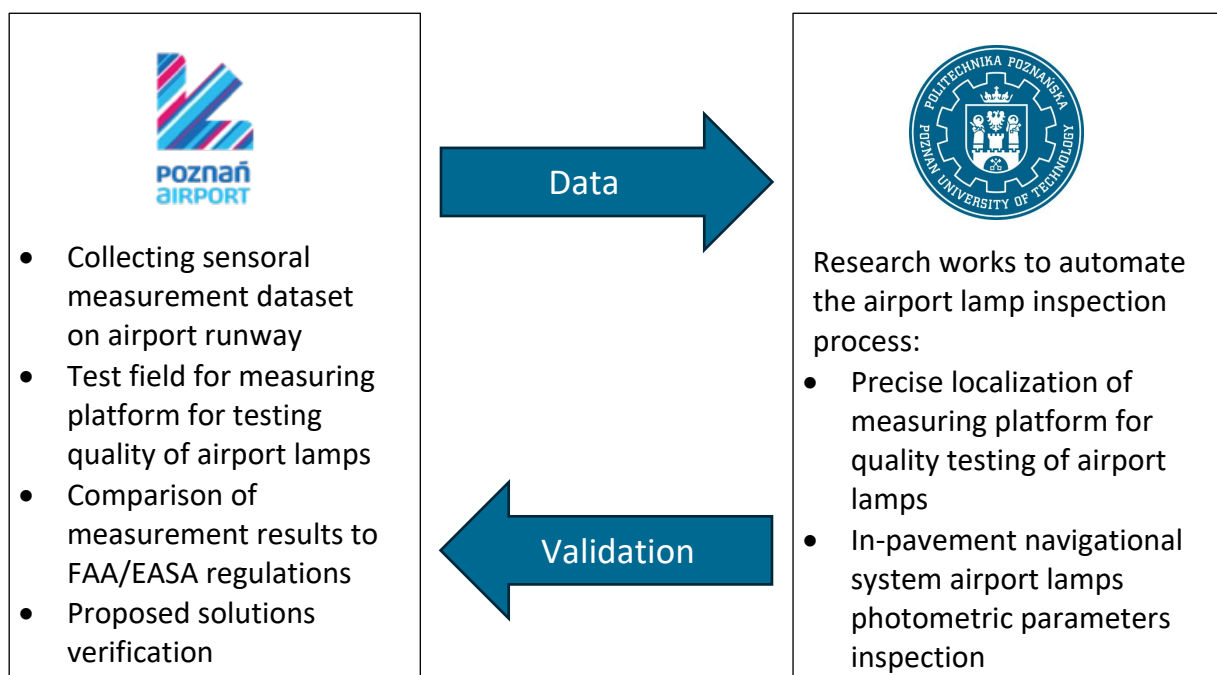


Figure 8 R&D cooperation between Poznań – Ławica Airport and Poznan University of Technology

The research works were part of the following scientific projects and their results are the part of the doctoral dissertation:

1. SMART4ALL (full name: Selfsustained Cross-Border Customized Cyberphysical System Experiments for Capacity Building among European Stakeholder) under Horizon 2020 framework under call DT-ICT-01-2019: Smart Anything Everywhere – Area 2: Customized low energy computing powering CPS and the IoT (Grant Agreement No 872614; 0211/PRKE/6428) from 01.07.2020 to 31.12.2023 - The program aimed to implement advanced technologies across various aspects of life,

making them "smart," while also providing small and medium enterprises from Central Europe with access to technologies and expertise developed by research institutions. One of the most significant achievements was the creation of a so-called Marketplace - a digital platform that facilitates the transfer of artificial intelligence knowledge and technology from academia to various industries, particularly transportation, agriculture, and environmental sectors. As part of the proposed technology, solutions relevant to air transport were analyzed, especially for detecting lines on runways and taxiways at airports. Solutions were also developed for a measurement platform to assess the performance quality of navigational lighting at airports, as well as a concept for testing the mechanical wear of in-pavement lighting prisms on runways and taxiways. Additionally, in response to the COVID-19 pandemic ongoing during the project, a vision system was developed to monitor proper mask-wearing, based on neural networks.

2. Inkubator Innowacyjności 4.0 (0614/MNSW/2948) from 01.02.2021 to 31.01.2023 - The program offered by the Ministry of Science and Higher Education aimed to support the management of research and development outcomes, particularly in the area of commercialization. As part of the activities carried out under subtask 4.5, "Platforma pomiarowa do badania jakości działania lamp lotniskowych" a measuring device was prepared for assessing the photometric parameters of in-pavement AGL. A measurement method was also developed, and in line with the project objectives, both the device concept and method were submitted to the patent office under the title: "Sposób pomiaru jakości działania lamp lotniskowych oraz zestaw pomiarowy do badania jakości działania zagłębionych lamp lotniskowych" application number P.442569 [25].
3. Investigation of Algorithms Supporting Positioning of a Mobile Measuring Device for the Inspection of Airport Runway Lighting Surfaces (0211/SBAD/0522) from 01.01.2022 to 31.12.2022- Project awarded through an internal competition for conducting scientific research by young staff at the Faculty of Control, Robotics and Electrical Engineering of the Poznan University of Technology. The objective of the project was to further develop an existing prototype of a measurement platform for assessing the performance quality of AGL. The project included an analysis of the feasibility of using embedded systems for processing segmentation and line detection algorithms applied to the inspection of in-pavement AGL, as well as for analyzing density maps and algorithms for autonomous vehicle navigation. Additionally, algorithms were examined for assessing wear on prisms of in-pavement AGL based on visual data. The type of neural networks and

parameters of selected algorithms were chosen and trained based on previously prepared data.

4. Integration of vision and sensory data in vehicle surrounding monitoring (0211/SBAD/0820) from 01.01.2020 to 09.12.2022 as the project manager and main contractor - Project awarded through an internal competition for conducting scientific research by young staff at the Faculty of Control, Robotics and Electrical Engineering of the Poznan University of Technology. The aim of the project was to conduct experimental research on the acquisition and processing of data from multiple sensors and vision systems, which can improve the effectiveness of obstacle detection in a vehicle's surroundings. Achieving this goal required the intense investigation of LiDAR sensor, which enables the creation of an environmental map using laser technology and serves as a complement to visual data from cameras. The research involved creating a dataset in laboratory conditions and developing algorithms that are further expanded as part of a doctoral thesis. Proper integration of data from various sources (sensors) can improve the system's performance quality and optimize the algorithms used for monitoring the vehicle's surroundings.

The implementation of the tasks described in the projects made it possible to obtain funds for equipment and prepare publications in high-ranking scientific journals, as well as to carry out a research internship at the Poznań - Ławica Airport.

1.3 Main scientific achievements

As part of the presentation of the research results conducted during the development of the doctoral dissertation, they were published in the following scientific journals, reports and patent application. Publications directly related to the topic of the doctoral dissertation are listed in Table 1.

Table 1 List of authored and co-authored publications directly related to the topic of PhD dissertation

Publication details	Citation number
K. Podbucki, T. Marciniak, J. Suder, „Laboratory Assessment of In-Pavement Airport Lamp's Luminous Intensity Distribution”, Applied Sciences, 2023, vol. 13, iss. 24, pp. 13242-1-132242-19, doi: 10.3390/app132413242	[26]
K. Podbucki, J. Suder, T. Marciniak, W. Mańczak, A. Dąbrowski, „Microprocessor-based photometric light intensity sensor for airport lamps	[27]

quality testing”, Opto-electronics Review, 2022, vol. 30, no. 4, pp. e143396-1-e143396-7, doi: 10.24425/opelre.2022.143396	
K. Podbucki, „Możliwości i ograniczenia monitorowania otoczenia z wykorzystaniem czujnika LiDAR”, Przegląd Elektrotechniczny, 2022, vol. 98, iss. 1, pp. 184-187, doi:10.15199/48.2022.01.40	[28]
K. Podbucki, J. Suder, T. Marciniak, A. Dąbrowski, „Elektroniczna matryca pomiarowa do badania lamp lotniskowych”, Przegląd Elektrotechniczny 2021, vol. 10, iss. 14, pp 1665-1-1665-22, doi: 10.15199/48.2021.02.12	[29]
K. Podbucki, J. Suder, T. Marciniak, A. Dąbrowski, „Influence of power supply on airport navigation lamps photometric test accuracy”, in 2023 Signal Processing: Algorithms, Architectures, Arrangements, and Applications (SPA), Poznan, Poland: IEEE, Sep. 2023, pp. 183–188. doi: 10.23919/SPA59660.2023.10274440	[30]
K. Podbucki and T. Marciniak, „Camera-based light source localization for precise luminous intensity measurement of airport lamps” in 2024 Signal Processing: Algorithms, Architectures, Arrangements, and Applications (SPA), Poznan, Poland: IEEE, Sep. 2024, doi: 10.23919/SPA61993.2024.10715614	[31]
J. Suder, K. Podbucki, and T. Marciniak, „Raport z pomiarów fotometrycznych zagłębionych lamp oświetlenia nawigacyjnego drogi startowej Portu Lotniczego Poznań – Ławica”, Politechnika Poznańska, Poznan, Poland, r3335_2022, Aug. 2022	[32]
Patent application: A. Dąbrowski, T. Marciniak, K. Podbucki, and J. Suder, „Sposób pomiaru jakości działania lamp lotniskowych oraz zestaw pomiarowy do badania jakości działania zagłębionych lamp lotniskowych”, P.442569, submitted 19.10.2022	[25]

The list of the authored and co-authored publications whose subject matter is partly related to the research aspects described in the doctoral dissertation is presented in Table 2.

Table 2 List of authored and co-authored publications partly related to the topic of PhD dissertation

Publication details	Citation number
J. Suder, K. Podbucki, T. Marciniak, „Power Requirements Evaluation of Embedded Devices for Real-Time Video Line Detection”, Energies - 2023, vol. 16, iss. 18, pp. 6677-1-6677-20, doi: 10.3390/en16186677	[33]
J. Suder, K. Podbucki, T. Marciniak, „Chromaticity measurement of airport navigation lighting using integrated colour	[34]

sensor”, Opto-electronics Review - 2023, vol. 31, no. 4, pp. e147040-1-e147040-9, doi: 10.24425/opelre.2023.147040	
T. Marciniak, K. Podbucki, J. Suder, „Application of the Nucleo STM32 module in teaching microprocessor techniques in automatic control”, Przegląd Elektrotechniczny - 2022, R. 98, nr 10, pp. 245-248, doi: 10.15199/48.2022.10.55	[35]
J. Suder, K. Podbucki, T. Marciniak, A. Dąbrowski, „Low Complexity Lane Detection Methods for Light Photometry System”, Electronics - 2021, vol. 10, iss. 14, pp. 1665-1-1665-22, doi: 10.3390/electronics10141665	[36]
J. Suder, K. Podbucki, T. Marciniak, A. Dąbrowski, „Spectrum sensors for detecting type of airport lamps in a light photometry system”, Electronics - 2021, vol. 10, iss. 14, pp. 1665-1-1665-22, doi: 10.24425/opelre.2021.139383	[37]
J. Suder, P. Maciejewski, K. Podbucki, „Platforma pomiarowa do badania jakości działania lamp lotniskowych”, Pomiary Automatyka Robotyka - 2019, nr 2, pp. 5-13, doi: 10.14313/PAR_232/5	[17]
K. Podbucki, T. Marciniak, „Aspects of autonomous drive control using NVIDIA Jetson Nano microcomputer”, in Proceedings of the 17th Conference on Computer Science and Intelligence Systems PTI, 2022, pp. 117-120, doi: 10.15439/2022F89	[38]
K. Podbucki, J. Suder, T. Marciniak, A. Dąbrowski, „Evaluation of Embedded Devices for Real-Time Video Lane Detection” in Mixed Design of Integrated Circuits and System MIXDES 2022, Lodz, Poland: Lodz University of Technology, 2022 - pp. 187-191, doi: 10.23919/MIXDES55591.2022.9838167	[39]
J. Suder, K. Podbucki, T. Marciniak, A. Dąbrowski, „Intelligent vision system for quality classification of airport lamp prisms” in SPA 2022 Signal Processing : Algorithms, Architectures, Arrangements, and Applications : Conference Proceedings, Poznan, 21st-22nd September 2022: IEEE, 2022 - pp. 151-154, doi: 10.23919/SPA53010.2022.9927908	[40]
J. Suder, T. Marciniak, K. Podbucki, „Real-time density maps generation of moving objects using embedded systems” in Proceedings of ELMAR-2022: 64th International Symposium ELMAR-2022, 12-14 September 2022, Zadar, Croatia, IEEE, 2022 - pp. 179-184, doi: IEEE, 2022 - pp. 179-184, doi: 10.1109/ELMAR55880.2022.9899807	[41]
T. Marciniak, K. Podbucki, J. Suder, A. Dąbrowski, „Analysis of Digital Filtering with the Use of STM32 Family Microcontrollers” in Advanced, Contemporary Control: Proceedings of KKA 2020 - The 20th Polish Control Conference, Łódź,	[42]

Poland, 2020, Cham, Switzerland : Springer International Publishing, 2020 – pp. 287-295, doi: 10.1007/978-3-030-50936-1_25	
K. Podbucki, J. Suder, T. Marciniak, A. Dąbrowski, „CCTV based system for detection of anti-virus masks” in SPA 2020 Signal Processing: Algorithms, Architectures, Arrangements, and Applications : Conference Proceedings, Poznan, 23rd-25th September 2020: IEEE, 2020 - pp. 87-91, doi: 10.23919/SPA50552.2020.9241303	[43]

The most important distinctions and awards granted for research and scientific work both during conferences and competitions:

- 1st Prize in the "Competition for an outstanding diploma thesis of full-time and part-time first or second cycle studies in the field of technology and organization of production and services" awarded by the FSNT NOT in Poznań in 2018 for the engineering diploma thesis entitled: "Platforma pomiarowa do badania jakości działania lamp lotniskowych"
- 1st Prize in the IEEE 2019 "Diploma Thesis Competition" awarded by the IEEE Poland Section for the engineering diploma thesis entitled: "Platforma pomiarowa do badania jakości działania lamp lotniskowych"
- Distinction of the Teleinformatics Forum Program Council in the category "Best substantive work" awarded by the Program Council of the Teleinformatics Forum 2019 for the project entitled "Platforma pomiarowa do badania jakości działania lamp lotniskowych" in the category "Best substantive work" in the competition of the Young Masters Forum "Economic Aspects of Informatisation of the State, Digital Modernization of Poland" at the XXV Teleinformatics Forum
- Distinction of the Scientific Committee of the 20th National Conference on Electronics in the "Young Scientists" competition in 2021 awarded for the paper "Color sensors in an application to detect the type of airport lights" in the thematic group Optoelectronics and photonics
- The Main Prize of the national inter-university Young Masters competition 2021 awarded by the Program Council of the XXVII Teleinformatics Forum and the Masovian Branch of the PTI for the project "Video monitoring system for detecting worn anti-virus masks based on deep neural network learning"
- Distinction of the Scientific Committee of the 21st National Conference on Electronics in the "Young Scientists" competition in 2022 awarded for the work "Application of the Nucleo STM32 module in teaching microprocessor techniques in Automatic control" in the thematic group Teaching electronics at the academic level

- Distinction of the Scientific Committee of the 21st National Conference on Electronics in the "Young Scientists" competition in 2022 awarded for the work "Microprocessor light intensity sensor for examining airport lamps" in the thematic group Metrology
- Best Student's Paper Award 29th International Conference MIXDES 2022 awarded by Scientific Committee of Mixed Design of Integrated Circuits and Systems (MIXDES) Conference for the presented article entitled "Evaluation of Embedded Devices for Real-Time Video Lane Detection".

The scientific and research internship from July 1, 2022 to September 30, 2022 was possible thanks to scientific cooperation with Poznań-Ławica Airport. During its duration, a number of studies were carried out on the quality of operation of the AGL, including a comparison of the characteristics of used and new lamps. In addition, a video and sensory measurements datasets in the working environment of the measurement platform for testing AGL were also prepared. The collected data allowed for further scientific work related to the preparation and implementation of data processing algorithms.

During the research work, concepts of various solutions and systems were proposed which are directly related to the PhD dissertation (Table 3). Their creation was possible thanks to participation in the Smart4All (Horizon 2020) and Inkubator Innowacyjności 4.0 (MNiSW) projects. Funds were also obtained thanks to the competition of the Faculty of Control, Robotics and Electrical Engineering for Young Staff no. 0211/SBAD/0820 as well as from the Division's research subsidy.

Table 3 List of concept systems and solutions directly related to the topic of PhD dissertation

Project/system topic	Reference number
Measurement platform for quality testing of airport lamps	[17], [25], [28], [29], [30], [31], [32], [33], [36], [37], [39]
Laboratory assessment system for in-pavement airport lamps	[26], [27], [29], [30], [32], [34], [35], [40], [42]
Measurement system for assessment quality of elevated airport lamps from approach system	[27], [29], [30], [34]
Chromaticity assessment system for airport lamps	[30], [34], [37]

The currently used systems for monitoring the measurement vehicle surroundings are not popular because most of measurements in specific conditions are still focused on assessment done by people. Technological progress is extremely fast and new tools, such as various

artificial intelligence algorithms, allow for better, more effective and the most important automatic examination. For this purpose detailed environment and object analysis must be provided.

The originality of the research topic is development of a supervisory measurement vehicle system, which use integrated data from different sensor sources and process it using embedded devices or PC. The development of new data processing algorithms and their integration contribute to the global development of systems that will be responsible for improving precision and efficiency of measurement vehicles in the future. The innovative approach of combining information from various types of environmental monitoring devices (visual and sensory) and their analysis will allow the development of an effective solution that can be used in various specific environments after adaptation. The final result is innovative in the field of assessment airport lamps photometric parameters using measurement vehicles.

1.4 Organization of the thesis

The organization of this dissertation is as follows: after an introduction outlining the general research area in Section 1.1, Subsection 1.2 describes the objective and scientific thesis of the study. Subsection 1.3 lists the main scientific achievements, while Section 1.4 discusses the structure of the work.

Chapter 2 presents a more detailed analysis of the research area. Section 2.1 focuses on multisensory location measurement. Next, Chapter 2.2 describes electronic measurement sensors. Specifically, Subsection 2.2.1 covers Global Navigation Satellite System (GNSS) modules, Subsection 2.2.2 examines the use of LiDAR sensors, Subsection 2.2.3 explores the application of vision monitoring and Subsection 2.2.4 discusses photosensitive elements for light measurement. Chapter 2.3 is dedicated to methods and devices for testing airport navigation lights. Subsection 2.3.1 reviews the requirements for AGL systems, while Subsection 2.3.2 describes methods for evaluating in-pavement airport navigation lights.

Chapter 3 outlines the proposed techniques for enhancing multi-sensor localization. Section 3.1 lays the groundwork by presenting the concept of a multi-sensor system specifically designed for monitoring a measurement vehicle. This system integrates various sensors to enhance the accuracy and reliability of localization. Section 3.2 focuses on GNSS data filtering using the HDOP parameter and number of visible satellites. Subsection 3.2.1 focuses on static localization error measurement using GNSS while Subsection 3.2.2 on dynamic conditions. Distance correction based on LiDAR sensors with the RANSAC algorithm is presented in Section 3.3 with preliminary experiments description in Subsection 3.3.1. Subsection 3.3.2 highlights the detection of elevated airport edge lamps using LiDAR, while

Subsection 3.3.3 focuses on classifying the LiDAR point cloud data, which is crucial for accurately interpreting the surroundings. Section 3.4 discusses the detection of characteristic points in video sequences. This includes a proposed modified algorithm for detecting light spots, detailed in Subsection 3.4.1, and an analysis of how varying lighting conditions affect the performance of this algorithm, covered in Subsection 3.4.2.

Chapter 4 proposes the integration of light sensors for evaluating AGL. Section 4.1 begins with an analysis of the luminous intensity distribution of in-pavement AGL. Subsection 4.1.1 examines the influence of different AGL power supply types on measurements using illuminance sensors. Subsection 4.1.2 presents a laboratory assessment of the photometric characteristics of AGL. A proposed polynomial correction for assessing AGL using illuminance sensors is detailed in Subsection 4.1.3, which is followed by an evaluation of the photometric parameters of selected used and refurbished AGL in Subsection 4.1.4. Section 4.2 focuses on the design of a matrix with a regular arrangement of photodiodes. Subsection 4.2.1 analyzes the time required to acquire measurements using these sensors, while Subsection 4.2.2 describes the design of the photodiode-based illuminance sensor itself. The measurement algorithm for the sensor matrix is then outlined in Subsection 4.2.3. Section 4.3 explores an alternative matrix design featuring an irregular arrangement of photodiodes. Subsection 4.3.1 evaluates the performance of this proposed measurement matrix in AGL applications. Finally, Subsection 4.3.2 provides a comparison of the proposed solution with reference measurements to validate its effectiveness and accuracy. Section 4.4 focuses on proposed AGL measurement platform with environment monitoring.

The dissertation is closed with the conclusions presented in Chapter 5.

Chapter 2

Current methods and solutions in sensorial measurements

2.1 Multi-sensors localization measurement

Multichannel data analysis thanks to the use of multiple measurement sources allows for obtaining more advanced and more accurate results. This can be achieved by combining sensors of different types or the same ones into systems that focus on other aspects that are not achievable by a single sensor due to its uncertainties and perceptual limitations [44]. Using multi-source and heterogenous information fusion (MSHIF) it is possible to obtain precise measurement data from sensorial system. The concept of sensor data fusion means using the diversity of sensors and their mutual spatial, geometric and temporal arrangement to effectively extract measurement information from them [10], [45]. For example to average the light intensity measurement in a given area by using multi-channel measurement and subsequent data analysis. An inherent aspect is the correct analysis of the received data, which is preceded by preprocessing and data integration to finally obtain extracted features, objects or measurement data depending on the task being performed [12]. The implementation of some tasks requires the use of multiple sensors, which has influenced the development of various data fusion techniques. In general, they involve correlating and combining data from one or more sources in order to obtain precise position coordinates and assess the current situation and threats and identify their significance [46]. This allows predicting and estimating the states of an object or the environment in which it is located [5], [47].

The application of the approach using MSHIF has a wide spectrum, ranging from cars and robotic vehicles to advanced driver assistance systems (ADAS) [48], [49] and simultaneous localization and mapping (SLAM) [50]. Moreover, it is used for locating and navigating in various environments by tracking objects [51] also in case unmanned aerial vehicle (UAV) eg. drones [52]. Systems using MSHIF also support vision systems, allowing for the improvement of object tracking by eliminating noise and blind spots of individual cameras, creating a system operating on an information matrix and a weight vector [53]. Multi-channel data analysis also directly concerns people, starting from monitoring their health [54] as well as human-machine interaction [55]. One of the most important areas focusing the application of MSHIF

systems is broadly understood robotics [11], [56] and production processes, including fault detection [57] and remote sensing [58].

In the case of automated driving (AD), the use of sensors is crucial for the correct perception of the environment, and their cooperation determines the safety of autonomous vehicles [59]. The aspect of the sensor system's resistance to single sensor failures [5], [60], [61] is also extremely important. If the signal sources are multiplied and complement each other, safe operation of navigation algorithms and detection of objects and obstacles is possible. AD vehicles use seven types of sensors, such as: global navigation satellite system (GNSS), LiDAR, camera, radar, inertial measurement unit (IMU), ultrasonic sensors and communication module, which, when combined with each other, use their advantages while eliminating the impact of their individual disadvantages [12].

In the case of vehicles, including autonomous vehicles, sensors are divided into two main categories: those responsible for locating the vehicle in the environment, e.g. on the road, and those checking the environment for the detection of objects around the vehicle (Figure 9) [62]. The first group includes the Global Navigation Satellite system (GNSS), Inertial Measurement Unit (IMU) and odometer sensors whose task is to determine the position in relation to the environment. The second category, in turn, is responsible for perception using sensors such as LiDAR, camera, radar and, in the case of specialized measuring vehicles, e.g. light intensity sensors [63].

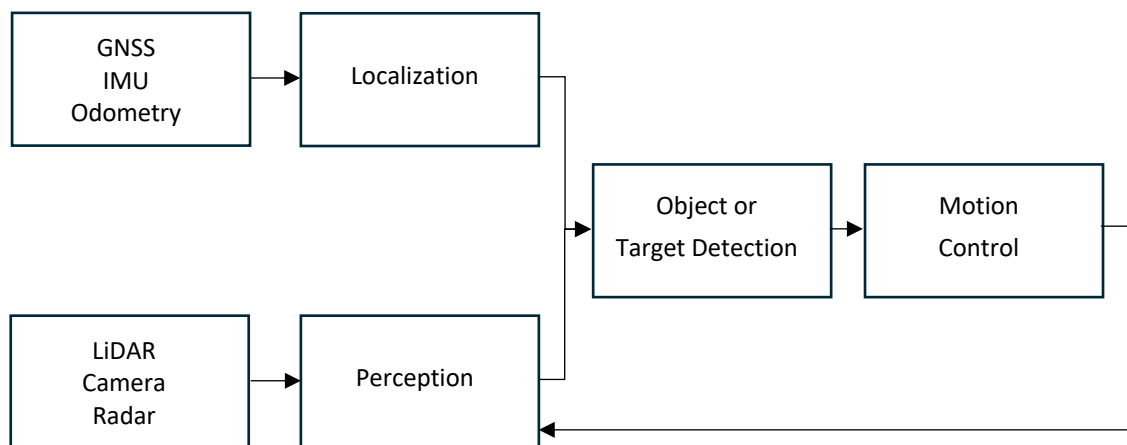


Figure 9 General scheme of multi-sensory vehicle environment monitoring

Raw data captured by the sensors are subjected to mathematical transformations thanks to digital signal processing [64], including, for example, filtration, transformation by a mathematical model or a neural network model. The multi-sensor environment monitoring solutions requires enormous workload of data collection to obtain high accuracy models [12]. As a result of these processes, the output includes extracted special features and classified objects, which constitute data for further fusion and analysis. Both static and moving objects

can be detected and classified using the same data. Classification stage requires creation of model of environment that after implementation to control algorithm can perform object type identification [61] e.g. vehicles, pedestrians, buildings, etc. Such data information can be valuable in known and pre-mapped environments as well as unknown ones [65]. The key element of MSHIF is calibration stage which is necessary to combine different coordinate systems and data rates from sensors to correspond with each other by mapping simultaneous target information in heterogeneous information for unified coordinates system [6], [19]. This type of calibration is called extrinsic and is used to compare data from different types of sensors. However, it is worth mentioning the intrinsic calibration, which is responsible for a constant and correct measurement from a single sensor. Repeatable differences in the received data can be recalculated in such a way as to eliminate errors between the expected and received results. Most often, they are caused by the physical characteristics of the sensors, their production process and quality [65]. For accurate detection of objects and therefore for safe and correct operation of decision-making algorithms in the case of autonomous vehicle (AV), it is necessary to individually and mutually arrange many sensors that make up the entire measurement system.

Various sensors have certain limitations in given environments, which affects their reliability and accuracy in object detection. They differ from each other in characteristics such as detection range, so multi-sensor fusion significantly improves the effectiveness of recognizing and locating objects in the environment. The correct selection of specifications and types of sensors has a direct impact on the quality and quantity of information collected by the system monitoring the vehicle's surroundings. Table 4 summarizes the advantages, disadvantages and maximum operating range of selected sensors [12], [66], [67].

Table 4 Features comparison of different types of sensors

Sensor type	Advantages	Disadvantages	Max operating distance
GNSS	<ul style="list-style-type: none"> Widely used in portable devices Suitable for rough positioning 	<ul style="list-style-type: none"> Presence of drift Data refresh rate Satellite visibility dependence 	No limitations
LiDAR	<ul style="list-style-type: none"> High range resolution High angle resolution Wide field of view (FoV) 	<ul style="list-style-type: none"> High cost May be interfered with by other LiDARs Errors occur in bad weather conditions 	~200 m
Camera	<ul style="list-style-type: none"> Color distribution information Excellent discernibility Large data content 	<ul style="list-style-type: none"> Requires high computational complexity Weather and light conditions susceptible 	~250 m (depending on the lens)

MSHIF technology has great advantages in the form of very accurate quality and performance results [10], [45]. Currently, the most common sensor combination in data fusion is radar camera (RC) 69%. In second place with 17% was the combination of camera radar and lidar (RCLi) data. Fusion of data from the camera and LiDAR occurs in approximately 12% of MSHIF solutions, while the combination of information from radar and LiDAR is less than 2% [12]. One of the problems of using data fusion is the increasing complexity of the structure of the network processing information from sensors in order to achieve an increase in recognition accuracy with an increasing amount of input data. Some studies show that the aspect of communication between vehicles should be added to MSHIF methods in order to achieve an appropriate level of safety in the context of autonomous vehicles [12].

The most frequently used data fusion method in computer vision tasks, in addition to traditional methods [68] using single sensors and single fusion, is the use of deep learning [69], [70], [71], [72] based on data from LiDARs and cameras. There is also an approach using multi-sensor systems with a single fusion method [73]. By monitoring the vehicle's surroundings in this way, accurate perception of the entire surrounding area is possible. By using complementary sensors such as a camera, LiDAR or radar, their mutual weak points resulting from their characteristics are eliminated, while increasing the tolerance for errors and the accuracy of perception of the entire system [63].

There are two types of data fusion: homogeneous and heterogeneous data fusion. The first one includes sensory data from sensors of the same type, which may or may not differ in type or model. Heterogeneous data fusion involves integrating data from sensors of different types and being robust, tolerating small differences between measurements of the same sensor, and combining the discrepancies into a consistent reading [65]. The use of data fusion for multiple heterogeneous sensors allows for achieving greater data accuracy and eliminating and solving problems of a mechanical nature as well as those resulting from measurement errors and noise [74].

There are three main frameworks that determine at what stage multisensory data fusion occurs [63], [75], [76], [77], [78]:

- High-Level fusion (HLF)
- Mid-Level fusion (MLF)
- Low-Level fusion (LLF).

They differ from each other in their sequential approach to performing the multisensory data fusion task. In HLF, each sensor independently performs an object detection or tracking algorithm, and then fusion of these outputs is performed. With LLF, raw sensor data is correlated at the lowest level so that another higher-level algorithm can further analyze it to

detect features and objects. The MLF framework combines these two approaches into one at the feature level, where sensory fusion is implemented both at the level of raw data as well as partially already extracted features. The advantages and disadvantages of each described multisensory data fusion frameworks are summarized in Table 5 [7], [8], [77].

Table 5 Advantages and disadvantages of sensor fusion approaches

Sensor Fusion Framework	Advantages	Disadvantages
High-Level Fusion (HLF)	<ul style="list-style-type: none"> • Lower complexity • Requirement of less computational power and communication resources • Standardizing the interface towards the fusion algorithm • Not necessitate an in-depth understanding of the involved signal processing algorithms 	<ul style="list-style-type: none"> • Omits some data information • Classifications with a lower confidence value are discarded • Fine-tuning the fusion algorithms has a negligible impact on the data accuracy and latency
Low-Level Fusion (LLF)	<ul style="list-style-type: none"> • Lower signal-to-noise (SNR) ratio • More accurate data than the sensors operating independently • Potential to improve detection accuracy • Latency reduction due to no waiting time for previous data processing 	<ul style="list-style-type: none"> • Generates large amount of data • Issues in terms of memory and communication bandwidth • Requires precise calibration of sensors to accurately fuse their perceptions • Challenge to handle incomplete measurements • Data redundancy which results in low efficiency
Mid-Level Fusion (MLF)	<ul style="list-style-type: none"> • Generates small information spaces • Requires less computation power than LLF • Provides a powerful feature vector • Recognition accuracy improvement by features selection algorithms that detect corresponding features and features subsets 	<ul style="list-style-type: none"> • Requires large training sets to find the most significant feature subset • Requires precise sensor calibration before extracting and fusing the features from each sensor

Research [22], [79], [80] shows that the use of data fusion from multiple sensors is much more effective than the use of single sensors without data integration. Moreover, some types of sensors used in selected environments allow for the detection of unique data containing the features of objects and their location with varying accuracy and detail [13], [45], [61], [81], [82].

Environmental monitoring systems with only a single measurement sensor have certain limitations and drawbacks. The first is the risk of loss of perception when the sensor stops working and there is no device that could replace it in an emergency situation. Moreover, in the case of measurement uncertainties, when there is no information about certain features of an object or the environment, it is impossible to measure all aspects using only one sensor.

The use of one measurement module causes measurement inaccuracies, which result from a limited time range, limited frequency of measurements and a limited spatial range limited to a certain section of the surroundings [65].

The described system limitations resulting from the use of a single measurement sensor can be reduced or even completely eliminated by using multiple measurement modules [9], [10], [81], [82], [83]. One of the advantages of this solution is increased reliability in the event of a failure of some sensors, while the remaining ones are still able to monitor the surroundings. In addition, measurement reliability is increased by confirming measurement accuracy by other modules. Measurement resolution is also improved thanks to multiple independent data readings for the same property. Multi-sensor systems are also characterized by increased resistance to interference and reduced measurement uncertainty due to the complementation of measurement data. The temporal and spatial scope of the area where the environment is monitored is also extended. Measurement data, after processing by a complete algorithm that integrates readings from many sensors, also reduces the amount of interference and noise at the output.

Multi-sensor system data collection can be performed in different scenario: distributed, concentrated and mixed (Figure 10) [84]. In the first method, data from sensors are collected sequentially and the fusion result is calculated after each polling procedure. In the case of the concentrated method, measurements from the sensors are read simultaneously and the data are combined into a collective result. The mixed method involves combining the first and second approaches.

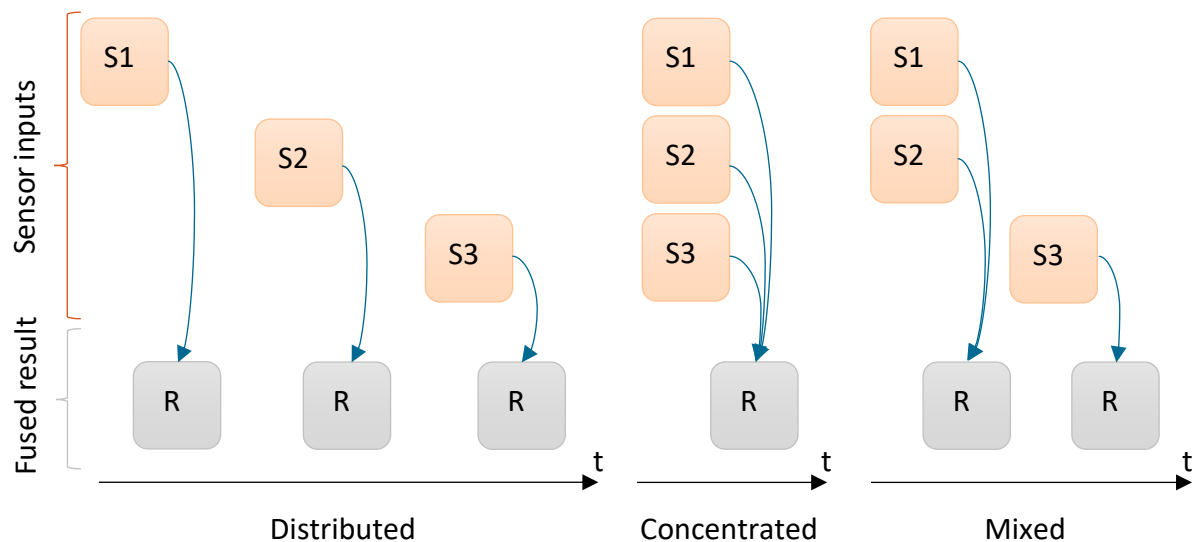


Figure 10 Multi-sensor system data collection scenario

There are two main types of data processing system architecture: decentralized and centralized. In the first approach, all agents participate in the data integration process by

operating on their own and neighbors' data. This allows for processing smaller portions of data, which speeds up the process, but there is an increased demand for resources to ensure communication between systems, the cost of which is $\omega(n)^2$ at each stage of communication, where n is the number of nodes. In a centralized architecture, one efficient system allows for data fusion. However, it requires high computing power, which often results in significant hardware costs. Moreover, in multi-sensor systems, the use of a centralized architecture can lead to a situation where most of the resources will be used for the data fusion operation [21], [85], [86].

One of the disadvantages of using multi-sensor systems is their additional complexity, however, the use of appropriate data integration techniques allows for the optimization of algorithms monitoring the environment in which the system is used [65]. There are many ways to implement sensor fusion, ranging from classic algorithms derived from probabilistic, statistical, knowledge-based, evidence reasoning, interval analysis methods, but also deep learning algorithms using convolutional neural networks (CNN) with single-stage detectors or two-stage detectors and recursive neural networks (RNN). There is no clear indication of what solution will be optimal for a specific device or environment [4]. Some studies [2], [87] indicate that due to the multidisciplinary nature and diversity of the proposed data fusion algorithms, it is very difficult to compare them and select the only correct and most efficient solution.

2.2 Localization using electronic measurement sensors

A sensor is an electronic measuring device that allows to collect data about the physical aspects of the environment and transmit it in digital form to a computer. Thanks to them, it is possible to directly perceive the environment in which they are placed, and in order to perform an in-depth analysis of various physical aspects, sets of sensors are most often used to increase the accuracy and completeness of the data [65].

Sensors can be divided into two groups: non-smart sensors and smart sensors. The first group includes sensors that measure the appropriate parameters for which they were designed and send information to the system in the form of raw data, which is processed on an external device. The concept of the second group of smart sensors has evolved thanks to the development of the Internet of Things (IoT) and means devices that allow not only to collect data and send it without using an additional computer, but also to perform additional processing, interpretation and decision-making [88]. In the case of sensors installed in vehicles, examples of smart sensors are cameras, LiDARs and radars that allow tracking objects or describing events. Sensors are considered smart devices when they are equipped with resources that allow for data processing [88]. A good practice when designing systems monitoring the vehicle's surroundings is to use sensors from both described groups, so as to

increase the perception and capabilities of the entire system by fusion of collected data [4], [7], [88].

Monitoring the environment is a task that requires a thorough analysis of various types of obstacles in the environment. In specialized applications, e.g. in measuring devices, it is necessary to use a more advanced system for observing the environment in order to improve the precision of the results [17],[36]. In most cases, it is therefore necessary to make accurate distance measurements using remote techniques. There are various methods for assessing the distance from objects, e.g. using ultrasonic, radar or optical sensors. Autonomous vehicles are an extremely developing field that requires reliable and accurate solutions. The fact of their introduction to the consumer market remains only a matter of the next few years and appropriate legal regulations. Many companies are already testing their solutions on closed tracks and announcing that their vehicles with an advanced level of autonomy will enter the market in 2025 [89].

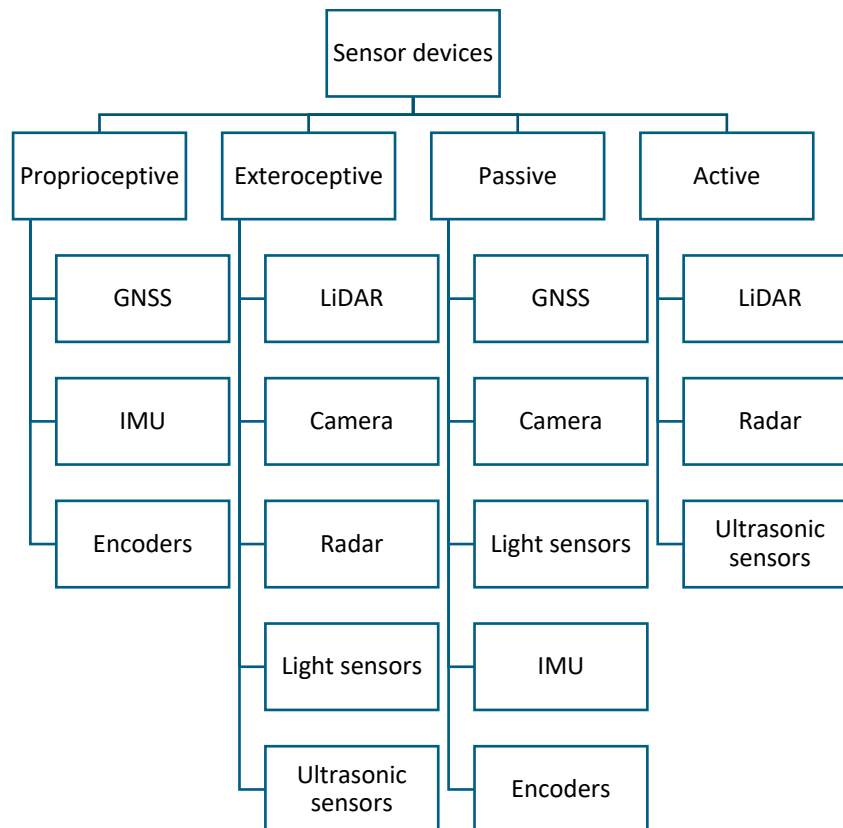


Figure 11 Division of environment monitoring devices with examples

Obtaining increasingly higher levels of driving automation for vehicles is possible thanks to the integration of sensory and vision data from various types of sensors. They act as a source of data about the surroundings in specific support systems, e.g. active cruise control, emergency braking, surrounding mapping, digital side and rearview mirrors, parking assistant, lane assistant [7]. Sensors as well as vision systems are divided into four categories (Figure 11). The first of them are proprioceptive sensors, i.e. those responsible for recording and

measuring the internal dynamics of the vehicle. Their equivalent regarding measurements of the object's surroundings are exteroceptive sensors that detect and collect information such as distance measurements. Additionally, monitoring systems can be divided into passive and active depending on the method of operation. The first of them only receive energy emitted from the environment and produce their output signal based on it. This group includes, among others, video cameras. Active sensors base their operation on emitting energy into the environment and measuring the environment's response to this energy [7].

Currently, three main trends in the approach to sensor fusion in the context of obstacle detection can be mentioned in the literature:

- CL – camera – LiDAR [90]
- CR – camera – radar [91]
- CLR – camera – LiDAR – radar [92].

Therefore, a very frequently used sensor solution supporting vision systems is the use of LiDAR. This combination allows to obtain higher measurement resolution over a larger range and precisely recognize the surroundings based on point cloud analysis and depth map information [93]. Data fusion also uses stereo vision sensors, which analyze the recorded image and provide depth information. The combination of this data with Point Cloud Data (PCD) from LiDAR and radar scans is a good source for object detection by the [94], [95], [96] algorithms, also when combining raw data [97]. This significantly improves the security redundancy of the entire autonomous system. Companies that rely on this solution to implement their solutions in autonomous vehicles include Waymo and Navya [7], [12], [63], [98], [99]. LiDAR is also used to detect objects in various environments such as ground, air and underwater [97], [100], [101], [102], [103].

Different types of acoustic and visual sensors provide different information about the environment and its elements, including obstacles and objects. A list of data types and characteristic sensors is provided in Table 6 [7], [12], [65], [104].

Table 6 Vision and acoustic sensors data types and characteristics

Data type/characteristic	LiDAR	Vision camera	Thermal camera	Ultrasonic	Radar
Data density	10^5	10^2	10^3	10^5	10^7
Low light operation	Yes	Yes	Yes	Yes	No
Position information	Yes	Yes	Yes	No	Yes
Velocity information	No	No	Yes	No	No
Class	Yes	Yes	Yes	Yes	No

Size information	Yes	Yes	No	No	Yes
Color availability	No	No	No	Yes	Yes

Based on information provided, it can be stated that there is no sensor that would be able to measure all possible types of information, so in order to supplement them as much as possible, so that the necessary data reaches the system monitoring the environment, fusion of multiple sensors should be used. Table 7 compares the performance assessment of individual sensors and their fusion under different factors in context of vehicle environment monitoring. The comparison was made based on sensor characteristics and external factors [7], [63], [65].

Table 7 Camera, LiDAR and Radar performance assessment in different conditions vs their fusion

Factor	Camera	LiDAR	Radar	Fusion
Range	Moderate	Moderate	Good	Good
Resolution	Good	Moderate	Bad	Good
Distance accuracy	Moderate	Good	Good	Good
Velocity	Moderate	Bad	Good	Good
Color perception	Good	Bad	Bad	Good
Object detection	Moderate	Good	Good	Good
Object classification	Good	Moderate	Bad	Good
Lane detection	Good	Bad	Bad	Good
Obstacle edge detection	Good	Good	Bad	Good
Illumination resistance	Bad	Good	Good	Good
Weather resistance	Bad	Moderate	Good	Good

The most commonly used sensor fusion for monitoring the vehicle environment is the various connections between the camera, LiDAR and radar. The measurement data obtained in this way from the individual sensors complement each other, providing a full picture of the environment and the vehicle's surroundings. The measurement system's resistance to lighting or weather conditions is also increased.

2.2.1 Global Navigation Satellite System

The term Global Navigation Satellite System (GNSS) encompasses satellite constellations and user equipment for civil or specialized applications. The International Civil Aviation

Organization defines GNSS in the context of civil aviation in document Annex 10 to the Convention of International Civil Aviation as *"worldwide position and time determination system that includes one or more satellite constellations, aircraft receivers and system integrity monitoring, augmented as necessary to support the required navigation performance for the intended operation"* [105].

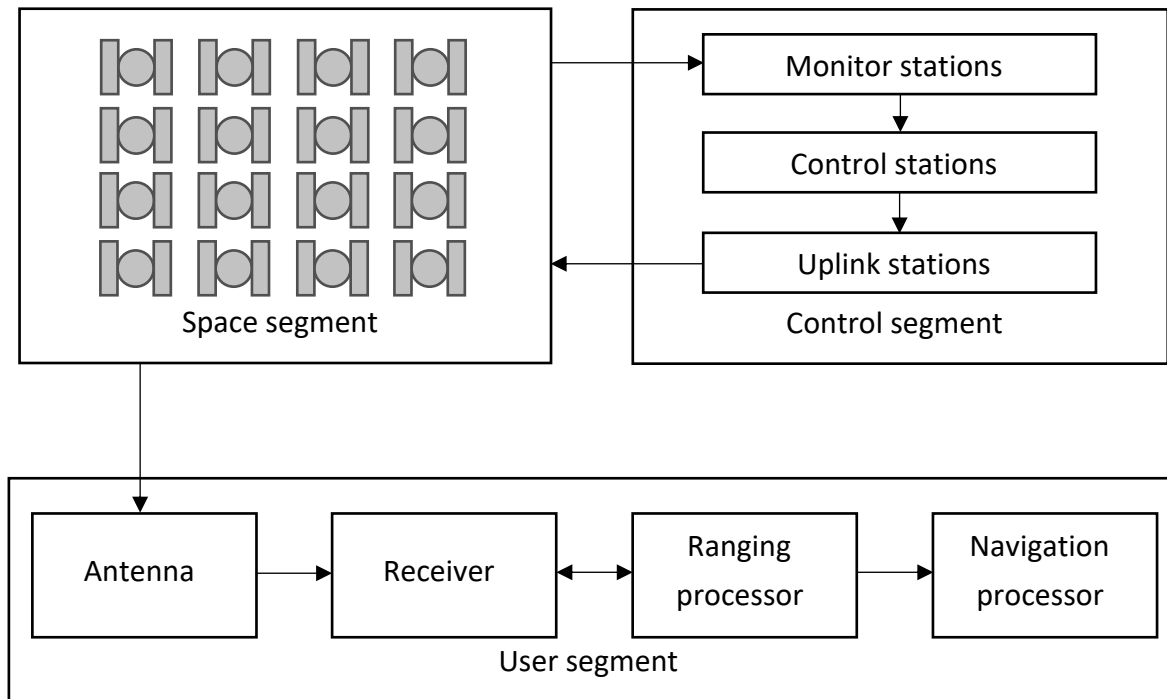


Figure 12 Global Navigation Satellite System architecture

GNSS systems usually consist of three segments: space, control and user (Figure 12) [66], [106]. User equipment has ability to use signals from one, two or multiple GNSS systems and the space but control and space segments are different for individual systems [107]. Positioning is performed using the user segment, which measures the receiver's distance from several GNSS satellites at the same time. Such measurements are subject to various types of errors - from the satellite: orbit error, clock error, signal bias, as well as during transmission - ionospheric and tropospheric delay, but the greatest deterioration in accuracy occurs on the receiver side [62], [66]. In order to reduce the impact of these errors on correct positioning, observation space representation (OSR) and state space representation (SSR) are used [108], [109]. The first method uses direct observations of the reference station or uses provided distance corrections, while the second method uses real state space data and ionospheric and troposphere models to determine the GNSS state [108]. Correction of location errors is provided at the receiver stage so that the end user is able to use the positioning device as accurately as possible. There are also different variants of GNSS systems such as differential GNSS (DGNSS) and real-time kinematic (RTK). The first one is based on pseudorange and enables positioning with meter accuracy by calculating and transmitting position and

measurement corrections using an additional base station [110]. The second variant uses the double difference ambiguity resolution to achieve precision of centimeters by introducing corrections from the base station [111], [112].

Localization is one of the most basic issues related to vehicle positioning in the environment, especially in the context of autonomous vehicles. A map of the environment in which the vehicle is located is uploaded to it or created on an ongoing basis during its calibration runs. Thanks to the possibility of localization using sensors, the vehicle's position at a given time is known, and therefore the system is able to predict what objects or characteristic features are located in its vicinity, and on their basis, provide detailed information about the position in a given environment. Due to its accessibility and availability, outdoor navigation is used in various applications such as guiding a car driver to the destination, tracking sports training, precision farming or locating measuring vehicles [113].

GNSS is currently the most common, cost-effective, and dominant technology framework for outdoor positioning [87]. Most systems are equipped with two services: one designed for civilian, commercial, and scientific applications, and one restricted to military and government purposes [88]. Currently, the available global GNSS satellite navigation systems are presented in Table 8 [114]:

Table 8 Global GNSS satellite navigation systems

GNSS system	Origin	Full operational year	Total number of satellites	Operational satellites
GPS	USA	1993	38	32
GLONASS	Russia	2011	26	24
Galileo	Europe	2016	23	5
BeiDou	China	2020	35	35

In the case of vehicles, and especially autonomous vehicles, the GNSS system, by acquiring positioning and time data, is a reference for all autonomous systems [115]. It also provides information on position, altitude, regardless of weather conditions [62]. Using a GNSS system to locate a vehicle seems to be an obvious approach, but additional sensors are used to improve positioning accuracy. As a support information for GNSS data inertial measurement unit (IMU) can be used for tasks such as simultaneous localization and mapping (SLAM) [116]. The other method is to use a dual-antenna system and an IMU to eliminate the effect of bias, which, however, increases the cost of the system. A low-cost method that allows for lateral slip estimation based on GNSS and IMU is preferable to using a camera to monitor this process, although useful angle data can be unreliable in the final comparison [117]. However, the combination of GNSS and IMU is not sufficient in the task of positioning the vehicle on

the driving lane. When tracking objects using a combination of both of these sensors, differences still appeared between the tracking trajectory and the actual path [118]. It is therefore obvious that it is necessary to use an additional data source for fusion. For this reason, camera or LiDAR information is applied to the SLAM task to accurately calibrate the position within the closed detection loop [119]. Data fusion must, however, take into account that GNSS data are subject to measurement error and drift [65].

Recently, new ideas have emerged regarding the creation of intelligent transportation system (ITS), the purpose of which is to manage connected autonomous vehicles (CAV), which requires time synchronization and accurate positioning [120], [121]. Data obtained from GNSS can be used in route planning tasks and monitoring traffic flow for entire groups of vehicles. In addition, GNSS is also used for passive vehicle safety systems and active control [122]. It should be noted that in some environments, such as urban areas, there are blockages and interferences of GNSS signals, which results in limited effectiveness of positioning. These problems can be minimized by GNSS augmentation using other localization techniques and data fusion from other sensors such as LiDAR sensors, radar or IMU [122], [123], [124].

The performance criteria for GNSS navigation are accuracy, integrity, continuity and availability [125], [126]:

- Accuracy refers to how closely the estimated position or velocity of the user matches the ground truth value [124]
- Integrity is used to define the level of correctness of data provided by the navigation system. It is applied to the level of protection and the associated integrity risk [127], which are correlated with the pseudorange measurement from each epoch [128]. Furthermore, from the user's perspective, it means the system's ability to provide various types of warnings when measurement inaccuracies occur [129], [130], [131]. There are 4 types of warnings: alert limit (AL), integrity risk (IR), time to alert (TTA) and protection level (PL) [122]
- Continuity defines the reliable operation of the system when there are no failures for a given period of time [132]. It allows to estimate the probability of reliable operation of the GNSS system assuming that it was available from the beginning of a given phase of operation. Continuity is closely related to integrity and accuracy [129]
- Availability describes the percentage of time when the GNSS system operates in a usable manner. It can also be defined as the percentage of measurement epochs during which, regardless of the signal quality, information is delivered with the required performance [133].

An additional factor influencing the performance of GNSS systems is the satellite geometry. The parameter that determines the user's position and the distribution of visible

satellites is the dilution of precision (DOP) [134]. DOP coefficients are calculated as a function of the geometrical arrangement of satellites relative to the observer [135]. The values of the coefficients are inversely proportional to the number of satellites and their mutual arrangement relative to the operator, and at least four linearized distance equations are needed to determine them.

$$A = \begin{bmatrix} \frac{-X^{S1} - X_R}{\rho_R^{S1}} & \frac{-Y^{S1} - Y_R}{\rho_R^{S1}} & \frac{-Z^{S1} - Z_R}{\rho_R^{S1}} & 1 \\ \frac{-X^{S2} - X_R}{\rho_R^{S2}} & \frac{-Y^{S2} - Y_R}{\rho_R^{S2}} & \frac{-Z^{S2} - Z_R}{\rho_R^{S2}} & 1 \\ \frac{-X^{S3} - X_R}{\rho_R^{S3}} & \frac{-Y^{S3} - Y_R}{\rho_R^{S3}} & \frac{-Z^{S3} - Z_R}{\rho_R^{S3}} & 1 \\ \vdots & \vdots & \vdots & \vdots \\ \frac{-X^{Sn} - X_R}{\rho_R^{Sn}} & \frac{-Y^{Sn} - Y_R}{\rho_R^{Sn}} & \frac{-Z^{Sn} - Z_R}{\rho_R^{Sn}} & 1 \end{bmatrix} \quad (1)$$

The observation matrix A contains a system of linearized n -distance equations (1), where: X^{Sn}, Y^{Sn}, Z^{Sn} - satellite coordinates, X_R, Y_R, Z_R - receiver coordinates, ρ_R^{Sn} - geometrical distance between the satellite and the receiver.

$$C = [A^T A]^{-1} = \begin{bmatrix} \sigma_X^2 & \sigma_{XY}^2 & \sigma_{XZ}^2 & \sigma_{Xt}^2 \\ \sigma_{YX}^2 & \sigma_Y^2 & \sigma_{YZ}^2 & \sigma_{Yt}^2 \\ \sigma_{ZX}^2 & \sigma_{ZY}^2 & \sigma_Z^2 & \sigma_{Zt}^2 \\ \sigma_{tX}^2 & \sigma_{tY}^2 & \sigma_{tZ}^2 & \sigma_t^2 \end{bmatrix} \quad (2)$$

$$C_{XYZ} = \begin{bmatrix} \sigma_X^2 & \sigma_{XY}^2 & \sigma_{XZ}^2 \\ \sigma_{YX}^2 & \sigma_Y^2 & \sigma_{YZ}^2 \\ \sigma_{ZX}^2 & \sigma_{ZY}^2 & \sigma_Z^2 \end{bmatrix} \quad (3)$$

Based on least-squares normal matrix A (1), the covariance matrix C consists of each calculated covariance σ (2), which describes the quality of the geometrical arrangement of satellites relative to the receiver in the Earth Centered Earth Fixed (ECEF) geocentric coordinate system. The last row and column of the matrix C describing the receiver clock error can be eliminated to obtain the matrix for Cartesian coordinates C_{XYZ} (3) and converted to the one corresponding to the NEU (North-East-Up) topocentric coordinate system using the transformation matrix F (4).

$$F^T = \begin{bmatrix} -\sin\lambda & \cos\lambda & 0 \\ -\sin\varphi\cos\lambda & -\sin\varphi\sin\lambda & \cos\varphi \\ \cos\varphi\cos\lambda & \cos\varphi\sin\lambda & \sin\varphi \end{bmatrix} \quad (4)$$

The topocentric C_{NEU} matrix after transformation using F matrix has the following form:

$$C_{NEU} = F^T C_{XYZ} F = \begin{bmatrix} \sigma_E^2 & \sigma_{EN}^2 & \sigma_{EU}^2 \\ \sigma_{NE}^2 & \sigma_N^2 & \sigma_{NU}^2 \\ \sigma_{UE}^2 & \sigma_{UN}^2 & \sigma_U^2 \end{bmatrix} \quad (5)$$

Then, based on the obtained matrix (5), the following equations of DOP coefficients are defined:

$$PDOP = \sqrt{\sigma_N^2 + \sigma_E^2 + \sigma_U^2} \quad (6)$$

$$TDOP = \sqrt{\sigma_t^2} \quad (7)$$

$$GDOP = \sqrt{PDOP^2 + TDOP^2} = \sqrt{\sigma_N^2 + \sigma_E^2 + \sigma_U^2 + \sigma_t^2} \quad (8)$$

$$VDOP = \sqrt{\sigma_U^2} \quad (9)$$

$$HDOP = \sqrt{\sigma_N^2 + \sigma_E^2} \quad (10)$$

Position DOP (PDOP) coefficient (6) defines the three-dimensional dilution of precision describing the influence of the satellite constellation on the X, Y, Z coordinates. Time DOP (TDOP) described by the equation (7) defines the influence of the satellite constellation on time errors. From both coefficients results another Geometric DOP (GDOP) (8) which specifies the geometric dilution of precision describing the influence of the satellite constellation on the X, Y, Z coordinates and time measurement. Vertical DOP (VDOP) coefficient (9) defines the vertical dilution of precision describing the influence of the satellite constellation on the altitude coordinate of the position, while Horizontal DOP (HDOP) (10) defines the horizontal dilution of precision describing the influence of the satellite constellation on the longitude and latitude coordinates. Table 9 lists the ranges of DOP parameter values along with the GNSS positioning quality assessment and a brief description of the individual assessment categories [136].

Table 9 Dilution of precision (DOP) values categories

DOP Value	Rate	Description
<1	Ideal	The highest possible level of GNSS certainty that enables use in applications requiring the highest possible precision.
1-2	Excellent	This level of GNSS assurance provides position measurements considered accurate enough for most sensitive applications.
2-5	Good	GNSS confidence level is usually defined as the minimum level of accuracy required to make accurate decisions. Position measurements should be considered as guidance for navigation by the user rather than for independent operation in an automated system.

5-10	Moderate	In this case, the GNSS position measurements can be used for certain calculations, however, it is advisable to improve the quality e.g. relocate the receiver antenna to a location with a better view of the sky.
10-20	Fair	Very low level of GNSS confidence for which the obtained position measurements can be treated as a rough estimate of the true position.
>20	Poor	For this level of GNSS confidence, position measurements should be discarded.

In the case where the satellites are spread too close to each other, the quality of GNSS performance is deteriorated and the DOP value increases [137]. On the other hand, when they are stretched and spread out relative to each other, the performance increases and the DOP value decreases [138]. Based on the readings of the HDOP parameter, it is possible to use an algorithm which, in the case of high inaccuracy of the GNSS system, can increase the weight of the other systems responsible for localization and filter out inaccurate positioning using the satellite system [139].

Examples of GNSS receiver systems are Teseo-LIV3F [140], NEO-6M [141] and SIM28 [142] and comparison of their specifications is included in Table 10. They are chips that are mounted in various types of modules designed to work with Nucleo family microcontrollers [143] (shown in Figure 13), Arduino boards or Raspberry Pi microcomputers.

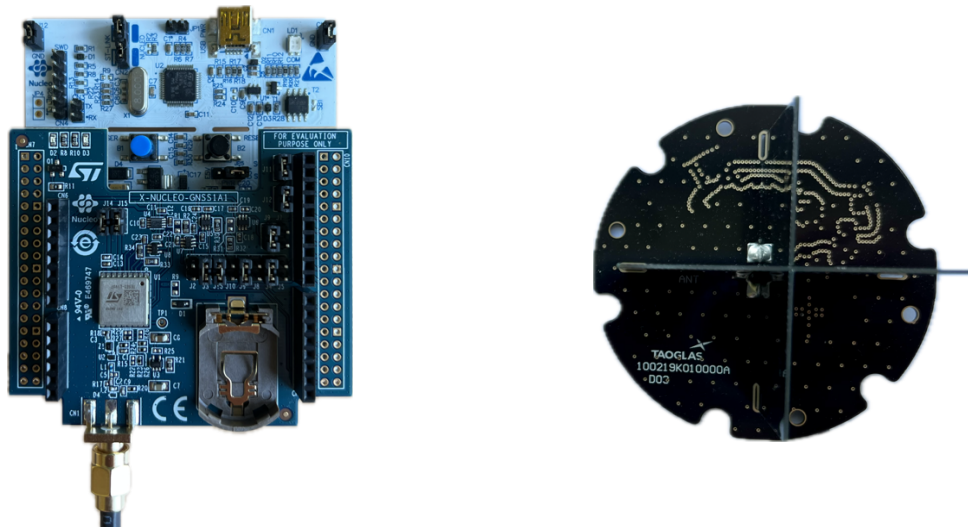


Figure 13 X-NUCLEO-GNSS1A1 expansion board based on Teseo-LIV3F for STM32 Nucleo

Table 10 Comparison of different GNSS receiver modules

	Teseo-LIV3F	NEO-6M	SIM28
Sensitivity [dBm]	-162	-161	-167
Supported GNSS	GPS Galileo GLONASS BeiDou QZSS	GPS	GPS

Communication interface		UART I ² C	UART	UART SPI I ² C
Data protocol		NMEA	NMEA UBX RTCM	NMEA PMTK
Horizontal position accuracy [m]		1.5	2.5	2.5
Time to first fix [s]	Cold start	< 32.0	27.0	13.0
	Warm start	< 25.0	27.0	1.0 – 2.0
	Hot start	< 1.5	1.0	< 1.0

Of the above, the Teseo-LIV3F system is characterized by the highest horizontal positioning precision, which is possible thanks to the possibility of using multiple GNSS systems simultaneously. The remaining modules have almost 2 times worse accuracy, which may result from collecting data only from the GPS system. All chips allow the use of the NMEA protocol to process location data, and the NEO-6M and SIM28 modules additionally support the use of UBX, RTCM and PMTK protocols. The common communication interface is UART, and the Teseo-LIV3F chip also offers I²C support, and SIM28 also SPI. The modules differ in sensitivity, with the SIM28 chip showing the highest sensitivity, which also has the shortest times to obtain the first position fix. The Teseo-LIV3F and NEO-6M systems have similar sensitivity and the time to obtain the position fix at a cold start is very similar. In the case of a warm and hot start, the difference is visible in favor of the Teseo-LIV3F system.

2.2.2 Light Detection and Ranging sensor

The LiDAR (Light Detection and Ranging) sensor is an exteroceptive active device used, among other things, to monitor the environment. The result of the sensor operation is obtaining information about a cloud of points constituting a representation of the environment in which LiDAR is located. The measurement principle used for imaging is the TOF (Time-of-Flight) method. Ambient depth is measured by counting the time delays in events in the light emitted by the source. This non-contact distance measurement technique is achieved by projecting an optical signal (laser beam) onto an object, called a target, and then detecting the reflected or backscattered signal and processing it to determine the distance. In this way, two- or three-dimensional maps of the environment are created in the form of point clouds [67].

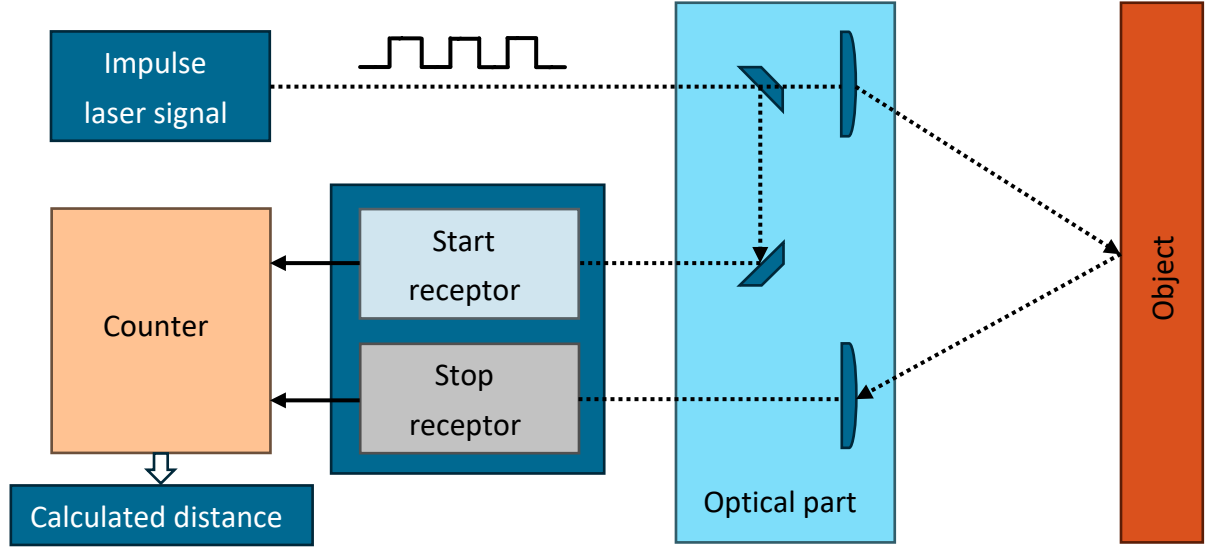


Figure 14 Scheme of the distance measurement principle in a LiDAR sensor based on pulsed modulation of the laser beam [28]

The most common approach to determining distances in ToF sensors such as LiDAR is based on the pulse modulation of the emitted laser beam (Figure 14). The measurement result is determined by the relationship between the speed of light in a given medium and the time needed for the beam pulse to cover the distance to the target. The speed of light is a constant physical value, and when the object is in the same medium, the distance to the tested object is directly proportional to half the period needed for the beam to return to the sensor. The time measured by the sensor represents twice the distance from the target, because the emitted laser signal must travel both from the emitter and back to the receiver. The relationship between the calculated distance is expressed in (11), where R is the calculated distance, $c = 299792458$ [m/s] is the speed of light, and t_{oF} is the measured value of the time needed for the return of the laser pulse emitted by the sensor after reflection from the object (12), where t_{start} is the initial beam emission time and t_{stop} is the return time to the receiver [144], [145], [146].

$$R = \frac{c}{2} t_{oF} \quad (11)$$

$$t_{oF} = \Delta t = t_{start} - t_{stop} \quad (12)$$

Equation (11) also shows a strict dependence of the resolution of the obtained distance measurements on the resolution of the counter used to measure time. The main factor influencing the obtained values are therefore hardware limitations, consisting in the selection of appropriately fast modules responsible for determining the period. Typically, the resolution of the time interval measurement is in the range of 0.1 ns, which translates into the resolution of distance measurement with an accuracy of approximately 1.5 cm [99]. These are values that can be corrected in hardware by using various types of statistics that calculate the result point based on several impulses in a given target area. However, the cost of such

an operation is a lower frame rate and spatial resolution. Theoretically, it can be assumed that the maximum distance that can be measured using LiDAR is limited by the maximum range of the counter, but in practice it depends on other factors, mainly the dispersion of the laser beam and the speed of pulse emission. When using the method of pulse modulation of the emitted laser beam for ToF devices, the aim is to use the shortest possible pulses of several nanoseconds. Their characteristic features are also fast rise and fall times while maintaining high optical power.

It is also crucial to use reflected beam receivers with a very sensitive detection level operating at high frequencies, to be able to properly interpret even a weak signal from the environment. An additional difficulty is the environmental conditions in which the measuring device operates, which may result in the absorption of laser pulses by e.g. clouds, fog, water, asphalt or tar, but it should be noted that apart from the factors mentioned above, LiDAR is almost independent of weather and lighting conditions, however the working environment is defined by the manufacturer of a specific module. The effect of interference is minimized by observing the scattered rays with a telescope. Then they are recorded by a detector that examines the phase shift between the transmitted and received waves, as well as the intensity of the return signal [147]. Equation (13) is supplemented by equation (11) with the value of the phase shift $\Delta\varphi$ between the transmitted and received signal.

$$R = \frac{c}{2} \cdot t_{\text{oF}} \frac{\Delta\varphi}{2\pi} \quad (13)$$

The pulsed approach currently remains the most frequently used solution by LiDAR manufacturers due to its simplicity of operation while maintaining sufficient accuracy in the case of sensors monitoring the vehicle environment [67].

Among LIDARs, there are three types of sensors, depending on the number of dimensions they can observe. The simplest 1D sensors only allow to measure the distance to objects. 2D LiDAR also returns information about the angle relative to the object to which the distance was measured, while 3D LiDAR allows to determine the elevation [7]. There are three main LiDAR applications: obstacle detection, positioning and environmental reconstruction. In vehicle applications, especially autonomous vehicles, LiDAR plays a key role in environmental monitoring due to its ability to provide three-dimensional (3D) data, which is a significant advantage over two-dimensional (2D) data [12], [148], [149], [150].

Depending on the technology used to perform the scan measurement, the following types of LiDAR can be distinguished [151], [152]:

- mechanical-scanners
- non-mechanical-scanners

- flash-LiDAR-non-scanners
- structured light-non-scanners
- multicamera-stereo-non-scanners.

Two-dimensional LiDAR has a single-layer structure, while the 3D variant is a multi-layer device. Due to its advanced design, it is also more expensive than a basic 2D sensor. LiDAR allows to monitor the environment both during the day and at night. There are three types of LiDARs depending on the motion unit [12]: most popular time-of-flight (TOF), phase-ranging and triangulating. Two major classes of LiDAR can be distinguished due to principle of work: mechanical LiDAR and Solid State LiDAR (SSL). Mechanical one also known as spinning LiDAR has rotating lenses driven by electric motor to scan a desired field of view (FoV) in environment. SSL instead of additional motor uses steering the laser beam on electronic level. This kind of LiDAR is more reliable, robust but they have smaller and limited FoV [63].

One of the disadvantages of LiDAR is its sensitivity to weather conditions. The analyzed impact of rainfall on the operation of LiDAR [153] showed that the range of object detection, the maximum detection range and the number of points in the point cloud are significantly reduced by up to approximately 20% compared to good weather conditions. In the case of LiDAR applications in monitoring the vehicle environment, the most common use is sensors using class 1 lasers with a wavelength of 905 nm. Their advantage is that the beam is less susceptible to absorption by water than in the case of lasers with a wavelength of 1550 nm. They also provide higher point cloud resolution in unfavorable weather conditions [154], but with the note that fog or snowfall can reduce the sensor's efficiency by up to 25% [155].

Estimation of the position of vehicles in the environment using LiDAR can be performed with a very high accuracy of up to 15 cm, which is much better than methods using GNSS [156]. Using additional methods, such as determining position using WiFi, it is possible to develop a local robot navigation system for low-light conditions, where LiDAR is responsible for detecting obstacles [157]. Despite the very good parameters and capabilities of LiDAR in monitoring the environment, its susceptibility to bad weather conditions makes it necessary to obtain additional measurement data from other types of sensors such as cameras or radars, the combination of which will provide a trustworthy and accurate measurement system, however, at a relatively high cost in purchase [12].

An example of a LiDAR model for use in environmental monitoring in laboratory conditions is the basic RPLIDAR A1M8 sensor produced by SLAMTEC (Figure 15). It allows for two-dimensional scanning of the environment within a range of 12 m, and thanks to the use of a rotating head, the measurement covers a full 360 degrees. The resulting data can constitute the basis for mapping, determining the location, modeling objects and the

environment, including detecting obstacles based on distance measurement and their positioning thanks to determining the angle. The manufacturer ensures that LiDAR can be used inside buildings and in open spaces provided there is no direct exposure to daylight [158].



Figure 15 SLAMTEC RPLIDAR A1M8 laser scanner module [28]

The device consists of two parts: a head with laser optics, which is responsible for the two-dimensional scanning process itself, and a drive part. The whole thing was mounted on a thick PCB, which, in addition to the electronic connections, is the basis for individual components, including the moving head.

Table 11 SLAMTEC RPLIDAR A1M8 technical parameters [28]

Parameter	Value
Distance range [m]	0.15 – 12.0
Angular range [°]	0 – 360
Flatness of the scanning field [°]	-1.5 – 1.5
Distance resolution [mm]	<0.5 for distance <1.5 m <1% measured distance
Angular resolution [°]	≤ 1 for frequency 5.5 Hz
Sample duration [ms]	0.125
Sampling rate [Hz]	≥8000 (max. 8010)
Scan frequency [Hz]	5.5 - 10

The scanner is an example of budget equipment (the price is around PLN 500) in its class of measuring devices while maintaining very good technical parameters (Table 11). It should be noted that the maximum distance measurement range of 12 m is possible when scanning white objects. Increasing the scan frequency to 10 Hz is possible by connecting an additional

motor power source with a maximum voltage of 9 V. The basic frequency value of 5.5 Hz is achieved by simultaneously powering both parts of the device from a 5 V source.

Additionally, the A1 series sensors are equipped with rotational speed measurement and an adaptive system that automatically adjusts the laser frequency to the current engine speed. It is also possible to read the value of this speed by the user. The laser used is modulated pulsed infrared light in the range between 775 and 795 nm. The power of the emitted beam is in the range of 3-5 mW, and the pulse length, depending on the engine speed, is typically 110 μ s to a maximum of 300 μ s [158].

The device uses the UART communication protocol for data transmission operating at a speed of 115,200 bps with a voltage of 3.3 V. To simplify connections between the computer and the laser scanner, the manufacturer included UART to USB converter. It allows the system to detect the device via the COM port. The data frame sent by the sensor contains information about the measured distance, the angular orientation of the LiDAR relative to a given point in space and the quality of the measurement. Individual measurement points are separated from each other by a start flag, which is a Boolean value.

The LiDAR sensor returns point cloud data (PCD) as output containing the position (x, y, z coordinates) and intensity information of detected object. The intensity value is equivalent to object's reflectivity. Due to the very large information content, which may significantly affect the processing efficiency and demand for computing power, the operating scheme presented in Figure 16 is used, which consists of the following main stages: downsampling and data filtering.

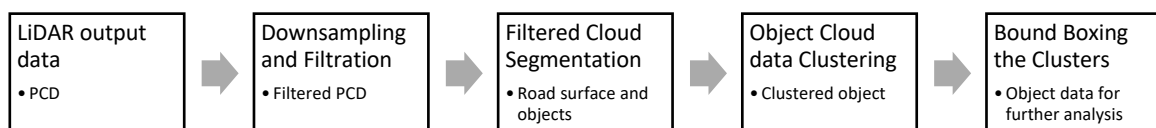


Figure 16 LiDAR data processing pipeline

In a further step, the processed data is limited to the region of interest (ROI) to filter out those points that should not be taken into account by the algorithm, in order to be able to perform PCD segmentation into objects and surface in the next step. Based on the similarity to neighboring points, e.g. using the Euclidean Clustering method, a new coordinate system is assigned to each cluster, which is the average of all PCD points within the cluster. The last stage is to define bounding boxes to visualize individual detected objects, knowing their size and location [63].

One of the methods for segmenting PCD into objects and road surfaces is the use of the Random Sample Consensus (RANSAC) algorithm [159]. By taking a random sample of the

point cloud, the algorithm aims to adapt them to the road surface. Points included in it are classified as inliers, and any objects deviating from the road surface are classified as outliers. As output, the road surface is returned as the class containing the largest number of inliers or least number of outliers, which are the objects that are being searched for [63]. The block diagram of the RANSAC algorithm is shown in Figure 17.

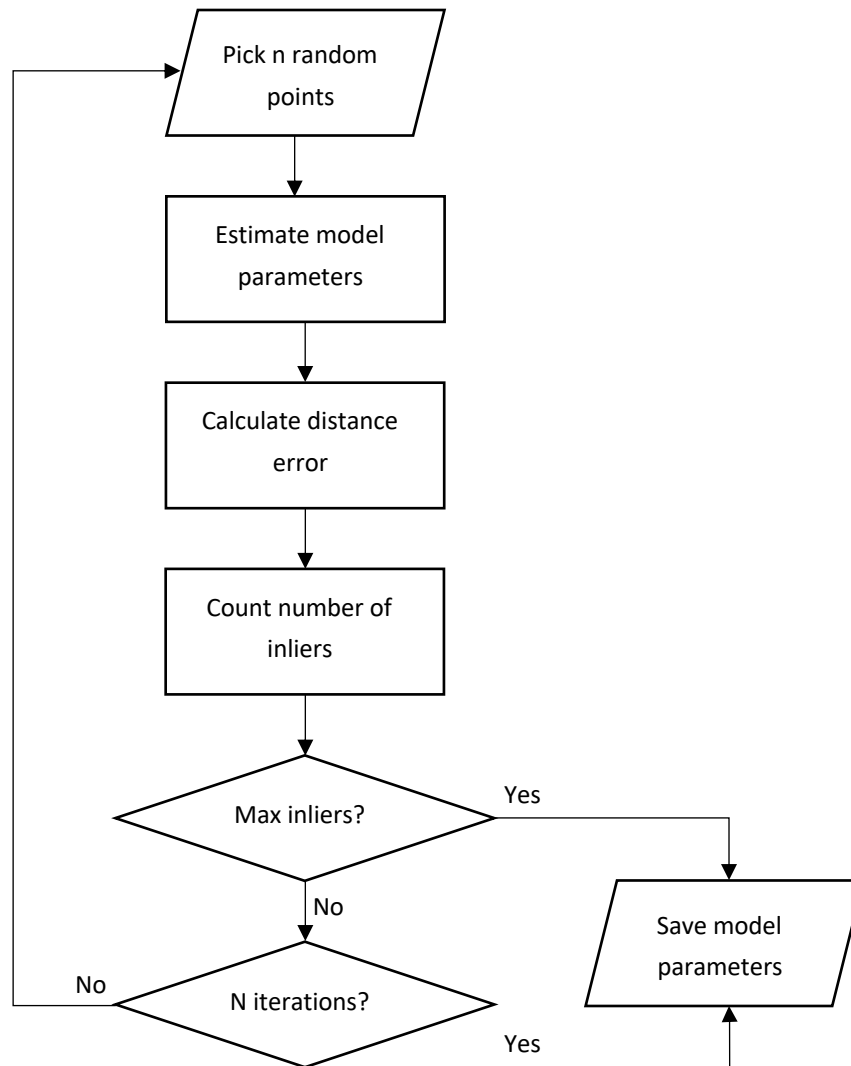


Figure 17 RANSAC algorithm block scheme

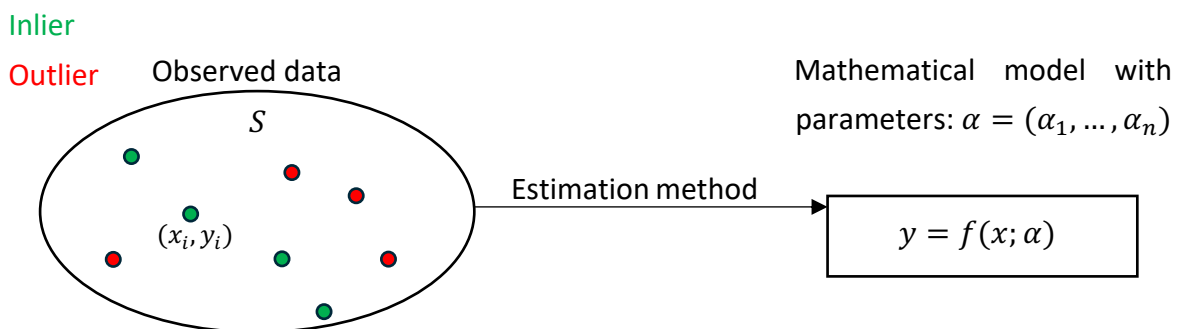


Figure 18 RANSAC algorithm data classification

The RANSAC algorithm is presented using equations assuming that there is a data set S consisting of i points with coordinates (x_i, y_i) . The goal of the algorithm is to iteratively estimate the model parameters from the set S of observed data, which contains outliers by taking randomly chosen n points in every iteration. The general mathematical equation of the model with parameters $\alpha = (\alpha_1, \dots, \alpha_n)$ is represented by (14).

$$y = f(x; \alpha) \quad (14)$$

The most common models that are a linear function, quadratic function and cubic function. Data are collected for calculations iteratively, and the model estimation is based on the number of inliers, e.g. the least squares method. By denoting the number of iterations by N , it should be chosen in such a way as to provide probability p (as close as possible to 0.99), which means that one of the sets of random samples does not contain an outlier. Let u denote the probability that any data point is an inlier and $v = 1 - u$ the probability of observing an outlier point. Therefore, N iterations of the algorithm are required for a defined minimum number of inlier points m , which is given by the equation (15) and after transformation (16).

$$1 - p = (1 - u^m)^N \quad (15)$$

$$N = \frac{\log(1 - p)}{\log(1 - (1 - u)^m)} \quad (16)$$

The RANSAC algorithm works effectively when it allows for the correct classification of inliers and outliers points. On their basis, it is possible to further analyze the point cloud for object detection and the environment background, which can be used for object detection.

2.2.3 Analysis of vision sequences in video monitoring

The popularity of vision solutions is increased by relatively low cost camera modules which are frequently used sensors in the context of monitoring the surroundings of vehicles and was one of the first to be used in this application. Cameras allow to record an image that carries information such as color, texture, contour and a given object seen through the lens from a specific angle. They are used in various tasks, including: lane detection, pedestrian detection, obstacle detection, for recognizing and tracking objects, pedestrians, vehicle information or planning local traffic paths [1], [12], [160], [161]. In recent years, solutions using deep learning are gradually replacing traditional image analysis methods, especially in the case of very large amounts of data [12].

In monitoring the surroundings of vehicles, various camera systems are used: monocular cameras, binocular cameras or their combination. The first one takes a series of photos using

a single camera, which results in the limitation of the lack of direct information about the depth of the image, however, there are computationally complex methods that, using e.g. dual-pixel autofocus hardware, are able to calculate it [162], [163], [164]. It is also possible to use two cameras with a single matrix to build a binocular camera set. Binocular cameras known as stereovision cameras use two matrices with a small spacing between them, which is called the baseline. This is a solution that also has its roots in the case of human spatial vision, where two eyes enable the perception of image depth. In the case of cameras, thanks to the use of algorithms based on triangulation methods and epipolar geometry, it is possible to determine disparity maps serving as a source of information about the depth of the image [7].

There are various types of cameras available on the market, from USB cameras to RGB cameras, including mono cameras and cameras with image depth information, 360-degree cameras and Time-of-Flight (TOF) cameras. USB and RGB cameras do not require special drivers for use, are rather easy to use, and at the same time allow for collecting the right amount of data for further image processing [65]. More advanced technological solutions are used in the case of 360-degree cameras to obtain their full field of view. Starting with hardware solutions, where two lenses with a 180-degree field of view are most often used, and ending with software that allows for combining images into one. The big disadvantage of this type of solution is the high price, reduced image quality, long rendering time and increased memory demand due to the large volume of data [65], [95], [165]. TOF cameras combine camera technology with IR-based depth information with the difference that they use a one-look approach in contrast to laser sensors. It results in fast algorithm operation, which however increases with the measured distance. Solutions of this type are characterized by the need for high computing power despite low image resolution. They are also susceptible to the complexity of the environment, they may require additional illuminators for correct operation, and moreover, several TOF cameras working simultaneously in a small area may cause interference [166], [167], [168].

Depth cameras, similarly to LiDAR, provide information about distances in the environment. However, they differ in the method of measurement. LiDAR allows for generating information about depth by interacting directly with the environment, while cameras are most often based on disparity information from the image. This type of solution has its advantages in the form of rich data about depth and luminance, but a major limitation is the small field of view. In contrast, LiDAR is characterized by a very wide field of view, but does not provide any additional information apart from geometric and spatial dependencies of the environment [169], [170]. These sensors can therefore complement each other very well, reducing false positives and improving the quality of disparity images [171].

Currently, there are two main types of camera sensors: complementary metal-oxide-semiconductor (CMOS) and charge-coupled device (CCD) [172]. CMOS sensors are faster and do not require as much current to operate - at the expense of lower sensitivity and higher noise. CCD converters are characterized by higher sensitivity and lower noise - at the expense of high current demand and the associated heating of the matrix itself. In CCD systems, photosites (RGB blocks) operate passively and the electrons on the sites are processed for individual columns. Analog-to-digital conversion and amplification take place outside the sensor itself. In turn, in CMOS systems, photosites are active and each of them already has an ADC conversion and an amplifier included. It is expected that in the near future CCD cameras will be mostly replaced by CMOS matrices [2], [63]. A new Live-MOS technology has also been developed, which combines the advantages of CCD and CMOS matrices [63]. A typical camera processing pipeline is presented in Figure 19.

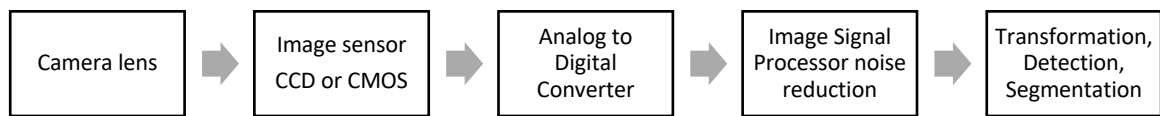


Figure 19 Camera processing pipeline

The principle of operation of the camera is based on the detection of light emitted by objects through the lens onto a photosensitive surface. Photons of light that pass through the lens reach the photosensitive surface, creating several electrons. This surface measures the light that reaches it and converts it into electron movement. In turn, the movement of electrons creates a charge, which is converted into voltage by the capacitor and then goes to the Analog-Digital-Converter (ADC). It is responsible for converting the amplified voltage into digital values. In the next step, the Image Signal Processor (ISP) reduces noise resulting from imperfections in lenses, filters and photosensitive elements, improving image quality. Typically, image sensors operate independently of wavelength and therefore record images in grayscale. To obtain a color image, micro lenses or filters are used in front of each pixel to allow a specific wavelength of light to pass through. One of the most common filtration patterns is red green blue (RGB) [63].

Due to its specificity, the camera transforms 3D information about the environment into 2D data. Therefore, in order to be able to determine the position and information about the object in the image, it is necessary to establish the relationship between the image pixel and the relationships in real conditions. There are various camera calibration methods using transformation matrices, optimization methods [18] and the use of chessboard or other checkerboards representation of known objects to obtain a lens distortion model [63], [173]. In the case of multisensory systems using cameras, calibration algorithms based on depth information [20], [165], [174], [175] are used.

Compared to other sensors, the camera has a worse resolution range than LiDAR [92], [176]. A big problem for cameras is also the adaptation time to changes in lighting conditions, which means that in the case of frequent sudden changes in light, a dynamic change of exposure is needed. In the case of autonomous vehicles, it is possible to use information from other sensors, e.g. GPS, to predict when the lighting conditions will change, e.g. when entering or leaving a tunnel [12].

In the case of autonomous vehicles, the main purpose of using data fusion with multiple sensors is to avoid false detections that could result in incorrect vehicle control. Moreover, only vehicles that achieve 100% recognition accuracy regardless of environmental and weather conditions can receive the highest safety level of the European NCAP organization [177], [178].

Image processing is a field that, due to its wide range of applications, has many methods and algorithms that allow for image modification. They enable the extraction of selected features, characteristic points in order to detect the desired object or its elements. The use of image processing allows for the optimization of algorithms in terms of the demand for computing power as well as the effectiveness of the program analyzing visual information [31], [33], [39]. There are various libraries such as OpenCV that allow for the implementation of image processing functions in programming languages such as C, C++ or Python [179]. In the case of the MATLAB environment, the Image Processing Toolbox [180] performs a similar function.

Geometric transformations are frequently used in the vision preprocessing step. Their general mathematical equation has the form (17) [181].

$$\begin{bmatrix} x_2 \\ y_2 \end{bmatrix} = A \begin{bmatrix} x_1 \\ y_1 \end{bmatrix} + B \quad (17)$$

A single pixel of the input image with coordinates (x_1, y_1) is transformed to a pixel (x_2, y_2) in the output image. Image translation (Figure 20e) is an operation that changes the position of the input image content (Figure 20a) and is performed using values given in matrix B . Matrix A contains values that allow scaling, rotation and reflection of the image. Scaling (Figure 20b) allows changing the size of the image content or the entire image by specifying the desired size of the output image or the scaling factor for each axis. Rotation (Figure 20c) is responsible for the orientation of the image content, i.e. rotation by a given angle, while reflection (Figure 20d) is responsible for flipping over the image content. Affine transformation (Figure 20f) uses both matrices A and B of the equation (17) and allows the described geometric transformations of the image to be applied simultaneously.

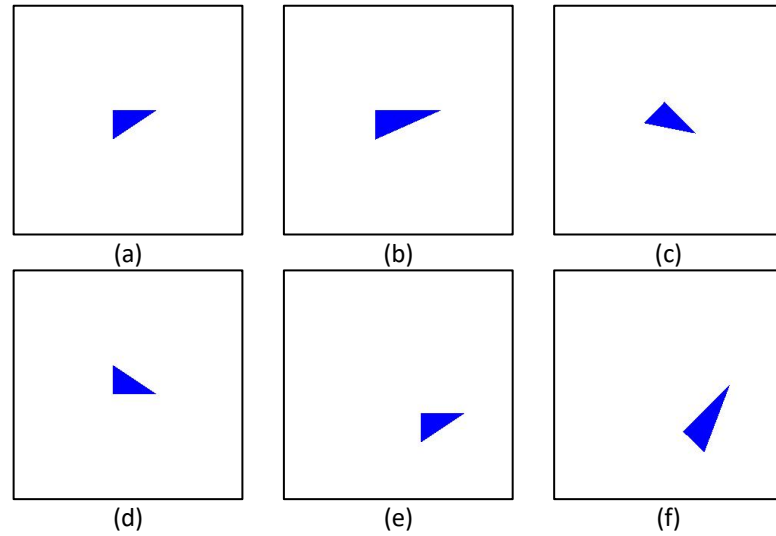


Figure 20 Geometric image transformations: original image (a), scaling (b), rotation (c), reflection (d), translation (e), affine transformation (f)

Another issue related to digital image processing is the color space. The most popular of them are the representation of three components RGB (Red, Green, Blue), CMY (Cyan, Magenta, Yellow), CMYK (Cyan, Magenta, Yellow, Black) and the HSI space (Hue, Saturation, Intensity). The first three color spaces define the content of individual components for a given pixel to obtain color reproduction. The RGB color model is most common in cameras and monitors, while CMY and CMYK are used in printing. In contrast, the HSI model reflects colors similarly to how a human does it. In addition, it separates information about the color and grayscale of the image, which allows the use of many image processing algorithms to analyze their content [182].

Images in both color and grayscale representations allow the use of thresholding techniques, which aim to extract image features and segment them. This method consists in binarizing the image by dividing pixels into two categories depending on their values - object pixels and background pixels. This division depends on a defined threshold T , which can be global for the entire image. Assuming the input image function as $f(x, y)$, where (x, y) are the coordinates of any point in the image, one can define the segmented image function $g(x, y)$ as (18) [182].

$$g(x, y) = \begin{cases} 1 & \text{if } f(x, y) > T \\ 0 & \text{if } f(x, y) \leq T \end{cases} \quad (18)$$

The use of thresholding in image processing allows the separation of the necessary objects and their features from the image, which allow for further analysis, focusing only on the essential image elements. This approach is used in the case of determining regions of interest (ROI), i.e. areas that, from the point of view of the image processing task, contain key elements to be analyzed. ROI can be determined, for example, based on threshold processing

to obtain the coordinates of pixels containing the object [182]. Determining such areas not only improves the efficiency of algorithms analyzing only a selected image section, but also reduces the demand for computing power, because it is not necessary to load the entire image into memory.

A binarized image allows the use of operations from the group of morphological transformations. They base their operation on the so-called structuring elements of the image, which consist of a specific subset of its elements, most often with dimensions of 3×3 pixels, with a selected central point. Using such an element, it is possible to transform the image in order to analyze the shape and arrangement of objects in the image. After comparing the structuring element and the binary image, a set of comparators (intersection, union, inclusion, complement) is used, which process the objects of the binary image based on their features and the shape of the structuring element [181]. The structuring element is moved through the image and the value of each pixel of the input image is compared with the values of the structuring element. If the condition defined by the operator is met for both sets, the image pixel located under the central point of the structuring element takes on a defined value of 0 or 1. Morphological transformations are used, among others, to reduce noise in the image or to select objects with a specific direction [182].

Assuming the designations: I - input binary image containing one object O , S - structuring element, d - displacement, O^c - background pixels, \hat{S} - foreground elements, patterns for individual types of operations were defined.

$$I \ominus S = \{d|(S)_d \subseteq O \text{ and } O \subseteq I\} \cup \{O^c | O^c \subseteq I\} \quad (19)$$

$$O \oplus S = \{d|[(\hat{S}_d) \cap O] \subseteq O\} \quad (20)$$

$$O \circ S = \bigcup \{(S)_d | (S)_d \subseteq O\} \quad (21)$$

$$O \cdot S = \left[\bigcup \{(S)_d | (S)_d \cap O = \emptyset\} \right]^c \quad (22)$$

There are four basic morphological image transformations: erosion (19), dilation (20), opening (21) and closing (22) and their illustrated operation is shown in Figure 21.

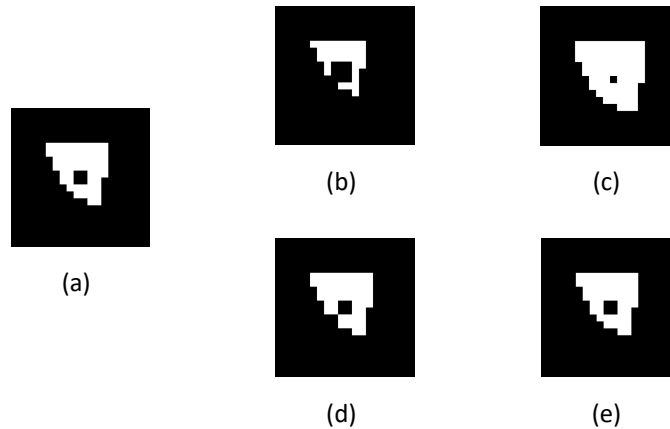


Figure 21 Morphological image transformations: original image (a), erosion (b), dilation (c), opening (d), closing (e)

The purpose of erosion is to reduce the foreground pixels of the image as well as to increase the size of the holes in those areas. This is because it erodes the boundaries of the foreground pixel areas, as shown in Figure 21b.

Dilation, unlike erosion, gradually enlarges the boundaries of the foreground areas while simultaneously reducing the size of the holes in them. Figure 21c shows how this operation works.

The opening and closing operations are derived from erosion and dilation. The effect of the opening operation is to remove some of the foreground pixels from the edges of the foreground pixels, but it is less destructive than erosion because it is followed by dilation using the same structuring element. The effect of the operation is shown in Figure 21d.

The closing operation is represented as a dilation followed by erosion using the same structuring element for both operations. This results in a less aggressive action than the dilation. The operation is shown in Figure 21e.

The obtained binary image after applying morphological operations is prepared for further analysis by the algorithm. One of the frequently used methods is contour detection, which allows to determine the position and sometimes also the type of the object in the image. Functions for contour detection are included in OpenCV libraries as well as for MATLAB software [179], [180]. They work in a similar way, searching the binary image according to the algorithm [183] depending on parameters that allow for the selection of external and internal contours displayed in the form of a hierarchy. The found contours are stored in the form of coordinates (x, y) of pixels constituting the contour. In order to save memory used by the program, the list of coordinates can be reduced by assuming as the function argument a method approximating the position of pixels. Knowing the settings of the camera lens relative to the object, it is also possible to determine its dimensions, orientation and assess its quality.

The interpretation of the image content is possible thanks to the information that can be extracted from it. One of them is the analysis of the frequency of occurrence of subsequent pixel values of the image. It is presented in the form of a histogram, which shows the number of points with different brightness levels, assuming that the first element has a value of 0 and the last $2^n - 1$ if the color representation is n -bit. In the case of monochrome images, there are 256 levels of gray (Figure 22), and in the case of the color RGB representation, three separate histogram lines are used for each component separately, maintaining 256 levels for each of them.

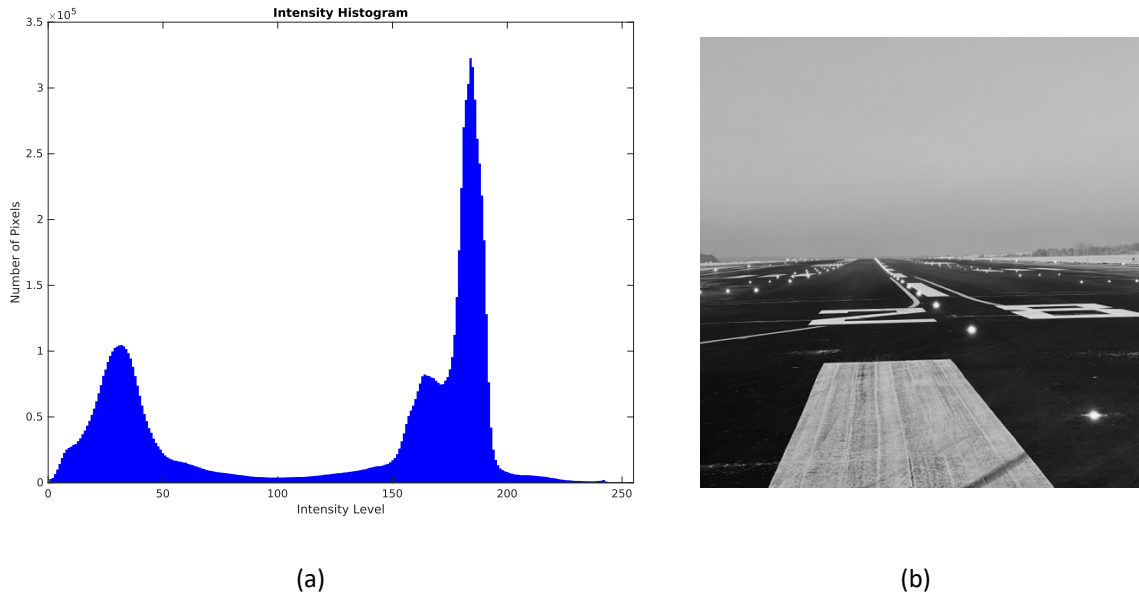


Figure 22 Histogram graph (a) of monochrome image (b)

Based on the analysis of the histogram, it is possible to evaluate the image and change its quality using, for example, histogram stretching. It consists in stretching the range of component values so that the histogram covers the entire range of the scale. In this way, the brightness and contrast values are selected. In the case of histogram analysis, it is also possible to check the number of pixels with specific values, which allows for additional data filtration [181], [182].

Using vision cameras to detect distinct objects and features within the vehicle's environment is one of the methods for determining the vehicle's position. This approach employs various image processing techniques and algorithms to extract features for further analysis. Based on this extracted data, the vehicle's position is determined by identifying the locations of notable objects within its surroundings.

To assist the operator of a mobile AGL measuring device, vision systems are utilized. These systems can analyze images to provide guidance on adjusting the driving path by detecting lamps [15], [184] and other specific markings such as lines [36]. However, a significant

limitation of the line detection algorithm is its inability to function at night. Commercial solutions do not reveal the algorithms they use or the specific types of devices that are part of their vision systems.

Detecting light points in an image can be achieved using image filtering techniques. Various methods for detecting these objects exist, each tailored to specific purposes. Detecting light and its sources is useful in augmented reality and AI, as it enables automatic adjustments to images based on the direction and location of the light, ensuring a natural appearance [185]. To identify light sources, the image is converted to the BGR color space, and Gaussian blur is applied. Then, the Canny algorithm is used to detect the edges of the light sources, and the results are sorted by area size from largest to smallest [185]. A comparable application for detecting light sources is used to enhance realism when illuminating rendered scenes [186]. The core concept of this method involves calculating the luminance of each channel in the RGB image based on the D65 white point standard and then identifying local maxima using the Monte Carlo method [186].

A task similar to detecting in-pavement airport lamps and navigation lighting is the traffic signals lights detection. However, a notable difference is that traffic signals emit much lower luminous intensity, making it impractical to directly use methods developed for traffic lights. In this context, spot light detection (SLD) is performed using an algorithm on a grayscale image [187], which utilizes the top-hat morphological operator [188], [189] to match shape filters to the detected light points. Additionally, a template matcher using a cascade classifier was suggested for filtering traffic lights [190] (Figure 23).

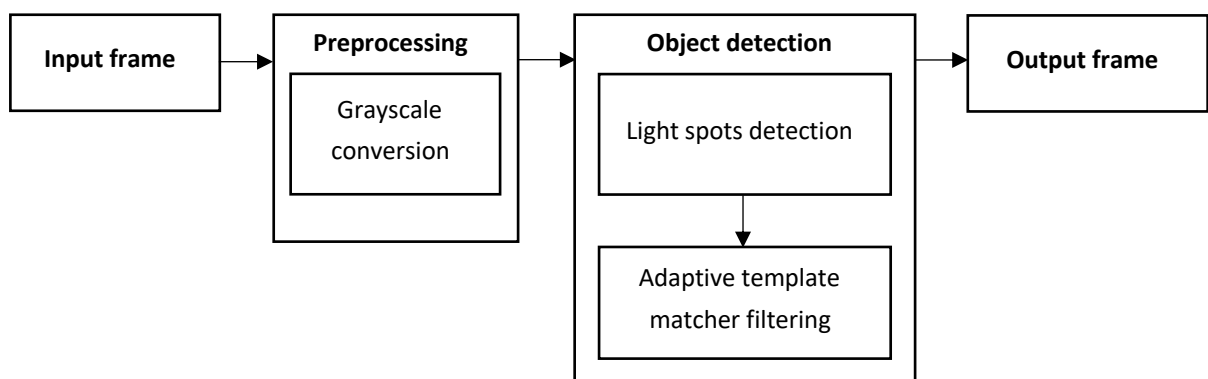


Figure 23 Example of spot light detection algorithm [187]

For detecting only green and red traffic lights at intersections, binarization can be applied to specific thresholds after converting the RGB color space to HSV [191]. This method benefits from the previously mentioned low luminous intensity of the light-emitting points, which helps maintain the circular shape of the light point. In contrast, airport lamps, due to their high brightness, cause the emitted light from rectangular prisms to take on various shapes on the camera lens, ranging from a rectangle to an oval, or even resembling a circle.

The literature also presents solutions for detecting multiple points of light in an image using the OpenCV library. These methods utilize fundamental operations, including conversion to grayscale, threshold binarization, Gaussian blur, erosion, dilation, and contour detection [192].

Algorithms for detecting in-pavement AGL lamps are mainly developed by manufacturers of commercial devices that allow to test the photometric parameters of airport lamps [15], [184]. These manufacturers do not disclose details about the algorithms and methods they use, because of unique environment and task their systems are operating in.

Devices that are well suited for outdoor vehicle applications must be weatherproof and shockproof. Therefore, the use of a sports camera to record images for a vision system is reasonable solution. Cameras designed for the commercial market have certain limitations. They cannot be freely configured or their parameters cannot be influenced beyond the options provided by the manufacturer. A device as durable as GoPro is the ArduCam B0241 camera with the IMX477 module (Figure 24). It is compatible with Raspberry Pi and NVIDIA Jetson microcomputers. The GoPro Hero 8 and ArduCam B0241 cameras specification parameters are listed in Table 12 [193], [194], [195].

Table 12 GoPro Hero 8 and ArduCam B0241 cameras technical parameters

Parameter	GoPro Hero 8	ArduCam B0241 IMX477
Sensor type	CMOS	CMOS
Matrix size	12 megapixels	12.3 megapixels
Image stabilization	Digital	None
Max resolution	3840×2160	4056×3040
Frames per second	60 FPS (4K) 120 FPS (2.7K and QHD) 240 FPS (FullHD)	60 FPS (4K and 2K) 240 FPS (FullHD) 40 FPS (12-bit) 2 FPS (DOL-HDR)
Communication	Bluetooth WiFi	4-line MIPI CSI-2
Aspect ratio	16:9 4:3	4:3
Lens	Digital lens: SuperView: 16 mm, 122.6° Wide: 16-34 mm, 118.2° Linear: 19-39 mm, 85.8° Narrow: 27 mm, 41.6°	Focal length: 6 mm FoV: 65°



Figure 24 ArduCam B0241 camera with IMX477 module

The GoPro Hero 8 camera allows to remotely transfer images to mobile devices or save recordings to an SD card. They are saved using h.264 or h.265 codecs. The 12-megapixel CMOS sensor allows to record images in 4K resolution. Digital image stabilization ensures good quality recordings regardless of the choice of digital lens. The ArduCam B0241 camera with the IMX477 module allows for image transmission to the Raspberry Pi or NVIDIA Jetson microcomputer using the CSI connector. The image can be freely processed and saved using libraries dedicated to Raspberry Pi Camera solutions.

There are various methods for assessing the quality of object detection and classification in images. One of them is Mean Average Precision (mAP) which use the confusion matrix, also known as an error matrix [196]. Its rows represent possible real labels of the objects being examined, and the columns represent labels predicted by the algorithm used for classification. In the case of a binary classifier, the matrix has dimensions of 2×2 , and the possible labels for both the objects being examined and the classification algorithm take on a positive or negative value (Figure 25).

		Predicted condition	
		Positive (PP)	Negative (PN)
Actual condition	Positive (P)	True Positive (TP)	False Negative (FN)
	Negative (N)	False Positive (FP)	True Negative (TN)

Figure 25 Confusion matrix

Based on the frequency of the positive state in the population and the mutual relations between correct and incorrect classifications, it is possible to determine the values of indicators assessing the predictive power of the classifier, such as [196]:

- Sensitivity/True Positive Rate (TPR)/Recall:

$$TPR = \frac{\sum T_P}{\sum T_P + \sum F_N} \quad (23)$$

- Specificity/True Negative Rate (TNR):

$$TNR = \frac{\sum T_N}{\sum F_P + \sum T_N} \quad (24)$$

- Accuracy (ACC):

$$ACC = \frac{\sum T_P + \sum T_N}{\sum T_P + \sum F_N + \sum T_N + \sum F_P} \quad (25)$$

- Precision/Positive Predictive Value (PPV):

$$PPV = \frac{\sum T_P}{\sum T_P + \sum F_P} \quad (26)$$

- Negative Predictive Value (NPV):

$$NPV = \frac{\sum T_N}{\sum T_N + \sum F_N} \quad (27)$$

- False Positive Rate (FPR):

$$FPR = \frac{\sum F_P}{\sum F_P + \sum T_N} \quad (28)$$

- False Negative Rate (FNR):

$$FNR = \frac{\sum F_N}{\sum T_P + \sum F_N} \quad (29)$$

- F_1 score resulting from precision and sensitivity:

$$F_1 = \frac{2 \times \sum T_P}{2 \times \sum T_P + \sum F_P + \sum F_N} \quad (30)$$

Using the above-mentioned indicators, it is possible to precisely compare the effectiveness of classification algorithms. They are often used in the literature as a measure of quality in the case of image processing analysis [196].

2.2.4 Photosensitive elements for light measuring

Light is an electromagnetic phenomenon in the form of a wave of various lengths consisting of discrete particles - photons [197], [198]. Humans perceive the spectrum of light with their eyesight, i.e. colors depending on differences in wavelength [199], [200], [201], which are typically presented in the range from 380 to 750 nm [202]. However, it should be noted that due to the structure of the human eye, where light is focused on the retinal cones adapted to specific wavelengths, three categories can be distinguished: cones sensitive to short, medium and long wavelengths. They show the strongest response for 420 nm (blue

light), 530 nm (green light), 570 nm (the border of green and yellow light). The physical properties of the biology of the human eye have determined the perception of light also by measuring devices, including devices and sensors used to study photometric parameters [203].

In 1931, the Commission Internationale de l'Eclairage' (CIE), an organization for worldwide cooperation and exchange of information in the field of light and lighting, defined a standard curve of the relative sensitivity of the eye for photopic vision V as a function of wavelength λ (Figure 26) [202]. This curve is of key importance in lighting technology, as it is a link between photometric and radiometric physical quantities and also their units [203]. In addition to the course of the curve itself, the maximum point corresponding to the wavelength of 555 nm is very significant. Modern light meters such as luxmeters or modules based on photodiodes and other photosensitive elements refer in their characteristics to the representation of the $V(\lambda)$ curve [204], [205], [206], [207], [208].

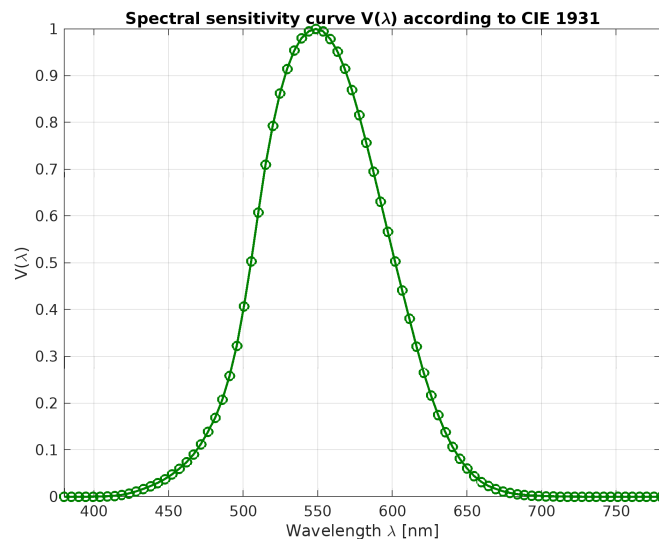


Figure 26 Spectral sensitivity curve $V(\lambda)$ according to CIE 1931

The basic physical quantities used in optics and photometry are lumens included in SI units. It is a unit of measurement of luminous flux, i.e. the total amount of light emitted by a specific light source, e.g. a light bulb.

The value of the luminous flux incident on a given surface is called illuminance. The SI unit of this physical quantity is lux, which has been defined for 1 lumen of luminous flux incident on 1 m² of surface.

The visual brightness of a light source, i.e. the intensity of the light source flux, is called luminous intensity and is expressed in candelas, which are SI units. The value of luminous intensity I_v is expressed by the formula (31), where the illuminance E_v is multiplied by the square of the distance d from the light source.

$$E_v[cd] = l_v[lx] \cdot d^2[m^2] \quad (31)$$

Among others, standards for airport navigation system lamps [209] (Figure 27) are expressed in candelas. They define luminous intensity values for individual using isocandelas, i.e. lines connecting points with the same luminous intensity value. They define areas for given horizontal and vertical angular values for which the conditions for the minimum luminous intensity value must be met - this is how the luminous intensity distribution is determined. A similar way to represent measurement data of illuminance or light intensity is a graph in the form of a heatmap [26] presenting values as colors on a given scale (Figure 28).

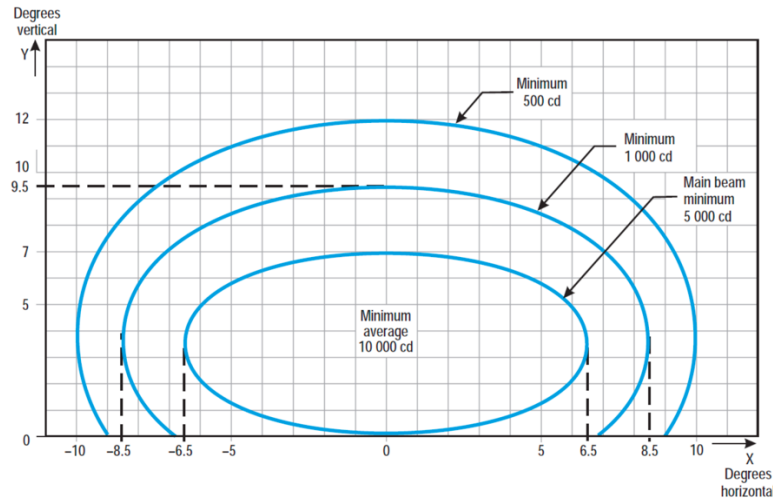


Figure 27 Isocandela diagram for runway edge light where width of runway is 60 m (white light) [209]

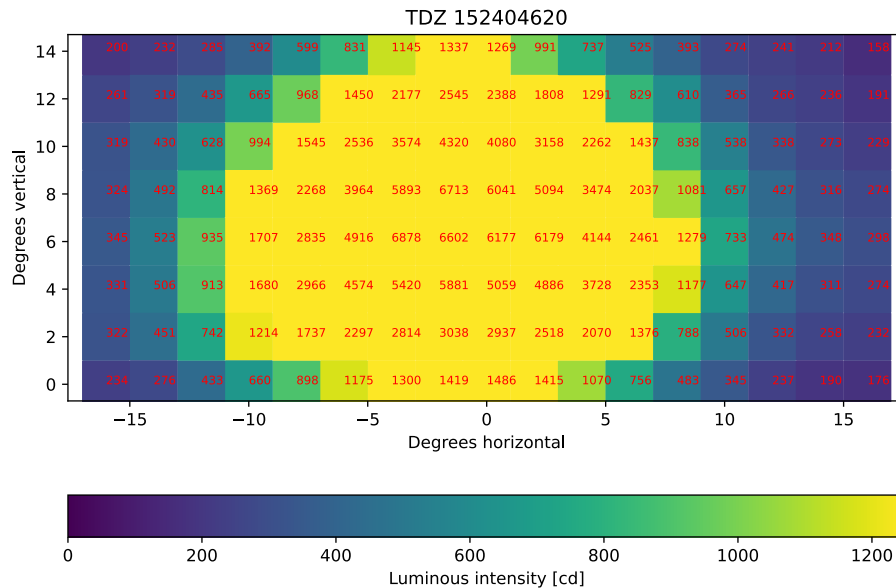


Figure 28 Touchdown zone lamp heatmap luminous intensity chart

Light intensity sensors are divided into digital ones generating a discrete, discontinuous output signal and analogue ones with a continuous output signal. Their operating principle is based on the conversion of environmental parameters into an electrical signal interpretable

by electronic devices [201], [210]. In the case of photometry, various types of photosensitive elements are used for this purpose, such as photodiodes or photoresistors [203].

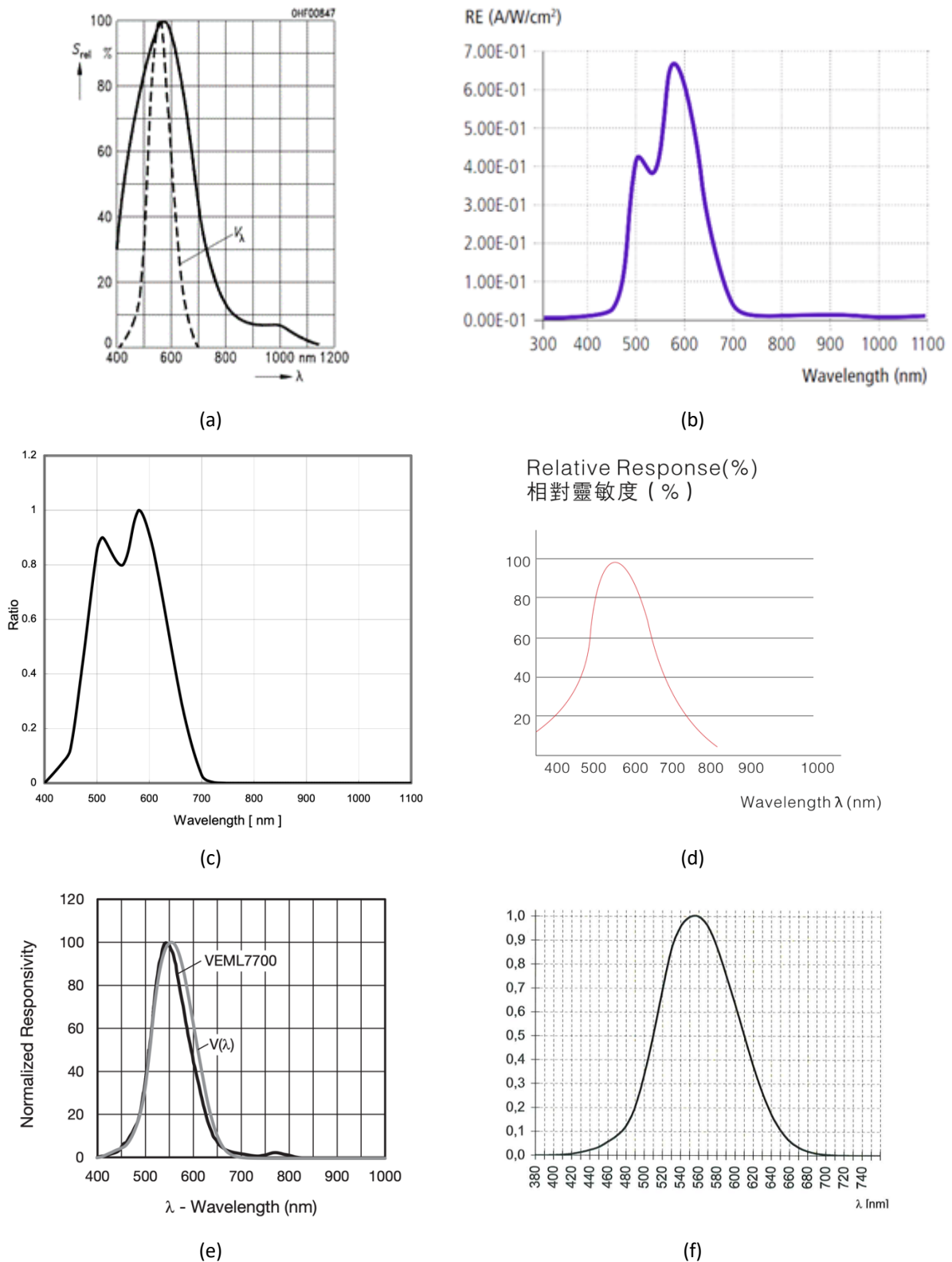


Figure 29 Spectral sensitivity of: BPW21 photodiode [204] (a), VTP1220FBH photodiode [205] (b), BH1750 sensor [206] (c), LS06-S photoresistor from Grove Light Sensor v1.2 [211] (d), VEML7700 sensor [212] (e), Sonopan L-200P luxmeter with no. 217 photometric head [213] (f)

The BPW21 photodiode operates within a wavelength range of λ_d from 350 to 820 nm [204], [214], with its maximum sensitivity occurring at 550 nm (Figure 29a). It has a 55-degree viewing angle and a photosensitive area of 7.45 mm². The photodiode features a turn-on and turn-off time of 1.5 μ s and a dark current of 2 nA. Enclosed in a hermetic package, it is commonly used in exposure meters for daylight and artificial light with high color temperatures in photography, as well as in color analysis.

The VTP1220FBH photodiode, on the other hand, has its maximum sensitivity at a wavelength of 550 nm [205] and operates in a wavelength range of λ_d from 400 to 700 nm (Figure 29b). It has a wider viewing angle of 70 degrees and a smaller photosensitive area of 1.219 mm². Its dark current is 10 nA. Equipped with an IR filter, this photodiode is primarily used in applications such as streetlight switching, contrast control, colorimeters, and camera exposure control.

The BH1750 is a digital ambient light sensor that plays a significant role in optimizing visibility under various lighting conditions. It is widely used in devices such as smartphones, weather stations, and home automation systems to dynamically adjust display brightness or control lighting based on ambient light levels. The BH1750 operates via an I²C interface, making it easily integrable with numerous devices, which enhances its versatility in measuring ambient light across a range of applications.

The sensor can detect illuminance levels between 1 and 65535 lux, making it suitable for a wide range of lighting conditions, from complete darkness to direct sunlight. It provides highly precise measurements, ensuring consistent and reliable light data. Its spectral response (Figure 29c) closely matches that of the human eye [206]. A notable feature of the BH1750 is its selectable measurement modes: High resolution, High resolution mode 2, and Low resolution mode [206], allowing to balance higher precision with lower power consumption depending on the needs of the application (Table 13). The sensor also includes a power-down mode, which reduces energy use when inactive, making it ideal for energy-efficient projects.

Table 13 BH1750 measurement modes [206]

Measurement mode	Measurement time [ms]	Resolution [lx]
L-Resolution Mode	Typ. 16	4
H-Resolution Mode	Typ. 120	1
H-Resolution Mode2	Typ. 120	0.5

The module has the software ability to change the resolution of the measurement. It can be used to take readings with a resolution of 0.5 lx, which, according to the manufacturer, requires a time of 120 ms (maximum 180 ms). Another operating mode is measurement with a resolution of 1 lx, while the declared acquisition times are identical. The fastest mode, lasting 16 ms (maximum 24 ms), is the 4 lx resolution mode. Additionally, it is possible to select a continuous measurement method or perform a single measurement for each of the above-mentioned resolutions [206].

The GY-302 module features an integrated BH1750 sensor, along with a voltage stabilizer, capacitors, and pull-up resistors for the I²C interface [206], [215]. This module is widely used in several applications, such as controlling runway edge lights with drones [216], [217] and automotive systems [218]. Communication is conducted through the I²C bus, and its address can be changed from 0x23 to 0x5C using the ADDR pin by switching the high or low state. Despite the sensor's good measurement quality, its main limitation is the slow data acquisition speed. As indicated in [29], the BH1750 module can accurately read light intensity at a maximum frequency of 20 Hz. At higher frequencies, some readings show missing or zero values between consecutive flashes of the light source. Even though this results in incomplete data, the drop in values is typically enough to identify the lamp and the areas between flashes.

The Grove Light Sensor v1.2 module, on the other hand, utilizes an LS06-S photoresistor (Figure 29d) and an LM358 operational amplifier in a voltage follower configuration [219]. Like the BH1750, it operates with a supply voltage range of 3–5 V. However, unlike the BH1750, it provides an analog output instead of an exact lux value, representing the relative light intensity within a range of 0 to 11,000 lux. A key difference from the GY-302 module is that the output of the Grove Light Sensor v1.2 requires analog-to-digital conversion.

The next light intensity sensor is the VEML7700. It has a digital module with a 16-bit resolution for measuring light intensity, a high-sensitivity photodiode and an amplifier with a low noise level. This sensor has a much larger measurement range than the BH1750 system, from 0 to 120,000 lx with a maximum resolution of up to 0.0036 lx with a refresh time of 4800 ms. In the case of the shortest possible refresh rate of 600 ms, the resolution is 0.0288 lx [212]. Its spectral response characteristic is similar to human eye's (Figure 29e). The communication is provided by I²C bus interface.

Each sensor is characterized by a given level of noise, and despite the mass production of such devices, achieving measurement repeatability between several copies is very difficult to achieve. For this reason, methods are used to mitigate the impact of these inaccuracies and measurement uncertainties [65]. Using a standard in the form of a certified measuring device and filtering algorithms, it is possible to introduce appropriate corrections.



Figure 30 Sonopan L-200P luxmeter (a), GL Spectis 1.0 Touch + FLICKER (b)

The Sonopan L-200P luxmeter (Figure 30a) is a widely-used device that measures illuminance with high precision, making it indispensable in fields such as photography, cinematography, interior design, and workplace safety due to the design of the device in class A according to the DIN 5032-7 and CIE classification [207]. The L-200P can measure light intensities from as low as 0.1 lux to 200,000 lux, providing flexibility across a range of lighting conditions [207]. Its precision stems from a silicon photodiode sensor calibrated to align with the CIE photopic luminosity function, mimicking human eye sensitivity. Certification documents indicate that the spectral matching of the Sonopan L-200P luxmeter used during the tests was $f_1' = 1.07\%$ (Figure 29f). The luxmeter is user-friendly with its large digital display and features such as data hold, min/max recording, and auto-ranging, which simplifies the measurement process in various lighting scenarios.

The GL Spectis 1.0 Touch + FLICKER (Figure 30b) is a spectrometer that allows to measure many photometric parameters of light sources such as natural light, LED or halogen lights. The illuminance measurement range is from 10 to 100,000 lux for white light. The device also allows to measure luminous intensity, which is done using the GL SPECTROSOFT software. The GL SPECTIS 1.0 Touch + FLICKER is equipped with a 256-pixel CMOS sensor and a 16-bit analog-to-digital converter [208].

One of the frequently used communication buses for electronic sensors is the I²C bus, developed in the early 1980s by Philips. It is a serial, bidirectional bus using two lines: SDA for data transmission and SCL for managing transmission using a clock. It is characterized by the fact that all devices connected to the bus identify themselves with an individual address, and controllers can act as transmitters and receivers. I²C provides control of transmitted data and prevents collisions, e.g. when two transmitters want to transmit at the same time. A major advantage of the I²C bus is also the speed at which data transmission takes place. Four operating modes are offered for bidirectional transmission in the 8-bit standard: Standard-

mode 100 kbit/s, Fast-mode 400 kbit/s, Fast-mode Plus 1 Mbit/s and High-speed mode 3.4 Mbit/s. The unidirectional data transferred in the 8-bit standard in Ultra Fast-mode can reach a transfer speed of 5 Mbit/s [220]. The only limitation of the use of the I²C bus is its bandwidth. In the case of multi-sensor measuring devices, the characteristics of the I²C bus make it very often used in such solutions [27], [29].

2.3 Methods and devices for AGL lamps testing

2.3.1 Requirements of in-pavement AGL lamps system

Due to the increasing demands of aviation agencies, airports around the world are increasingly burdened with the task of improving the safety of aviation operations. One of the important aspects in this field is the proper lighting of airport planes, especially runways where the most critical aviation operations take place. For this purpose, measuring devices are built that are able to measure the light efficiency of each lamp and assess its degradation, and then classify the lamps as suitable for further use or requiring replacement. The lighting efficiency of the lamps decreases as a result of weather conditions and runway use [17].

AGL lamps can be divided into in-pavement luminaires (Figure 31a), i.e. those built into the airport surfaces, e.g. runway, taxiway or apron. There are also elevated lamps (Figure 31b), which are mounted on special posts and are located outside the maneuvering areas or on their edge. These lighting systems are an integral part of airport design and function, providing safety for aircraft during take-off, landing, and taxiing, especially in poor weather conditions or at night.

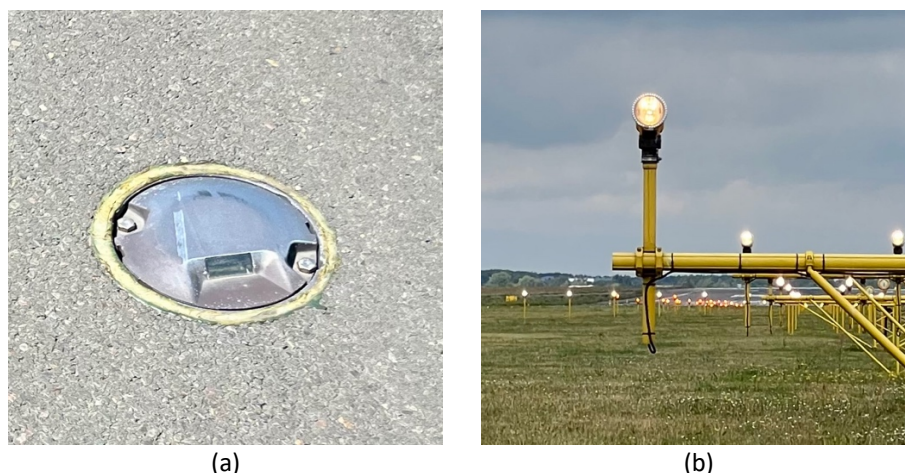


Figure 31 Airport lamps: in-pavement lamp (a), elevated lamp (b)

In-pavement lamps used for navigation lighting are a component of the visual aid system for flight operations. These lamps help pilots determine the course and distance to the runway, establish the approach path during the final phase of landing before touchdown, and assist with taxiing. In-pavement lamps are recessed into airport surfaces and designed not to

obstruct aircraft movement. When installed, they extend 6.3 to 10 mm above the ground. Their reflectors direct the light beam vertically upward from the bulb, while the angle of light dispersion outside is controlled by a prism made from high-quality, high-temperature-resistant borosilicate glass [221], [222].

The elevated approach light systems, which often extend far from the runway threshold, give pilots essential visual cues for proper alignment with the runway during the final stage of flight. The runway centre line lights, installed within the runway surface, offer important visual guidance for aircraft during takeoff and landing, using specific colors and spacing that adhere to international aviation standards. Touchdown zone lights, indicating the optimal landing area, enhance safety by aiding in precise landings, particularly in low-visibility conditions.

Given the nature of these systems, international aviation authorities like EASA (European Union Aviation Safety Agency), ICAO (International Civil Aviation Organization), and FAA (Federal Aviation Administration) have established standards [223], [224] that airports must comply with to conduct air operations. The operation of lamps specified in the standard of the European Aviation Safety Agency (EASA) in the chapter on airport design guidelines [223] presents the intensity of individual lights and their dependence on the angle of incidence. The values given vary depending on the type of lamp and the color of the light. The standards also define requirements referring to the airport category. One of the most important parameters is the minimum luminous intensity for the main beam, which is located in a different angular range depending on the type of lamp. It should be noted that more stringent guidelines have been provided for the runway than for other airport areas, which is justified by the safety requirements of air operations.

The parameters for airport lamps are outlined in the EASA standard within the chapter titled “Colours for aeronautical ground lights, markings, signs, and panels” [209]. This document specifies the luminous intensity for each light point, considering their angular relationships in the form of isocandelas. The diagrams differ based on the lamp type and light color. The standards also establish requirements according to the airport category. A key parameter is the minimum luminous intensity for the main beam, which varies across different angular ranges depending on the lamp type. Notably, the runway has more stringent guidelines than other airport areas due to the heightened safety requirements for air operations. The luminous intensity distributions in the form of isocandelas depending on the lamp type are shown in Figure 32 - Figure 36:

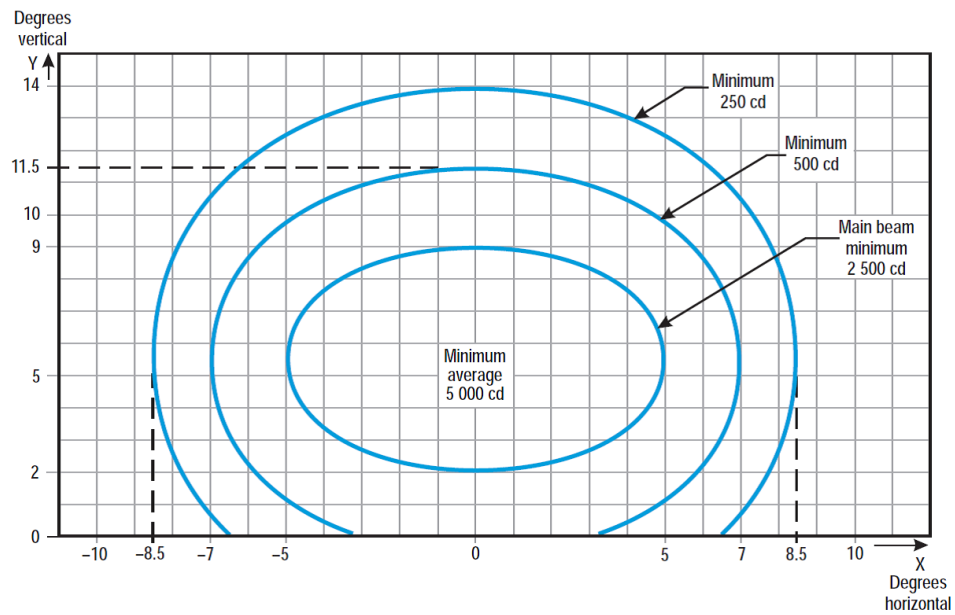


Figure 32 Light distribution required for airport touchdown zone luminaires [209]

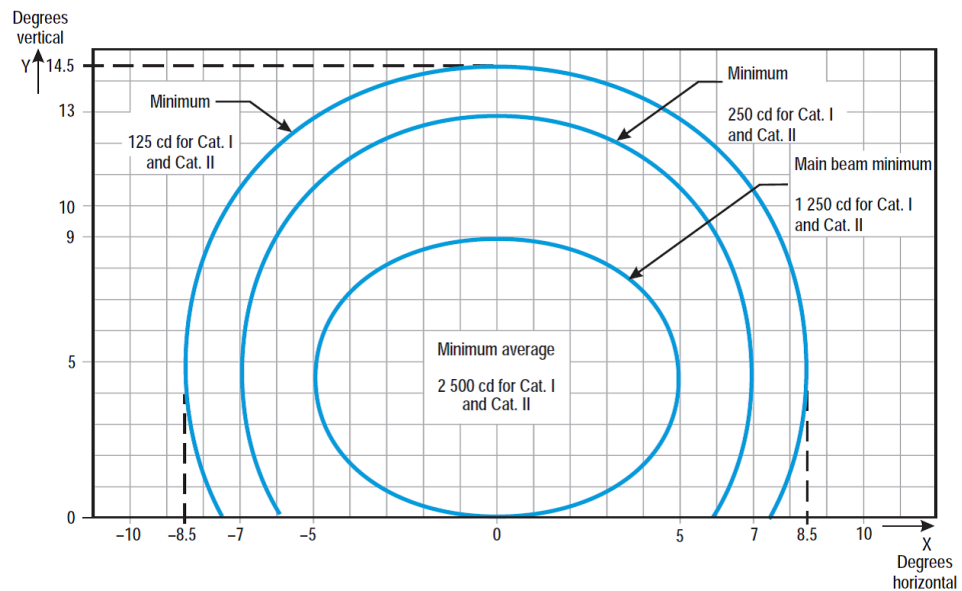


Figure 33 Light distribution required for airport runway centre line luminaires (white light) [209]

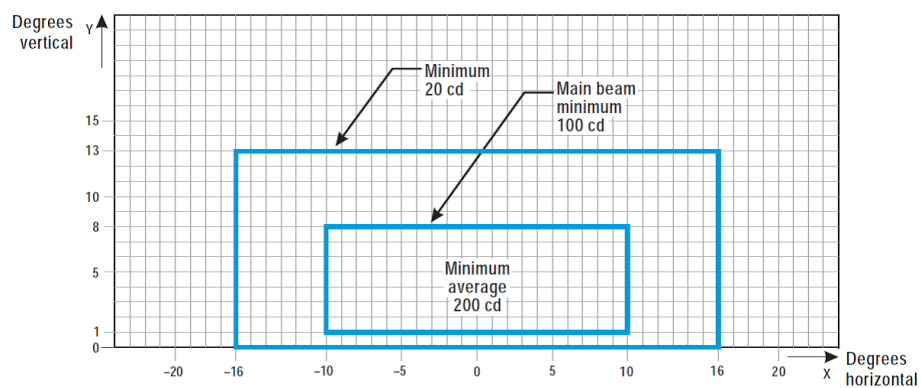


Figure 34 Light distribution required for airport taxiway centre line and stop bar luminaires [209]

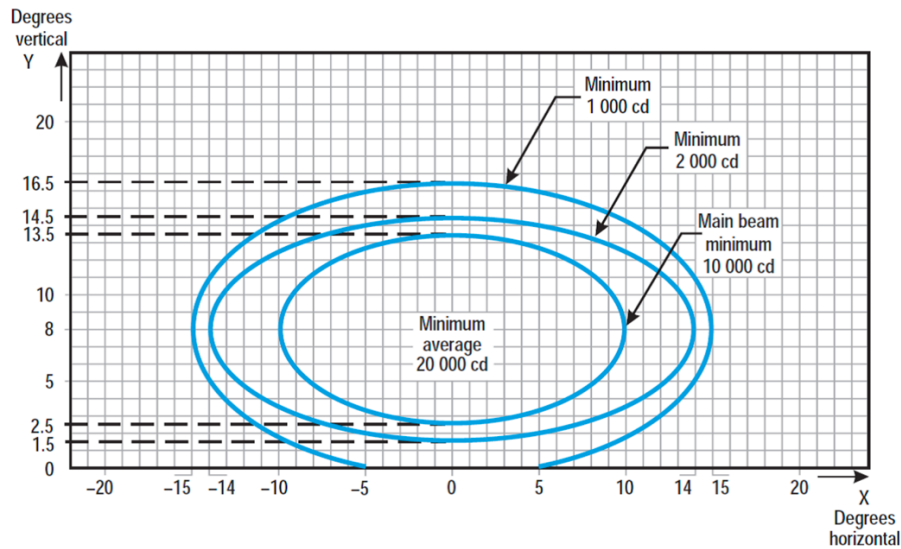


Figure 35 Light distribution required for airport approach luminaires (white light) [209]

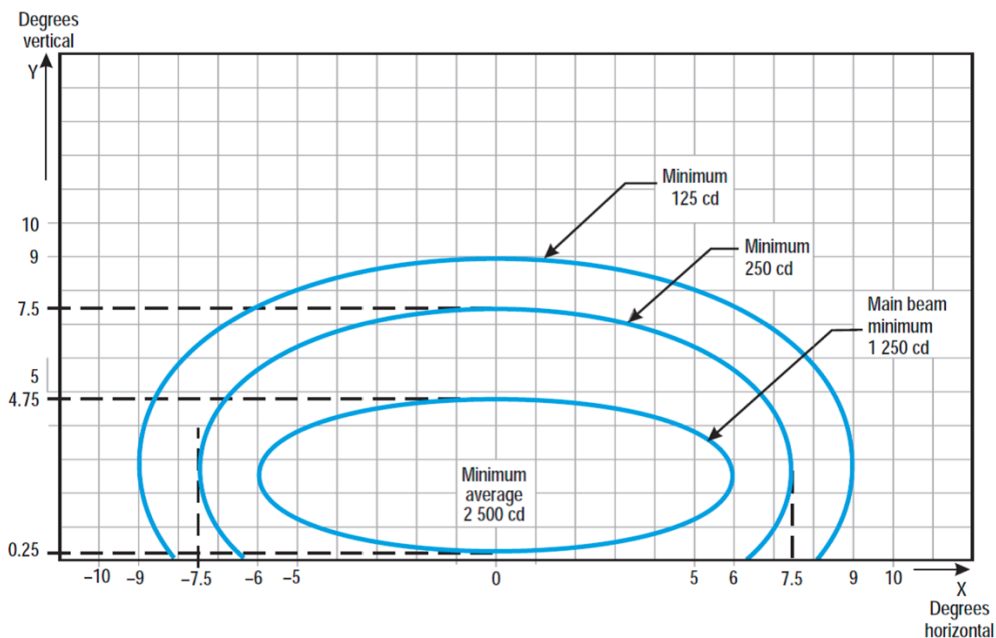


Figure 36 Light distribution required for airport end of runway luminaires [209]

In the case of runway centre line lamps, which come in white and red versions, the conversion factor for red is 15% of the value for white, according to EASA guidelines. In the case of taxiway centre line lights, which come in green and yellow, the standards for both colors are identical.

Table 14 presents the values of the required minimum illuminance value according to EASA for a new lamp, the maintenance threshold, the value of which is 60% of the standard given by EASA and the illuminance threshold below which the lamp cannot be used (it is 50% of the EASA value). The values given in the table are given for measurement at a distance of 1 m from the light source and refer to the main beam.

Table 14 Airport lamps main beam illuminance requirements

Lamp type	Color	Luminaire type	EASA requirement [lx]	Maintenance threshold [lx]	Minimum threshold [lx]
Touchdown zone	White	In-pavement	2500	1500	1250
Runway centre line	White	In-pavement	1250	750	625
	Red	In-pavement	187.5	112.5	93.75
Taxiway centre line	Green	In-pavement	100	60	50
	Yellow	In-pavement	100	60	50
Approach white	White	Elevated	10000	6000	5000
End of runway red	Red	Elevated	1250	750	625
Stop bar red	Red	Elevated	100	60	50

Laboratory experiments [17] involving testing airport lamps made it possible to compare the illumination of lamps with brand new and worn-out lamps in order to qualify the lamps as unfit for further use. The research has shown that there are significant changes in the characteristics of the emitted light between two lamps of the same type but with different operating times. Damaged (scratched and chipped) lamp prisms cause the main beam to shift relative to the standards, as well as scattering it in some situations. In the case of new luminaires, the guidelines for the minimum luminous intensity are significantly exceeded, while used lamps are characterized by much lower light intensities. This is a problem mainly related to the runway, where the luminaires are particularly exposed to mechanical damage. A comparison of a new and used lamps is shown in Figure 37.

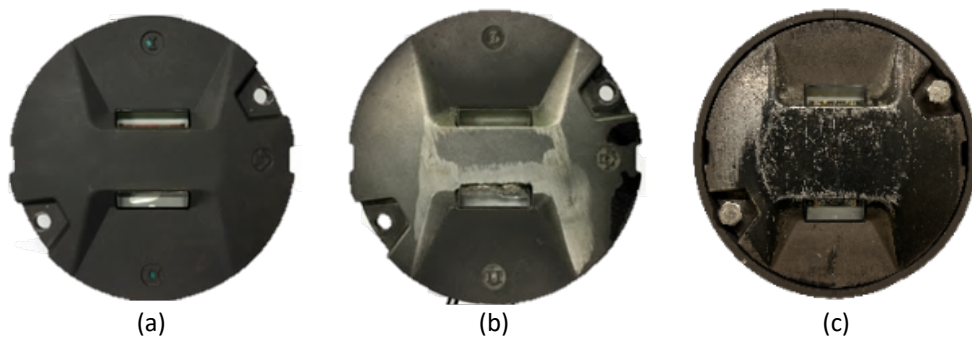


Figure 37 Runway centerline lamp (IDM5582): (a) new, (b) damaged, (c) covered with rubber from plane's tires

The greatest worn out of recessed fixtures is observed during the winter snowplowing action. It involves thorough cleaning of airport surfaces from snow and mud using chemicals and specialized plows equipped with wire brushes (Figure 38).



Figure 38 Wire brushes on plows clearing snow from airport surfaces [29]

In-pavement navigation lamps are fitted with light sources that have a limited lifespan [225], [226]. The reduction in these lamps' luminous efficiency can also result from contamination of the prisms, such as the accumulation of rubber from aircraft tires. Weather conditions also play a role; for instance, heavy snowfall necessitates the use of snowplows, which can damage the lamp housings and scratch or chip their prisms with their metal brushes.

In some cases, a prism that appears to be in good condition can still significantly reduce the illumination intensity. Therefore, testing the correct angular distribution of lighting is crucial for enhancing the safety of air operations. Accurate measurements can help minimize unnecessary replacements of expensive lamp components.

Airport lamps, according to the information on the rating plates, should be powered by alternating current. They are current-controlled with the possibility of regulating the light output expressed as a percentage:

- 1% for power supply current 2.8 A
- 3% for power supply current 3.3 A
- 10% for power supply current 4.1 A
- 30% for power supply current 5.2 A
- 100% for power supply current 6.6 A.

The KIKUSUI PCR1000MA is a versatile power supply capable of delivering both AC and DC current, making it ideal for applications such as product testing, research, and quality control. It is part of the PCR-MA series, with a maximum output power of 1000 VA and an output frequency range of 40 to 500 Hz. The PCR1000MA operates in two voltage ranges, with maximum output currents of 10 A for AC and 8 A for DC in the 155 V mode, and 5 A for AC and 4 A for DC in the 310 V mode [227]. One of its standout features is its ability to function as both a frequency converter and power supply, making it crucial for testing electrical products for global markets. Additionally, it offers arbitrary waveform generation for

simulating conditions such as power line distortion, making it useful for developing products that can withstand challenging environments.

2.3.2 In-pavement AGL system assessment methods

Airports are required to perform numerous inspections of their infrastructure, including lighting systems such as lamps embedded in the runway and taxiways [223]. Given the vast area of airports and the large number of lamps, conducting daily inspections can be a time-intensive process. In the context of air operations, both safety and time efficiency are crucial. Any delays or prolonged occupation of the runway, even for maintenance tasks, can result in significant costs for airports. Consequently, considerable efforts are made to complete all maintenance work as swiftly as possible, without compromising safety or quality standards.

Airport operation rules are governed by the requirements of aviation agencies such as the European Aviation Safety Agency (EASA) and the Polish Air Navigation Services Agency (PANSa). These rules are standardized in documents like “Easy Access Rules for Aerodromes,” which outline best practices for enhancing aviation safety [209], [228]. Meeting these requirements influences the design of devices used for the quick and reliable inspection of all critical equipment at an airport. One crucial aspect in this area is ensuring proper navigation lighting at airports, particularly on runways, where the most critical flight operations occur.

The daily inspection of navigation lighting functionality is performed visually by the airport maintenance team. If a lamp is found to be malfunctioning, it is either disassembled and replaced or turned off, in accordance with applicable standards [209]. Periodic evaluations of airport lamp performance are conducted using specialized commercial devices tailored for specific airports. Various measurement devices [17], [37] are developed to assess the luminous efficiency of each lamp, evaluate its condition, and determine whether it is fit for continued use or needs replacement.

There are many types of lamps in the airport. For example, on the runway of the Poznań - Ławica Airport there are over 350 embedded fixtures, spread over a distance of approximately 2.5 km. Due to the short time slots between flight operations, ranging from 5 to 10 minutes, this determines the need to quickly check the correct operation of airport lighting, e.g. carried out using the measurement platform.

The quality of airport lamps can be evaluated either stationary, using a light goniophotometer [16], [229], [230], or mobile, with platforms such as illuminance measurement vehicles [14], [15], [17], [184], [231], or drones [216], [217]. Mobile measurements provide comprehensive information about lamps that might have reduced

efficiency. These systems enable the assessment of both in-pavement and elevated lamps across airport areas.

There are three solutions available for stationary testing of navigation lighting lamps that provide highly accurate measurements of angular relationships. One such solution, PAC MATRIX [16], can be used in real-life conditions without needing to remove the lamp from its housing on airport areas. The other two solutions, PAC LAB II [230] and PTS-200 [229], are designed for use in laboratory conditions.

The first solution is the PAC MATRIX (Figure 39) system, produced by FB Technology. This stationary matrix (array of sensors) is designed for photometric measurements of various types of airport lamps [16]. The device features 17 measuring sensors and must be manually positioned in airport areas before each measurement, which has the advantage of not requiring the lamp to be removed from its housing. However, this also results in a longer measurement time. The sensor placement on the measuring board follows the angular dependency standards set by EASA [209]. The measured values are recorded in lux and must be processed through software to determine the average luminous intensity in candelas, as specified in the regulations [209].



Figure 39 FB Technology PAC MATRIX [16]

PAC LAB II (Figure 40) is a stationary system provided by FB Technology [230], designed to complement the PAC² V5 mobile system [184]. This laboratory-based setup for measuring airport lamps enables the calculation of average illuminance values, which are then converted to candela. Additionally, it determines the maximum and minimum values of the main beam, presenting this data to the user. During the measurement process, the lamp rotates within a specialized housing while the sensors remain fixed. The final report includes an isocandela diagram of the light beam, showing the International Civil Aviation Organization (ICAO) grid points and indicating whether the lamp meets ICAO maintenance standards.



Figure 40 FB Technology PAC LAB II [230]

Another commercial system designed for laboratory measuring the luminous intensity of airport lamps is the PTS-200 (Figure 41) from Airsafe Airport Equipment Co. [229]. This device allows the lamp to be placed in a specialized housing that can rotate both vertically and horizontally, while the light sensor needs to be manually set up on a tripod. In addition to luminous intensity testing, the PTS-200 also supports chromaticity measurements. Like the previously mentioned systems, it is compatible with most types of in-pavement and elevated lighting and automatically generates test reports, comparing the results to ICAO standards [229].

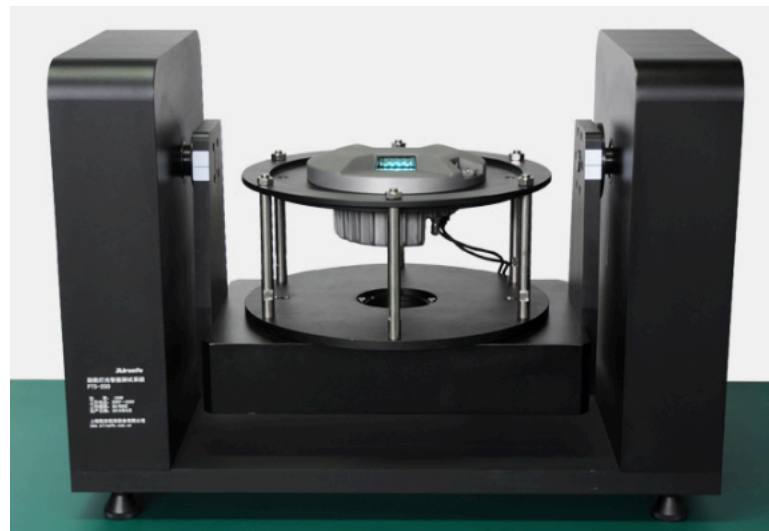


Figure 41 Airsafe PTS-200 [229]

There are also solutions using drones to test airport lamps [216]. In this paper, the authors introduced a photometric method that employs a measurement matrix suspended from a drone, thereby minimizing reliance on airport infrastructure. This device comprises two subsystems: a data acquisition unit and a master station, which communicate wirelessly.

However, this system has several other limitations, including the need to perform inspections at significant intervals from flight operations and dependence on weather conditions.

The operating conditions for devices used to assess the quality of in-pavement airport lamps are closely tied to airport operations. While ensuring safety is crucial, maintaining efficient air operations is also a priority. Thus, a device designed for testing in-pavement airport lamps on runways and taxiways must be capable of quickly measuring several hundred lamps. At a medium-sized airport, measurement intervals range from 5 to 15 minutes, depending on the time of day. To accurately measure the luminous intensity distribution for each lamp, the airport would need to be closed for several days. Consequently, for routine on-site checks, devices are used to provide a general assessment of in-pavement lamps' quality. Detailed examination of luminous intensity is conducted in a laboratory under dark room conditions, where the lamp can be removed and its angular characteristics thoroughly tested.

An example of such mobile system is the patented DeWiTec Airfield Light Mobile Analyzing System (DALMAS), produced by DeWiTec GmbH [231]. This device is a single-axle trailer specifically designed to measure the lighting intensity of both in-pavement and edge aeronautical navigation lamps [15]. The operator is supported by vision system and optional DGPS for the correct approach during measurement. The device is presented in the Figure 42.



Figure 42 DeWiTec Airfield Light Mobile Analyzing System (DALMAS) [15]

Another mobile system is PAC² V5 (Figure 43) measurement matrix bar produced by FB Technology [184]. It is designed to test both in-pavement and elevated airport navigation lamps. A key distinction from its predecessor is that this device necessitates the installation of a special rack on the front or rear of the measurement vehicle. It is equipped with illuminance sensors. The camera module ensures taking measurement in a proper way by hints to the operator to move left or right and the positioning can be also provided using optional DGPS.



Figure 43 FB Technology PAC² V5 measurement matrix

The MALMS Mobile Photometric Test System (Figure 44) has been designed to check the performance of navigation lighting lamps in accordance with the standards specified by ICAO Annex 14 as well as other international and national standards [232]. It has the form of a trailer with sensor arrays allowing measurement of the most important points of the emitted light beam of the lamps. The limitation is the necessity to carry out the tests at night and the necessity to switch off all other light sources except the type of lamp being tested, because the measurement is made in the direction opposite to the movement of the device and it is not equipped with a darkroom limiting the measurement area. The positioning of the device is based on GPS data [232].



Figure 44 MALMS Mobile Photometric Test System

A simple and low-cost device was designed by the author in the preliminary research during BSc and MSc studies. The details of proposed solution are described in [17], which is a mobile measurement platform intended for assessing the performance of airport lamps (Figure 45). This platform is designed to be towed by an airport service vehicle, functioning as a trailer. High-speed illuminance sensors, similar to those described in [27], can be

arranged in matrices [29] and positioned beneath a rubber cover at the bottom of the platform. For localization purposes only a single GPS module is used.



Figure 45 First version of proposed measuring platform for quality testing of airport lamps [29]

Chapter 3

Proposed improvement of multi-sensor localization techniques

3.1 Concept of multi-sensor system for monitoring measurement vehicle

The use of a multi-sensor system for localization of the position and monitoring the environment is intended to improve the quality of such solutions. The preprocessing stage is crucial for the final result, for data from each type of sensor used in the system. General scheme of proposed integration sensor data was presented in Section 1.2 in Figure 5. An illustration of elements application is shown in Figure 46.

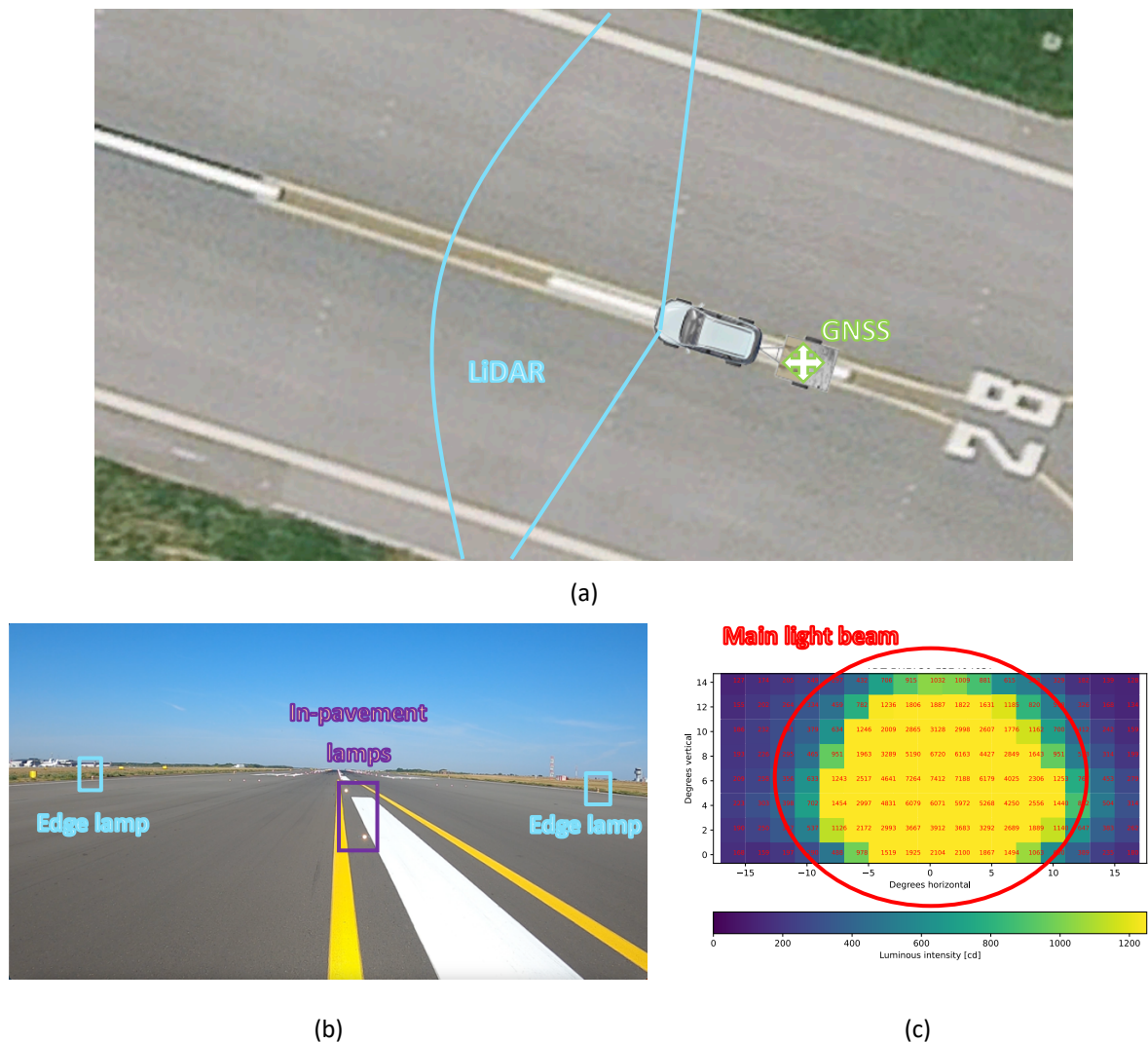


Figure 46 Illustration of concept elements for airport environment monitoring system: GNSS and LiDAR tasks (a), LiDAR and camera objects (b), light sensors measurement heatmap (c)

The GNSS module allows for a rough determination of the position of the measuring platform on the airport area, i.e. whether it is at the beginning or end of the runway (Figure 46a). The accuracy of the module does not allow for independent determination of the appropriate position of the measuring matrix with sensors in relation to the tested lamp. The LiDAR module mounted on the front of the car allows for the detection of characteristic points in the form of elevated lamps located on the edges of the runway (Figure 46a - blue). Due to the width of the runway, which is approx. 60 m, it is difficult to find the edge of the surface - it is impossible to base measurement data on grass because it has a different height depending on the season. Therefore, the elevated lamps, which are mounted on special posts protruding significantly above the level of the surface, are always visible elements (Figure 46-blue). By checking the distance from the lamps opposite each other, it is possible to determine whether the measuring platform is in the middle of the runway or in another place on it, knowing the angular dependencies and the distance measured by LiDAR. Another source of information is a camera, the task of which is to locate the position of the light points (in this case the type of lamp being tested) and to determine their position in relation to the vehicle axis and thus the axis of the measuring platform (Figure 46b – purple bounding box). This solution allows for more precise positioning of the measuring platform in relation to the tested lamp. The last source of information about the position of the measuring device in relation to the tested light source is the measuring matrix consisting of light sensors. The values read from them allow for determining where the main light beam is located in relation to the platform's measuring head (Figure 46c).

The proposed solutions focus on GNSS signal filtration using the HDOP parameter, distance estimation correction for a chum of points using the RANSAC algorithm, localization of characteristic points on vision sequences based on morphological operations and histogram analysis, and the use of sequences with characteristic markings for the movement of a robot - a vehicle equipped with an embedded system.

3.2 Filtering of positioning data of GNSS measurement

GNSS devices, after determining their position based on calculations involving information obtained from satellites within range, present the results in some manner. One of the most commonly used methods is utilizing the NMEA 0183 protocol, which is the successor to the NMEA 0180 and NMEA 0182 standards [233]. This protocol specifies the format for presenting data, namely that it is transmitted in the form of NMEA sentences recorded in ASCII code [234]. Each sentence can contain a maximum of 82 characters. The first character, \$ is the start delimiter that indicates the beginning of a sentence. Next, without any spaces, a prefix is transmitted, serving as the sender identifier – for devices using only GPS, this consists of the letters GP, for GLONASS, GL, and when using more than one constellation, the identifier

is GN. The following three characters, also without any separation, indicate a specific type of data from the GPS device. After a comma, fields containing transmitted information follow, separated by commas as well. At the very end of the sentence, a two-character sequence <CR><LF> (Carriage Return, Line Feed) signals the end of the current line of text.

During own tests of GNSS modules, a data frame received from the Teseo-LIV3F module on the serial port monitor had a structure as shown in Figure 47.

```
$GPRMC,073912.000,A,5225.28158,N,01649.47711,E,48.1,287.8,051224,,,A*50
$GPGGA,073912.000,5225.28158,N,01649.47711,E,1,18,0.6,085.14,M,40.8,M,,*61
$GPVTG,287.8,T,,M,48.1,N,89.1,K,A*05
$GNGSA,A,3,09,05,11,20,07,30,16,06,04,13,,,1.1,0.6,0.9*2E
$GNGSA,A,3,78,69,68,85,84,79,86,70,,,,,1.1,0.6,0.9*2B
$GPGSV,3,1,11,07,75,111,32,20,56,283,36,30,54,206,38,09,44,090,19*76
$GPGSV,3,2,11,11,31,248,32,05,28,310,28,04,15,090,24,16,15,034,26*7D
$GPGSV,3,3,11,06,13,212,34,13,09,268,36,36,28,161,33,,,,,*40
$GLGSV,3,1,09,69,71,339,22,78,54,068,30,68,46,096,24,79,43,157,30*61
$GLGSV,3,2,09,85,26,304,34,84,15,250,23,70,11,299,28,86,10,356,25*6D
$GLGSV,3,3,09,77,08,022,,,,,,,,,,,,,*54
$GPGLL,5225.28158,N,01649.47711,E,073912.000,A,A*5F
$PSTMCPU,76.88,-1,49*4E
```

Figure 47 Example GNSS data frame from Teseo-LIV3F module

The individual sentences represent different data collected by the module, which can be processed in various ways to achieve specific functionalities. Special attention should be paid to the DOP (Dilution of Precision) parameter that appears in certain sentences, which describes the impact of satellite constellation geometry on location determination using the GNSS system. Based on this parameter, GPS data can be filtered, i.e., rejecting location measurements where the parameter was unfavorable, indicating a significant measurement error resulting from the current satellite constellation.

The first type of information transmitted in the NMEA data frame for the GNSS module used pertains to the RMC sentence. It includes data characterizing time, latitude, longitude, system status, course, and date. A detailed description of the individual elements of the sentence is presented in Table 15.

Table 15 Description of the data contained in RMC sentence

ASCII code	Description	Value
\$	Start delimiter	-
GP	Device Sender ID	GPS
RMC	Information type	RMC (Recommended Minimum Specific GPS/Transmit data)
073912.000	Timestamp	07:39:12 (GMT)
A	Data Status	A = Valid

3 Proposed improvement of multi-sensor localization techniques

5225.28158	Latitude	52°25.16.8924"
N	Latitude direction	North
01649.47711	Longitude	16°49.28.6248"
E	Longitude direction	East
48.1	Speed over ground in knots	48.1
287.8	Course made good	287.8
051224	Date	05.12.2024
	Empty space for magnetic variation	-
	Empty space for magnetic variation direction	-
A	NMEA Positioning System Mode Indicator	A = Autonomous
*	Separator before checksum	-
50	Checksum	50
<CR><LF>	End of line character	-

The second line of the data frame, GGA sentence, contains information about time, latitude, longitude, system operation quality, the number of satellites used, and altitude. A breakdown of the specific data is provided in Table 16.

Table 16 Description of the data contained in GGA sentence

ASCII code	Description	Value
\$	Start delimiter	-
GP	Device Sender ID	GPS
GGA	Information type	GGA (Global Positioning System Fixed data)
073912.000	Timestamp	07:39:12 (GMT)
5225.28158	Latitude	52°25.16.8924"
N	Latitude direction	North
01649.47711	Longitude	16°49.28.6248"
E	Longitude direction	East
1	GPS quality	1 = GPS
18	Satellites number	18
0.6	HDOP	0.6
085.14	Height	85.14 m
M	Height measurement unit	Meters
40.8	Geodial separation	40.8 m
M	Geodial measurement unit	meters
	Empty space for DGPS data	-
*	Separator before checksum	-
61	Checksum	61
<CR><LF>	End of line character	-

The next NMEA sentence concerns VTG, which allows for determining the travel course and speed. The decoded information from stationary measurement are presented in Table 17.

Table 17 Description of the data contained in VTG sentence

ASCII code	Description	Value
\$	Start delimiter	-
GP	Device Sender ID	GPS
VTG	Information type	VTG (Recommended Minimum Specific GPS/Transit data)
287.8	Track in reference to "true" earth poles	287.8
T	Type of earth pole	T (Terrestrial)
	Empty space for track in reference to magnetic earth poles	
M	Type of earth pole	M (Magnetic)
48.1	Speed over ground in knots	48.1
N	Nautical speed indicator	N = Knots
89.1	Speed km/h	89.1
K	Speed indicator	K = km/h
A	Positioning system mode indicator	A (Autonomous)
*	Separator before checksum	-
05	Checksum	05
<CR><LF>	End of line character	-

The following two lines pertain to the GSA sentence when using multiple constellations, as indicated by the GN identifier. This sentence includes information about the measurement mode (2D or 3D), the number of satellites used to determine the position, and measurement accuracy expressed by DOP coefficients. A detailed description of the specific data is provided in Table 18.

Table 18 Description of the data contained in GSA sentence

ASCII code	Description	Value
\$	Start delimiter	-
GN	Device Sender ID	GN = GPS and GLONASS constellations enabled
GSA	Information type	GSA (GNSS DOP and active satellites)
A	Operating mode	A = Auto (2D/3D)
3	Satellites list in position fix (max 12)	Satellite ID: 3
09		Satellite ID: 9
05		Satellite ID: 5
11		Satellite ID: 11
20		Satellite ID: 20
07		Satellite ID: 7

3 Proposed improvement of multi-sensor localization techniques

30		Satellite ID: 30
16		Satellite ID: 16
06		Satellite ID: 06
04		Satellite ID: 04
13		Satellite ID: 13
		Satellite ID: empty
		Satellite ID: empty
1.1	PDOP value	1.1
0.6	HDOP value	0.6
0.9	VDOP value	0.9
*	Separator before checksum	-
2E	Checksum	2E
<CR><LF>	End of line character	-

The subsequent six GSV lines contain information about the number of visible satellites, their identification, elevation, azimuth, and SNR values. The first three lines concern the GPS constellation (GP identifier), while the next three relate to GLONASS (GL). An example of the data fields for one of the lines is described in Table 19.

Table 19 Description of the data contained in GSV sentence

ASCII code	Description	Value
\$	Start delimiter	-
GP	Device Sender ID	GPS
GSV	Information type	GSV (Satellites in View)
3	Total amount of GSV messages	3
1	Number of GSV message	1
11	Total number of satellites in view	11
07	Satellite PRN (pseudo-random-noise) number	7
75	Elevation (in degrees)	75°
111	Azimuth (in degrees)	111°
32	SNR (Signal-to-Noise ratio) [dB]	32 dB
20	Satellite PRN (pseudo-random-noise) number	20
56	Elevation (in degrees)	56°
283	Azimuth (in degrees)	283°
36	SNR (Signal-to-Noise ratio) [dB]	36 dB
30	Satellite PRN (pseudo-random-noise) number	30
54	Elevation (in degrees)	54°
206	Azimuth (in degrees)	206°
38	SNR (Signal-to-Noise ratio) [dB]	38 dB
09	Satellite PRN (pseudo-random-noise) number	9
44	Elevation (in degrees)	44°
090	Azimuth (in degrees)	90°
19	SNR (Signal-to-Noise ratio) [dB]	19 dB

3 Proposed improvement of multi-sensor localization techniques

*	Separator before checksum	-
76	Checksum	76
<CR><LF>	End of line character	-

The GLL sentence contains information about geographic positioning – latitude and longitude. In the examined case, the decoded information is presented in Table 20.

Table 20 Description of the data contained in GLL sentence

ASCII code	Description	Value
\$	Start delimiter	-
GP	Device Sender ID	GPS
GLL	Information type	GLL (Geographic Positioning Latitude / Longitude)
5225.28158	Latitude	52°25.16.8924"
N	Latitude direction	North
01649.47711	Longitude	16°49.28.6248"
E	Longitude direction	East
073912.000	Timestamp	07:39:12 (GMT)
A	Data Status	A = Valid
A	NMEA Positioning System Mode Indicator	A = Autonomous
*	Separator before checksum	-
5F	Checksum	5F
<CR><LF>	End of line character	-

The last information received is PSTMCPU sentence which does not belong to the standard NMEA sentences. It is a proprietary sentence used by STMicroelectronics. The first letter of the sentence, P, indicates it is proprietary, and the next three, STM, specify that it is proprietary to STM. The CPU sentence provides real-time CPU usage and its speed settings. The decoded sentence is shown in Table 21.

Table 21 Description of the data contained in PSTMCPU sentence

ASCII code	Description	Value
\$	Start delimiter	-
P	Type of sentence	P = proprietary
STM	Device Sender ID	STM = STMicroelectronics
CPU	Information type	CPU (Real time CPU usage and CPU speed setting)
76.88	Percentage of CPU usage	76.88%
-1	PLL (Phase Locked Loop) status	-1 (disabled)
49	CPU clock frequency	49 MHz
*	Separator before checksum	-
4E	Checksum	4E
<CR><LF>	End of line character	-

The above examples of NMEA sentences show that a single data frame sent by a GPS device contains an enormous set of information. Various parameters can be determined based on such data, which are often essential for implementing functions in a specific product. Among the sentences in the entire frame, the most interesting for geolocating a measurement platform to study the performance of airport lamps were those related to GGA and GSA, as they contained information about latitude, longitude, and DOP parameters.

3.2.1 Static localization error measurement using GNSS

In order to check the measurement errors of the tested GNSS modules: Teseo-LIV3F, NEO-6M and SIM28, a static test of their location accuracy was first carried out. Their antennas were placed in the same place next to each other at a point with known geographic coordinates (52.40235 N, 16.953366 E), which was located on the roof of the building of the Centre for Mechatronics, Biomechanics and Nanoengineering of the Poznań University of Technology. The modules were synchronized with each other based on the UTC time obtained from the satellites, so that each measurement could be related to the measurements from the other two modules at a given moment of time. They worked continuously for 3.5 hours collecting location data, which after extraction from the GGA and GSA sentences are presented in Figure 48.

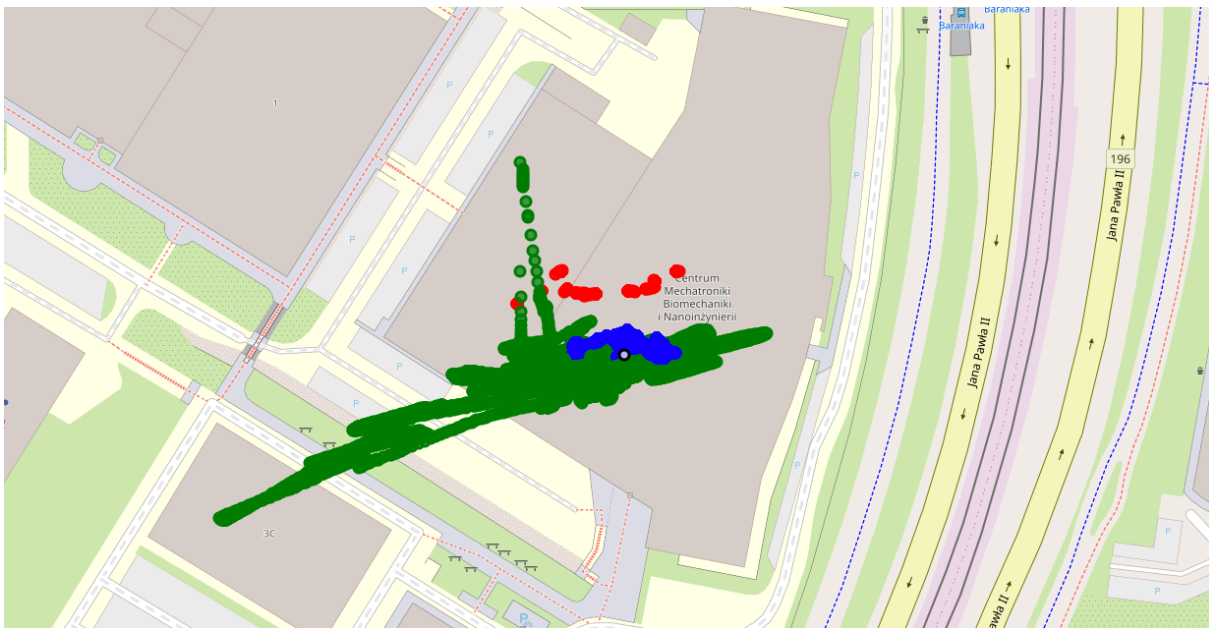


Figure 48 Map of GNSS modules raw measurements: reference point (black), Teseo-LIV3F (blue), NEO-6M (green), SIM28 (red)

Since the reference point is known, it is possible to calculate the distance error of the individual measurements of each module using the Haversine formula:

$$d = 2R \arcsin \left(\sqrt{\sin^2 \left(\frac{\Delta\varphi}{2} \right) + \cos(\varphi_1)\cos(\varphi_2)\sin^2 \left(\frac{\Delta\lambda}{2} \right)} \right) \quad (32)$$

where: $\Delta\varphi = \varphi_2 - \varphi_1$ is equal to difference in latitude, $\Delta\lambda = \lambda_2 - \lambda_1$ is equal to difference in longitude and $R = 6371 [km]$ is the value of Earth's radius. Based on the calculated errors, a box plot of the positioning errors of individual GNSS modules is presented in Figure 49.

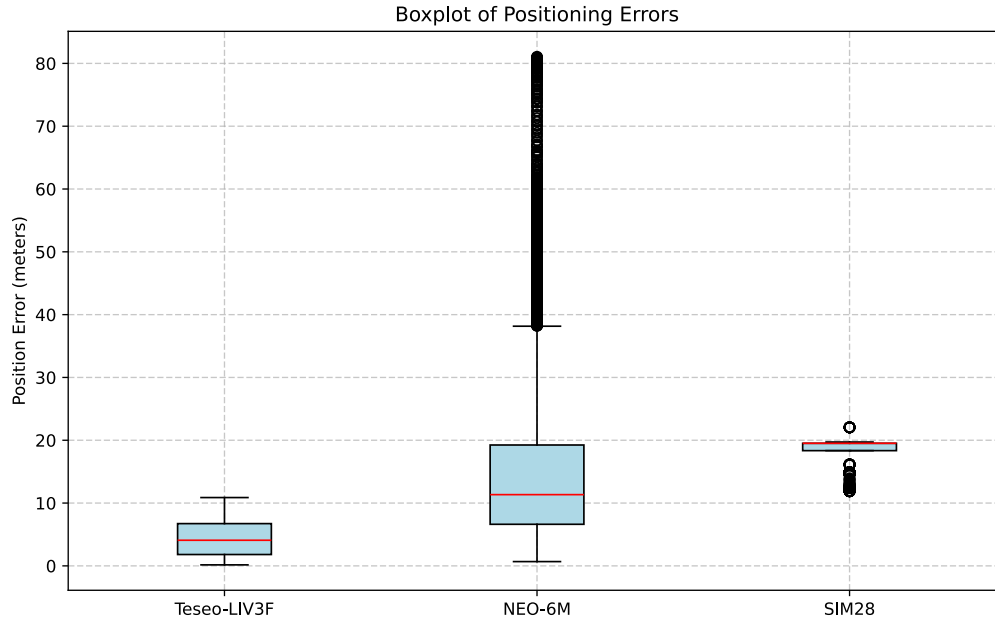


Figure 49 Teseo-LIV3F, NEO-6M and SIM28 GNSS modules raw positioning data errors boxplot

Its analysis shows that the most advanced Teseo-LIV3F module has the smallest measurement error. Its error range is within 10 m. The SIM28 module has a similar spread of measurement errors, but it occurs in the range from about 12 m to 22 m relative to the reference point. The NEO-6M module has the largest data spread and at the same time the largest range of measurement errors. This data was additionally visualized in error histogram graphs for individual modules (Figure 50).

Another observation results from the analysis of the location measurement error histograms for individual GNSS modules. Namely, the SIM28 module performed most of the measurements with a very large measurement error, and was also very repeatable, as evidenced by the high frequency of errors of around 18 and 20 m. For the NEO-6M module, the error distribution is concentrated mainly in the measurement error range up to 25 m, while in the case of Teseo-LIV3F, the distribution covers practically the entire range up to 10 m with particular intensity for values from 0 to 2 m, which is a very promising result.

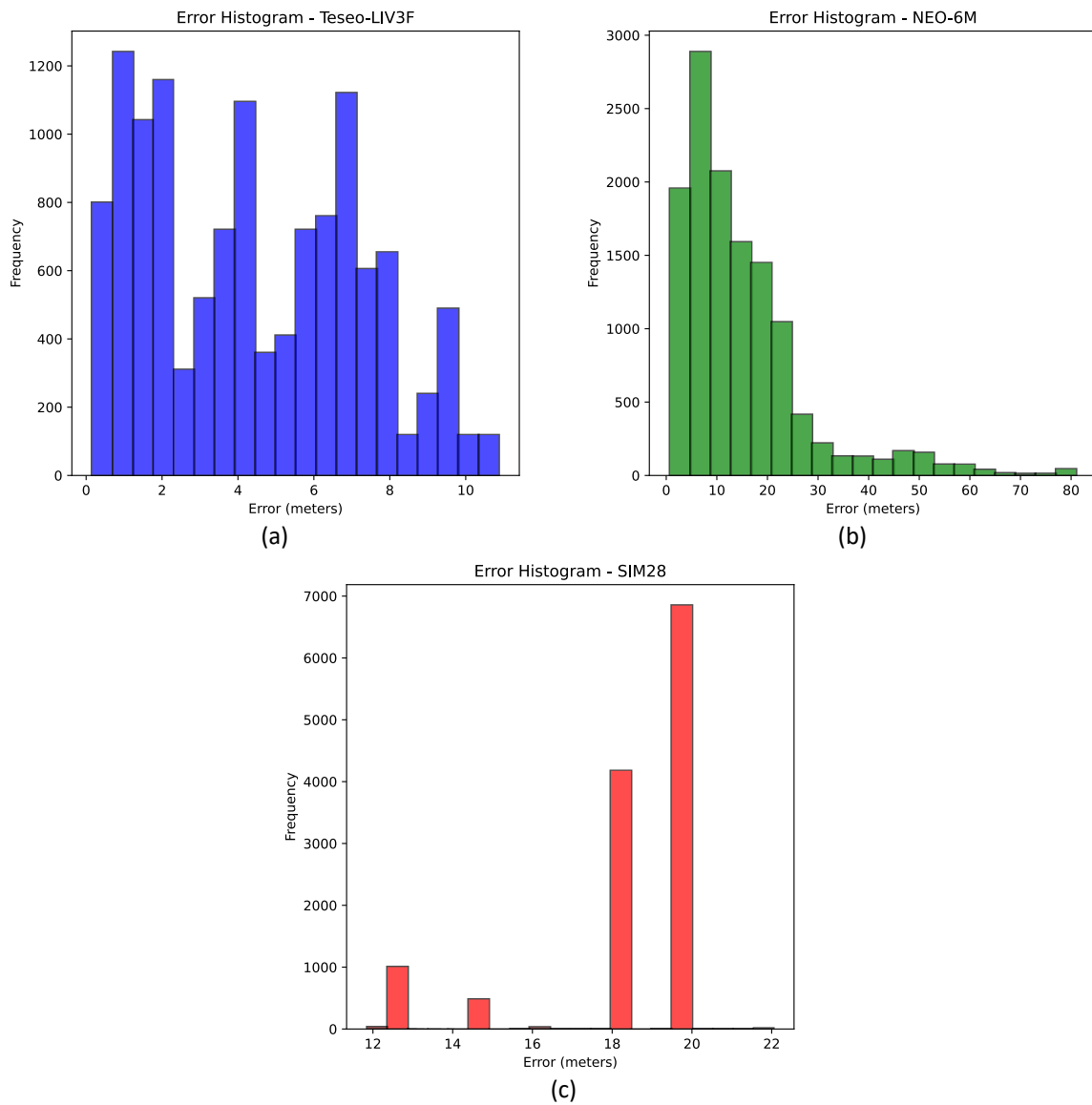


Figure 50 Error histograms of Teseo-LIV3F (a), NEO-6M (b) and SIM28 (c) GNSS modules - raw positioning

The change in measurement errors during the measurement was also observed to see if their increase or decrease was observed at the same time or if they occurred independently. A graph of this data is shown in Figure 51.

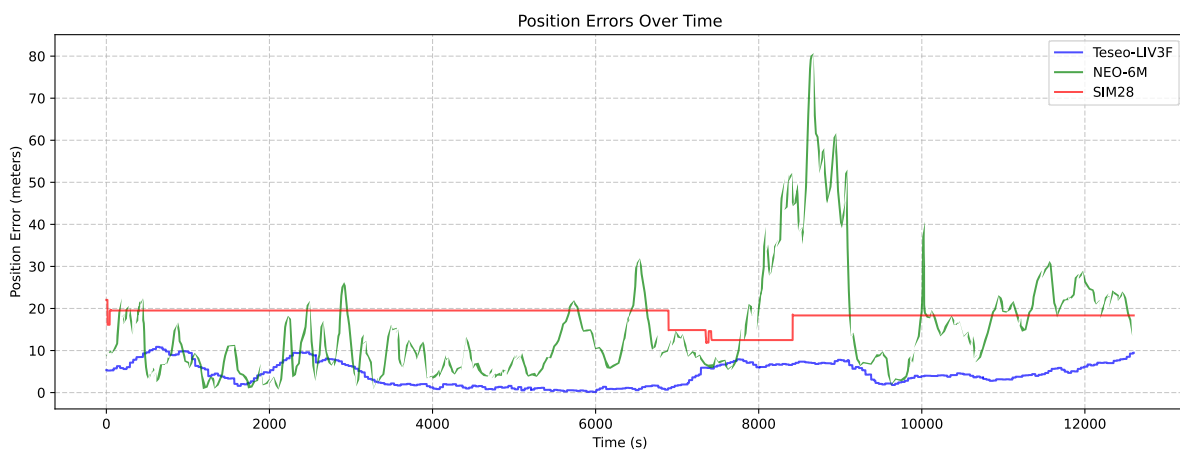


Figure 51 Teseo-LIV3F, NEO-6M and SIM28 GNSS raw positioning data errors over time chart

Its analysis shows that the error for the SIM28 module was almost constant with a clear decrease when the errors from the other two modules increased at about 7000 seconds. The NEO-6M module is the opposite of the SIM28 module, because the measurement errors fluctuate in a very large range, reaching as much as 80 m at the peak. It is a very unstable module, which, despite several measurement values close to the reference point of about 2000 seconds of measurement, is otherwise characterized by very high inaccuracy. However, one can observe a slight similarity in the moments for which these fluctuations occurred also for the most stable and accurate Teseo-LIV3F module. This may indicate factors such as the number of visible satellites and the distribution of their constellations (Figure 52), which in turn reflects the HDOP parameter (Figure 53).

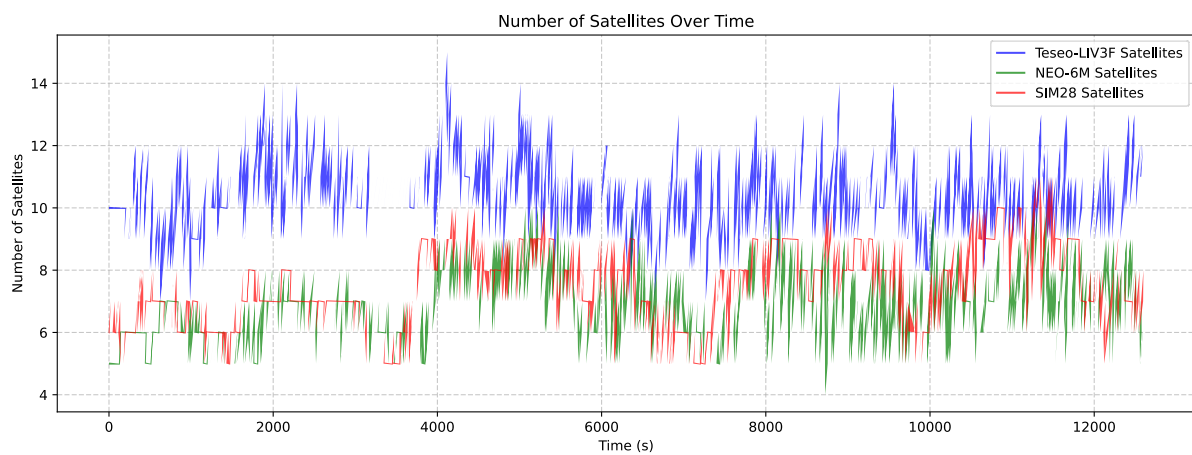


Figure 52 Number of satellites observed by Teseo-LIV3F, NEO-6M and SIM28 GNSS modules for raw data

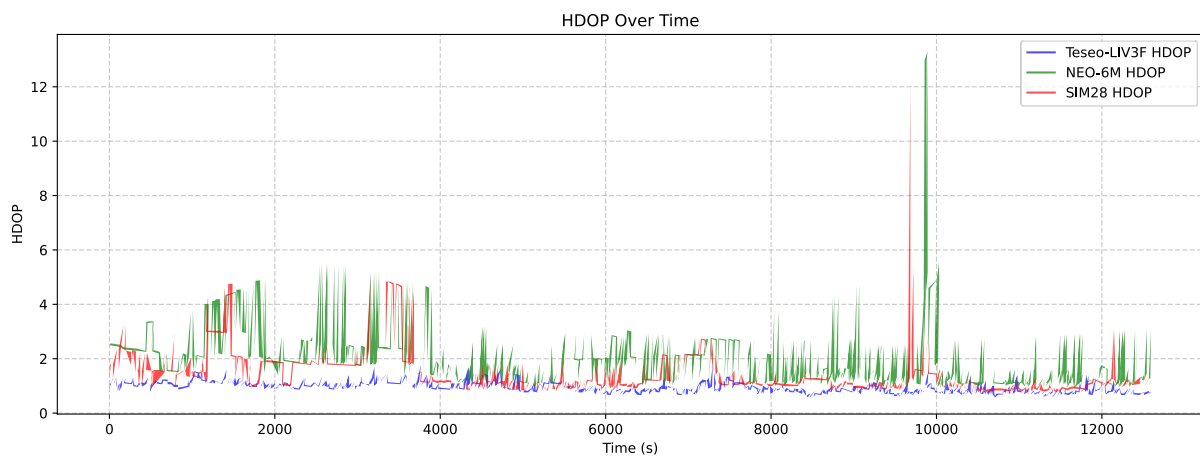


Figure 53 HDOP parameter value for raw data of Teseo-LIV3F, NEO-6M and SIM28 GNSS

The number of visible satellites by the Teseo-LIV3F module illustrates its advantage over the other two modules due to the simultaneous use of GPS and GLONASS satellites. This results in a significantly greater number of visible satellites, which may translate into its measurement accuracy. During the test, the NEO-6M and SIM28 modules were characterized by a similar number of visible GPS satellites, with moments of advantage in this aspect of the

less accurate SIM28 module (Figure 52). Analysis of the graph of changes in the HDOP parameter for individual modules, in accordance with the assumptions, indicates the highest accuracy of the Teseo-LIV3F module. It should also be noted that there are several peaks for the NEO-6M and SIM28 modules before the 10,000th second of measurement (Figure 53), when the graph of the distribution of measurement errors over time also shows similar peaks for the NEO-6M module (Figure 51). The above observations suggest a dependence of the positioning accuracy on the number of visible satellites and the position of the receiver relative to their constellation, and their relationships are shown in Figure 54 and Figure 55.

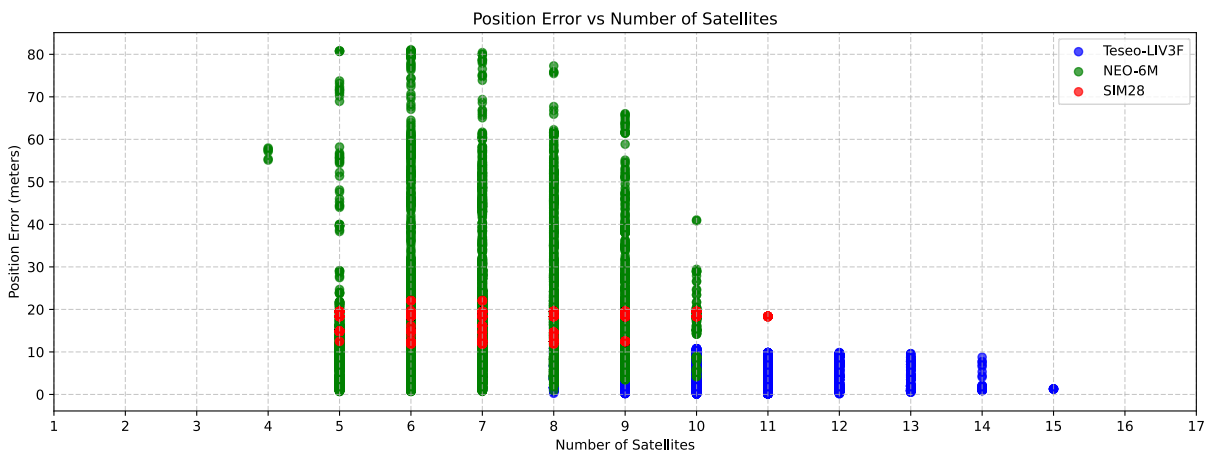


Figure 54 Position error in comparison to number of satellites visible by Teseo-LIV3F, NEO-6M and SIM28 GNSS raw data

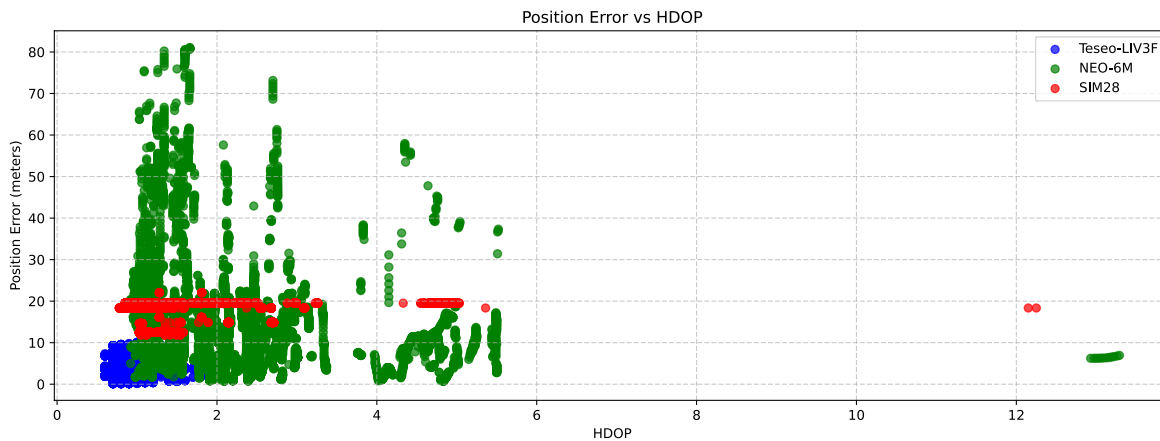


Figure 55 Position error in comparison to HDOP value of Teseo-LIV3F, NEO-6M and SIM28 GNSS raw data

Analysis of the graph of the positioning error versus the number of visible satellites clearly shows that with better satellite coverage, the size of measurement errors decreases. Therefore, we can assume a limiting minimum number of visible satellites for which, after filtering the location data, a smaller measurement error will be obtained. After a thorough analysis of the location data from the tested modules, this value was assumed to be at least 9 visible satellites by the module.

A closely related issue is the position of the GNSS receiver relative to the satellite constellation, which affects the correctness of the calculations of the module's position. The HDOP parameter clearly indicates that only values below 1.0 are charged with the smallest error, which is about 10 m. For higher values of this parameter, the NEO-6M module behaved in a very unstable way, burdened with very large errors. Interestingly, the SIM28 module, regardless of the HDOP value, showed a constant error of about 20 m from the reference point.

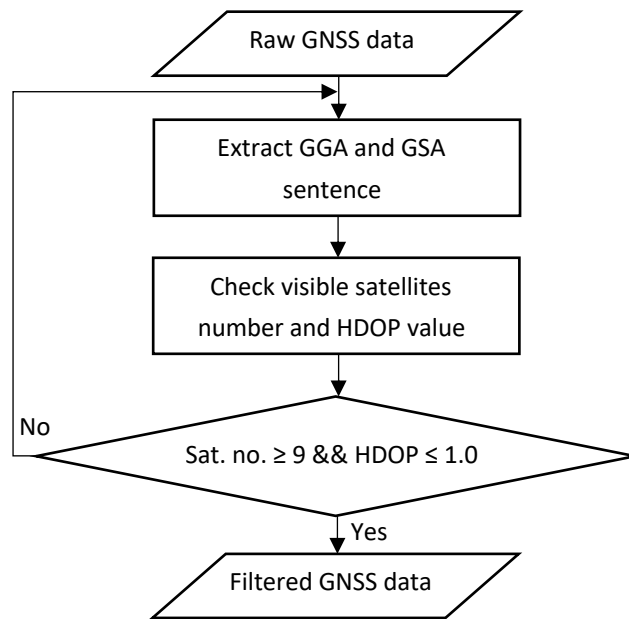


Figure 56 Proposed solution for reducing GNSS positioning data error

Assuming the above assumptions regarding data filtration based on visible minimum 9 satellites and HDOP parameter value less than or equal to 1.0, the proposed method of improving the positioning accuracy of GNSS modules (Figure 56) was verified. Figure 57 shows the map of the distribution of measurement points after the applied correction. After implementation of proposed solution there are significantly fewer measurement points and a much smaller spread than before the filtering (Figure 48). As expected, Figure 57 clearly shows the density of measurement points from the Teseo-LIV3F module, then the closer position points read by the NEO-6M module, while the furthest away are only the two points determined by the SIM28 module.

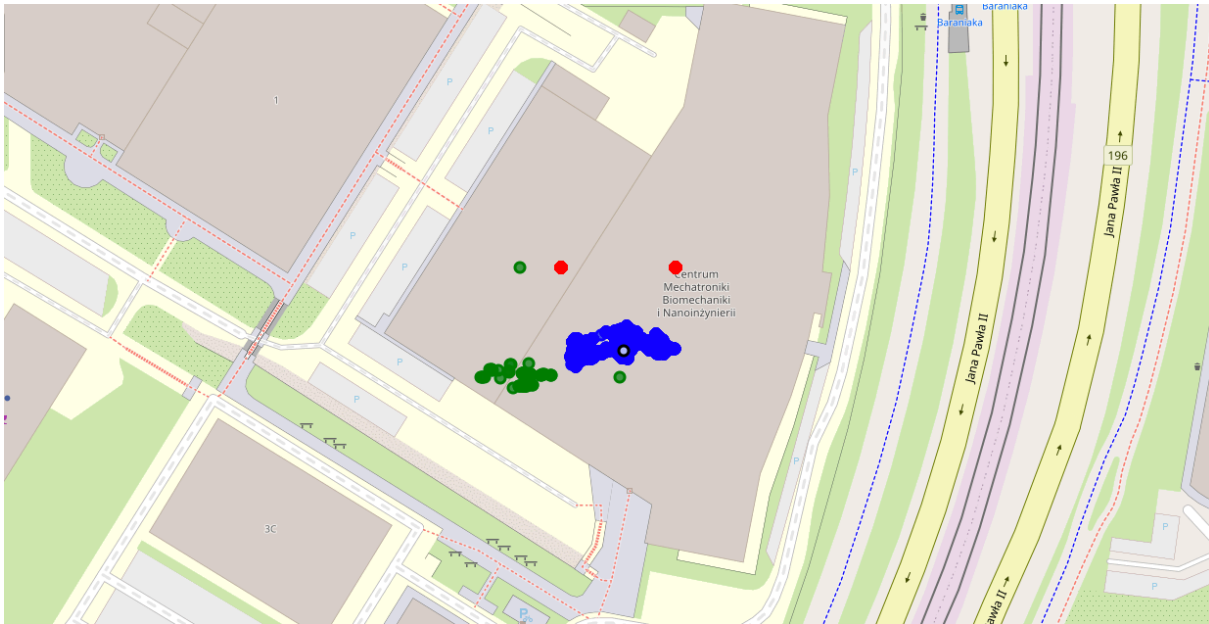


Figure 57 Map of GNSS modules filtered measurements: reference point (black), Teseo-LIV3F (blue), NEO-6M (green), SIM28 (red)

For the filtered location data, their distances from the reference point were also calculated using the Haversine formula (32) and presented in a box plot of errors for individual modules (Figure 58). The analysis of collected data shows a significant reduction in the outlier error values for the NEO-6M and SIM28 modules. However, these modules have a measurement error of about 20 m. The Teseo-LIV3F module contrasts greatly with them, with a median of about 4 m and the data dispersion itself, excluding the maximum and minimum values, is within 5 m. Confirmation of these observations can be found in the error histogram graphs of the individual modules (Figure 59).

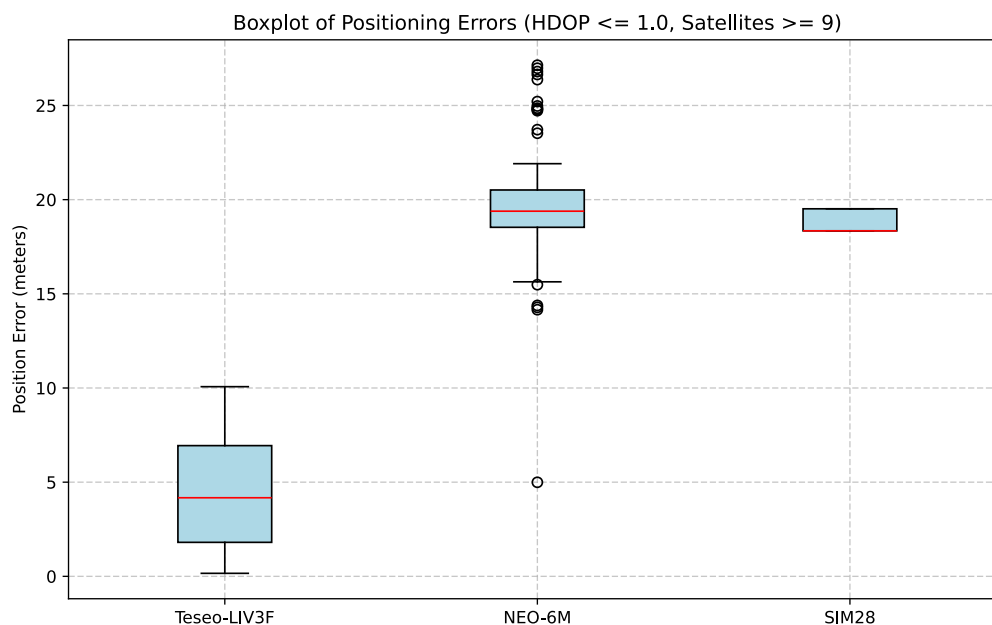


Figure 58 Teseo-LIV3F, NEO-6M and SIM28 GNSS modules filtered positioning data errors boxplot

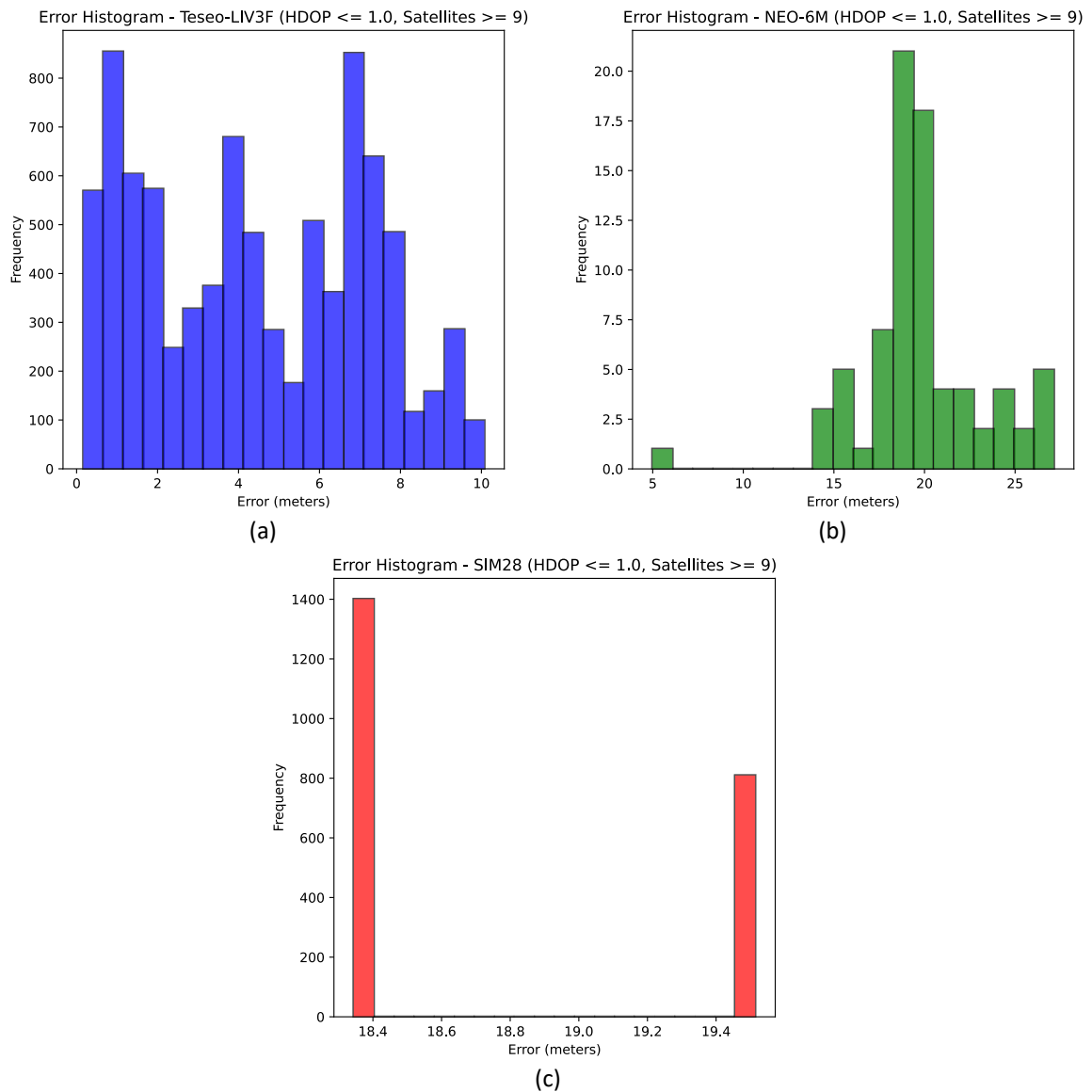


Figure 59 Error histograms of Teseo-LIV3F (a), NEO-6M (b) and SIM28 (c) GNSS modules - filtered positioning

The analysis of the histograms for individual modules shows that measurement points burdened with a very large measurement error were eliminated and it was reduced, looking globally at all modules from over 80 m to about 27 m. Moreover, in the case of the most accurate Teseo-LIV3F module, a clear density of measurement error values of up to 1.5 m is visible, which confirms the manufacturer's declarations regarding its accuracy [140]. The NEO-6M module showed a significant limitation of useful measurement data to only a few measurements burdened with an already large error of about 20 m. Unfortunately, this is due to the class of the device, which operates only on the basis of the GPS system. A slightly smaller data dispersion, ranging from 18.4 to 19.5 m, was shown by the GPS SIM28 module, whose measurement repeatability, which should be an advantage, turns out to be its biggest disadvantage, because the measurement error is quite high.

3.2.2 Dynamic localization measurement using GNSS

Thanks to the proposed correction consisting in filtering the measurement data of the GNSS module locations, those with a very large measurement error were rejected. This had a positive effect on the rough determination of the module position relative to the reference point. Based on a comparison of position information from the three modules tested, it can be stated that the most accurate of them is Teseo-LIV3F. In the next study on the positioning accuracy during the movement of the measuring platform for testing AGL, it was selected as the reference point for the remaining two modules due to the impossibility of determining a more precise position of the moving device behind the vehicle controlled by a human. During the measurements, filtration based on the number of visible satellites and the HDOP parameter value was already applied, as was proposed for static measurements. The graph of the number of visible satellites (Figure 60) and the HDOP value (Figure 61) during measurements in motion is shown in graphs depending on the measurement duration.

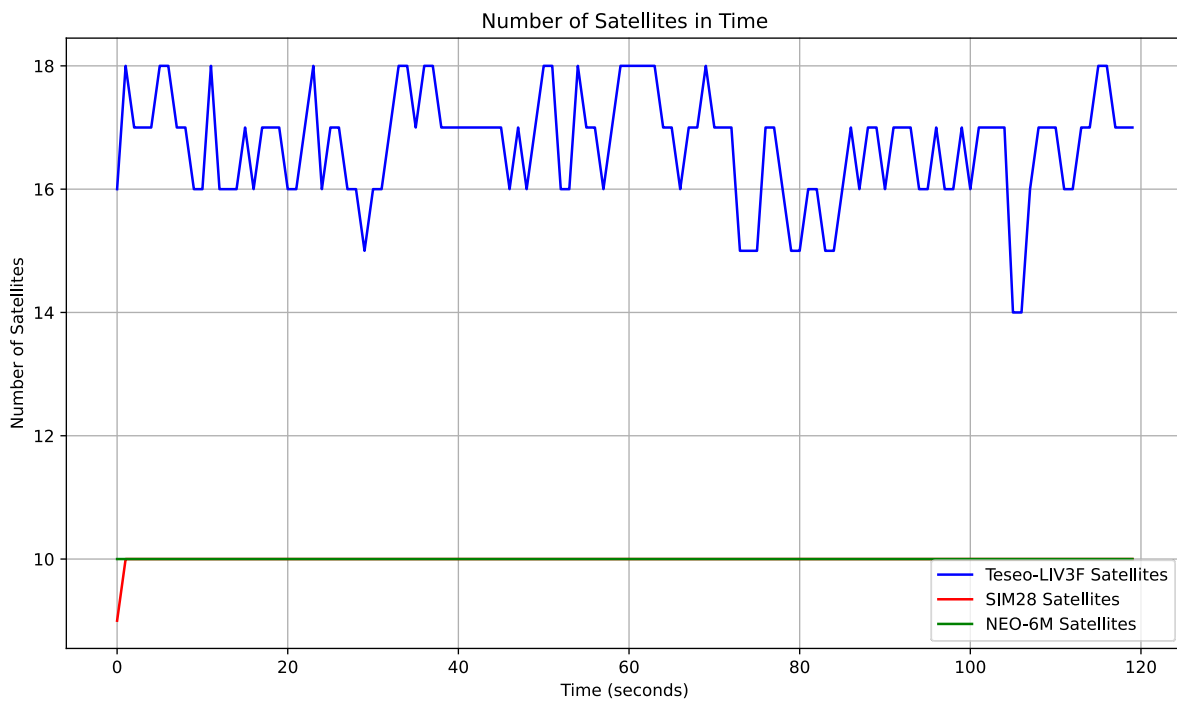


Figure 60 Number of satellites observed by Teseo-LIV3F, NEO-6M and SIM28 GNSS modules during movement test

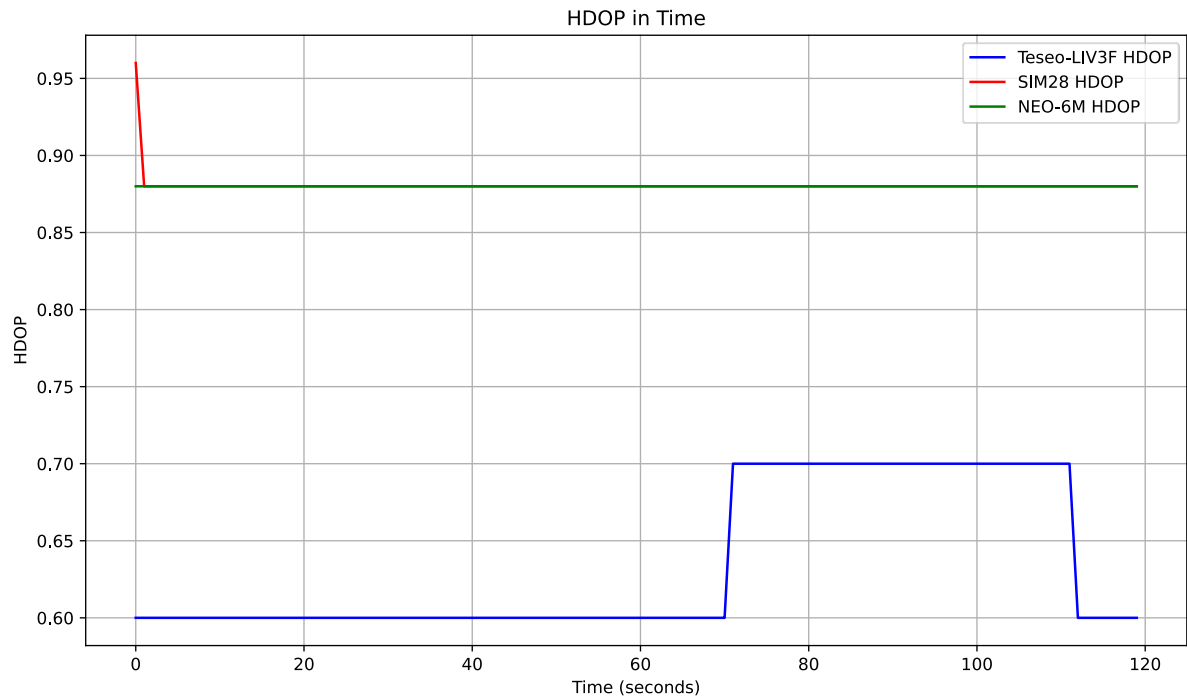


Figure 61 HDOP parameter value of Teseo-LIV3F, NEO-6M and SIM28 GNSS during movement test

The test of GNSS modules in motion was carried out at the Poznań-Ławica Airport. During the test run, the vehicle moved along the runway along the axis of the runway center line lights from the approach direction 28. The vehicle pulling the measuring platform started the run by starting from a standstill and then moved at a constant speed of about 60 km/h. The GNSS module antennas were set up, just like in the case of the stationary test, next to each other, and the operation of the modules was synchronized based on the UTC time reading from the satellites. The course of the movement of the measuring platform for testing quality of AGL is shown in Figure 62.

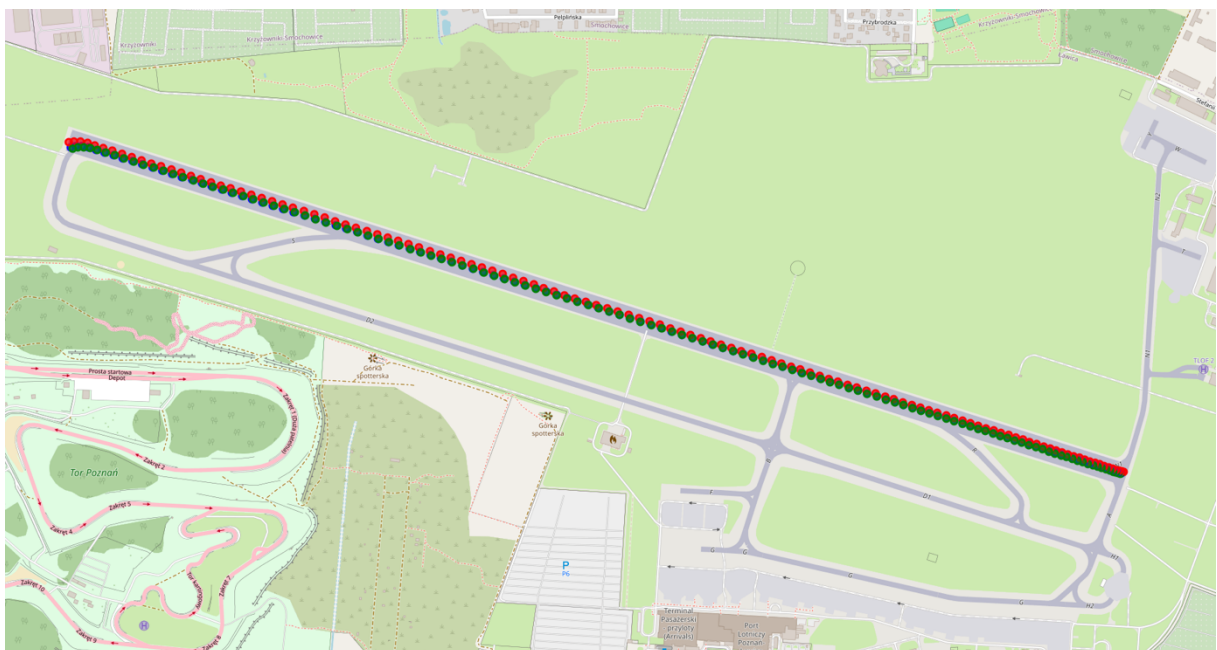


Figure 62 Map of GNSS modules during movement: Teseo-LIV3F (blue), NEO-6M (green), SIM28 (red)

The main observation is that the position measurements made by the modules roughly agree, as they are within the runway. However, if we analyze the location of the individual location points, differences are noticeable. For example, Figure 63 shows the beginning of the measurements, and Figure 64 shows the end of the measurements.



Figure 63 Map of GNSS modules at the beginning of the measurement: Teseo-LIV3F (blue), NEO-6M (green), SIM28 (red)



Figure 64 Map of GNSS modules at the end of the measurement: Teseo-LIV3F (blue), NEO-6M (green), SIM28 (red)

The maps illustrate a shifts between the measurements from the individual modules. It should also be noted that the measurements taken using the Teseo-LIV3F module are located on the runway axis, which means that they most accurately reflect the trajectory of the measuring platform. An interesting relationship can be observed for the SIM28 module, which at the beginning of the measurements stays behind the other two modules, and with increasing movement speed - overtakes them, additionally increasing its distance from them until the end of the measurement. This may indicate its low resistance to errors during

movement and high inertia. The NEO-6M module, on the other hand, lags slightly ahead at the beginning of the measurement, and at the end lags behind the reference points from the Teseo-LIV3F module. In order to illustrate the size of the measurement errors, the Haversine formula (32) was used to calculate the distances of the measurement points from the NEO-6M and SIM28 modules relative to the Teseo-LIV3F and presented on a graph, depending on the measurement duration (Figure 65).

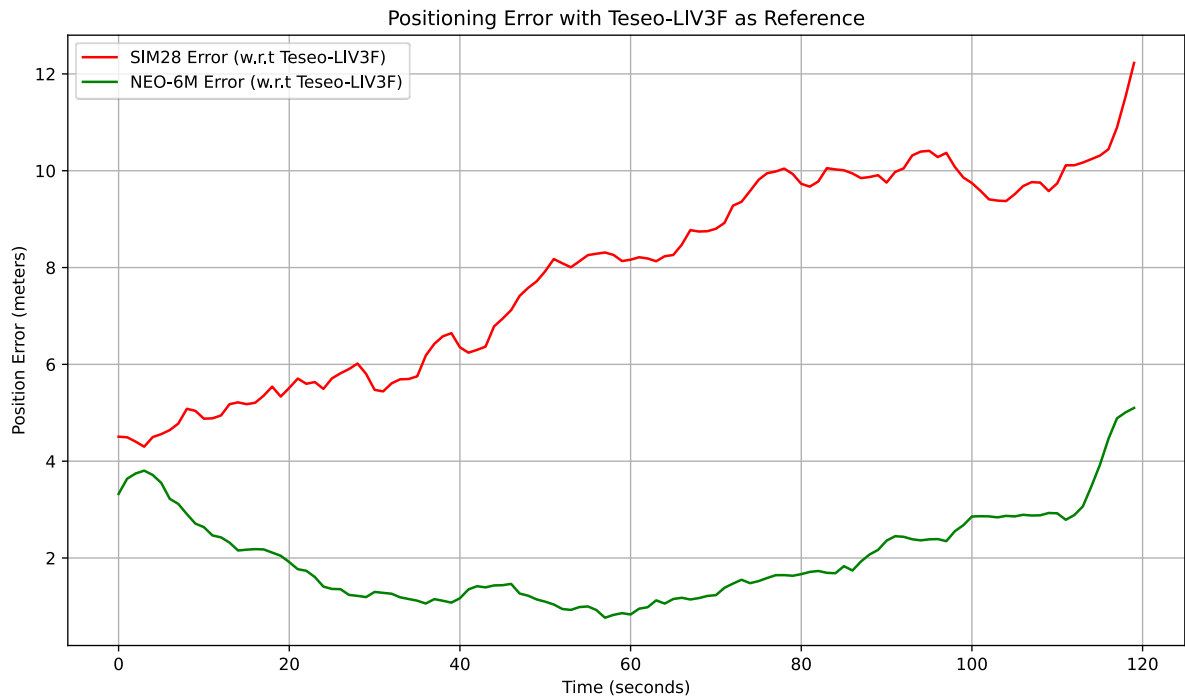


Figure 65 NEO-6M and SIM28 GNSS w.r.t Teseo-LIV3F positioning data errors over time chart

According to the observations based on the map of measurement points, a continuous increase in the measurement error for the SIM28 module can be observed. This is the result of the Teseo-LIV3F module overtaking the measurements and moving them sideways from the module. The NEO-6M module, also in accordance with the observations on the map, was initially behind the reference module, with a slight shift to the left. Then, catching up with the Teseo-LIV3F module, it led to a decrease in measurement errors from about 4 m to 1 m approximately in the middle of the measurement, to then gradually increase its error and finally exceed the error value again by about 5 m. The distribution of measurement errors of the NEO-6M and SIM28 modules is shown in Figure 66.

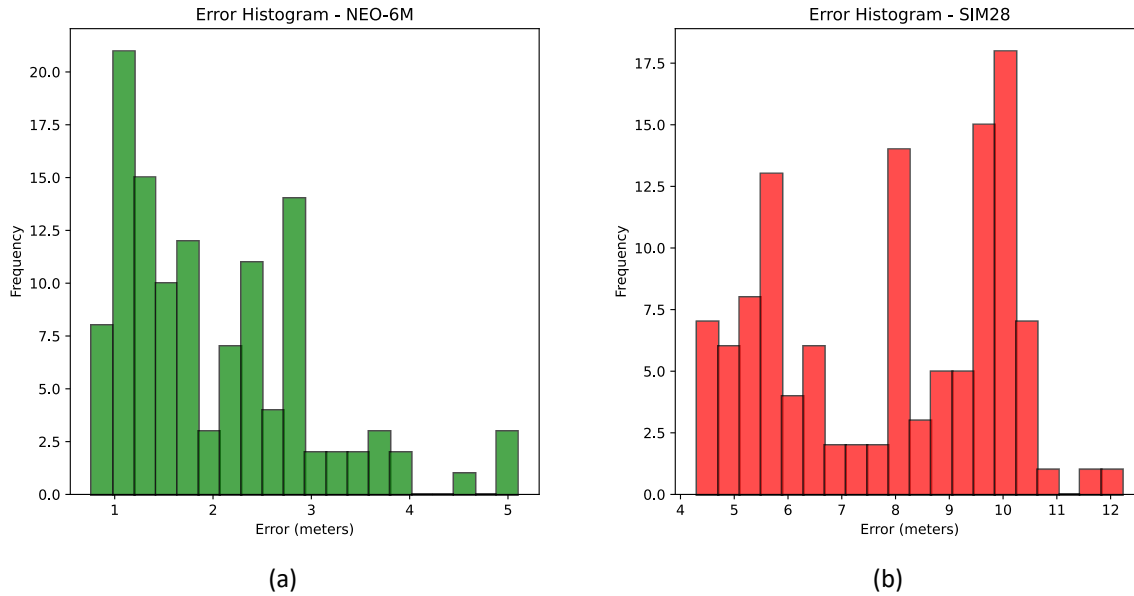


Figure 66 Error histograms of NEO-6M (a) and SIM28 (b) w.r.t. Teseo-LIV3F measurement

The analysis of the histograms for both modules confirms the previous observations. The NEO-6M module is characterized by a much smaller measurement error compared to the SIM28 module, whose smallest error value is equal to the highest of the latter. In the case of NEO-6M, errors occur mainly up to a value of less than 3 m, and above this value there are rare occurrences of errors. For the SIM28 module, the situation is completely opposite and the largest number of errors occurs for larger values of distance from the reference point.

In summary, the use of GNSS modules is associated with the risk of location measurement errors of even a few or a dozen meters. It depends on the type of receiver, which can use one or more types of satellite constellations. For modules using only GPS the error range was from 0 m to 80 m for NEO-6M and 12 m to 20 for SIM28. The more advanced GNSS module Teseo-LIV3F which use both GPS and GLONASS has much smaller error range from 0 m to 11 m for raw positioning data. In addition, GNSS devices positioning efficiency strongly depends on the number of visible satellites and the receiver's positioning relative to their constellation, which as an impact on the calculation of flat coordinates determines the HDOP parameter.

Proposed measurement data filtration based on the number of visible satellites and the HDOP parameter value can effectively reduce the occurrence of very large position errors, which was proven by conducting static tests of Teseo-LIV3F, NEO-6M and SIM28 modules. Setting the conditions of the minimum number of visible satellites to 9 and the HDOP value less than or equal to 1.0 limited the error range for the Teseo-LIV3F module to 0 m to 10 m, for NEO-6M from 5 m to 27 m and for SIM28 narrowed the error distribution from 18.4 to 19.5 m.

Using the same filtration methods during the test of movement on the runway of Poznań - Ławica Airport, very good results were obtained for the Teseo-LIV3F module, which best reflected the trajectory traveled. The NEO-6M module did this task satisfactorily, while SIM28 came out the worst. However, this does not change the fact that GNSS modules are only suitable for a rough assessment of the position of the measuring platform for testing AGL, due to the required measurement accuracy of several centimeters. It is unattainable for modules that do not use DGPS and RTK technology, the use of which also depends on the base stations available in the area and in some cases requires additional permits.

3.3 Correction of distance estimation using LiDAR

3.3.1 Preliminary experiments

As part of testing the limitations and possibilities of using LiDAR for environmental monitoring, the SLAMTEC RPLIDAR A1M8 laser scanner was tested [28]. Its operation was verified in differently arranged environment models. Obstacles in the form of cardboard boxes of various sizes were placed around the module, and then the correctness of the distance reading with the actual value and the spatial mapping related to their angle relative to the device axis were checked.

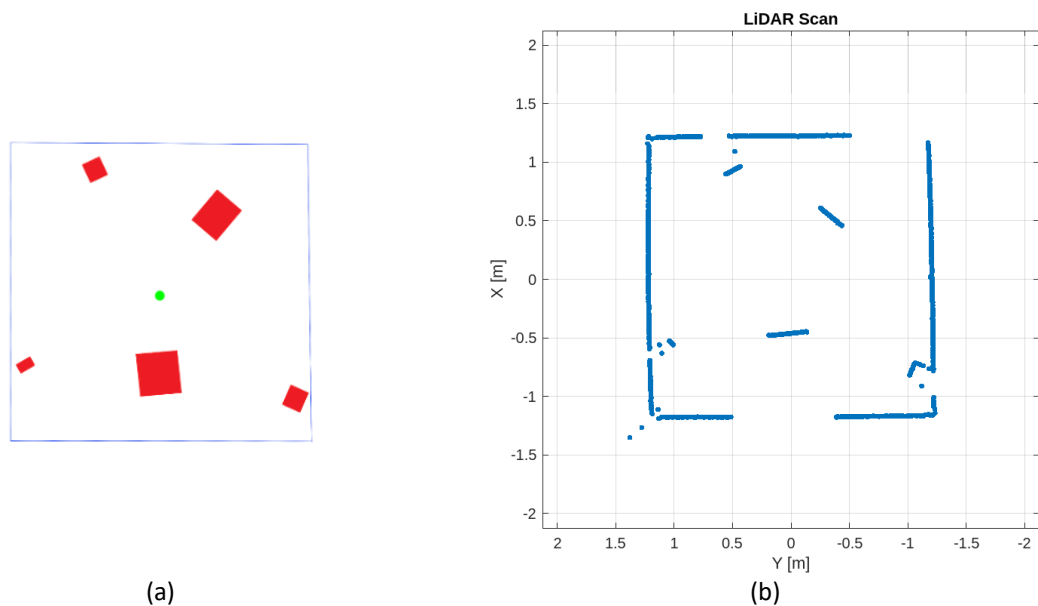


Figure 67 Test stand of arranged environment model (a) and its LiDAR map [28]

First, the test was carried out in laboratory conditions, where the objects were within the distance range declared by the manufacturer (Figure 67a). The blue lines mark the walls that separated the research area in the form of a square with a side of 2.41 m. LiDAR was placed in the central point of the environment (green point), and the objects marked with red rectangles were obstacles of various sizes. The values obtained after the scan were each time verified by manual measurement from the scanner axis to the center of the obstacle plane

and were (starting from the upper left obstacle clockwise): 62.8 cm, 105 cm, 114.3 cm, 45.8 cm and 128.5 cm. All results obtained were correct. The measurements were made in three different LiDAR operating modes, which differ in the number of measurement points: 2000, 4000 and 8000. The map created on the basis of measurements of the scanned area with the highest accuracy is presented in Figure 67b. The conclusions drawn from its analysis are, above all, a very accurate reflection location and angular setting of obstacles. However some distortions near the walls in the lower right corner can be observed. This shows how accurate the scanner is, because when constructing the test area, a small gap in the corner, which was a few millimeters in size, was not noticed. It should also be noted that monitoring the environment only using LiDAR has certain limitations in the form of shadows left by obstacles. This phenomenon makes it impossible to thoroughly examine the entire environment without moving the sensor.

Subsequent experiments were intended to check the operation of the device in extreme cases, i.e. when exceeding the lower measurement range and approaching the upper measurement range. The data presented by the manufacturer specify these limits at distances of 15 cm and 12 m, respectively [158]. If an obstacle is placed too close, the object becomes invisible to the scanner (Figure 68). This is a very dangerous phenomenon, especially in environments with moving objects, where the spaces between obstacles can change very dynamically. In the case of static objects located in the research area, the lack of visibility of the corner of the obstacle was observed (object on the right) and, when positioned parallel to the LiDAR, the visibility of a fragment of the side plane was partially limited. Additionally, it is clearly visible how closely placed objects significantly limit the possibilities of monitoring the entire research environment. Obstacles at a distance of less than 15 cm were invisible to the module, which confirms the declarations of the device manufacturer.

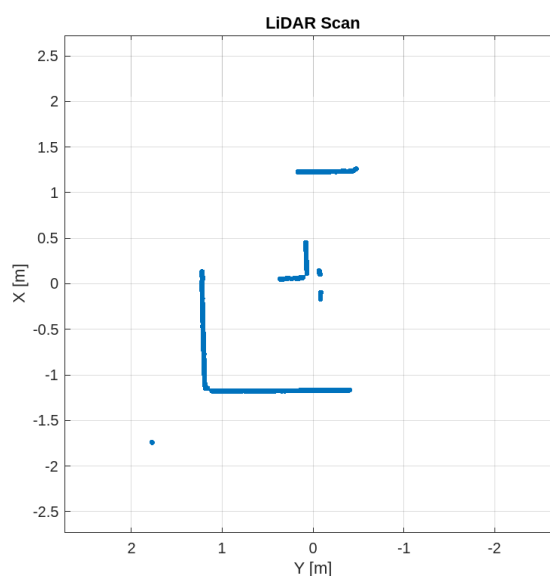


Figure 68 LiDAR ambient scan with two closely placed obstacles [28]

The test of the maximum range of distance measurement was carried out in an empty space limited by three walls, placing an obstacle at a distance of 12 m. Up to this limit, all distance measurements were correct and reflected the actual distance. When approaching the upper limit value declared by the manufacturer, disturbances occurred in the form of fading of the object, and after exceeding the 12 m barrier, the obstacle became completely invisible. When making measurements at large distances, it is also necessary to set the scan with the highest possible resolution, because for 2000 and 4000 points the interference was much more noticeable.

The tested LiDAR system allowed for accurate mapping of the visible area - this concerned both distance measurement (accuracy up to 1% of the measured distance) as well as the angular orientation of objects (precision up to 1°).

However, there are limitations that need to be eliminated to minimize the risk of missing or incorrect detection of obstacles. They mainly concern the measurement range of a given device. In the case of the tested RPLIDAR A1M8 scanner, measurement is impossible below 15 cm, so a good complement would be another laser sensor with a shorter range or a cheaper alternative in the form of an ultrasonic sensor that works easily in such a small range.

Similar comments apply to the upper measurement range, which should be taken into account when designing an environmental monitoring system. Obstacles located at a greater distance than predicted by the manufacturer also become invisible to the scanner. Operating within the intended measurement range, the obtained data are very precise and adequately reflect environmental parameters.

Too strong daylight intensity is a negative factor affecting the correctness of the results (especially for the tested SLAMTEC RPLIDAR A1M8). It causes disturbances in the form of disappearing objects. Therefore, user should pay attention to whether a given module is intended for operation inside buildings or in an outdoor environment. The tested scanner module allows to obtain measurements in 2D, while increasing the precision of the measurement and eliminating problems related to casting a shadow by some low objects can be eliminated by using a more advanced device that allows to scan the environment in 3D.

3.3.2 Elevated airport edge lamps detection using LiDAR

In the system supporting the assignment of the appropriate trajectory of the measuring platform for testing the quality of the AGL, the runway edge lamps are to be detected using a LiDAR sensor. They are elevated lamps that are placed along the runway on both sides and are located 60 m apart (Figure 69) and 3 m from the edge of the runway, which, given the width of the runway of 60 m, means a spacing between pairs of edge lamps of 54 m.

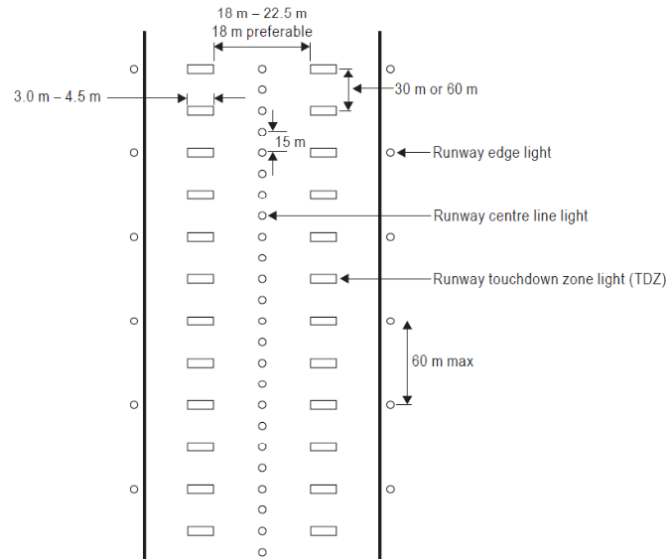


Figure 69 Placement and distances between different types of aeronautical ground lights [209]

The diameter of the narrowest part of the runway or taxiway edge lamp, i.e. the stand on which it is mounted, is 5 cm (Figure 70).



Figure 70 Runway (a) and taxiway (b) edge elevated lamp

Based on this data, the calculation of the minimum resolution distance of LiDAR points was undertaken, so that at least one edge lamp is in its field of view. It was assumed for the calculations that two points from the point cloud, which will be located on the post of the edge lamp, will be sufficient, so the distance between points is $p_d = 0.05 \text{ m}$. Assuming that the LiDAR is located at the farthest point from the nearest edge light, this means that it is located exactly in the middle of the runway, exactly between successive pairs of edge lights, i.e. the straight-line distance to each of the four is approximately $d = 40.36 \text{ m}$. A simplified diagram of the arrangement of measurement points relative to LiDAR and variables is shown in Figure 71.

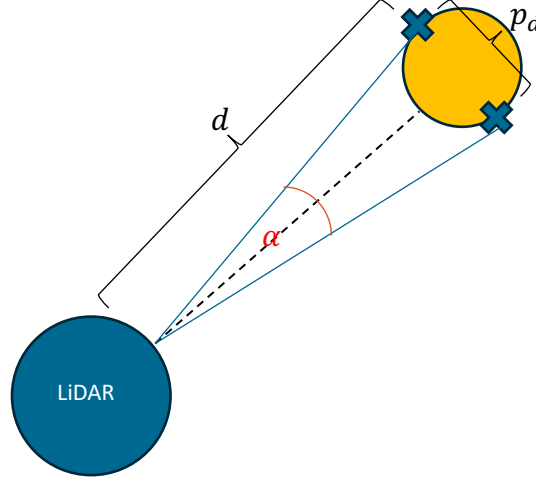


Figure 71 Schematic of LiDAR measurement of elevated runway edge lamp

The distance p_d can therefore be determined as (33), where angle $\alpha = \frac{360^\circ}{res}$. Therefore, after substituting it into equation (33) and transforming it, it is possible to calculate the minimum LiDAR resolution (res) that will allow meeting the requirements for the location of runway edge lights, and it is equal to (34).

$$p_d = 2d \cdot \operatorname{tg}\left(\frac{\alpha}{2}\right) \quad (33)$$

$$res = \frac{180}{\arctan\left(\frac{p_d}{2d}\right)} \approx 5072 \left[\frac{\text{measurements}}{\text{scan}} \right] \quad (34)$$

3.3.3 LiDAR point cloud data classification

An important aspect in the case of data obtained from LiDAR in the form of a point cloud is their proper interpretation. Due to the characteristics of the sensor, which is susceptible to minor interference resulting from the type and material of the surface from which the distance is measured, this data must be properly processed. In addition, in solutions such as detecting characteristic objects on a mostly uniform background, they must be properly interpreted. A solution may be to use the RANSAC algorithm to separate the object data from the background as outliers and inliers, respectively.

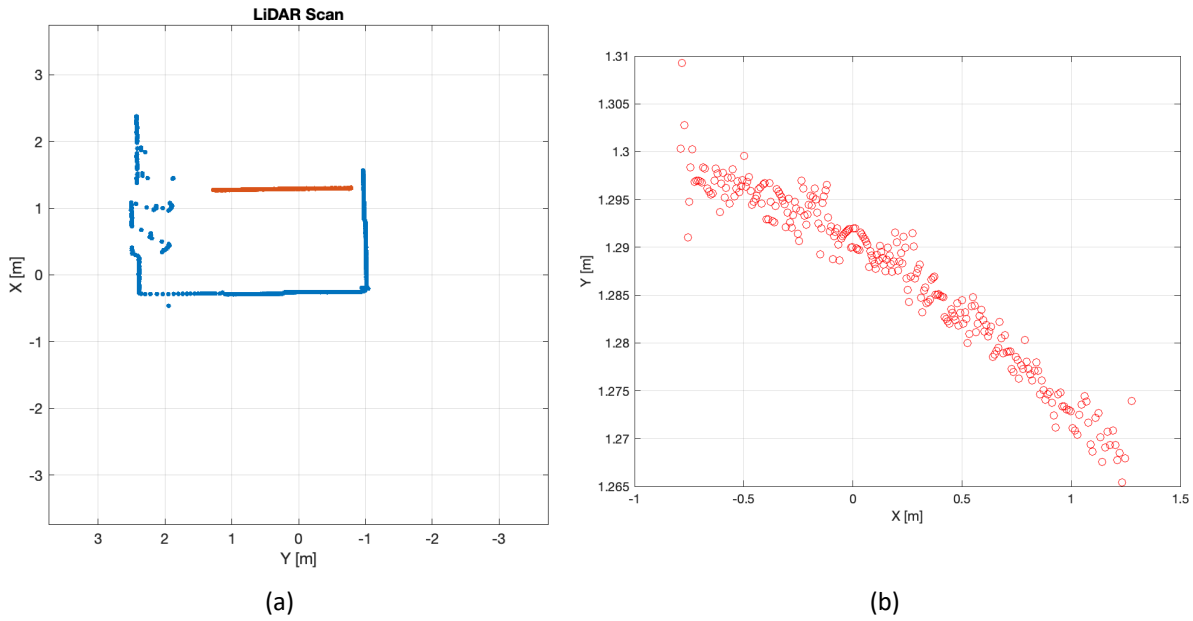


Figure 72 LiDAR scan with flat surface obstacle in overall view (a) and detail view (b)

During the experiment, an object with a flat and uniform surface was placed at a distance of approximately 1.30 meters in a straight line from the SLAMTEC RPLIDAR A1M8 module. It was marked on the point cloud map (Figure 72a) in red. It gives the impression of a uniform line constituting a point cloud of this obstacle, however, after a more detailed analysis of the point cloud section responsible for mapping the object, individual points located at a certain distance can be seen (Figure 72b).

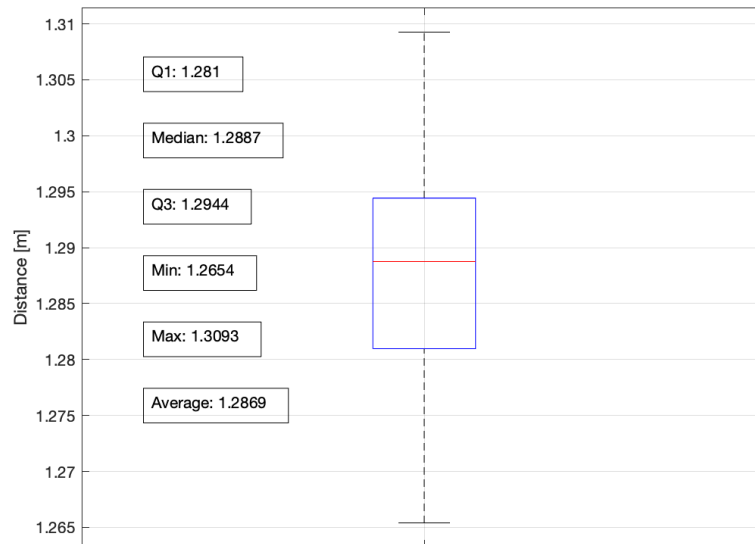


Figure 73 Analyzed data point cloud data statistical box plot

The data scatter is presented in the box plot in Figure 73. Its analysis shows that the mean and median for this point cloud section differ by only 0.0018, and the distance measurement is correct and falls within the range of 1% in accordance with the manufacturer's declaration. The RANSAC algorithm was used for the described data, which is an iterative method used to estimate the parameters of the sought mathematical model of the object in a data set with a significant number of points not belonging to the modeled surface - in this case the flat and

uniform surface of the obstacle. The RANSAC estimator is particularly interesting for processing point clouds burdened with noise and measurement errors.

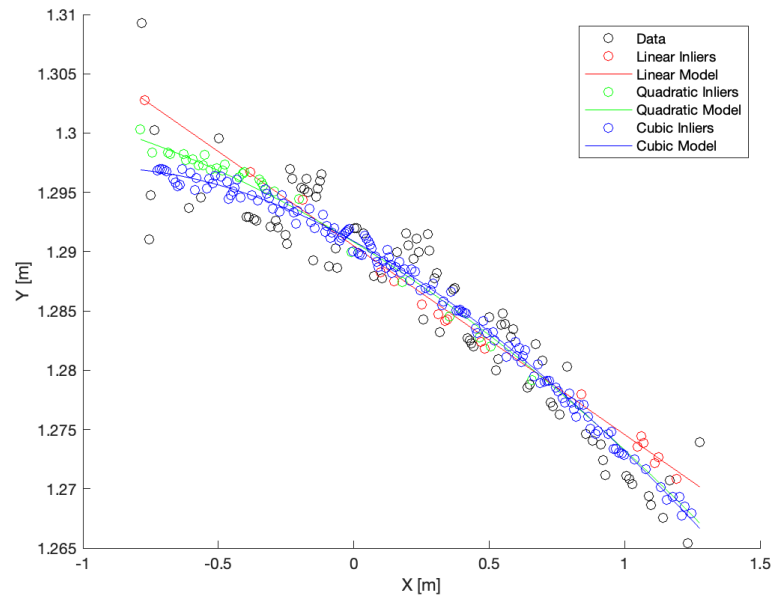


Figure 74 Comparison of linear, quadratic and cubic RANSAC model estimation

During the experiment, various estimation models were tested, including linear, quadratic and cubic (Figure 74). As a result of their operation, the number of inliers was checked. The highest value of this parameter obtained for a specific estimator model means its best fit to the data (Table 22).

Table 22 RANSAC estimator model results

RANSAC estimator model	Number of inliers
Linear	112
Quadratic	146
Cubic	142

In the tested case, the quadratic model obtained the highest result, and the cubic model turned out to be slightly worse. The worst fit was achieved by the algorithm using the linear model. It should be mentioned that the use of the RANSAC algorithm with the quadratic model allowed for reducing the tolerance of measurement errors and the buffer of results around the mean, which is shown in Figure 75.

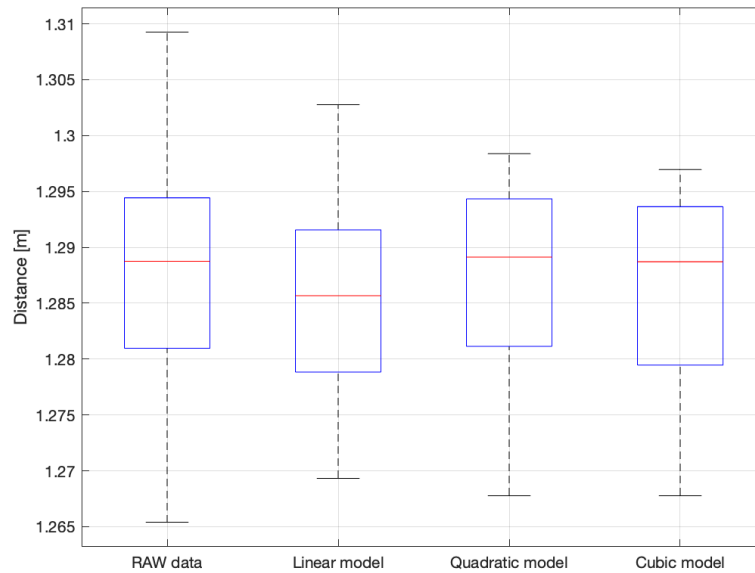


Figure 75 Data scatter of raw LiDAR data and linear, quadratic and cubic RANSAC model estimators

Similar solutions using the RANSAC algorithm are used in the case of vehicles moving on public roads. Their task is to capture objects that differ from the background (outliers), e.g. those that are not curbs. However, to correctly detect outliers, it is necessary to properly analyze the background points and classify them as much as possible as inliers that fit the estimator model.

3.4 Detection of characteristic points on video sequences

The next element of the proposed multisensory localization techniques is detection of light spots in video sequence. As shown in Figure 6 the camera is placed on the hood of the car which is towing the platform for AGL measurement assessment.

The airport setting, where these measurements are conducted using specialized devices, is unique due to its size and layout. A typical runway spans approximately 60 meters in width and over 2 kilometers in length, featuring markings like the central axis line, runway number, aiming points, and taxiways exit lines. At Poznań-Ławica Airport, for instance, the runway is equipped with 166 bidirectional centerline lamps and 180 touchdown zone lamps (Figure 76a). Detailed guidelines on the arrangement of lamps (Figure 76b) and lines are included in the EASA standards [209].

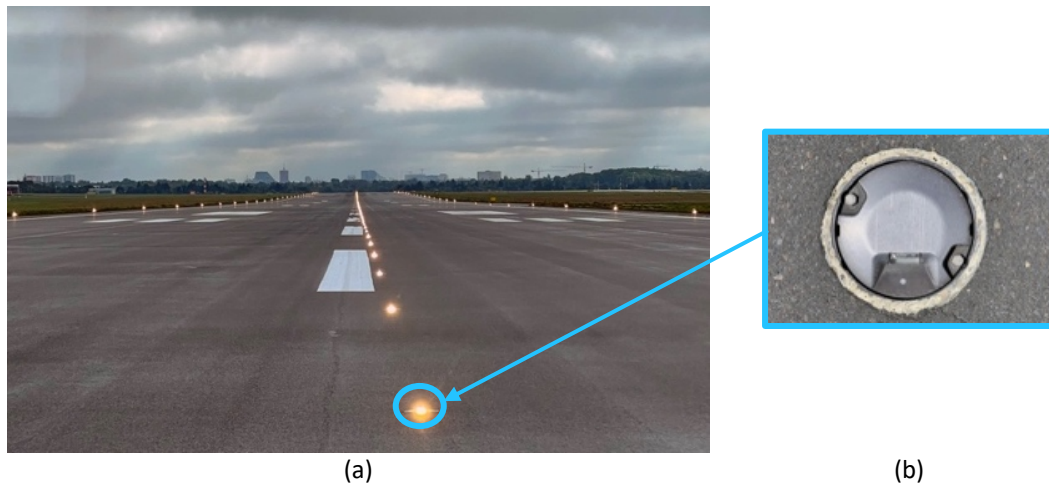


Figure 76 Runway view with lighting and line markings (a) and in-pavement airport lamp (b) [31]

The measurement method concept, utilizing a specialized inspection device, is illustrated in Figure 77. A common characteristic of mobile measuring systems [15], [17], [184], [232] is the inclusion of a matrix of light sensors, which enables the evaluation of the full spectrum of the light beam emitted by the lamp. Achieving accurate measurements with such a matrix requires precise alignment with the light source to ensure the emitted beam properly strikes the sensors.

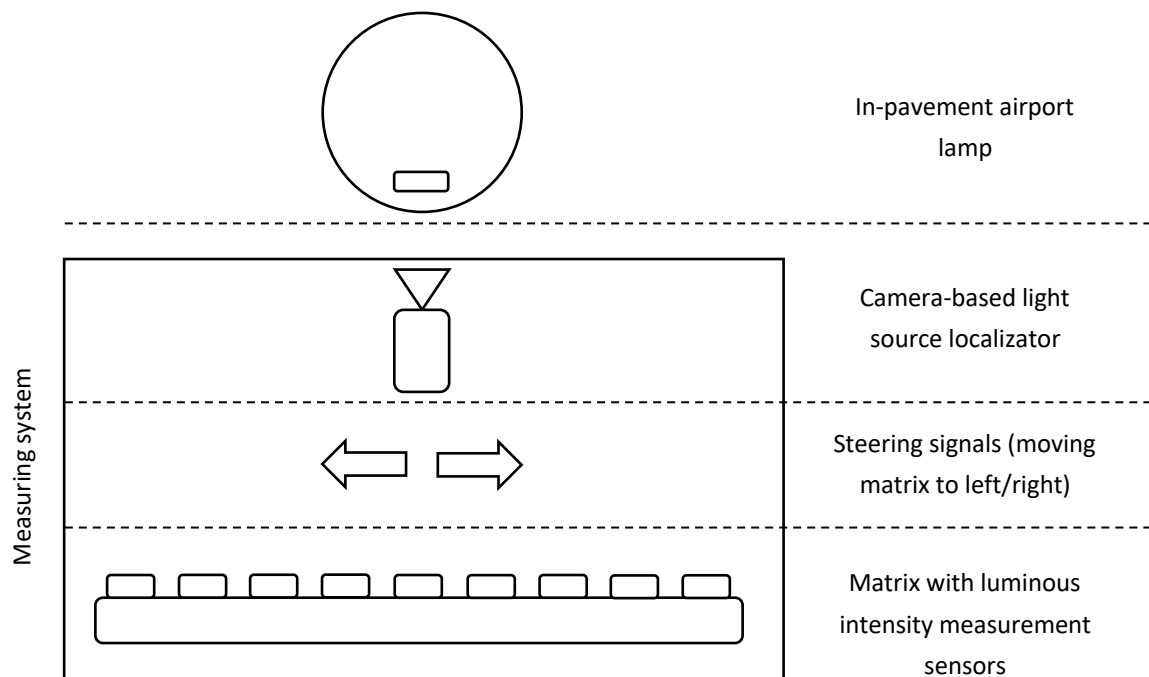


Figure 77 Concept of the moving luminous intensity measurement system [31]

The analysis of video recordings from the runway and taxiway runs confirmed that the detection of light points using video sequence processing is feasible. This conclusion results, among other things, from the size of these points Figure 78. The width of the embedded prism of the AGL lamp located just in front of the camera lens is about 19 pixels. The next lamp, located 15 m away, has a prism that is about 11 pixels wide on the video frame.

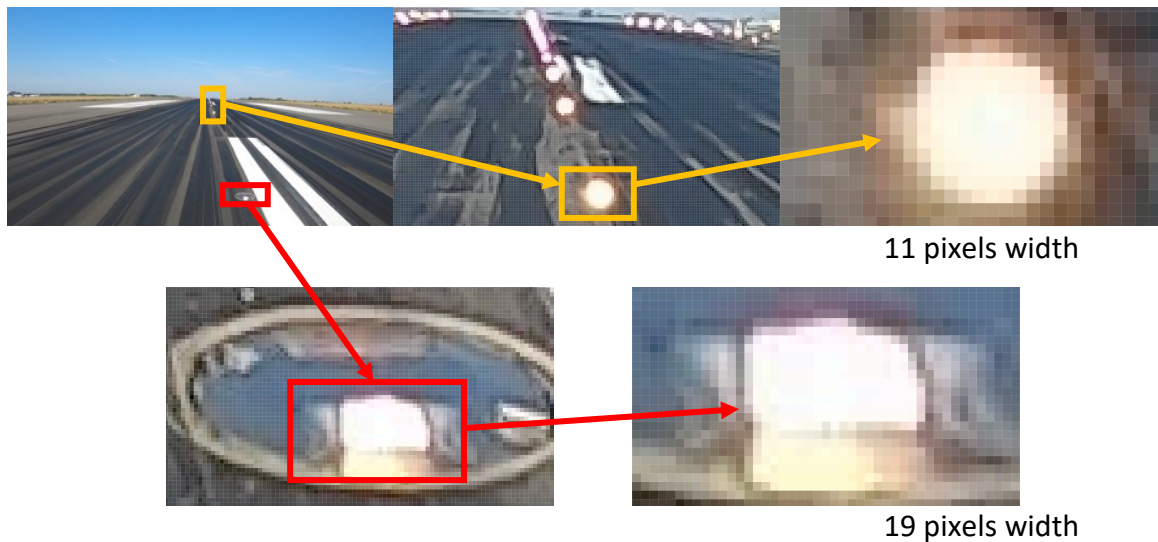


Figure 78 Analysis of AGL light spot size of the video sequence frame

As the result of the research, an algorithm was introduced for detecting and determining the position of in-pavement AGL lamps. This algorithm utilizes traditional image processing techniques, offering reliable performance with minimal computational requirements, while ensuring high operational efficiency.

Algorithms for detecting light sources typically rely on threshold processing. By applying a predefined brightness threshold, areas of interest can be distinguished from the background on which they are located. However, this approach introduces noise interference during image binarization, such as reflections from surfaces or unwanted bright objects. To address these issues, morphological operations like erosion and dilation are employed. Erosion removes isolated pixels and thin lines representing insignificant elements in the image, while dilation enhances objects by filling gaps, thickening lines, and closing holes. A common practice is to first apply erosion to eliminate noise, followed by dilation to emphasize the desired features.

3.4.1 Proposed modified light spots detection algorithm

Developing the algorithm to detect in-pavement AGL lamps in video sequences required experimental parameter tuning and image processing adjustments. These experiments were performed on a sample frame from a dataset totaling 98 GB of video recordings. Each run across the runway takes about 240 seconds and was recorded at 30 frames per second, with each run file occupying about 1.55 GB. Thanks to collaboration with Poznań-Ławica Airport (Figure 79), recordings were made under various weather conditions and times of day. These sequences included runs along the runway and taxiways in all directions. During recording, the operator varied speeds and trajectories, both along the lamp axis and in ways where the lamps' axis did not align with the vehicle's axis.



Figure 79 Energetics Department of Poznań–Ławica Airport car equipped with camera

When utilizing a vision system with a thresholding algorithm for detecting light points of in-pavement AGL lamps, the system can identify the light source and determine its position relative to the vehicle. This information enables the algorithm to guide the operator in adjusting the vehicle's trajectory so that the measuring platform, which assesses the lamp's performance, can correctly capture the necessary data. The proposed vision system algorithm is depicted in Figure 80.

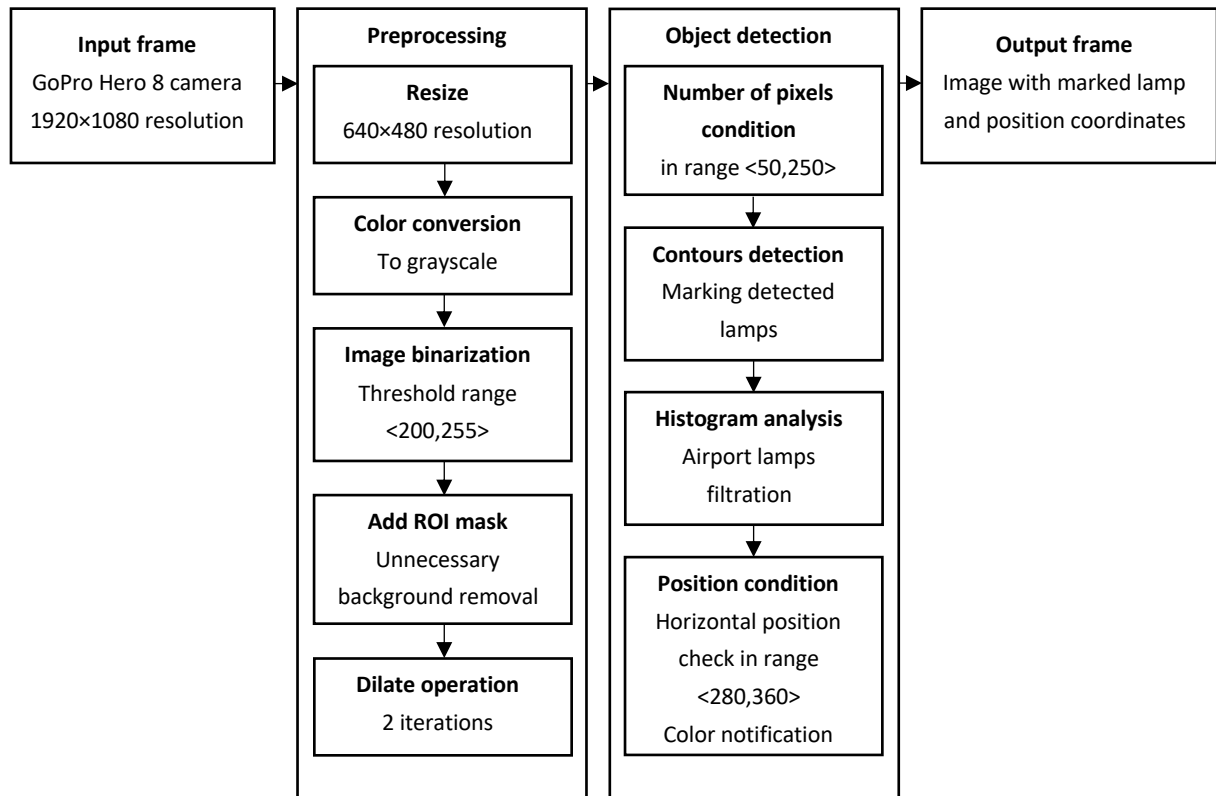


Figure 80 Proposed algorithm for the detection of airport lamps in a video sequence [31]

After loading an image frame from a GoPro Hero 8 camera with a resolution of 1920×1080, the preprocessing phase begins. The image resolution is first downscaled to 640×480, followed by converting the RGB image to grayscale. Based on pixel brightness in grayscale, the image is binarized using a threshold range of <200,255>. To restrict the search area for airport lights, a mask is applied to exclude the horizon and grassy areas, ensuring that the Region of Interest (ROI) is limited to the runway surface.

In the standard method, this step is typically followed by Gaussian blurring and two morphological operations (erosion and dilation) to reduce noise. However, combining Gaussian blurring and erosion can cause the pixels representing in-pavement navigation lights to be lost. To avoid this case, the algorithm employs two iterations of the dilation operation to enlarge the detected light sources. The direct application of algorithms designed for detecting luminous objects, such as traffic lights or light bulbs, did not work effectively for airport lamps, which were not detected as intended. This issue stemmed from the erosion operation used after the binarization stage, which removed small pixel groups, including lamp prisms in airport images. As a result, the algorithm detected larger bright objects, such as yellow and white lines, instead of the lamps (Figure 82a).

One challenge in detecting light points from in-pavement airport navigation lamps using a vision system is the presence of white and yellow runway lines (Figure 82d). These lines are detected similarly to lamps by the thresholding algorithm because their pixel color and brightness are comparable. To address this, additional conditions are applied to differentiate based on the size of the detected areas, as the lines typically cover a larger area than the lamps.

However, in high-use areas like the touchdown zone, where rubber accumulates on the runway surface (Figure 83), the lines become dirty, making it difficult for the algorithm to detect them as continuous objects. As a result, the fragmented lines resemble the size of the mask used for lamp detection, which is in the range of <50,250> pixels. This range is chosen to account for both distant lamps (smaller in the image) and closer lamps (larger in the image).

At this point, the outlines of objects filtered through the earlier steps are detected, and their positions are determined in the image frame. The camera is mounted along the axis of the measuring vehicle, meaning that the correct lamp position relative to the measurement matrix corresponds to the lamp's center in the video frame. For measurements to occur, the lamp must fall within the range of <280,360> pixels horizontally. To ensure the detected object is a lamp and not something like a runway line, a histogram is calculated for each detected area, enabling proper classification of lamps and extraction of their coordinates.

The algorithm produces an RGB image with a blue circle indicating the detected lamp, which, if correctly positioned, is additionally marked by green. If it's outside the expected area, it is circled in red. Furthermore, position data regarding the lamp's placement relative to the measuring vehicle is sent to the system.

Four different algorithms regarding detection of AGL light spot were examined: erosion, single and double dilation, and histogram filtration. The dataset consists of 120 selected frames recorded in sunny, daylight conditions, with 60 frames taken from one runway direction and 60 from the opposite. The test areas included sections with dense runway markings, rubber-covered touchdown zones, and sections where only lamps were visible. The results, shown in Figure 81, label correct lamp detections as TP (True Positives) and the detection of other objects misclassified as lamps as FP (False Positives).

The data analysis shows that the basic algorithm utilizing the erosion method is ineffective at detecting AGL lamps accurately. The success rate for correctly identifying lamps is just 0.83%, while incorrect detections reach as high as 32.5%. In contrast, the second algorithm, which replaces erosion with a single dilation, improves correct lamp detection to 53.3%, with 23.3% of cases detecting non-lamp objects. Implementing the double dilation algorithm further enhances detection efficiency, achieving a 90% success rate. Moreover, applying additional histogram filtering reduces false detections from 26.7% to 15%.

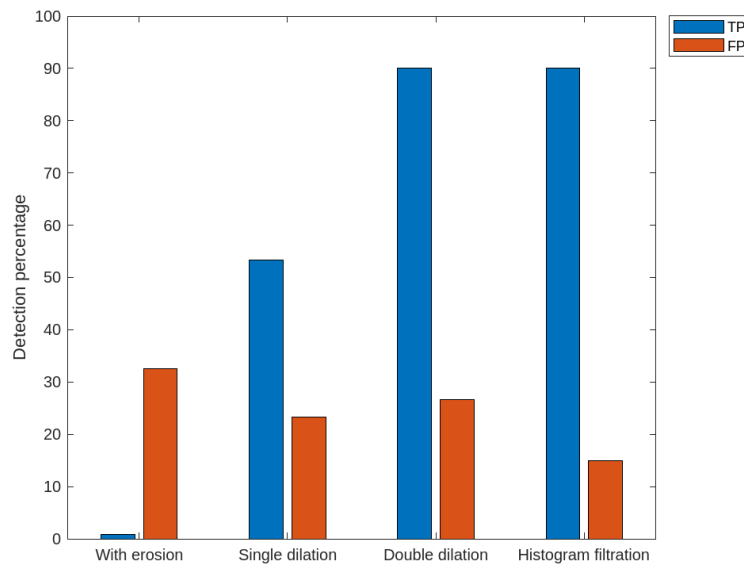


Figure 81 Comparison of the effectiveness of the tested algorithm [31]

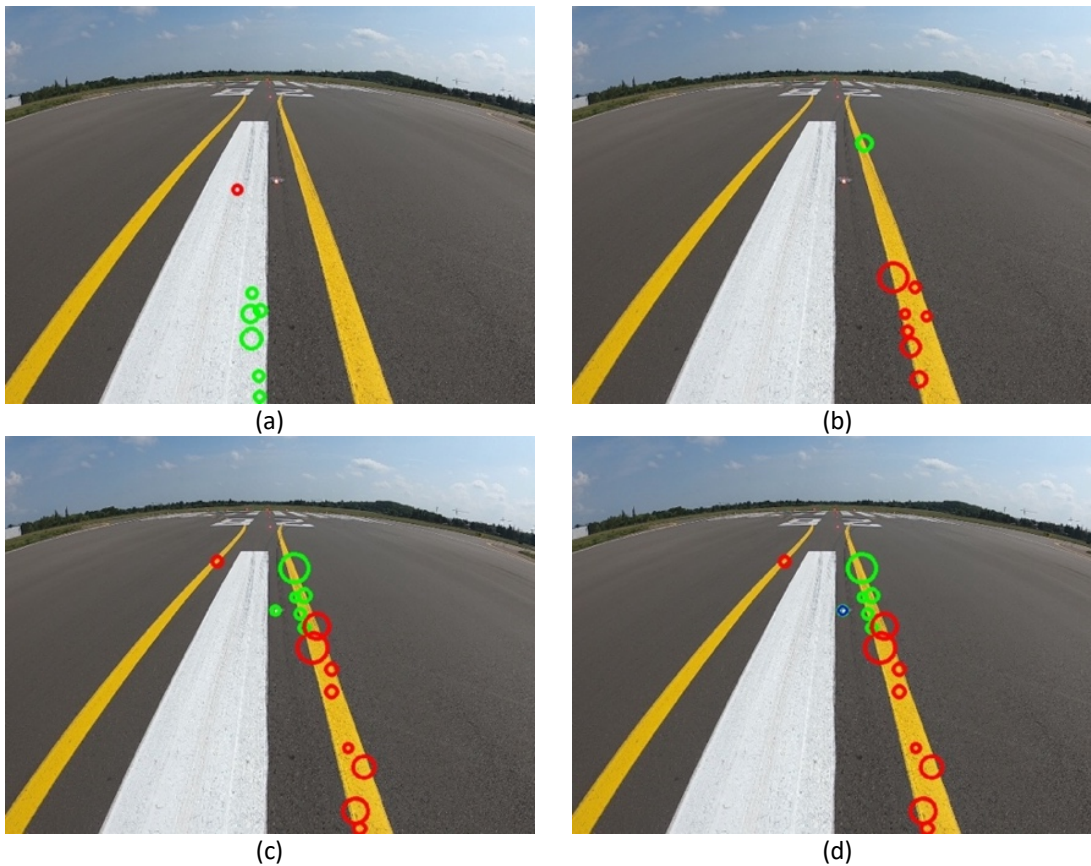


Figure 82 Output frames from algorithm using: erosion (a), single stage dilation (b), double stage dilation (c), histogram filtration (d) [31]

To address the problem of removing AGL prisms, the erosion operation was removed, and dilation was applied instead. The goal of dilation was to expand small, scattered bright spots so they could be detected as larger, unified areas. Several iterations of dilation were tested, as too few repetitions failed to sufficiently enlarge these areas, such as in the case of a single iteration (Figure 82b). Experimental results confirmed that two iterations of dilation (Figure 82c) were optimal, successfully detecting the glowing airport lamps while eliminating false detections, such as painted lines, through subsequent operations.

The final algorithm incorporates an additional step that calculates a histogram for each detected object, helping to filter out non-airport light detections. These non-lamp objects are rejected by the algorithm, while the correct lamp is highlighted in blue (Figure 82d). Green and red circles indicate whether the detected lamp is correctly aligned with the measurement matrix (green) or misaligned (red).

The final histogram-based filtering function was developed to effectively distinguish correct lamp detections from incorrect ones, which typically included yellow and white horizontal lines. The characteristics of these objects are illustrated using the example in Figure 83, where the algorithm numbered individual detections and plotted histograms for objects numbered 1, 3, 5, and 8.



Figure 83 Example frame of histogram filtration [31]

Object no. 1 represents a fragment of the yellow line marking the exit axis to the taxiway. The luminance histogram (Figure 84a) shows a significant number of pixels with values ranging from 60 to 130, while pixels with high luminance, i.e., above 200, are sparse and near the lower end of this range. The RGB histogram in Figure 84b further reveals a high concentration of the red component, along with a mix of blue and green components typical of yellow lines.

Object no. 5 is a segment of the runway center line, marked in white. This object poses the greatest challenge for the algorithm to filter out since it is located closest to the runway lamps and its color closely matches the spectrum of light emitted by AGL lamps. The luminance histogram (Figure 84c) shows that most pixels fall within the range of 70 to 150, while the RGB histogram in Figure 84d indicates a high content of the blue component in the spectrum.

In contrast, objects no. 3 and no. 8, which are correctly detected runway center line lamps, exhibit histograms distinct from the yellow and white lines. The luminance histograms for these objects (Figure 84e and Figure 84g) show a higher number of pixels with values exceeding 200. Although they contain pixels with lower values, this part of the histogram is not critical for differentiating lamps from lines. The RGB histograms (Figure 84f and Figure 84h) demonstrate a significant presence of red and green components in pixel values above 200, which clearly distinguishes lamp histograms from the others.

Using this information, the algorithm analyzes the histograms of detected objects, enabling the filtering and identification of airport lights. Implementing this processing stage significantly enhanced the accuracy of the airport lamp detection algorithm in video sequences.

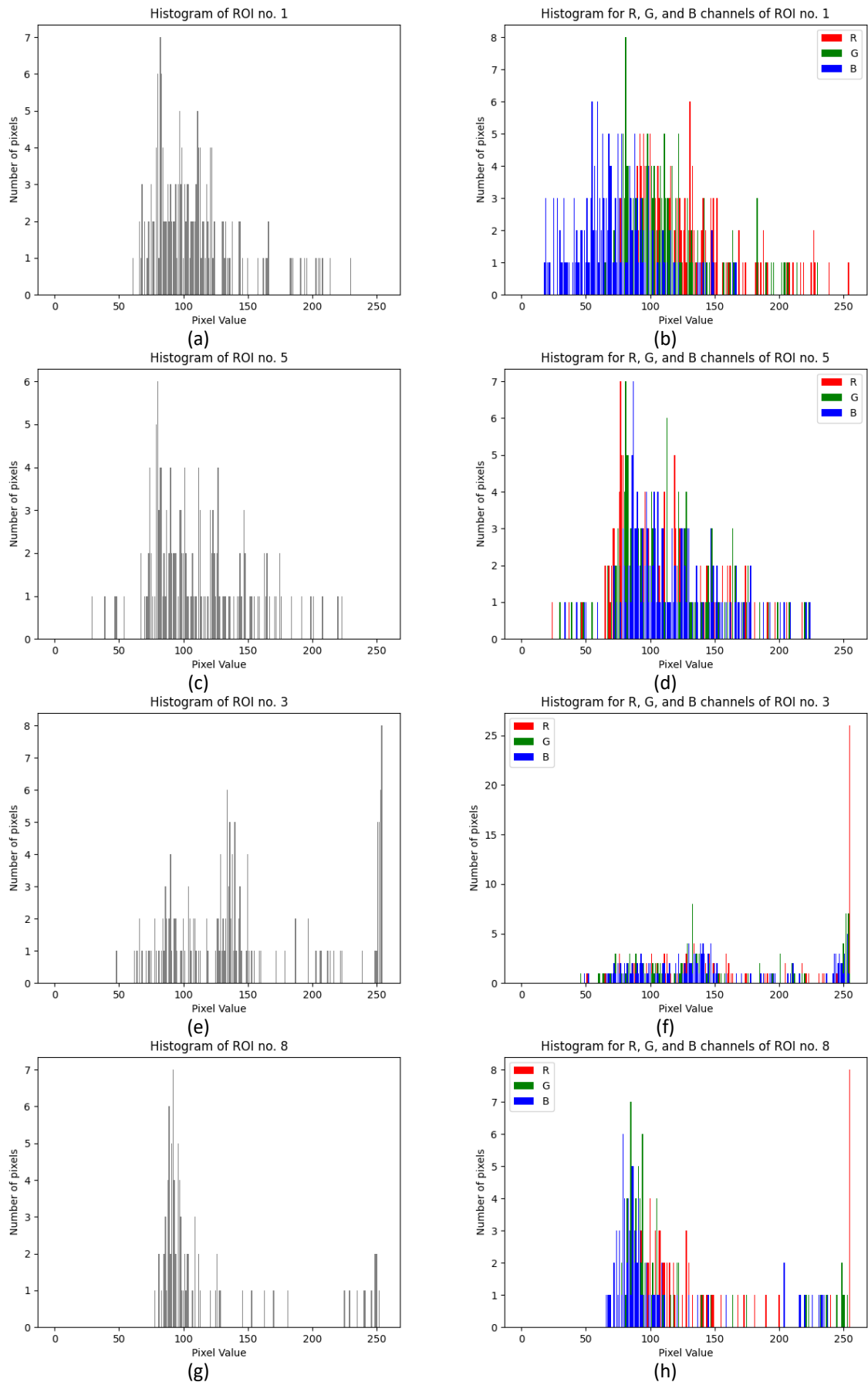


Figure 84 Yellow line luminance histogram (a), RGB histogram (b), white line luminance histogram (c), RGB histogram (d), 1st lamp luminance histogram (e), RGB histogram (f), 2nd lamp luminance histogram (g), RGB histogram (h) [31]

3.4.2 Analysis of the impact of lighting conditions on the algorithm's performance

The final algorithm, incorporating histogram filtering, was tested not only on a comprehensive dataset containing images from varying lighting and weather conditions but also on specific scenarios using 120 frames for each case. The algorithm's performance was evaluated under the following conditions: sunny, cloudy (wet), nighttime with car headlights on, and nighttime with car headlights off. Figure 85 illustrates the percentage of correct lamp detections (TP) and instances where other unwanted objects were misclassified as lamps (FP). As anticipated, the algorithm performed the worst in sunny daylight conditions (Figure 9). This is likely due to the high image brightness and the abundance of visible details during the day, which could potentially confuse the algorithm.

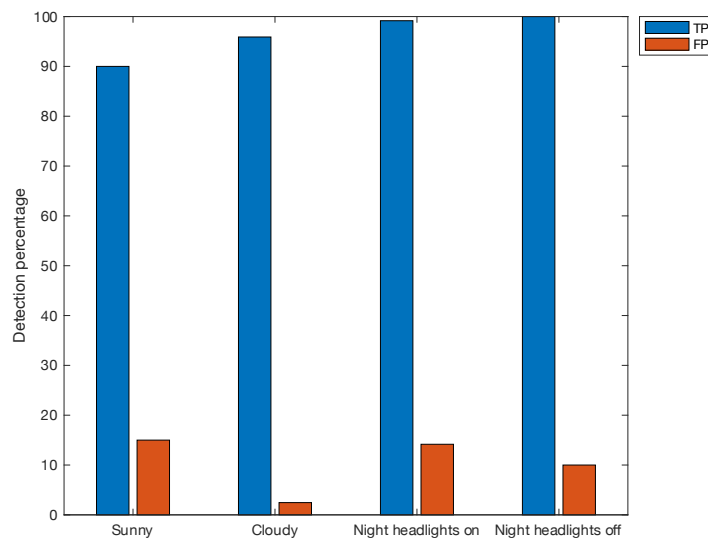


Figure 85 Overall detection statistics for different conditions [31]

Improved results were achieved under daytime cloudy conditions, with correct lamp detection recorded in 95.9% of the images, while incorrect detections occurred in only 2.46%, representing the lowest error rate across the entire dataset. This outcome is likely due to the reduced lighting on airport lines, which, in lower daylight, contain fewer pixels with high luminance values. As a result, the algorithm is better able to differentiate between detected lamps and line fragments, leading to more accurate classifications (Figure 86).



Figure 86 Example output frame for cloudy conditions [31]

In the research, night images were also captured, with the distinction that the vehicle carrying the camera had its headlights either on or off. When the headlights were on (Figure 87), particularly near the runway's start and end, where there are numerous markings in the form of lines, the illumination from the headlights led to occasional incorrect detections by the algorithm (14.17%). However, it is important to note that correct detection of the airport navigation lamps was achieved in 99.17% of the frames.



Figure 87 Example output frame for night conditions with headlights on [31]

In frames captured with the car's headlights turned off, the algorithm successfully detected 100% of the airport lights. However, despite the headlights being off, some horizontal markings, such as lines, were still visible in the frames due to illumination from the AGL. As a result, 10% of the frames contained incorrect detections of airport lamps.



Figure 88 Example output frame for night conditions with headlights off [31]

For each category, including different weather and lighting conditions, the True Positive Rate (TPR) (23), Positive Predictive Value (PPV) (26), Accuracy (ACC) (25) and F1-score (30) were calculated using the respective formulas. In this analysis, the airport lamp was defined as the positive class, while the horizontal marking line fragments represented the negative class. The calculated parameter values are compiled in Table 23, with an additional effectiveness graph shown in Figure 89.

Table 23 Metrics depending on weather conditions [31]

Weather conditions	TPR	PPV	ACC	F1
Sunny	0.9730	0.8571	0.8609	0.9114
Cloudy	1.0000	0.9750	0.9838	0.9873
Night lights on	1.0000	0.8750	0.8844	0.9333
Night lights off	1.0000	0.9091	0.9104	0.9524

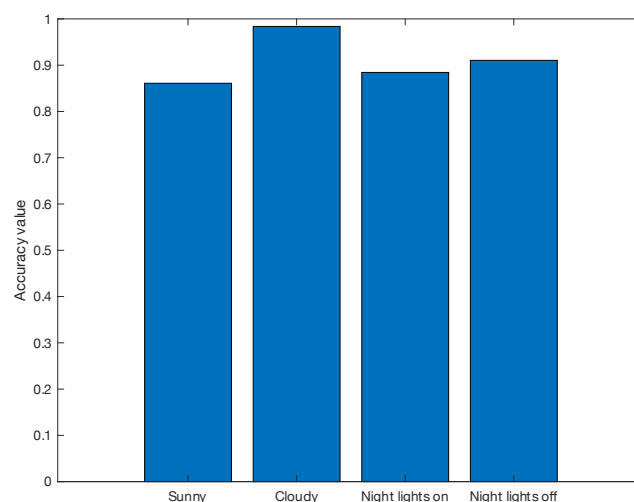


Figure 89 Algorithm accuracy metric for different conditions [31]

The analysis of the data corroborates earlier observations. The algorithm performs most efficiently under cloudy and nighttime conditions. However, when headlights are used, it increases false detections by illuminating horizontal markings like lines. The weakest performance, though still achieving 90% airport lamp detection, was observed in bright daylight conditions. In these cases, the luminance of areas mistakenly identified as lamps is sometimes very similar to actual lamps, leading the algorithm to misclassify more brightly lit parts of airport lines as lamps.

The study demonstrated improvements in airport lamp detection over previously known methods. In the traditional approach, where erosion precedes dilation, the detection rate was only 0.83%.

Modifying the algorithm by removing erosion and using a single dilation operation increased the correct lamp detection rate to 53.3%. Introducing double dilation further enhanced detection efficiency to 90%, and additional filtering based on histograms of detected objects reduced false lamp detections from 26.7% to 15%.

Depending on the weather and lighting conditions during runway traversal, the accuracy of airport lamp detection ranges from 90% to 100%, with false detections of other objects misclassified as lamps occurring at rates between 2.46% and 15%.

Chapter 4

Proposal of light sensors integration for AGL evaluation

4.1 Analysis of in-pavement AGL luminous intensity distribution

Until recently, daily inspecting lamps installed in airport areas for certain instrument landing system (ILS) categories did not necessitate the use of specialized equipment. Typically, these inspections were performed visually. However, current regulations now mandate the use of reliable devices for such checks. Additionally, manually preparing test reports is more time-consuming compared to systems that enable automated control and generate lamp quality reports during inspections. For automated testing of AGL quality, systems like a measuring car trailer can be employed [15], [16], [17], [25], [232] as described in Section 2.3.2.

The frame of PhD dissertation the measuring platform was designed used to assess the performance of airport lamps and it is fitted with light intensity sensors arranged in a matrix beneath the chassis [29]. These sensors are responsible for capturing the intensity of light emitted by the main beam of the tested lamps as the platform moves over the in-pavement fixtures. Given that the prisms in these lamps direct the main beam at a vertical angle of no more than 9 degrees, the matrix is positioned close to the ground. The spacing between lamps varies depending on their type and function, ranging from 7.5 to 15 meters on taxiways and up to 30 meters on runways [36], [37]. However, at intersections where the taxiway and runway centerlines converge, lamps of different types may be as close as 60 cm apart, which could cause interference in measuring the main beam intensity from neighboring lamps. To mitigate this issue, the measuring platform includes a cover that limits the illuminated area under the chassis to about 1 meter, reducing the risk of overlapping beams.

These constraints necessitate a relatively fast response time from the light-intensity sensors in the measurement matrix. The data collection process must occur at a pace that allows for measurements as the platform passes over the lamp being tested. The duration during which the luminaire remains in the darkroom under the device is brief and depends on the speed of the measurement system. During this short interval, multiple measurement series must be conducted to accurately determine the maximum luminous intensity of the lamp's main beam.

4.1.1 The influence of the AGL power supply type on the measurement using illuminance sensors

Due to the high cost of AC power supplies typically used for powering lamps, the aim of the research was to compare the effects of using a less expensive DC laboratory power supply with appropriate efficiency on the measurements obtained. For the experiments commonly employed in measuring illuminance BH1750 module was examined. To minimize interference, both sensor and the airport lamp were placed in a sealed dark room. The measuring module was connected to the Nucleo STM32F746 board via an I²C interface. Additionally, the tests included the professional KIKUSUI PCR1000MA power supply, which supported both AC and DC current for powering the tested light sources. The experimental setup is depicted in Figure 90.

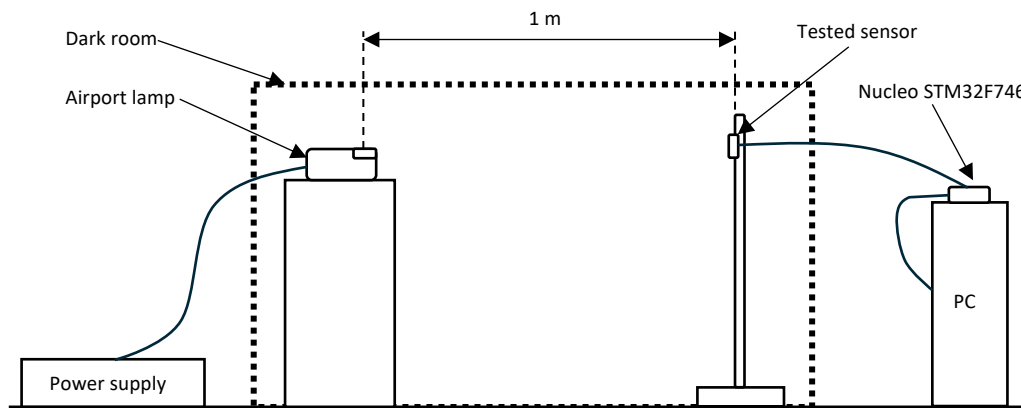


Figure 90 Experiment environment scheme [30]

As part of the experimental research, tests were conducted to evaluate the stability and repeatability of the measurements obtained from the illuminance sensor. Another variable was the power source of the airfield lamps, with both AC and DC sources tested. Each configuration was measured for approximately 30 minutes, with sensor readings taken every second. This duration was chosen due to the limitations of the SONOPAN L-200P luxmeter, which has a minimum automatic measurement time of 1 second. To maintain consistency, the same time interval was used for measurements with the BH1750 sensor. The tested aeronautical navigation lamps were equipped with bulbs [235] of different power:

- Approach system lamp (APP) 105 W
- Runway centre line lamp (RCL) 2×48 W
- Touchdown zone lamp (TDZ) 48 W.

Before measurements, the lamps were warmed up for 15 minutes, as required by EASA regulations [223], to stabilize power readings. The voltage values were adjusted so that the ammeter reading showed around 6.6 A, the maximum operational value for airport lighting. These settings align with EASA standards [223]. The parameters for the KIKUSUI PCR1000MA

power supply used during tests are summarized in Table 24, where the AC values are RMS, and the frequency was set to 50 Hz.

Table 24 Power supply parameters [30]

Bulb power [W]	48		2×48		105	
Type of current flow	AC	DC	AC	DC	AC	DC
Voltage [V]	8.40	8.40	16.50	16.50	25.80	25.70
Current [A]	6.61	6.61	6.59	6.60	6.60	6.60

The tests for the BH1750 illuminance sensor were conducted alongside those for the SONOPAN L-200P luxmeter. Representative samples of measurements, taken over a period of about 130 seconds, are discussed in this section. The results (Figure 91, Figure 92, Figure 93) suggest that depending on the type of lamp, a slight adjustment should be made to the BH1750 sensor readings to align them with those from a certified measuring device. Notably, for the approach zone lamps, the BH1750 produced lower values, while for the runway centre line lamps, it recorded higher values, and for the touchdown zone lamps, the measurements were lower again. In extreme cases, these deviations reached up to 300 lux. However, given the large overall illuminance values—approximately 22,000 lux—such a difference is minor and does not significantly affect compliance with standards, making it acceptable.

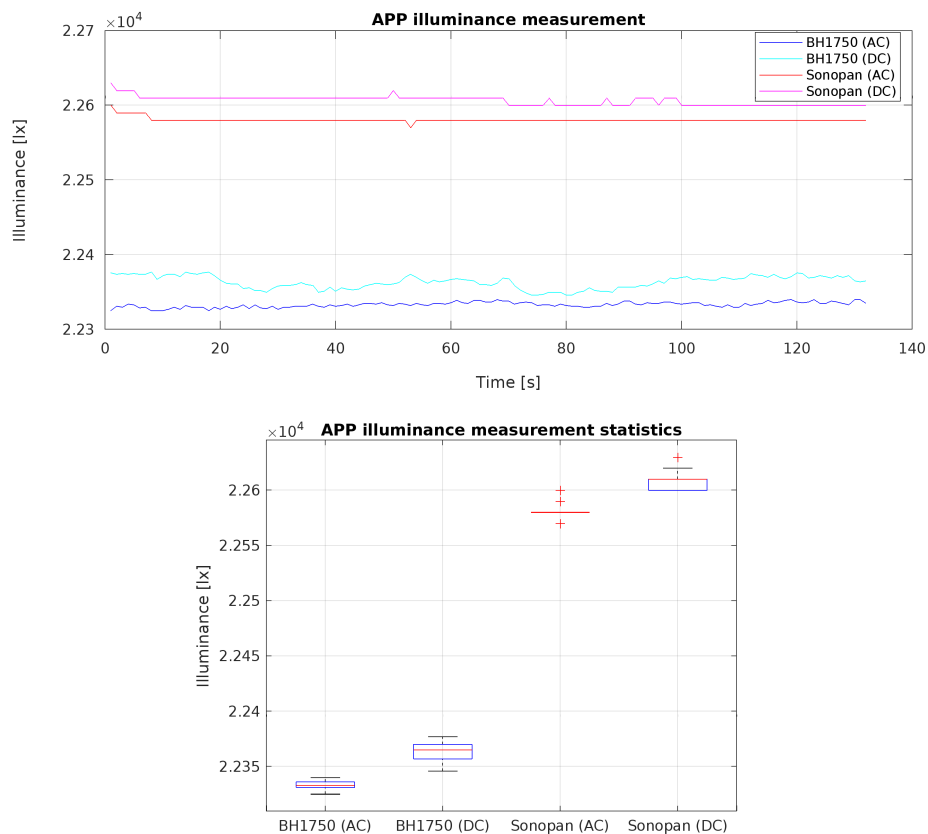


Figure 91 Approach system lamp illuminance measurements [30]

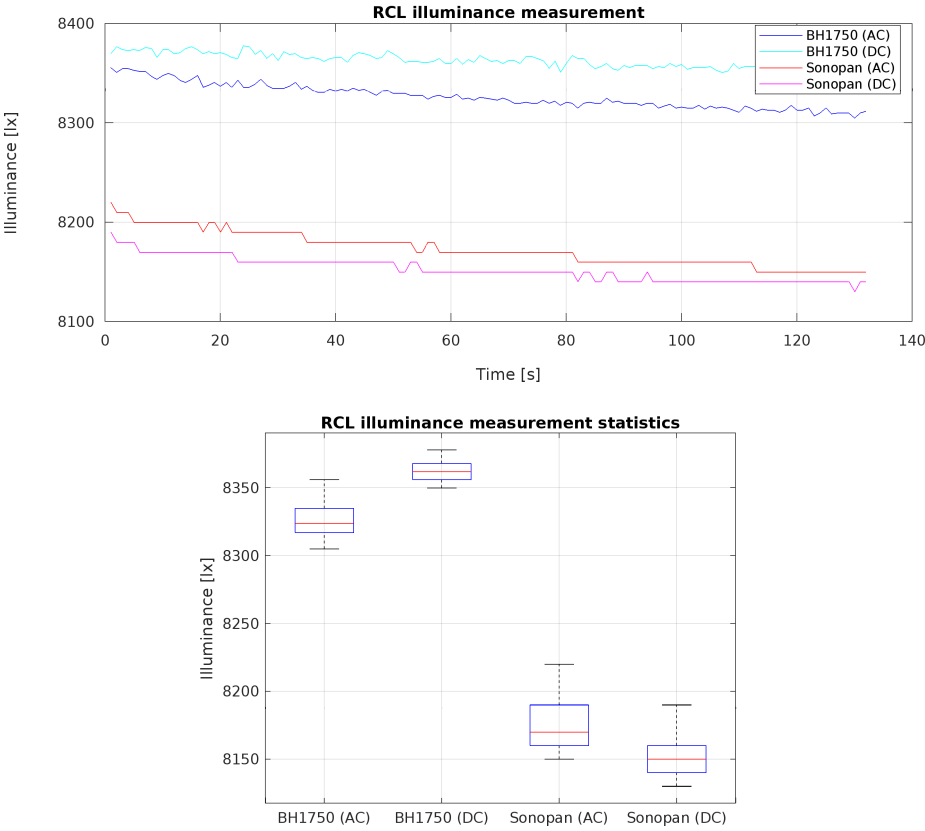


Figure 92 Runway centre line lamp illuminance measurements [30]

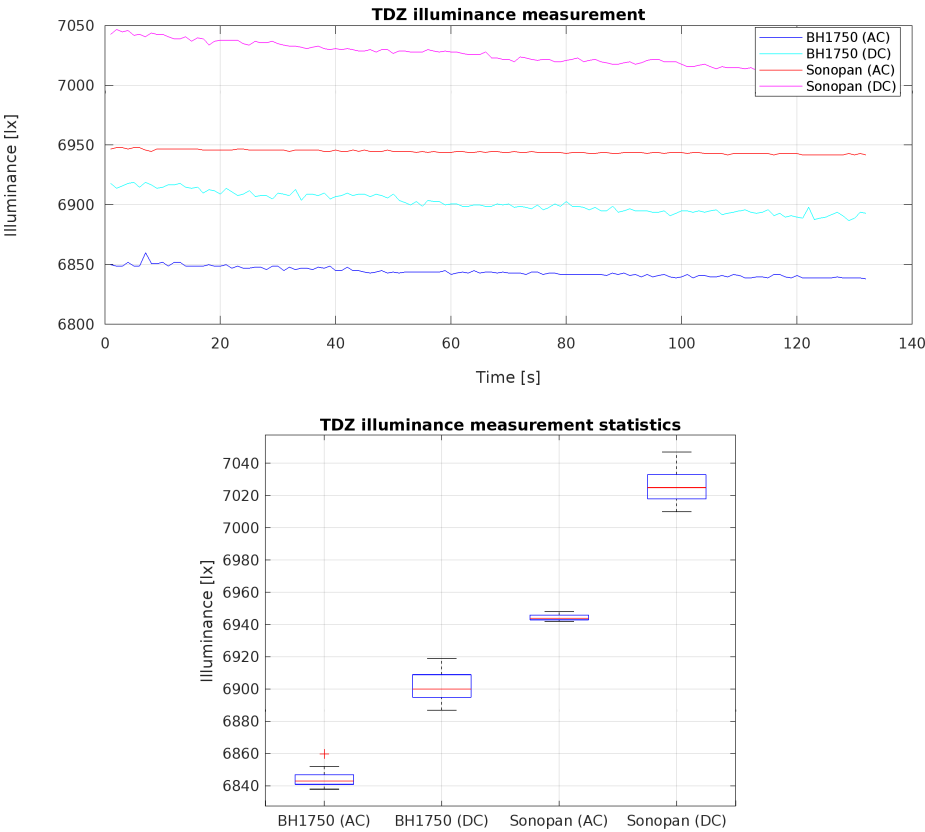


Figure 93 Touchdown zone lamp illuminance measurements [30]

The measurement deviations are also influenced by the device's range, with the BH1750 sensor offering an accuracy of 0.5 lx and the luxmeter ranging up to 8000 lx with an accuracy of 1 lx above 10 lx. Furthermore, these value fluctuations are not continuous but occur sporadically over time, eventually stabilizing. This supports the validity of the EASA guideline [223] that requires a 15-minute lamp warm-up before testing. During the warm-up period, a drop in current intensity is observed, leading to a decrease in illuminance until the bulb reaches optimal working conditions.

In analyzing the impact of the power supply type, the tests indicated that lamps powered by direct current produced slightly higher illuminance values, as measured by both the BH1750 sensor and the SONOPAN L-200P luxmeter. Regardless of whether the lamps were powered by AC or DC, the measured values fluctuated within the ranges shown in Figure 91, Figure 92, Figure 93. The absolute differences between the average illuminance values for AC and DC power supplies, as well as the relative differences, are detailed in Table 25.

Table 25 Illuminance differences depending on power source type [30]

	Mean (AC) [lx]	Mean (DC) [lx]	Absolute difference [lx]	Relative difference to Mean AC/DC [%]	
				AC	DC
APP Sonopan	22580.53	22606.44	25.91	0.11	0.11
APP BH1750	22333.22	22363.39	30.17	0.14	0.13
APP Absolute difference [lx]	247.31	243.05	-	-	-
RCL Sonopan	8173.18	8152.50	20.68	0.25	0.25
RCL BH1750	8326.62	8362.68	36.06	0.43	0.43
RCL Absolute difference [lx]	153.44	210.18	-	-	-
TDZ Sonopan	6944.55	7025.84	81.29	1.17	1.16
TDZ BH1750	6844.01	6901.86	57.85	0.85	0.84
TDZ Absolute difference [lx]	100.54	123.98	-	-	-

The research indicates that the type of power supply influences the performance of halogen bulbs, which in turn affects the illuminance measurements—this was a key focus of the experiments. Depending on the lamp type, the variation in illuminance measurements for the same device can reach several dozen lux, although it typically falls within a range of a few lux. The differences between measurements taken with the BH1750 sensor and the luxmeter can be attributed to the spectral response characteristics, which peak around a wavelength of 550 nm.

In summary, while the power source has only a minor impact on the measurements, manufacturers recommend using AC power. By applying the appropriate corrections based

on long-term data analysis, the BH1750 sensor can produce illuminance readings comparable to those of the certified SONOPAN L-200P luxmeter. The measurement deviations are minimal in relation to established standards and obtained values, making them negligible.

4.1.2 Laboratory assessment of AGL photometric characteristics

During the experimental research the module GY-302 module was selected after preliminary tests. It is equipped with a BH1750 sensor, the basic parameters of which are discussed in Subsection 2.2.4. As part of the research work, its correct operation was checked in relation to a certified device for measuring illuminance in the form of a Sonopan L-200P luxmeter.

The luminous intensity distribution was measured using a custom-designed device. This setup includes a turntable for mounting the tested lamp and a rotating arm equipped with a light sensor at its end. It operates by recording measurements at various angular positions of the table and the arm, resulting in luminous intensity values mapped to a grid on the spherical surface surrounding the light source. The block diagram of the automated airport lamp measurement device is shown Figure 94.

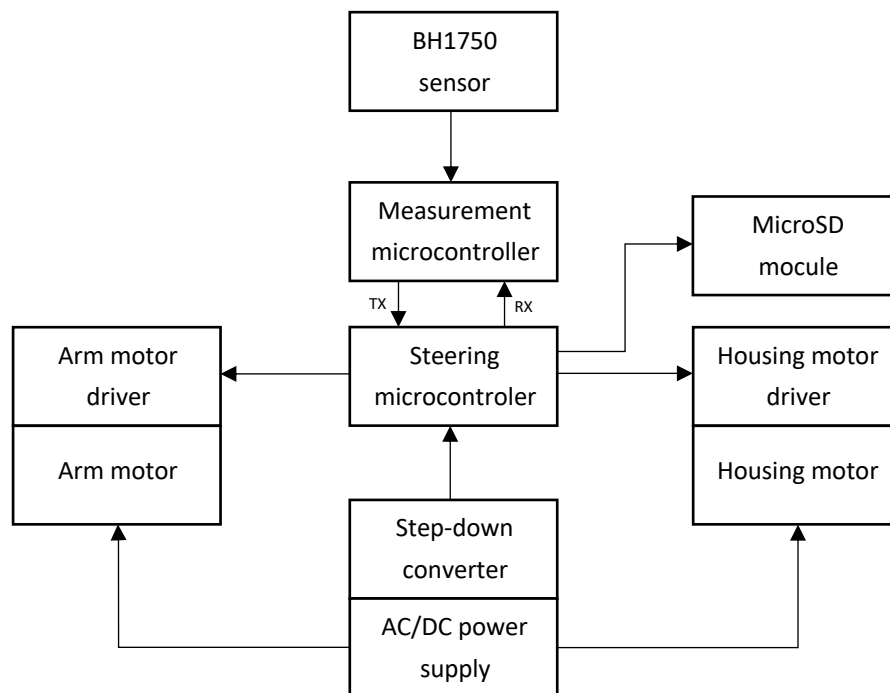


Figure 94 General concept of measuring device [26]

The BH1750 illuminance sensor serves as the system's measuring component. However, due to its spectral characteristics, additional calibration is required to align its measurements with those of the tested lamps. The sensor is mounted on the rotating arm, and its vertical position is adjusted by a stepper motor, while another stepper motor rotates the lamp horizontally. A 3D-printed mounting socket secures the lamp using two pins inserted into its

screw holes. JK57HS56-2504 stepper motors [18] drive the system, using belt transmissions and controlled by a TB6600 controller which is a driver for two- and four-phase stepper motors, supports step and direction control (step/dir) and ensures noise immunity through optoisolated control inputs [236], [237].

The BH1750 sensor, motor control, and data logging are managed by two ATmega328P microcontrollers, with measurement results stored on a MicroSD card. Heatmaps are generated from measurements taken at horizontal angles between -16° and $+16^\circ$ and vertical angles from 0° to 14° . The device, along with its key components, is shown in Figure 95.

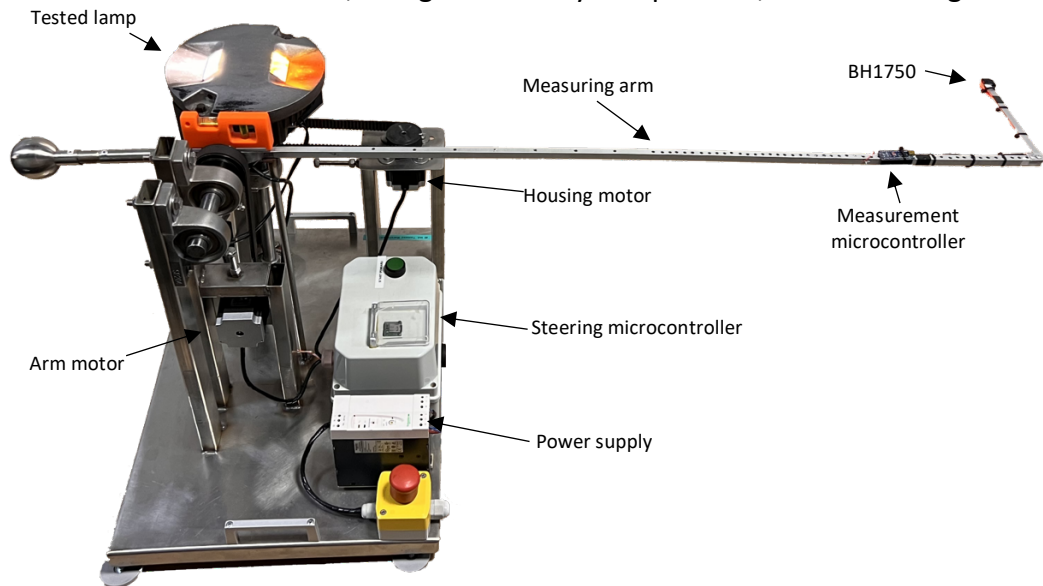


Figure 95 View of the device with marked key elements [26]

When measuring the photometric characteristics of an airport lamp, the luminous intensity of the main light beam is critical. Photodiode-based sensor modules [27] can be used for this task, converting their readings into luminous intensity values. Such sensors are resistant to variations in the light's angle of incidence [215] and offer excellent dynamic properties during measurement [214].

The actual measurement times may vary from those listed in Table 13 in Section 2.2.4 due to the increased data transfer time for larger values. In H-Resolution modes, the measurement time is long enough to eliminate 50/60 Hz noise [206].

A key factor when assessing airport lamps' photometric characteristics is the repeatability of measurements. Navigation lighting operates in five different modes, varying in illuminance levels based on power supply current. In an experiment involving 10,000 measurements of a new touchdown zone lamp (IDM 4671), using the GY-302 module and adjusting the lamp's power modes, the BH1750 sensor's operating modes were changed to assess performance. The certified Sonopan L-200P luxmeter [207] was also used to validate the illuminance measurements. The photometric distance corresponded to the 1-meter length of the

goniometer arm. Figure 96a, Figure 97a, Figure 98a, Figure 99a, Figure 100a show the measured illuminance values, with statistical box plots shown in Figure 96b, Figure 97b, Figure 98b, Figure 99b, Figure 100b.

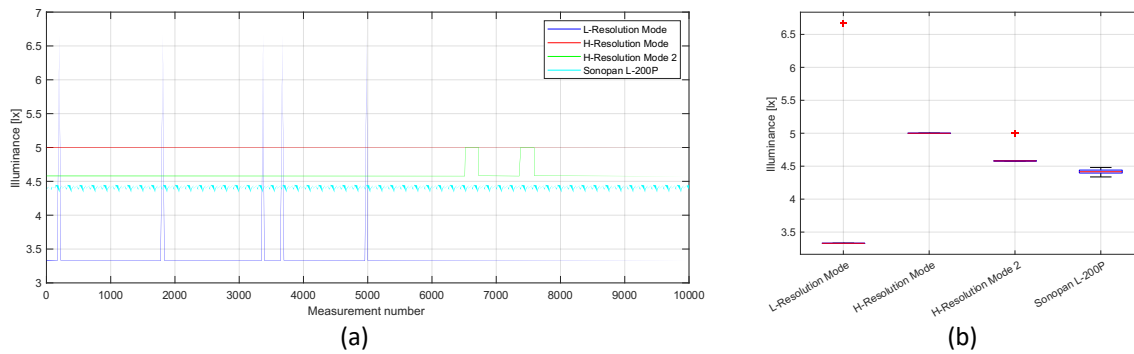


Figure 96 Measurements of illuminance in the 2.8A power mode: (a) linear chart; (b) box plot [26]

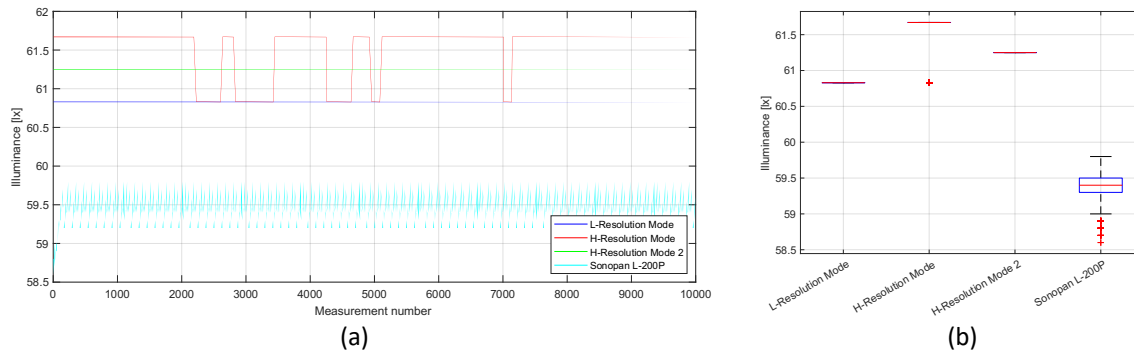


Figure 97 Measurements of illuminance in the 3.4A power mode: (a) linear chart; (b) box plot [26]

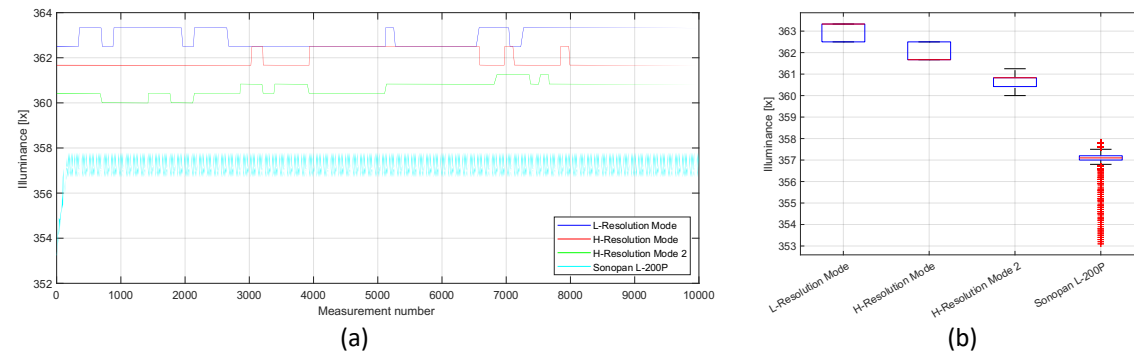


Figure 98 Measurements of illuminance in the 4.1A power mode: (a) linear chart; (b) box plot [26]

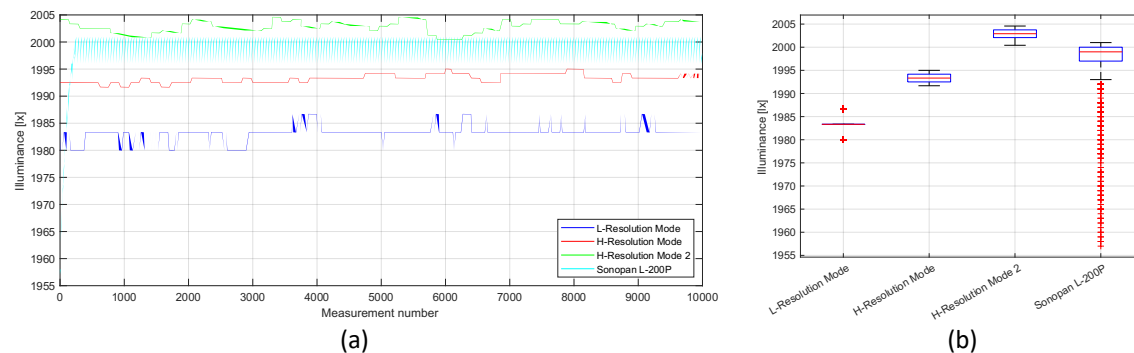


Figure 99 Measurements of illuminance in the 5.2A power mode: (a) linear chart; (b) box plot [26]

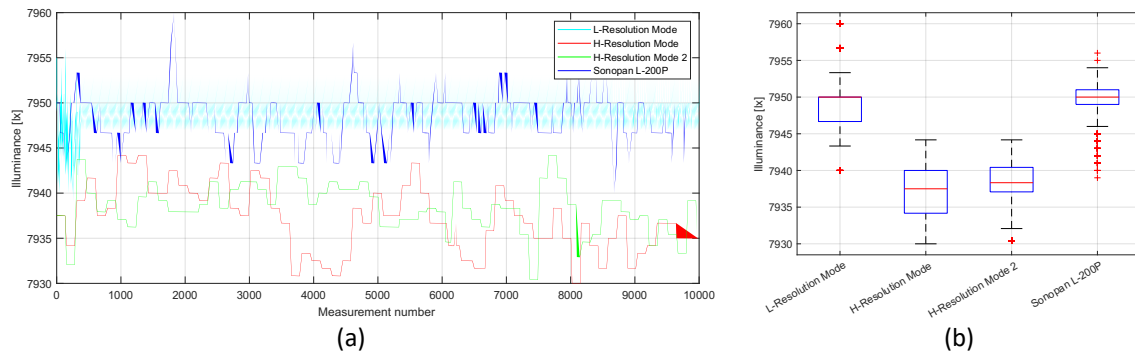


Figure 100 Measurements of illuminance in the 6.6A power mode: (a) linear chart; (b) box plot [26]

For the collected data, the mean, median, and standard deviation were calculated, as shown in Table 26.

Table 26 Results of the BH1750 experiment [26]

Airport Lamp Mode	Type of Data	L-Resolution Mode [lx]	H-Resolution Mode [lx]	H-Resolution Mode 2 [lx]	Sonopan [lx]
2.8A (1%)	Mean	3.38	5.00	4.60	4.42
	Median	3.33	5.00	4.58	4.42
	Standard deviation	0.39	0.00	0.09	0.03
3.4A (3%)	Mean	60.83	61.53	61.25	59.24
	Median	60.83	61.67	61.25	59.30
	Standard deviation	0.00	0.32	0.00	0.26
4.1A (10%)	Mean	362.94	361.93	360.64	355.49
	Median	363.33	361.67	360.83	355.60
	Standard deviation	0.41	0.39	0.32	1.18
5.2A (30%)	Mean	1983.20	1993.27	2002.87	1985.91
	Median	1983.33	1993.33	2002.92	1988.00
	Standard deviation	1.46	0.78	1.07	11.54
6.6A (100%)	Mean	7948.31	7937.18	7938.47	7946.43
	Median	7950.00	7937.50	7938.33	7947.00
	Standard deviation	2.67	3.65	2.68	2.91

The analysis of Table 26 reveals that as the lamp's supply current—and thus the illuminance—increases, the differences in the mean values between sensor modes also grow. A similar trend is observed for median values, while the standard deviation remains a small

percentage of the illuminance, especially at high current intensities. According to recommendations, airport lamp testing is done only at the highest illuminance level after a 15-minute warm-up period. This requirement compensates for the halogen bulbs' imperfections, which may also cause some fluctuations in the experimental values. Given the standards for in-pavement navigation lighting, slight lux-level errors are negligible. To improve accuracy, multiple measurements should be averaged.

For airport lamp evaluations, such as touchdown zone (TDZ) lamps with a required threshold of 1250 cd [209], high measurement precision is unnecessary. The process can be accelerated by up to 7.5 times using the L-Resolution mode (cf. Table 13). The data in Table 26 indicates that the BH1750 sensor's spectral characteristics [206] influence measurement values. However, after applying mathematical corrections, its results can closely align with those obtained using the certified Sonopan L-200P luxmeter [207] (Figure 101).

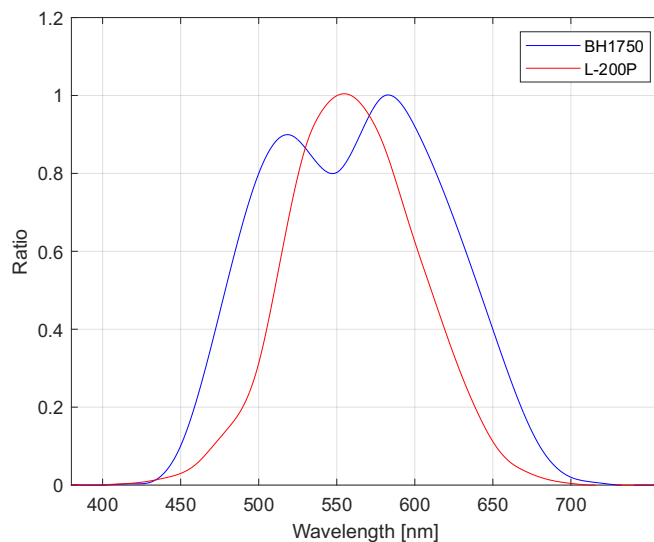


Figure 101 Spectral characteristic of BH1750 sensor and Sonopan L-200P luxmeter [26]

4.1.3 Proposed polynomial correction for AGL assessment using illuminance sensors

As mentioned in Section 2.3.1 the photometric parameters of AGL depends on their function and location. Different colors of emitted light help pilots quickly identify them, providing clear information on the aircraft's position in various airport areas. The most common lamp colors tested in laboratory conditions are white, red, green, and yellow. White lamps, depending on the type and location, vary in prism dimensions, which also results in differences in their photometric properties. In-pavement airport lamps can also be classified by the number of light sources, such as single- or double-sided lamps. These lamps may have identical or different colors, but this does not impact their photometric characteristics.

The tested in-pavement lamps include single-sided touchdown zone clear lamps (TDZ), double-sided runway centre line lamps that emit clear light on both sides (RCL C/C Clear I, RCL C/C Clear II), as well as clear and red light (RCL C/R Clear, RCL C/R Red). Additionally, there are double-sided green-yellow taxiway centre line lamps (TAXI G/Y Green, TAXI G/Y Yellow).

Measurements were conducted at a distance of 1 meter, with the airport lamp levels varying as specified by EASA [209]. At Poznań-Ławica Airport, the threshold values are defined as in Section 2.3.1.

Following the completion of 50 measurement series, the results from both the BH1750 sensor and the certified Sonopan L-200P luxmeter were averaged across all tests. The summarized data is presented in Table 27.

Table 27 Results of the BH1750 and Sonopan L-200P measurement [26]

Airport Lamp		2.8A (1%)	3.4A (3%)	4.1A (10%)	5.2A (30%)	6.6A (100%)
TDZ	BH1750 [lx]	4.00	112.00	320.00	2234.60	9598.60
	L-200P [lx]	4.05	101.26	386.50	2022.40	8728.00
RCL C/C Clear I	BH1750 [lx]	4.00	63.00	392.00	2321.60	9341.40
	L-200P [lx]	3.97	57.88	361.20	2141.40	8658.00
RCL C/C Clear II	BH1750 [lx]	4.00	56.00	341.00	1969.20	8312.40
	L-200P [lx]	3.74	51.03	311.74	1804.80	7600.00
RCL C/R Clear	BH1750 [lx]	3.00	52.00	370.00	2336.80	9278.00
	L-200P [lx]	2.65	48.28	337.02	2069.20	8488.00
RCL C/R Red	BH1750 [lx]	3.00	29.00	185.80	1017.40	3760.80
	L-200P [lx]	1.74	18.70	118.48	648.44	2410.60
TAXI G/Y Green	BH1750 [lx]	-	-	19.00	114.00	501.00
	L-200P [lx]	-	-	19.29	116.58	511.54
TAXI G/Y Yellow	BH1750 [lx]	-	5.00	31.00	198.00	789.80
	L-200P [lx]	-	4.35	28.64	182.52	759.42

Based on the results, functions were derived to approximate the values obtained by the BH1750 sensor in comparison to the reference values from the certified Sonopan L-200P luxmeter. Using the Curve Fitter App in Matlab [238], correction polynomials were determined for each type of tested airport lamp: TDZ (35), RCL Clear (36), RCL Red (37), TAXI

Green (38), TAXI Yellow (39). In these equations, the variable x represents the measurement value recorded by the BH1750 sensor, which must be adjusted to match the actual characteristics of the light source.

$$y_{TDZ}(x) = -0.0002x^2 + 1.2949x - 16.4338 \quad (35)$$

$$y_{RCL_C}(x) = -0.0001x^2 + 0.9991x - 8.587 \quad (36)$$

$$y_{RCL_R}(x) = -0.0001x^2 + 0.6557x - 0.2256 \quad (37)$$

$$y_{TAXI_G}(x) = 1.0254x - 0.2113 \quad (38)$$

$$y_{TAXI_Y}(x) = -0.0001x^2 + 0.9377x - 0.3371 \quad (39)$$

Equations (35), (36), (37) and (39) can be simplified into first-degree polynomials that maintain similar accuracy while improving the goodness of fit by better balancing the input data in the Matlab Curve Fitter App. The final simplified equations are:

$$y_{TDZ}(x) = 0.893x - 30.7233 \quad (40)$$

$$y_{RCL_C}(x) = 0.8966x + 2.7371 \quad (41)$$

$$y_{RCL_R}(x) = 0.6359x + 0.1086 \quad (42)$$

$$y_{TAXI_Y}(x) = 0.0001x^2 + 0.9084x + 0.0812 \quad (43)$$

The analysis of these equations and their respective coefficients reveals significant differences depending on the lamp type and color. These variations are influenced by several factors, such as the spectral characteristics of the light source, particularly the emitted beam color. For instance, the spectral response of the BH1750 sensor may cause measurement errors when color components coincide with the "saddle" area of the curve, which is not observable in the Sonopan L-200P luxmeter. Additionally, differences in the correction coefficients, which adjust the BH1750 sensor readings to align with those from a certified device, are also due to the lamp prisms. TDZ and RCL lamps, for example, require distinct equations.

For each equation, key metrics such as the sum squared error (SSE), coefficient of determination (R-square), decision feedback equalizer (DFE), adjusted R-squared (Adj R-sq), and root mean square error (RMSE) were calculated [238]. Table 28 presents the goodness-of-fit parameters for both simple polynomial equations and their more complex forms. The advantage of using simplified correction factors is faster computation while maintaining relatively small measurement errors.

4 Proposal of light sensors integration for AGL evaluation

Table 28 Goodness of fit parameters for the calculated polynomial conversion equations [26]

Airport Lamp Type	Equation number	SSE	R-square	DFE	Adj R-sq	RMSE
TDZ	(35)	9336.9456	1	1	0.9999	30.6096
	(40)	6780.5	0.9999	2	0.9998	58.2258
RCL Clear	(36)	8500.9	0.9999	6	0.9999	37.6406
	(41)	9828.9	0.9999	7	0.9999	37.4716
RCL Red	(37)	0	1	0	NaN	NaN
	(42)	0.1289	1	2	1	0.2539
TAXI Green	(38)	0	1	0	NaN	NaN
TAXI Yellow	(39)	0	1	0	NaN	NaN
	(43)	0.1881	1	1	1	0.4338

Equations (38) and (40), (41), (42), (43) were applied to the obtained measurements, and the data were visualized in Figure 102, Figure 103, Figure 104, Figure 105, Figure 106. These figures present a comparison between the raw values from the BH1750 sensor, the certified Sonopan L-200P luxmeter, and the BH1750 measurements after applying the mathematical corrections.

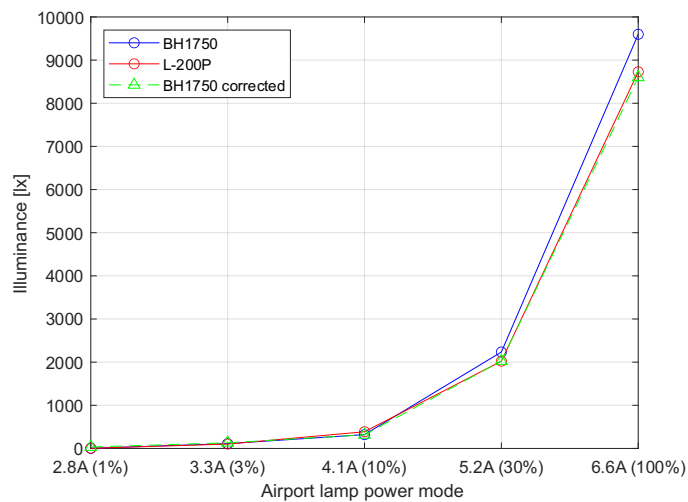


Figure 102 BH1750 correction for touchdown zone lamp TDZ [26]

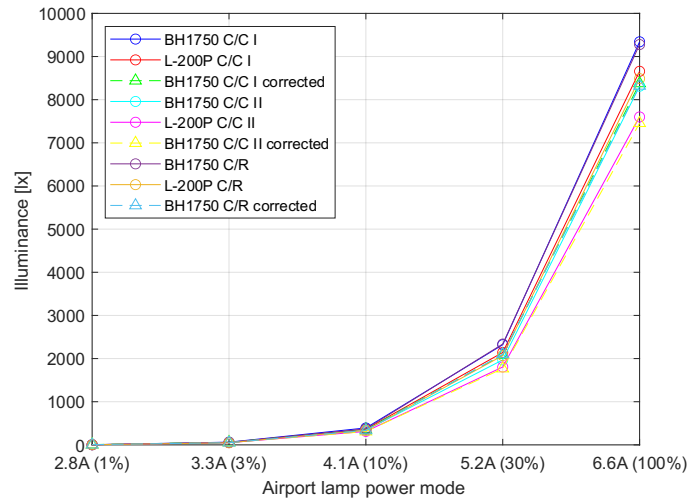


Figure 103 BH1750 correction for runway centerline clear lamp (RCL Clear) [26]

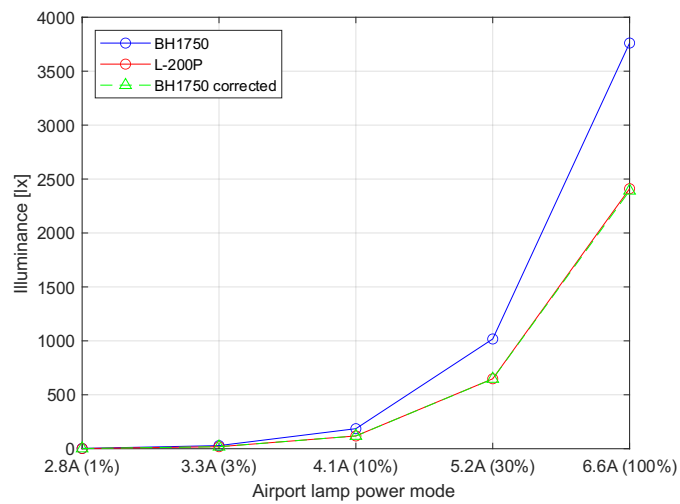


Figure 104 BH1750 correction for runway centerline red lamp (RCL Red) [26]

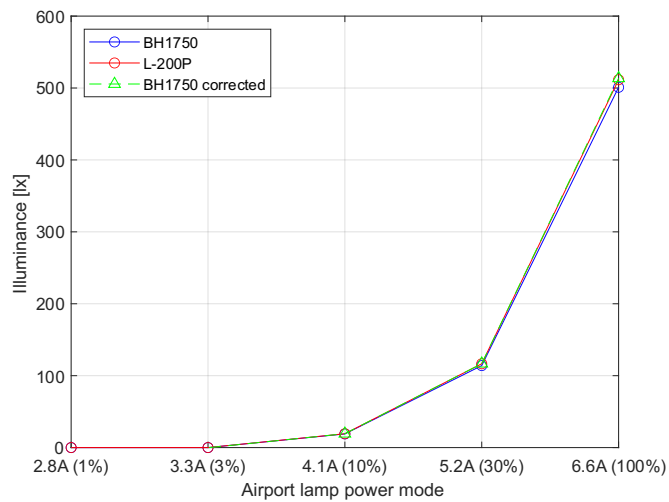


Figure 105 BH1750 correction for taxiway green lamp (TAXI Green) [26]

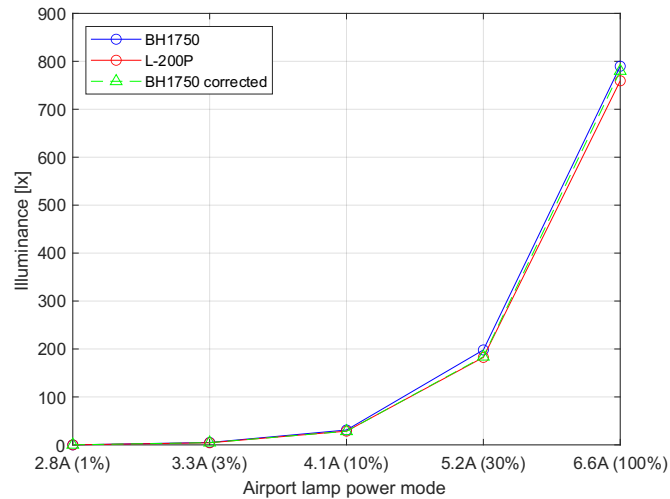


Figure 106 BH1750 correction for taxiway yellow lamp (TAXI Yellow) [26]

The analysis of the graphs in Figure 102, Figure 103, Figure 104, Figure 105, Figure 106 indicates that the conversion values from the equations align the raw BH1750 sensor data with the standard for each specific lamp. However, these were calibration data, so to verify the accuracy of the results, additional measurements were conducted using a goniophotometer with both the Sonopan L-200P luxmeter and the BH1750 sensor. The comparison of light distribution measurement data (heatmaps) are presented in Figure 107, Figure 108, Figure 109, Figure 110, Figure 111.

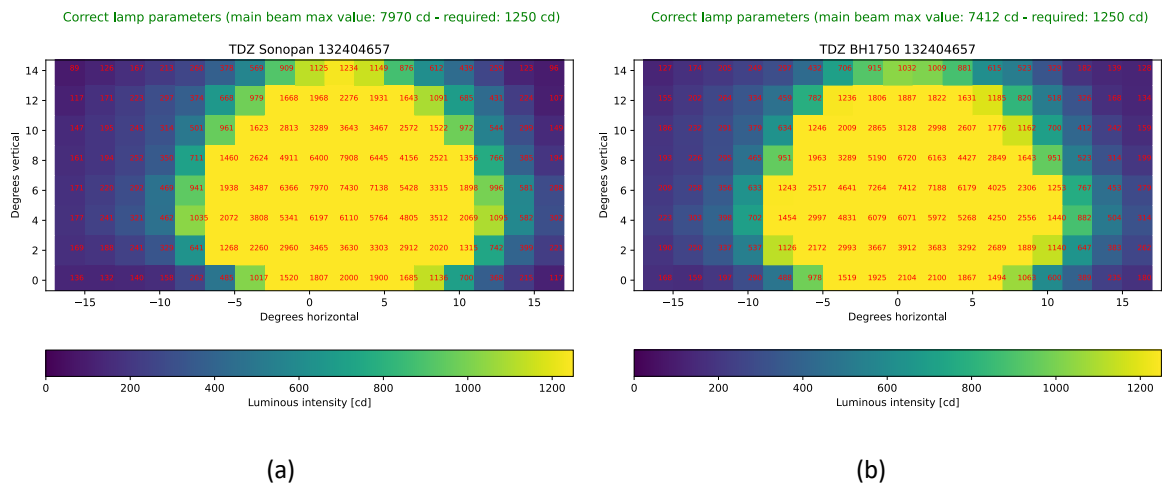


Figure 107 Luminous intensity measurements of TDZ lamp: (a) Sonopan L-200P; (b) BH1750 [26]

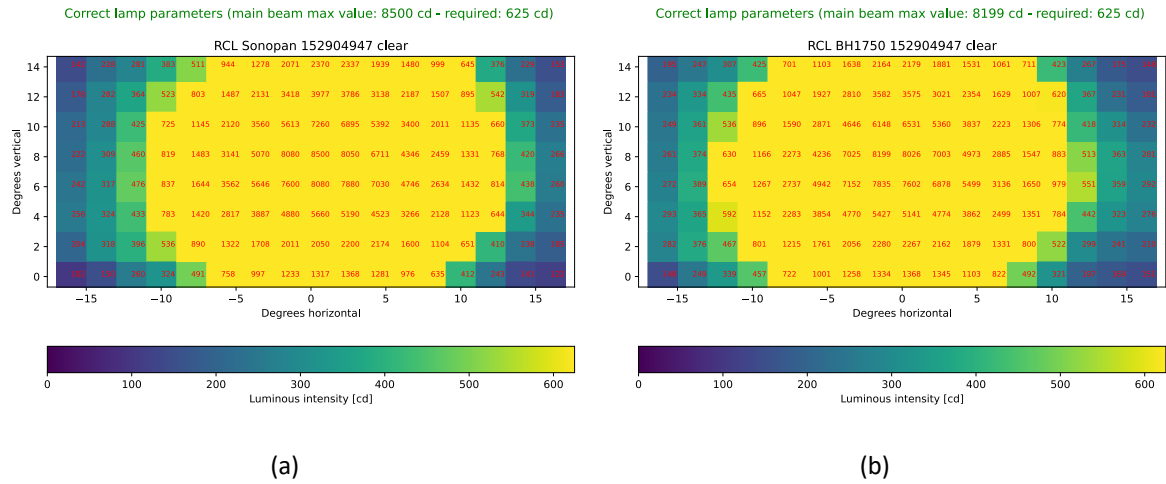


Figure 108 Luminous intensity measurements of RCL clear lamp: (a) Sonopan L-200P; (b) BH1750 [26]

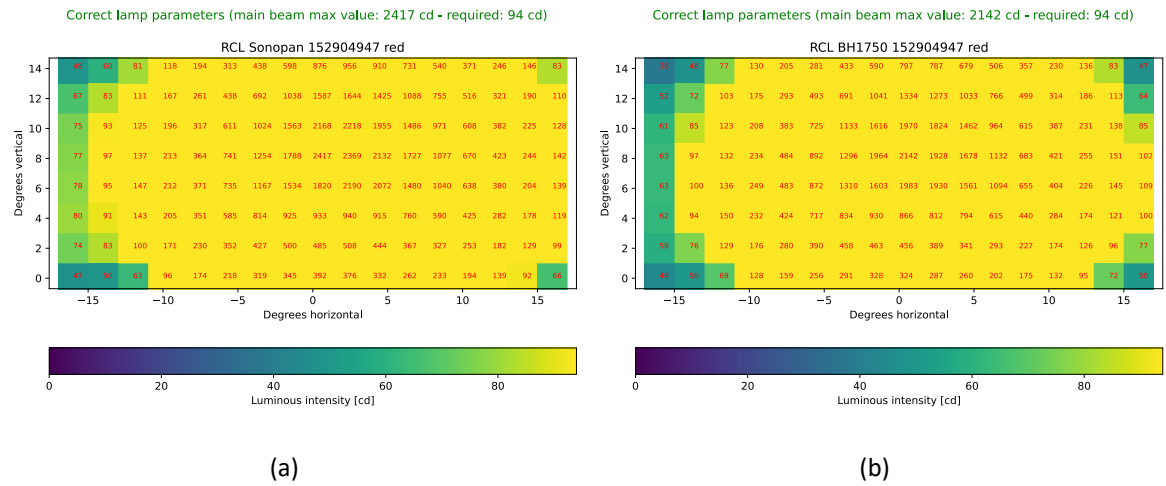


Figure 109 Luminous intensity measurements of RCL red lamp: (a) Sonopan L-200P; (b) BH1750 [26]

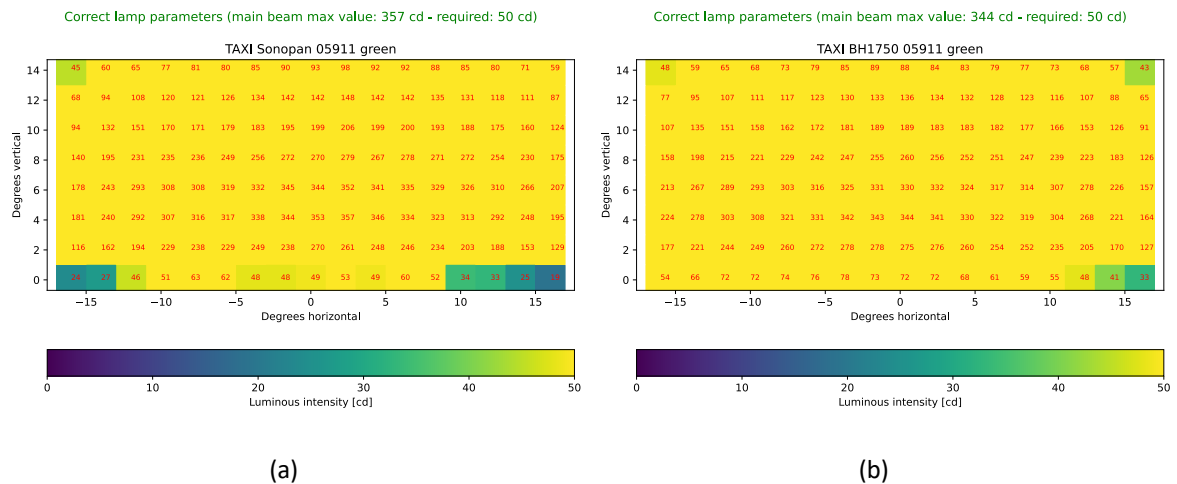


Figure 110 Luminous intensity measurements of TAXI green lamp: (a) Sonopan L-200P; (b) BH1750 [26]

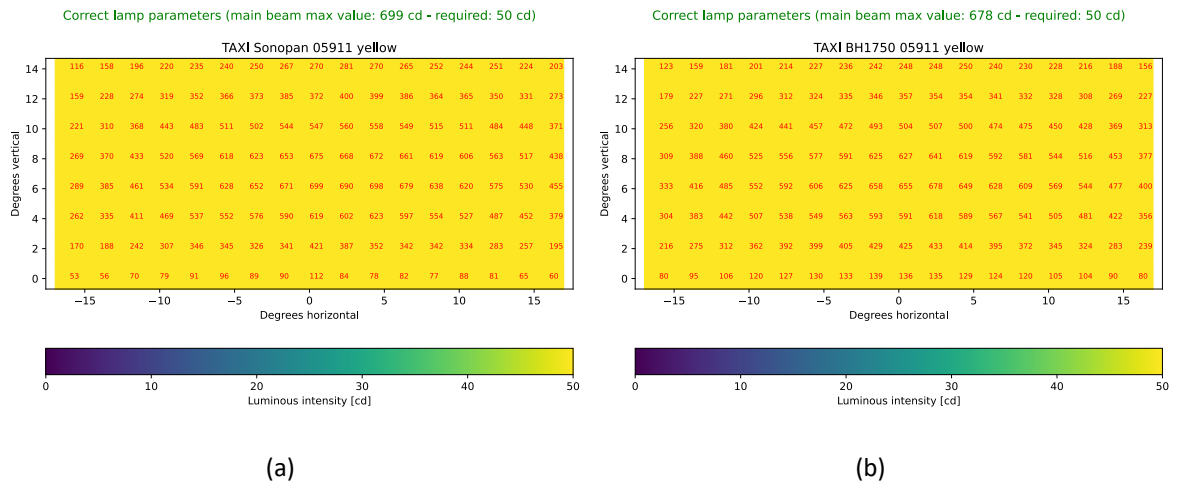


Figure 111 Luminous intensity measurements of TAXI yellow lamp: (a) Sonopan L-200P; (b) BH1750 [26]

Figure 107, Figure 108, Figure 109, Figure 110, Figure 111 reveals that the conversion factor applied to the BH1750 sensor introduces some measurement inaccuracies. These discrepancies may arise from the limitations of using a polynomial to model the conversion function for each type of lamp. Nevertheless, the values at the center of the lamps' angular characteristics closely match the reference data. Since this central region is critical for evaluating airport lamp performance, it can be concluded that the current version of the proposed device is highly effective and accurate for testing airport lamps in laboratory conditions.

4.1.4 Evaluation of photometric parameters of selected used and refurbished AGL using illuminance sensor

Extensive research on the quality assessment of in-pavement AGL was conducted in the frame of collaboration with Poznań-Ławica Airport. During tests to verify the automatic navigation lighting control device, several measurements were taken of lamps in operation within airport areas, particularly those identified for maintenance during routine inspections.

Statistical analysis suggests that touchdown zone lamps experienced the greatest degradation, likely due to frequent exposure to aircraft passing over them. In contrast, the red centre line lamps were in the best condition, as they typically mark the runway's end and are less frequently subjected to aircraft movement. White centre line lamps, located along most of the runway, also showed signs of wear, though not as pronounced as the touchdown zone lamps. These observations highlight the importance of regularly monitoring the photometric characteristics of AGL to ensure their proper functioning and to identify those that need replacement.

The measurement results obtained using the automatic control device for in-pavement AGL are presented as heatmap graphs. These graphs display the distribution of luminous

intensity at various measurement points, based on the sensor's horizontal and vertical positioning relative to the light source. Similar to the graphs outlined in the standards, these visualizations pinpoint the location of the main light beam, which is crucial for evaluating the efficiency of airport lamps. The graph's scale is adjusted depending on the lamp type and the color of the emitted light. Yellow areas represent values close to or exceeding the minimum standard, while blue shades indicate decreasing values. Figure 112, Figure 113, Figure 114 provide sample luminous intensity graphs for specific lamps requiring repair.

The heatmaps illustrating the photometric characteristics of the lamps indicate a notable decline in the intensity of the light beam. For the RCL clear lamp (Figure 112), the primary light beam is significantly below normal levels, as evidenced by the dark color on the scale. In contrast, the red light version of the same lamp (Figure 113) still complies with EASA standards, although a considerable reduction in luminous intensity is evident. The touchdown zone lamp (Figure 114) presents a challenge in identifying the area where the main beam is located on the graph due to extensive degradation of the prism.

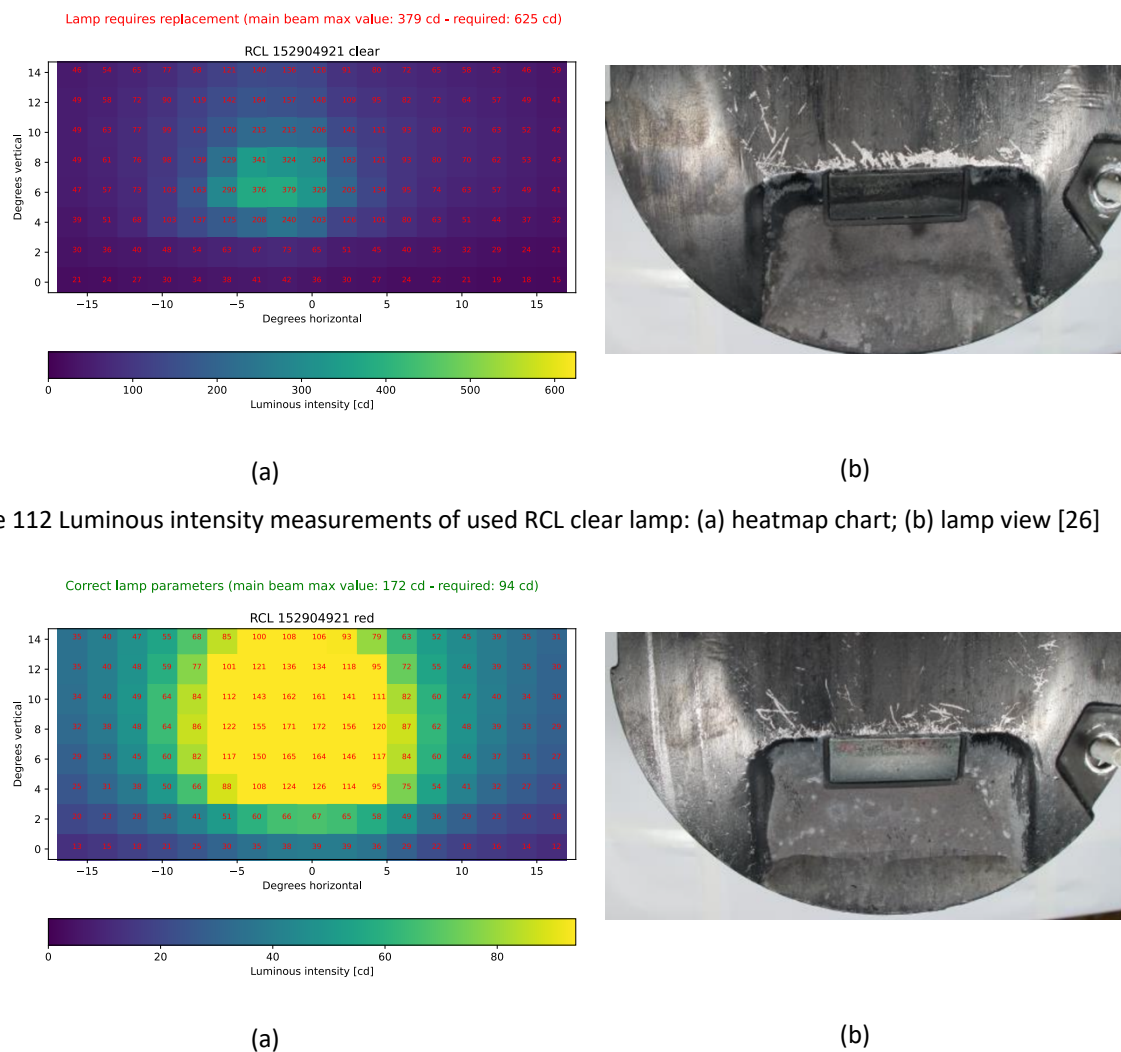


Figure 112 Luminous intensity measurements of used RCL clear lamp: (a) heatmap chart; (b) lamp view [26]

Figure 113 Luminous intensity measurements of used RCL red lamp: (a) heatmap chart; (b) lamp view [26]

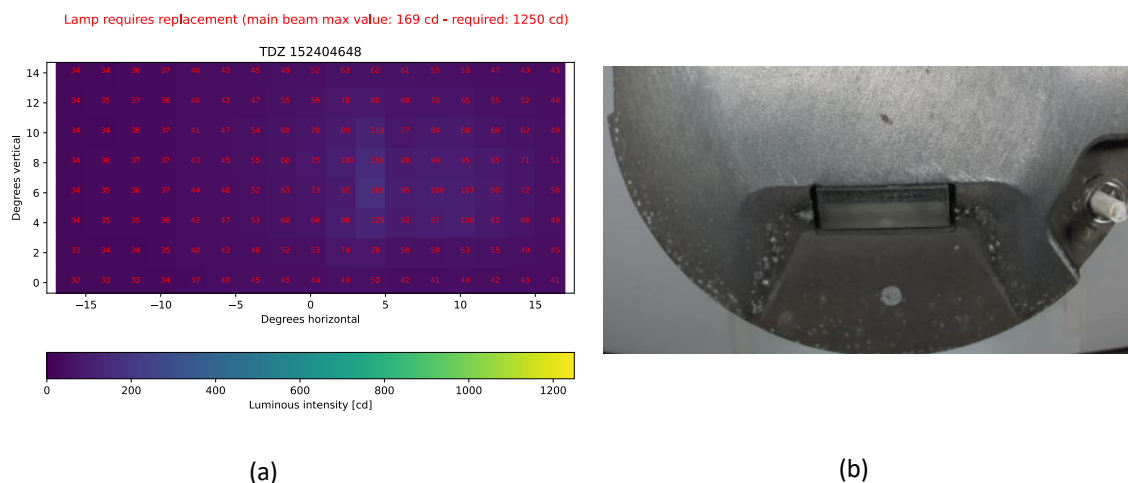


Figure 114 Luminous intensity measurements of used TDZ lamp: (a) heatmap chart; (b) lamp view [26]

Following refurbishment of the lamps which included replacing prisms, cleaning or replacing the housing, substituting halogen light sources, and sealing, the photometric characteristics were re-evaluated. The results indicated that all the in-pavement navigation lighting lamps met the required standards, significantly surpassing the established minima. Figure 115, Figure 116, Figure 117 are heatmaps of the photometric characteristics for the luminaires with the same serial numbers as those displayed in Figure 112, Figure 113, Figure 114.

The heatmaps illustrating the photometric characteristics validate the effectiveness of the luminaires. In every instance, the distinctly marked main beam of light significantly surpasses the minimum values mandated by the standards. These lamps are suitable for reuse on airport surfaces, and the angular pattern accurately indicates the position of the main beam, aligning with that of new lamps.

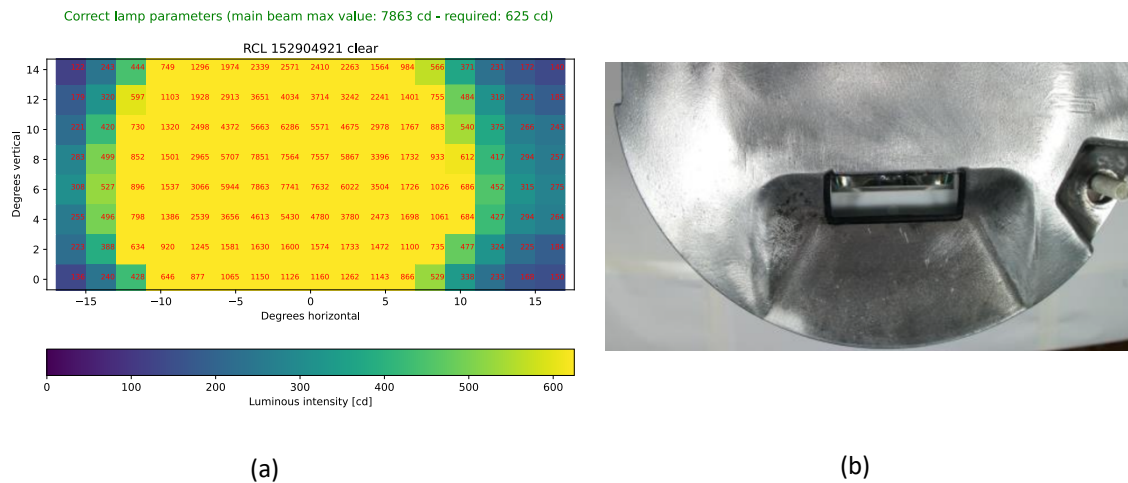


Figure 115 Luminous intensity measurements of refurbished RCL clear lamp: (a) heatmap chart; (b) lamp view [26]

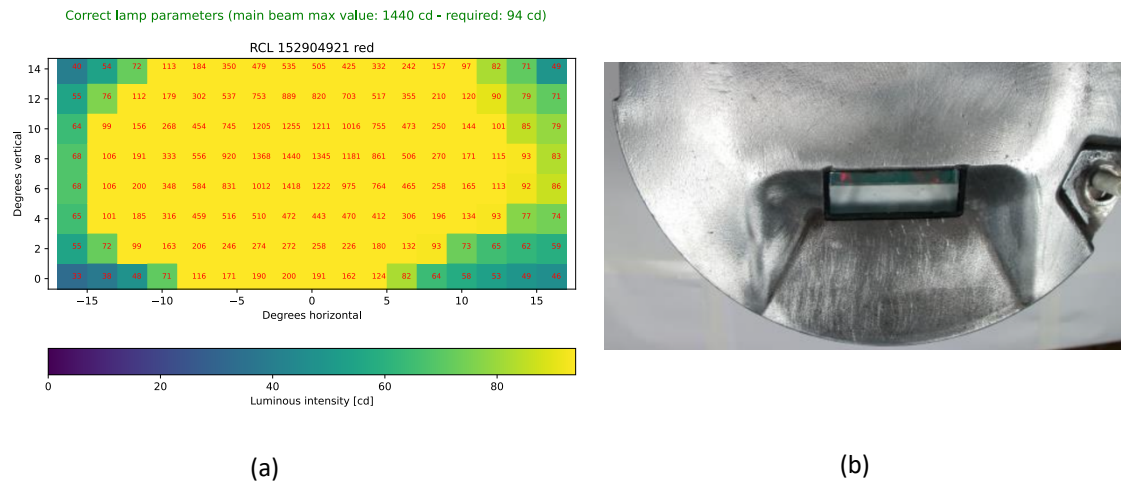


Figure 116 Luminous intensity measurements of refurbished RCL red lamp: (a) heatmap chart; (b) lamp view [26]

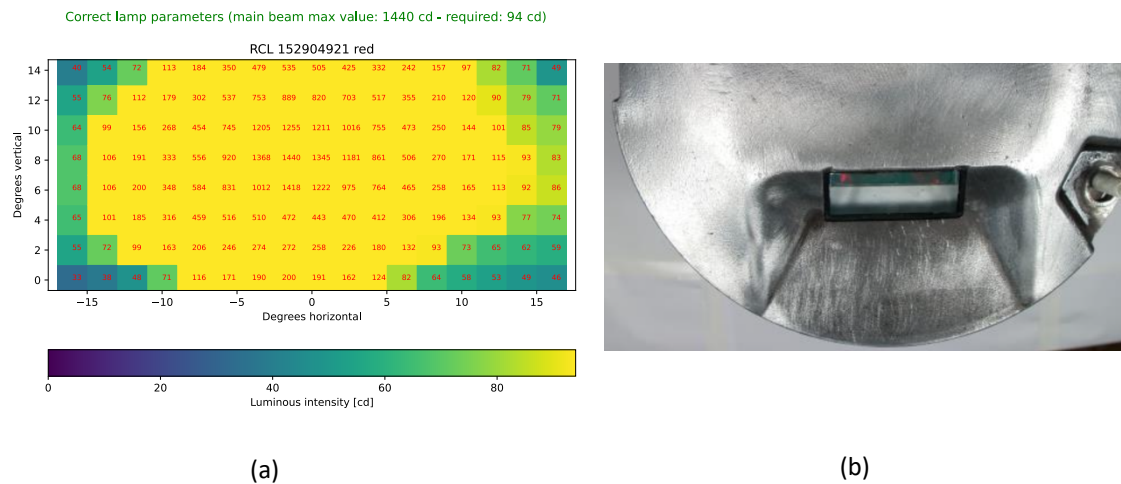


Figure 117 Luminous intensity measurements of refurbished TDZ lamp: (a) heatmap chart; (b) lamp view [26]

Experiments conducted with a device for automatic control of in-pavement navigation lighting demonstrated the importance of using such systems to assess photometric parameters under controlled laboratory conditions. This system facilitates the selection of lamps that remain usable despite wear, as well as identifying those requiring maintenance. Once this process is completed, further operation can continue, ensuring compliance with required standards.

Digital illuminance sensors, which allow for the relatively simple construction of measurement devices, provide adequate range and accuracy. Experiments performed at standardized power supply thresholds for airport lamps enabled a comparison between the BH1750 sensor and the reference Sonopan L-200P luxmeter. The stability of measurements based on the operating mode of the BH1750 was also examined. Given that airport lamps function at high illuminance levels, the L-Resolution Mode was chosen for its advantage of quicker data acquisition.

An analysis of the spectral response of the BH1750 sensor indicated the necessity for a mathematical correction to the obtained measurements for various light colors. Utilizing the Curve Fitter App in the Matlab environment facilitated the development of approximate polynomial equations, allowing for the adjustment of the sensor's spectral characteristics to align with the certified luxmeter's reference values.

Through a scientific research collaboration with Poznań-Ławica Airport, 498 lamps that had been in operation on the runway were tested. The inspection (as documented in the internal airport report) revealed that 7% of the lamps were nearing their wear limit. Although these lamps still met the standards, the identification of reduced photometric parameters led to more frequent inspections and maintenance of the navigation lighting system. Such preventive measures enable the airport to accurately assess the 2D spatial distribution of luminous intensity and compare it against EASA standards.

4.2 Design of matrix with regular arrangement of photodiodes

The design assumption was to develop a measurement matrix with light intensity sensors. The use of many modules results from the width of the light beam emitted by in-pavement lamps, but also from the inaccuracy of the platform's approach to the lamp. Figure 118 shows the connection diagram between the sensor modules (BH1750 or VEML7700), the address translator (TCA9548A or LTC4317) and the microcontroller (ATmega328P).

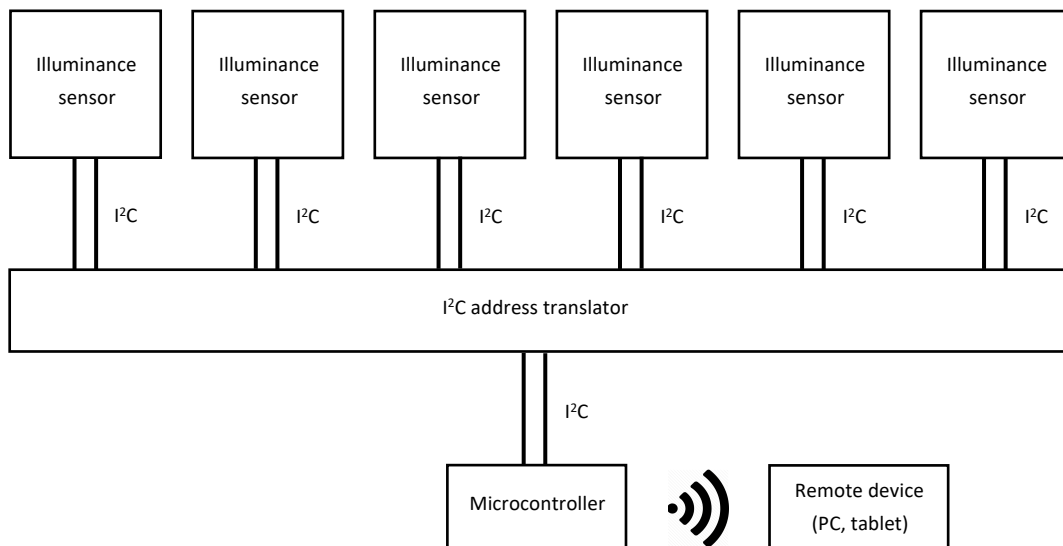


Figure 118 Conceptual diagram of the measurement matrix connections [29]

The basic element of the measurement matrix for AGL testing are sensors determining the intensity of the light beam. The most important parameters that should characterize them are the measurement speed and its range, because they determine the correctness of the result obtained during the inspection. An equally important aspect is the number of sensors

and their arrangement on the measurement matrix. The research compares two types of sensors: BH1750 and VEML7700.

Tests on an optical bench carried out using prototype systems in relation to measurements made with a professional luxmeter allowed for the determination of polynomial correction coefficients. They have been used to achieve the best possible light intensity readings over the full measurement range. The tests carried out showed differences between the BH1750 and VEML7700 systems both in the measurement ranges and in the accuracy of their operation depending on the color of the tested light [17].

4.2.1 Analysis of the measurement acquisition time using illuminance sensors

An important aspect of the design and construction of the measurement matrix for testing the quality of operation of airport lamps is the data acquisition time by the light intensity sensor. This is due to the need to carry out the lighting control process in critical airport areas such as the runway or taxiways as quickly as possible. Therefore, an experiment was carried out in laboratory conditions, the aim of which was to check the theoretical maximum speed of data acquisition. The lamp was replaced with an LED that was connected to a constant-amplitude square-wave signal generator. Only changes in the signal frequency were made to simulate changes in the speed of movement of the measuring system. The tests were carried out using cold white LEDs in the measurement system with different diameters - 5 mm and 10 mm, which respectively emitted light with a luminous intensity corresponding to a new and used lamp, but still meeting the standards. The sensor checking the light intensity level was connected to the ATmega328P microcontroller, and the received data was visualized online using Telemetry Viewer software receiving values from the serial port. Knowing the diameter of the lamp (20 cm) and simplifying it as a light "point" of this size, and assuming a minimum of 4 measurements for one fixture, the speed-frequency relationship was determined. It should be noted that the tests were performed at the maximum acquisition speed, which resulted in lower measurement resolution.

Table 29 Dependence of the theoretical driving speed of the matrix on the generated frequency [29]

Frequency [Hz]	Speed [m/s]	Speed [km/h]
2	0,1	0,36
4	0,2	0,72
6	0,3	1,08
8	0,4	1,44
10	0,5	1,8
12	0,6	2,16
14	0,7	2,52

16	0,8	2,88
18	0,9	3,24
20	1	3,6
25	1,25	4,5

In the case of the BH1750 module, correct light intensity readings were possible at a maximum frequency of 20 Hz (Figure 119), which corresponds to the theoretical maximum movement speed of the measurement matrix of 3.6 km/h (Table 29). At a higher frequency, changes occurred such that all zero readings were missing between subsequent diode flashes. In this situation, it is usually possible to recognize the lamps and the area between them because the decrease in value is visible. With such assumptions, the maximum theoretical speed of movement of the measurement platform with BH1750 sensors reaches approximately 4.5 km/h.

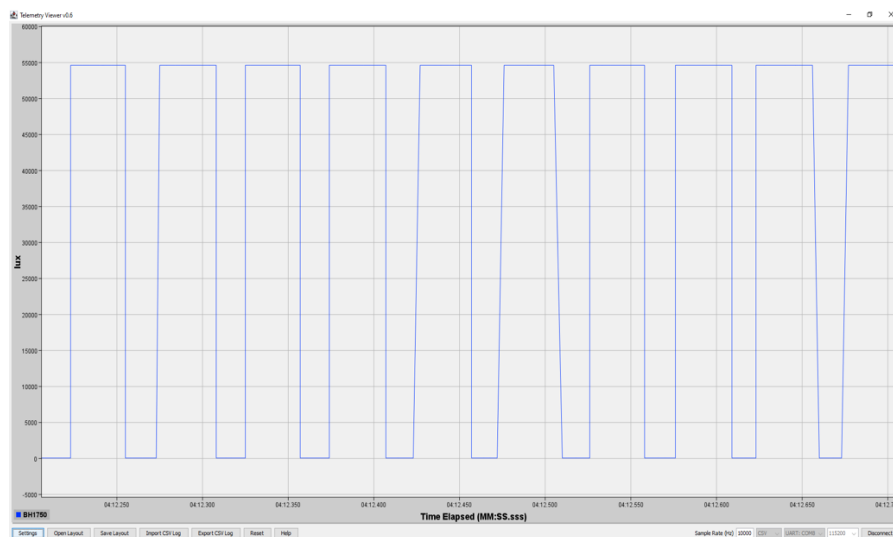


Figure 119 Reading the light intensity value for the BH1750 sensor at an LED frequency of 20 Hz [29]

The VEML7700 sensor is characterized by much longer measurement times of 600 ms, which was confirmed by tests with an LED diode. The maximum frequency at which all values can be read without any interference is 4 Hz, which corresponds to a speed of only 0.2 km/h. The use of this module in a measurement matrix for testing AGL is therefore not possible in practice.

It should be noted that the theoretical speed tested applies to the situation when data is collected from one sensor, and not the entire matrix, the construction of which requires an address translator.

In order to be able to support many light intensity sensors on the I²C bus, identifying themselves with the same address, it is necessary to use an address translator. This makes it possible to create a full sensor matrix consisting of at least several modules, instead of one

or two. This results in better quality of data readings and facilitates measurement, which does not require a very precise passage over the lamp.

For this purpose, two translator models were tested that enable appropriate address change operations to be performed. The LTC4317 module [239], shown in Figure 120, allows data to be transferred by up to 3 devices with the same ID on the bus. This is possible thanks to hardware address conversion using appropriate resistors, which are selected based on calculation software [239]. Due to the hardware implementation of the LTC4317 translation, it does not require additional software, so the translation efficiency is high and does not introduce any additional delays. The module has one signal input connector and 2 outputs for devices whose address can be modified, and there is also one output that leaves the ID unchanged. By selecting different resistances, the user can obtain up to 127 different address translations [239].

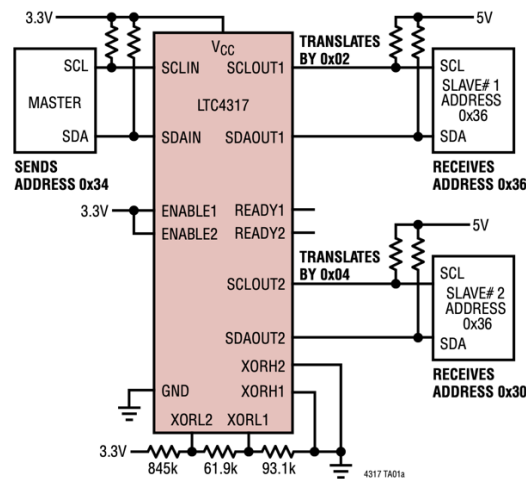


Figure 120 LTC4317 I²C address translators circuit diagram [239]

The second address translator tested is the low-voltage, 8-channel TCA9548A module (Figure 121), operating on the I²C or SMBus bus. It enables the connection of 1 to 8 bidirectional data transmission devices. In addition, the device is equipped with three address pins, which allows to connect up to 8 TCA9548A chips on the same bus, using addressing from 0x71 to 0x77. Thus, the TCA9548A module allows to connect up to 64 devices with the same I²C address [240]. Translation of identifiers is possible for voltages from 1.8 V to 5 V. The module also has two built-in "pull-up resistors". The user can select any individual SCn/SDn channel via an 8-bit register referenced programmatically.

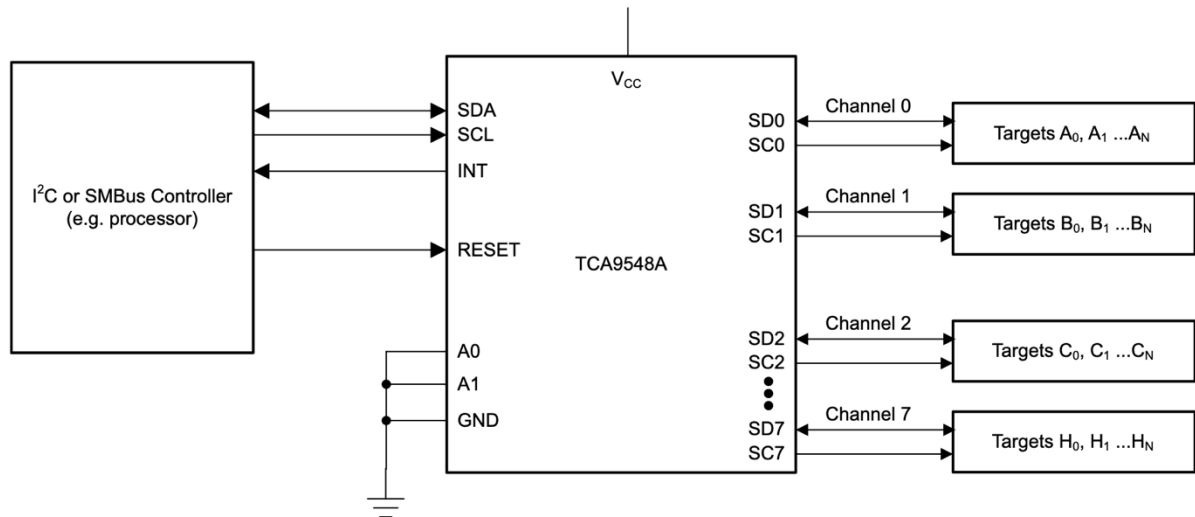


Figure 121 TCA9548A I²C address translators circuit diagram [240]

The BH1750 light intensity sensor module is visible on the I²C bus as 0x23, however, it is equipped with an additional address pin, enabling operation with a changed identifier 0x5C by specifying a high state. Using this type of system, a maximum of 6 BH1750 devices can be connected to the measurement matrix in conjunction with the LTC4317, and 16 BH1750 devices with the TCA9548A.

The VEML7700 light intensity sensor has only one addressing option, which is factory set to 0x10. The connection with the LTC4317 system therefore enables simultaneous communication of 3 devices, while using the TCA9548A module it enables read data from 8 sensors.

During laboratory tests, data reading times from individual light intensity sensors and the entire array of sensors with an address translator were measured. They were determined in software and verified using an oscilloscope, obtaining the same results. They are summarized in Table 30.

Table 30 Comparison of data acquisition time in various sensor configurations in the matrix [29]

Sensor system	VEML7700	BH1750		
	1 module	1 module	6 modules with LTC4317	8 modules with TCA9548A
Time [μs]	640	480	2960	87904

It can therefore be seen that the hardware implementation of address translation using the LTC4317 module does not introduce additional delays related to data transmission. In the case of systems operating based on additional shift registers and software support, the problem arises of performing all time-consuming operations. The main source of additional delays in the TCA9548A module is switching between individual SCn/SDn pairs, which takes approximately 10,000 μs. A comparison of the time consumption of operations in this translator and in the LTC4317 module with BH1750 sensors is presented in Figure 122.

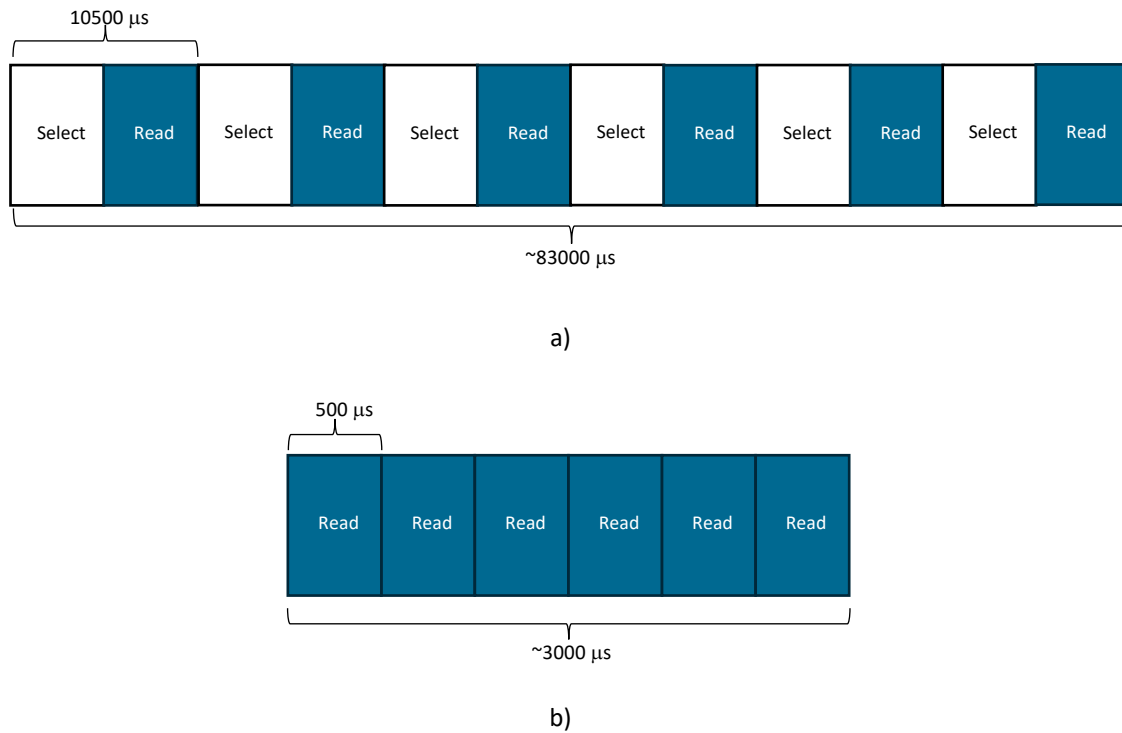


Figure 122 Comparison of operation times in various measurement matrix systems using the BH1750 system and: (a) the TCA9548A translator and (b) the LTC4317 translator [29]

It should also be borne in mind that the given times apply only to hardware implementation. Subsequent operations related to the calculation of the luminous intensity value and the visualization of the measurement results constitute further delays in the entire measurement system. The laboratory experiments carried out and the analysis of manufacturers' data allowed for the verification of the concept of a measurement matrix for testing AGL.

Taking into account the characteristics of light intensity sensors and I²C address translators, it was found that the appropriate elements of the measurement matrix design for testing the quality of operation of AGL is a set of 6 BH1750 modules combined with LTC4317 translators. This choice is determined by the shortest data acquisition time while maintaining measurement accuracy. The TCA9548A translator module offers much greater possibilities in terms of the number of light intensity sensors constituting the matrix, but it causes long delays that would require stationary measurements.

However, by setting the BH1750 sensor to the Low-Resolution mode with the highest speed at the expense of the reading resolution of 4 lux and changing the I²C bus speed to Fast mode 400 kbps, it is possible to achieve much faster operation of the sensors through the TCA9548A address translator. Laboratory tests have shown that when connecting 16

illuminance sensors, the time to read data from all of them is about 3370 μs , which in turn means about 297 measurements per second.

4.2.2 Design of photodiode based illuminance sensor

As part of laboratory tests, experiments were conducted to evaluate the accuracy of each sensor's measurements GY-302 with BH1750 module and Grove Light Sensor v1.2. Figure 123 and Figure 124 show the output voltage signal for square pulse-width modulation (PWM) light input signals at frequencies of 100 Hz and 1000 Hz for the Grove Light Sensor v1.2. The results indicate that at higher frequencies (such as 1000 Hz), accurate measurement of certain lamps is not feasible. Further details regarding platform speed and PWM response are covered in the following section.

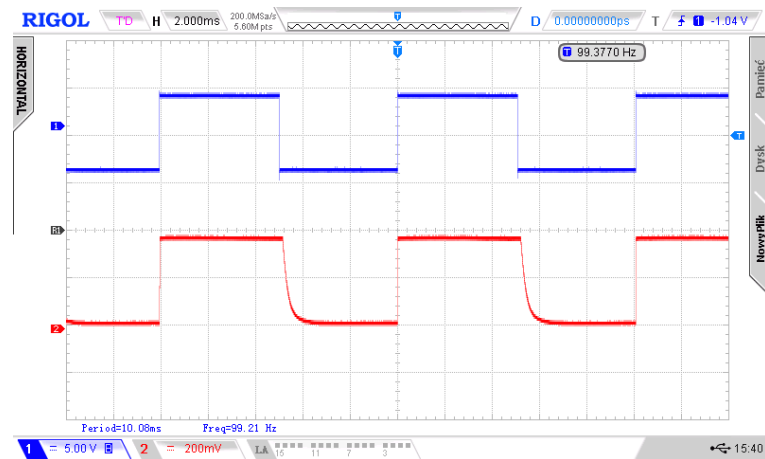


Figure 123 Grove Light Sensor v1.2 voltage output signal for a 100 Hz square PWM signal [27]



Figure 124 Grove Light Sensor v1.2 voltage output signal for a 1000 Hz square PWM signal [27]

Airports are obligated to carry out numerous inspections of their infrastructure, including lighting systems for runway and taxiway lights [223]. Given the large airport areas and the number of lights installed, daily inspections are time-consuming. In air operations, time is critical, alongside safety considerations. Any delay or runway occupancy, even for maintenance, can lead to significant costs for airports. Therefore, it is essential to complete

all maintenance work as swiftly as possible while maintaining high safety and quality standards.

The next phase of testing involved assessing the saturation of the measurement when illuminated by an IDM 4671 in-pavement airport lamp. The tests were conducted using a specially built stand designed for automatically measuring light intensity. This laboratory setup, shown in Figure 95, allows for the measurement of multipoint luminous intensity characteristics of an airport lamp depending on the sensor's horizontal angle and vertical position relative to the lamp's prism.

Sensors were mounted on a movable arm positioned 1 meter from the IDM4671 lamp. During the test, each sensor was placed at the point of incidence of the main light beam, and the voltage was gradually increased (which also increased the current), thereby raising the light intensity of the lamp. The maximum intensity values recorded by the sensors were compared to the light intensity supplied to the lamp, representing the saturation point of the main light beam (Table 31).

Table 31 Maximum ranges of light intensity measurement by sensors measured at a distance of 1 m [27]

Sensor	GY-302	Grove Light Sensor v1.2
Airport lamp current [A]	4.17	3.45
Airport lamp saturation [%]	10	3
Measured light intensity [klx]	65.536	11.093

In [29], where the authors utilized the BH1750 measurement module, it was demonstrated that the theoretical maximum speed of the measurement platform is approximately 4.5 km/h. This speed is relatively low, meaning it would take around 30 minutes to survey a runway over 2 km in length. As a result, it is crucial to address the limitations of data acquisition using the BH1750 and to develop a sensor incorporating a photodiode, which would enable higher measurement speeds.

Airport lamps have specific light spectra that vary depending on the airport zone. The characteristics of these lamps were analyzed in [17], revealing that their peak light intensity, depending on the type of lamp, falls within the wavelength range of 550 to 680 nm.

After reviewing available commercial photodiodes and considering important factors such as wavelength sensitivity and the application of V_λ correction, two photodiodes were identified as the best candidates for this application BPW21 and VTP1220FBH. These factors are critical to ensuring accurate brightness measurements for airport lamps.

Using the same conditions as outlined in [29], the estimated measurement platform speeds for the different sensors are summarized in Table 32.

Table 32 Estimated platform speeds assuming 4 measurements at a distance of 20 cm [27]

Speed of the platform [km/h]	Speed of the platform [m/s]	Required sampling rate [sample/s]
10	2.78	55.56
20	5.56	111.11
30	8.33	166.67
40	11.11	222.22
50	13.89	277.78
60	16.67	333.33

For the previously mentioned photodiodes, an initial test was conducted to observe the forcing process using an LED connected to a signal generator. The photodiode was linked to a current-voltage converter system built around an LM358 operational amplifier. Both the signal from the function generator and the output from the amplifier with the photodiode were connected to a RIGOL MSO2202A oscilloscope. This setup allowed for the observation of the differences between the input forcing signal and the system's output signal.

The tests involved generating a PWM signal with a 50% duty cycle and monitoring the output signal from the measurement system. As the PWM signal frequency was gradually increased, the shape of the output waveform changed, and the rise and fall times of the diode current at higher frequencies prevented accurate measurements from being taken.

According to the catalog, the BPW21 photodiode has rise and fall times of 1.5 μ s. When illuminated at frequencies up to 1 kHz (Figure 125), the circuit accurately reproduced the signal wave, although some delays were noticeable at the falling edge. At frequencies above 5 kHz, the signal lost its square-wave shape.



Figure 125 BPW21 current response for a 1000 Hz square PWM signal [27]

The VTP1220FBH photodiode was tested under conditions similar to those used for the BPW21. For this photodiode, the output signal mapping remained accurate up to approximately 5 kHz. Using the same amplifier circuit as for the BPW21, lower output voltages were observed at the current-to-voltage converter (Figure 126).



Figure 126 VTP1220FBH current response for a 1000 Hz square PWM signal [27]

The experiments conducted indicate that the tested photodiodes can operate properly at switching frequencies of around 1 kHz. However, the VTP1220FBH photodiode offers a broader range of accurate switching, which is why it was chosen for the PCB module. Additionally, its smaller photosensitive area results in fewer disturbances in the sensor response [241]. The operating frequency of the VTP1220FBH meets the criteria outlined in Table 32 and even allows for an increased acquisition rate, as shown in Table 33.

Table 33 Estimated platform speed assuming 4 measurements at a distance of 4 cm [27]

Speed of the platform [km/h]	Speed of the platform [m/s]	Required sampling rate [sample/s]
10	2.78	277.78
20	5.56	555.56
30	8.33	833.33
40	11.11	1111.11
50	13.89	1388.89
60	16.67	1666.67

The design of the sensor module system for testing light intensity was based on the concept introduced in [242]. This system incorporated two LM358 operational amplifiers and initially a BPW21R photodiode, which was later substituted by the VTP1220FBH photodiode for testing airport lamps [243]. The use of two amplifiers—one as a current-to-voltage converter and the other as a non-inverting amplifier—enabled a wider dynamic range for low-light intensities. Another advantage of this system is that it avoids the limitations associated with OP37 amplifiers and operates on a 5V power supply [244].

The prototype of the measuring module, equipped with I²C communication, was designed using an ATmega328P microprocessor. Depending on the selected mode (configured by the I²C master), data can either be streamed continuously (in ATmega Free Running Mode) or

requested individually via command. Additionally, the master can choose the point within the system from which the measurement is taken. The overall system block diagram is shown in Figure 127.

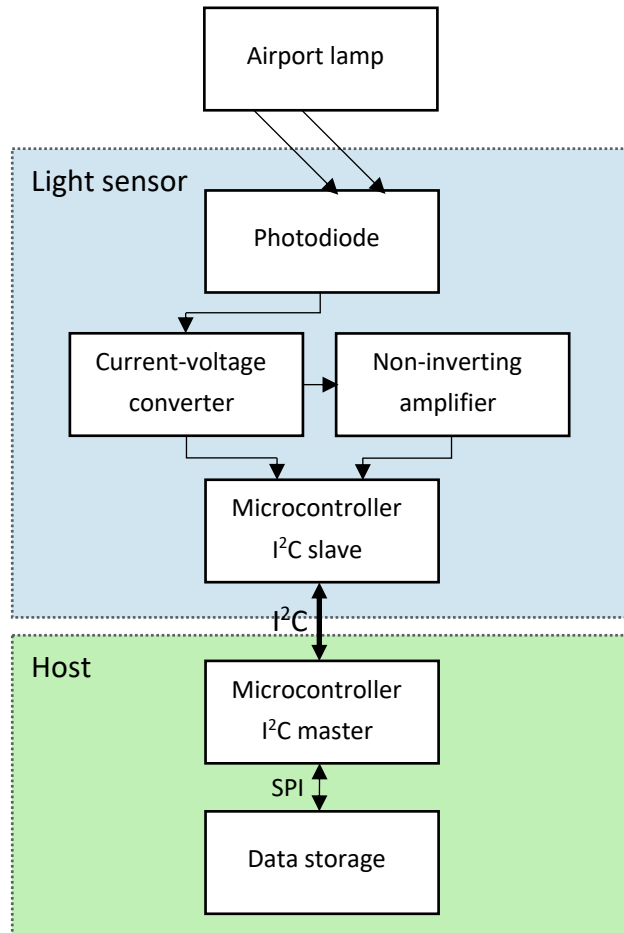


Figure 127 Overall concept block scheme [27]

Commands within the I²C protocol were implemented similarly to the GY-302 module's functionality, with options for OneTime/Continuous and LowRes/HighRes modes. The default I²C address of the device is set to 0x3F, but a DIP switch allows for address changes within the range 0x38-0x3F, removing the need for a TCA9548A multiplexer as used in other solutions [29], [217] and [216]. Figure 128 and Figure 129 illustrate I²C waveforms with and without a light source.

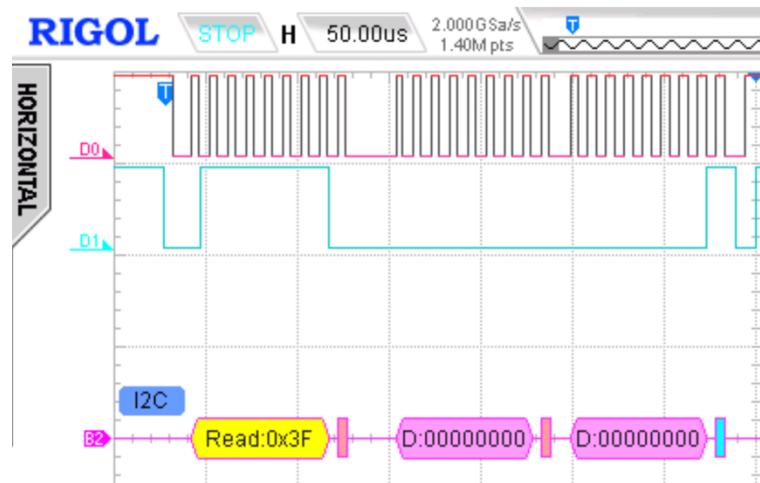


Figure 128 Example of an I²C frame measurement taken without light source [27]

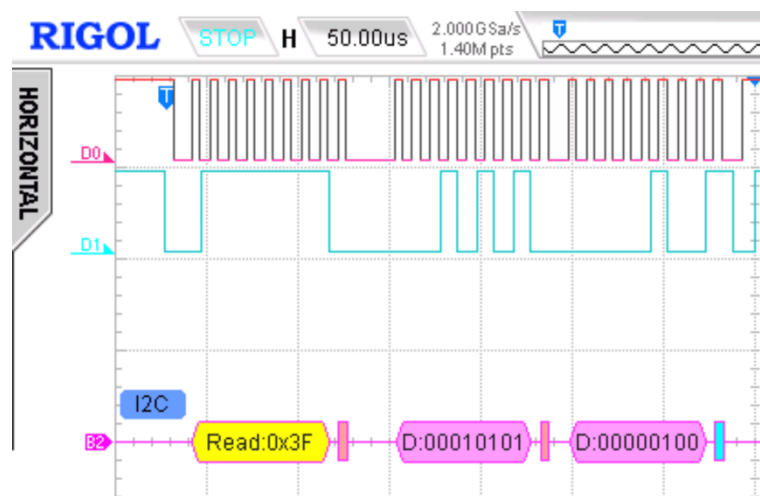


Figure 129 Example of an I²C frame measurement taken with light source [27]

Upon initializing the microcontroller, the system configures the registers and sets up communication, connecting to the I2C bus with a default address of 0x3F at a baud rate of 400 kb/s. The system utilizes the ATmega328P's internal reference voltage for full-range power measurements, and the analogue-to-digital converter (ADC) is configured to sample at 15,000 samples per second, with related interrupts enabled. Once a measurement is complete, the results are read, starting with the least significant part of the value – the right alignment of the registers allows to read full 10-bit measurement in easier way. To ensure seamless operation, the system can block readings during transmission if necessary.

After microcontroller configuration, the I²C communication protocol is employed. When the master device sends data, the slave (sensor module) processes the command and extracts the appropriate control bits to set the measurement mode (continuous/single) and resolution. The first 4 bits are responsible for setting the operating mode (continuous/single measurement), and the next 4 bits determine measurement resolution. The frame is then shifted 4 places to the right and converted to the correct operating mode, and the ADC registers are adjusted accordingly. The less significant bits and the choice of the measurement

source are set: unboosted for low resolution or enhanced causing high resolution of measurement. After master receive the signal, the device returns to the latest measurement stored on 2 bits and sends them in the order of the least significant– the most significant. The measured value is not converted to lux at this point.

Raw data obtained from the sensors require further calculations for accurate interpretation. Since the measurement errors vary for different lamp colors, calibration is necessary. Multiple series of measurements were conducted using a certified SONOPAN LUXMETER L-51 to establish a conversion factor in the form of a second-degree polynomial, allowing the result to be expressed in lux [17].

The design assumptions for the light-intensity sensor module led to the creation of a circuit diagram (Figure 130). Additional features of the system include a double gold-pin connector for communication, a precise potentiometer for gain adjustment, a DIP switch for setting the address, a reset button, and an LED indicator. An optional 100 nF capacitor (C4) is included.

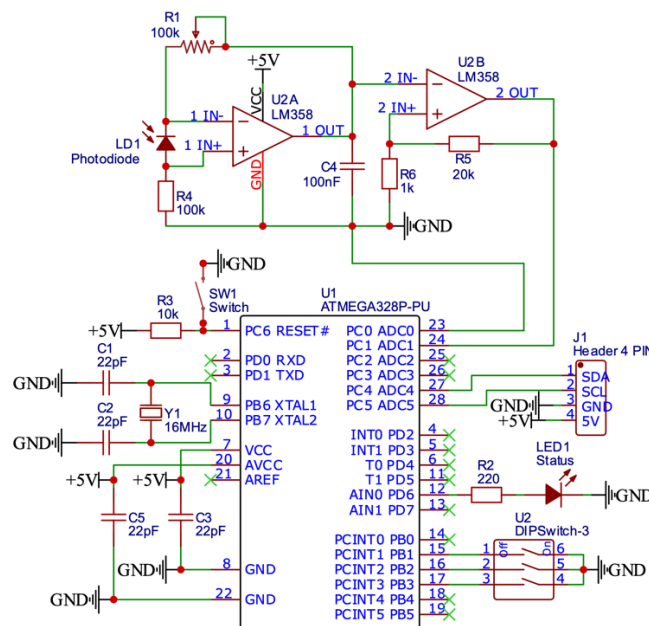


Figure 130 Circuit diagram [27]

The LED serves as an indicator for the device's operating status. It flashes during data transmission, stays lit continuously when the device is active but not transmitting, and remains off when the device is either turned off or blocked. Figure 131 shows the prototype PCB of the light-intensity sensor with the photodiode [243]. These sensors can be assembled into a measurement matrix for airport lamp quality testing.

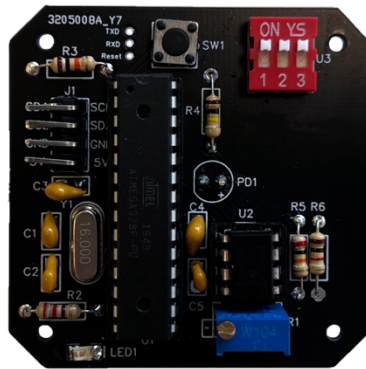


Figure 131 PCB realization of the light-intensity sensor with a photodiode [27]

In addition to the previously mentioned components, a reset button and connectors (TX, RX, reset) were added to the board, allowing for software updates directly to the microcontroller. The photodiode is mounted on the opposite side of the PCB to avoid obstructing light and to enable easy mounting in a specialized cover.

The PCB dimensions (50.8×50.8 mm) were chosen to facilitate installation in a measuring matrix with several modules connected in series. Central placement of the photodiode is crucial for measuring the main beam of the lamp after mounting the sensor in the matrix. The black PCB color was selected to minimize light reflections and avoid disturbances in light intensity measurements.

This microprocessor-based sensor module, designed for measuring visible light intensity, uses the VTP1220FBH photodiode. Due to the characteristics of this photosensitive element, the module is suitable for installation on a measurement platform for testing AGL quality. The key advantages of this solution include fast communication via the I²C protocol and the ability to select from eight different I²C addresses using physical switches. Additionally, these addresses can be customized during microcontroller programming, allowing multiple modules to be connected in a series for multipoint measurements.

At this stage, miniaturization of the sensor was not required due to the size of the measurement platform. Another benefit of the THT assembly method is the easy replacement of the microprocessor and quick reprogramming. Moreover, if future research identifies a better photosensitive element, it can be easily swapped out.

4.2.3 Proposed algorithm of measurement using matrix of illuminance sensors

The use of a matrix of illuminance sensors with a regular arrangement is intended to provide information about the place where the main beam of light emitted by the airport lamp falls. Thanks to this information, it is still possible to make a correction to the approach of the measuring platform so that the matrix with an irregular arrangement of illuminance

sensors can correctly perform measurement acquisition. A block diagram showing the principle of operation of both matrices is shown in Figure 132.

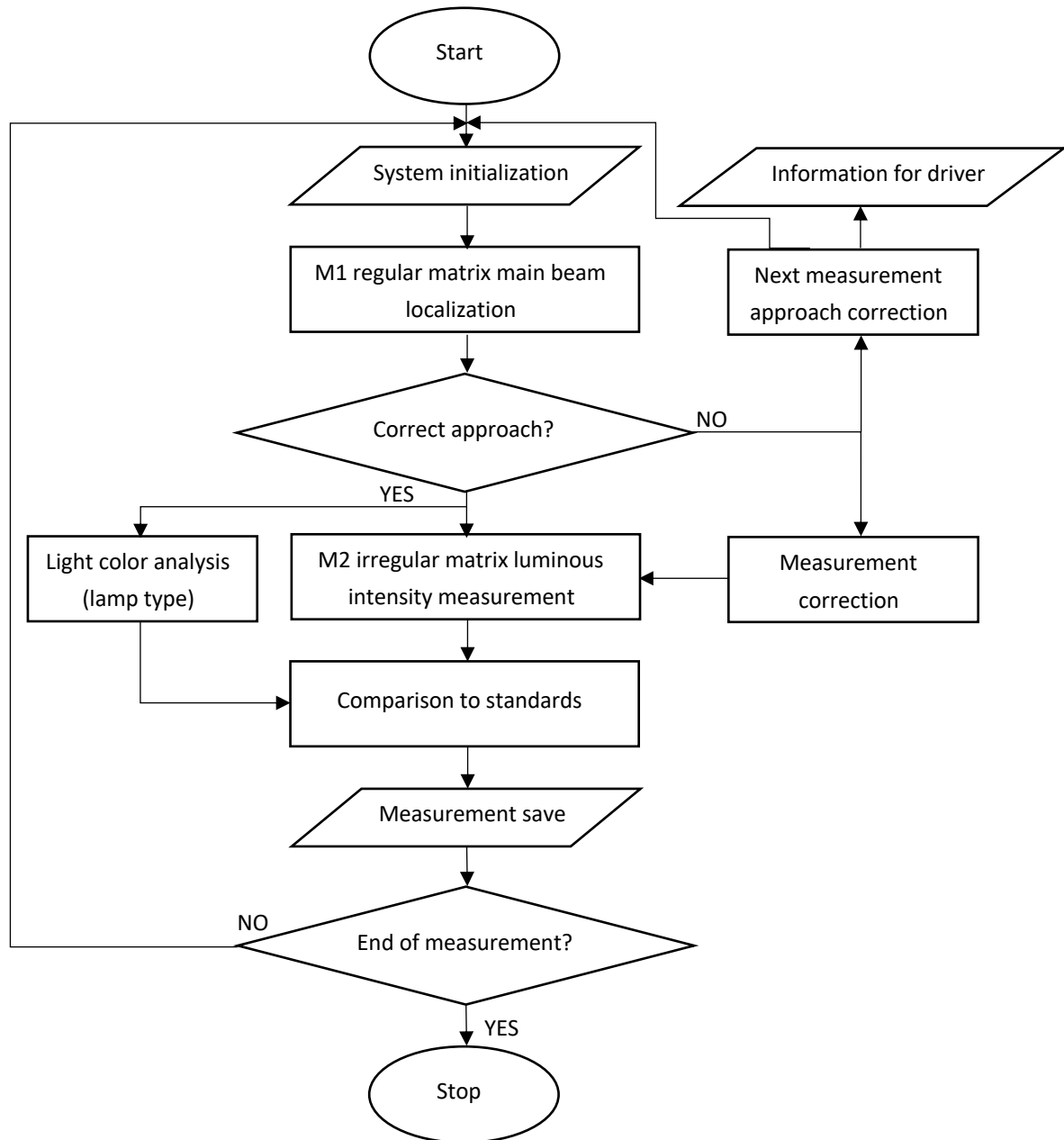


Figure 132 Measuring matrices principle of operation block scheme [25]

4.3 Proposed matrix design with irregular arrangement of photodiodes

The measurement platform for assessing the performance quality of inset airport lights is designed as a two-axle trailer with a swivel drawbar, featuring a waterproof enclosure for electronic devices and a rubber shield for a darkroom that isolates the tested light from others. Mounted to the lower surface of the measurement platform is a sensor matrix, consisting of a regular arrangement of illuminance sensor matrix (M1) and an irregular arrangement design one (M2). The distance between the lower surface of the measurement

platform and the airport surface with the lights is $H = 100$ mm. The distance from the measurement matrix to the airport surface is $h = 80$ mm. The photometric distance is $F = 1000$ mm, and the incidence angle $\gamma = 5^\circ$ in the vertical plane. These relationships are illustrated in Figure 133.

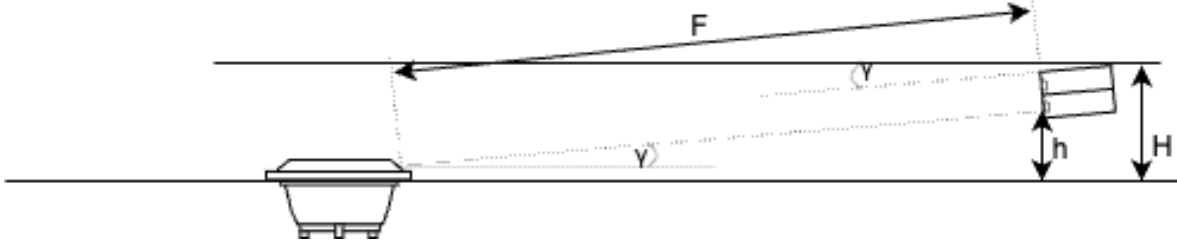


Figure 133 Placement of the measuring matrix under the measuring platform [25]

The main assumptions for the platform designed to measure the quality of AGL include positioning it using a multisensory system that incorporates GNSS data, LiDAR, and vision sequences processing. Additionally, two types of matrices have been developed and applied to measure the light distribution of airport lamps. The regular arranged matrix M1 allows determining the position of the measurement platform relative to the tested in-pavement lamp. The distances between individual illuminance sensors mounted on this matrix were calculated using the formula (44).

$$s_x = 20 + (x - 1) \cdot 50 \text{ [mm]} \quad (44)$$

where x represents the number of the illuminance sensor counted from the center of the matrix, and s_x is the distance from the center of the matrix.

The angular dependencies of light beam incidence on matrix M2 in the horizontal plane were determined based on EASA standards and the isocandela pattern for different types of navigational lamps. The angles are as follows: $\alpha_1 = 0.5^\circ$, $\alpha_2 = 2^\circ$, $\alpha_3 = 5^\circ$, $\alpha_4 = 7^\circ$, $\alpha_5 = 8.5^\circ$, $\alpha_6 = 14.5^\circ$, $\alpha_7 = 19.25^\circ$, $\alpha_8 = 20.25^\circ$. Based on these, the illuminance sensor distribution was symmetrically arranged on matrix M2, as shown in Figure 134.

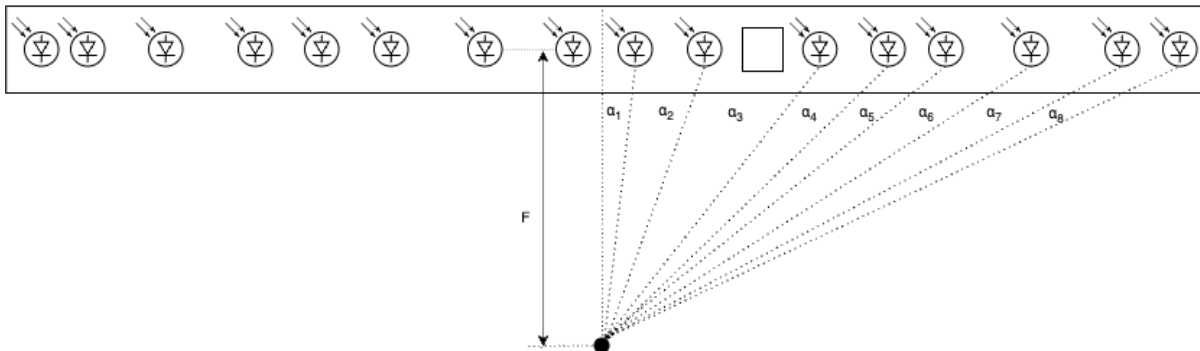


Figure 134 Angular dependencies of M2 irregular arrangement matrix illuminance sensors [25]

The distances of the sensor positions from the center of the matrix were calculated using the Pythagorean theorem, assuming the photometric distance $F = 1$ m and the known light beam incidence angles in the horizontal plane. The calculated distances of the illuminance

sensors relative to the center of matrix M2, adapted for isocandela measurements, are as follows: $d_1 = 8.73 \text{ mm}$, $d_2 = 34.92 \text{ mm}$, $d_3 = 87.49 \text{ mm}$, $d_4 = 122.79 \text{ mm}$, $d_5 = 149.45 \text{ mm}$, $d_6 = 258.62 \text{ mm}$, $d_7 = 349.22 \text{ mm}$, $d_8 = 368.92 \text{ mm}$ (Figure 135).

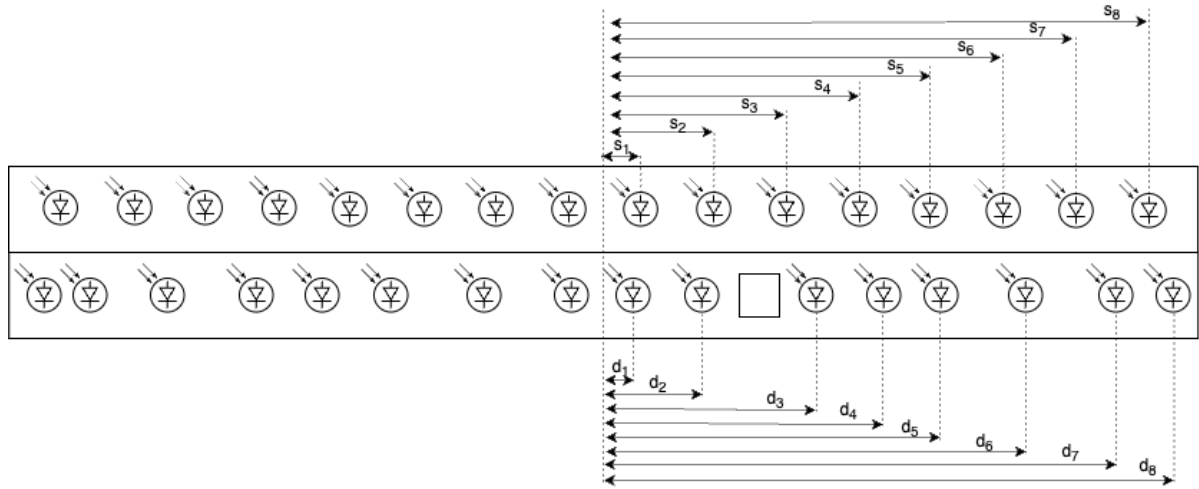


Figure 135 Distance dependencies of illuminance sensors for M1 and M2 matrices [25]

Matrix M1 evaluates the correctness of the measurement platform's alignment over the tested in-pavement lamp. After achieving maximum light intensity readings for the sensors positioned at the center of matrix M1, the light intensity of the main beam of the in-pavement lamp is measured using matrix M2 by simultaneously recording readings from all the illuminance sensors. Subsequently, the light color is assessed using a light spectrum sensor, which identifies the type of the tested inset light to apply an appropriate correction factor for the sensor readings. The data collected during the measurement is used to evaluate the functionality of the lamps by comparing the results with the relevant standard.

The measurement matrix was designed and constructed using 16 BH1750 illuminance sensors mounted in GY-302 modules. Their work is coordinated by the ATmega328P microcontroller via the I²C bus. Due to the fact that the illuminance sensor modules, according to the manufacturer's documentation, can use two addresses 0x23 and 0x5C, in order to ensure communication with a larger number of modules, an I²C address translator in the form of the TCA9548A module was used. The illuminance module operating mode was set to continuous low resolution mode, while the data transmission speed on the I²C bus was set to 400 kbps. Such settings allow for minimizing the time of reading the values from all sensors while maintaining the appropriate measurement accuracy with a resolution of up to 4 lux, because the values obtained during the examination of airport lamps are of the order of several hundred lux. The total time of one measurement series from all 16 illuminance sensors takes about 3370 μs , what means about 297 measurements per second. During the design of the measurement matrix, 4.7 k Ω pull-up resistors on the I²C bus lines and 47 μF filter capacitors in the power supply were also taken into account. In addition, the matrix was equipped with an AS7262 visible light spectrum sensor, which is connected to a separate

4 Proposal of light sensors integration for AGL evaluation

ATmega328P microcontroller due to the relatively long measurement time, which could delay the reading of data from the illuminance sensors if they shared a controller managing them. Data from the spectrum sensor allows for the recognition of the color of the light beam and thus the selection of an appropriate correction polynomial to calculate the reading value from the illuminance sensors. Both microcontrollers communicate via a serial port with an industrial computer processing the data. A detailed diagram of the measurement matrix system is shown in Figure 136.

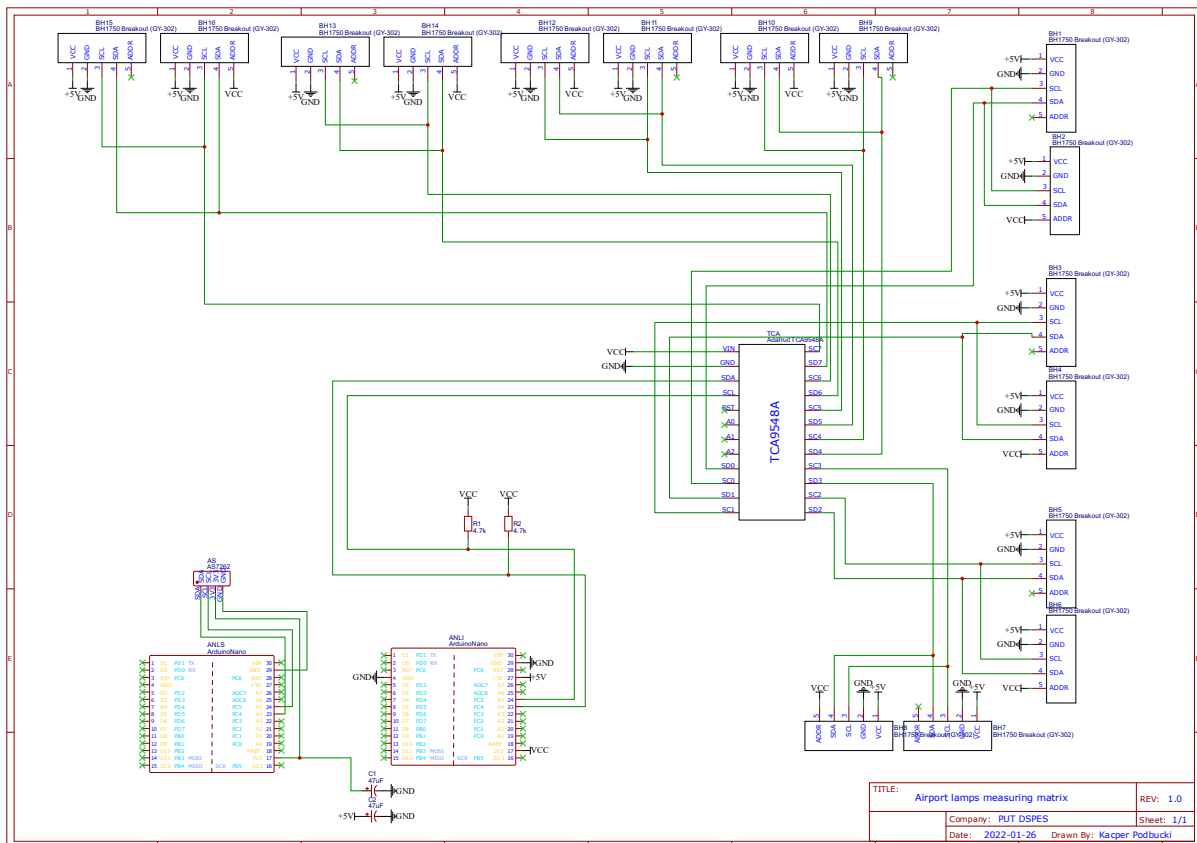


Figure 136 Airport lamps measuring matrix circuit schematic

Matrix M2 (Figure 137) with irregular alignment of illuminance sensors was tested in laboratory conditions to verify its operation. Proposed solution allowed for the examination of the value of the main beam of light as well as the horizontal angular distribution of the light spectrum emitted by the AGL.



Figure 137 Airport lamps measuring matrix with irregular alignment of illuminance sensors – designed by author

4.3.1 Evaluation of the performance of the proposed measurement matrix in AGL measurements

Laboratory tests (Figure 138) were conducted using a measurement matrix that was set precisely in accordance with the design assumptions of the measurement platform for quality testing of AGL. The operation of both new and damaged lamps as well as halogen lamps and those equipped with an LED light source was checked. The tests were carried out in a darkened room and the results presented in the graphs are an average of approx. 50 measurements for each lamp.

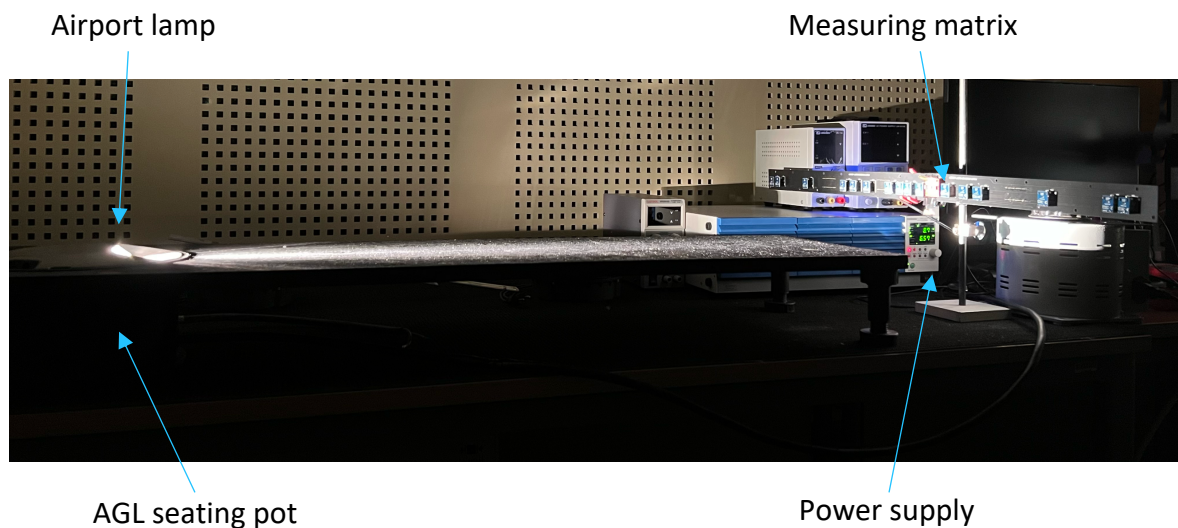


Figure 138 Laboratory experiments using measuring matrix

The first lamp tested came from the touchdown zone and was a new halogen luminaire type IDM4671 N - C TDZ (Figure 139a). This is a unidirectional luminaire equipped with a 48W light source emitting white light. The result of the inspection was the finding that, as expected, the lamp exceeded the standards prescribed by EASA (Figure 139b).

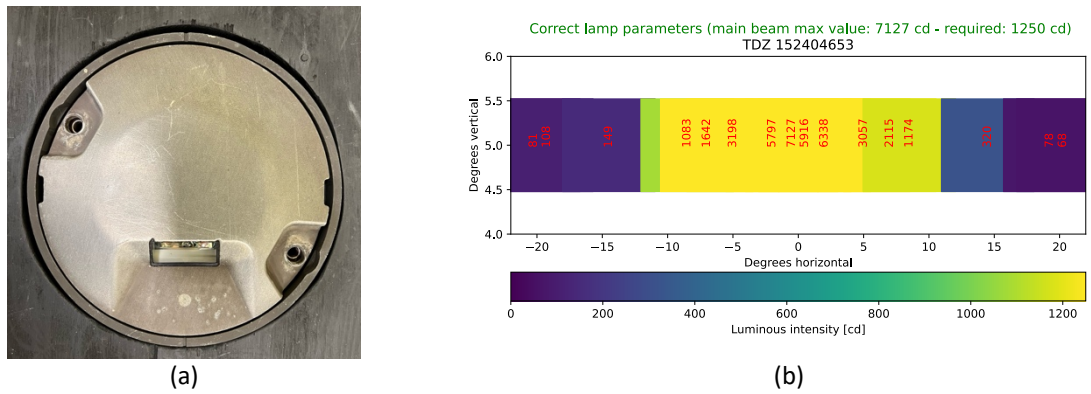


Figure 139 Measuring matrix inspection of TDZ lamp (a), luminous intensity heatmap (b)

The next lamp inspected was a refurbished bi-directional runway centre line luminaire that emits white light in both directions. It was a lamp marked IDM4582 N - C (Figure 140a) equipped with two 48W halogen bulbs each. The inspection showed that both light source no. 1 (Figure 140b) and light source no. 2 (Figure 140c) exceeded the standards required by EASA.

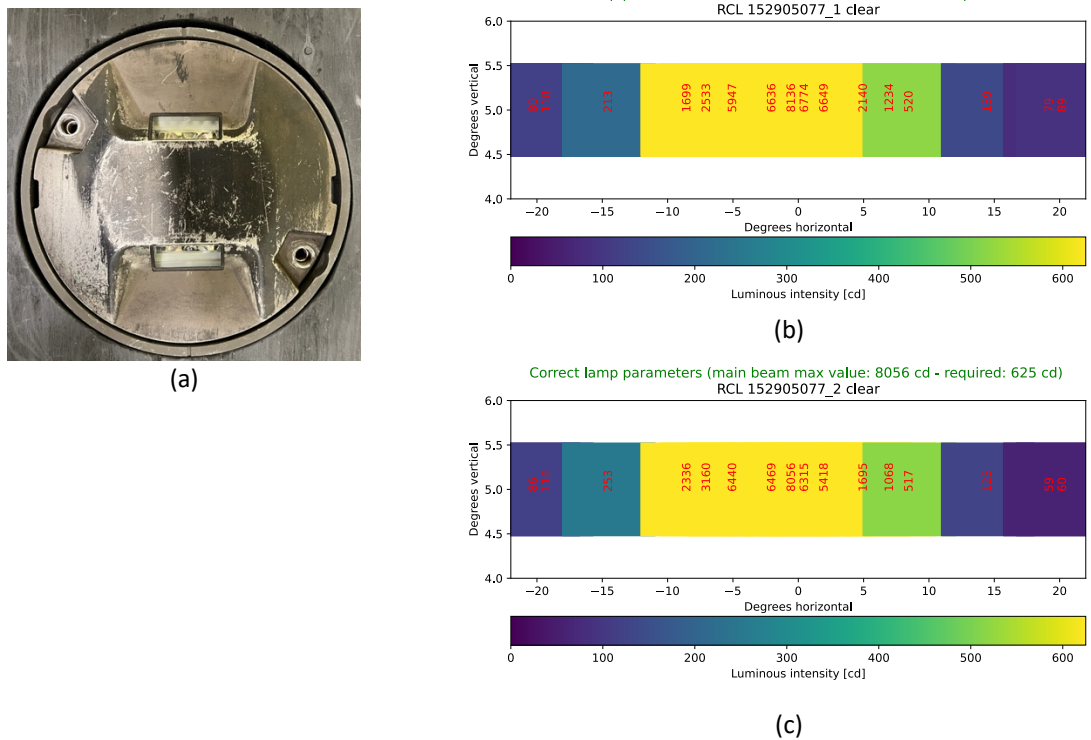


Figure 140 Measuring matrix inspection of RCL CC lamp (a), luminous intensity heatmap (b, c)

The next luminaire also came from the runway centre line, but unlike the previous one, it was a new lamp marked IDM 4582 N - C/R (Figure 141a). It is also equipped with two 48W halogen bulbs each, but thanks to the color filter placed in front of the prism, it emits white light on one side and red light on the other. Due to the fact that it was a new lamp, the inspection showed full efficiency in accordance with EASA standards for both light sources (Figure 141b and c).

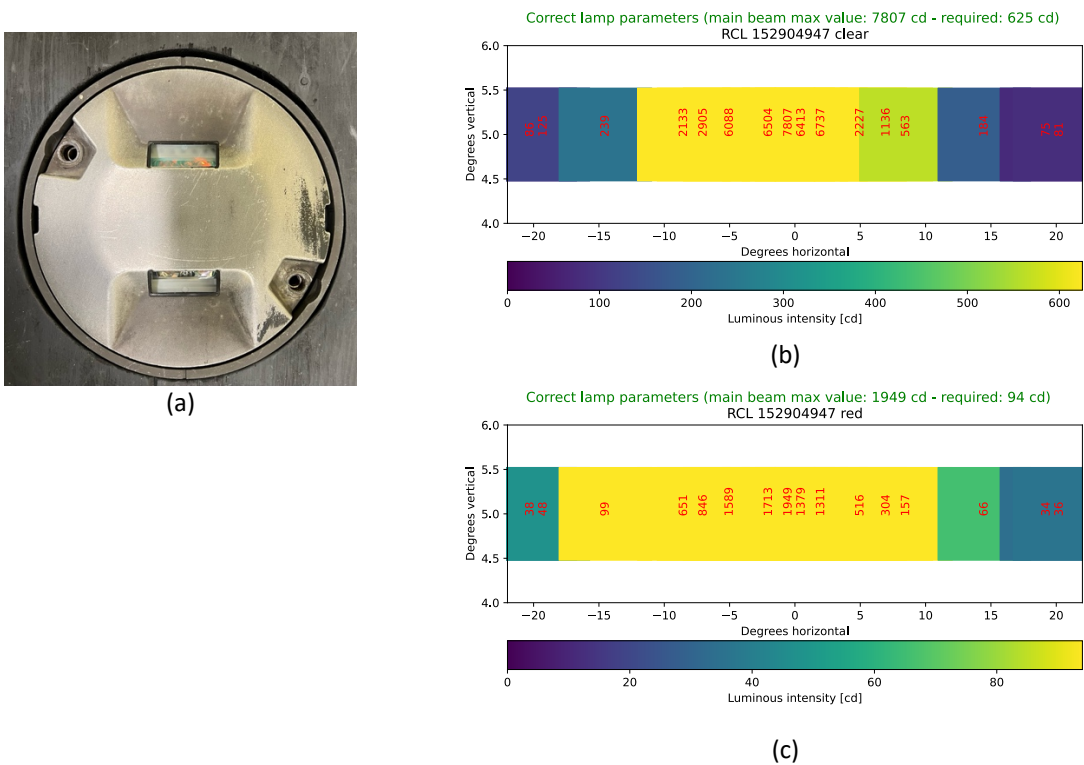


Figure 141 Measuring matrix inspection of RCL CR lamp (a), luminous intensity heatmap (b, c)

The lamp marked IDM 5582 W G/Y comes from the taxiway centerline (Figure 142a). The tested luminaire was a refurbished lamp with replaced prisms and two 40W bulbs each. Thanks to the color filters used, it emits yellow light on one side and green light on the other. After the refurbishment of critical lamp elements, the inspection showed compliance with EASA standards for both light sources (Figure 142b and c).

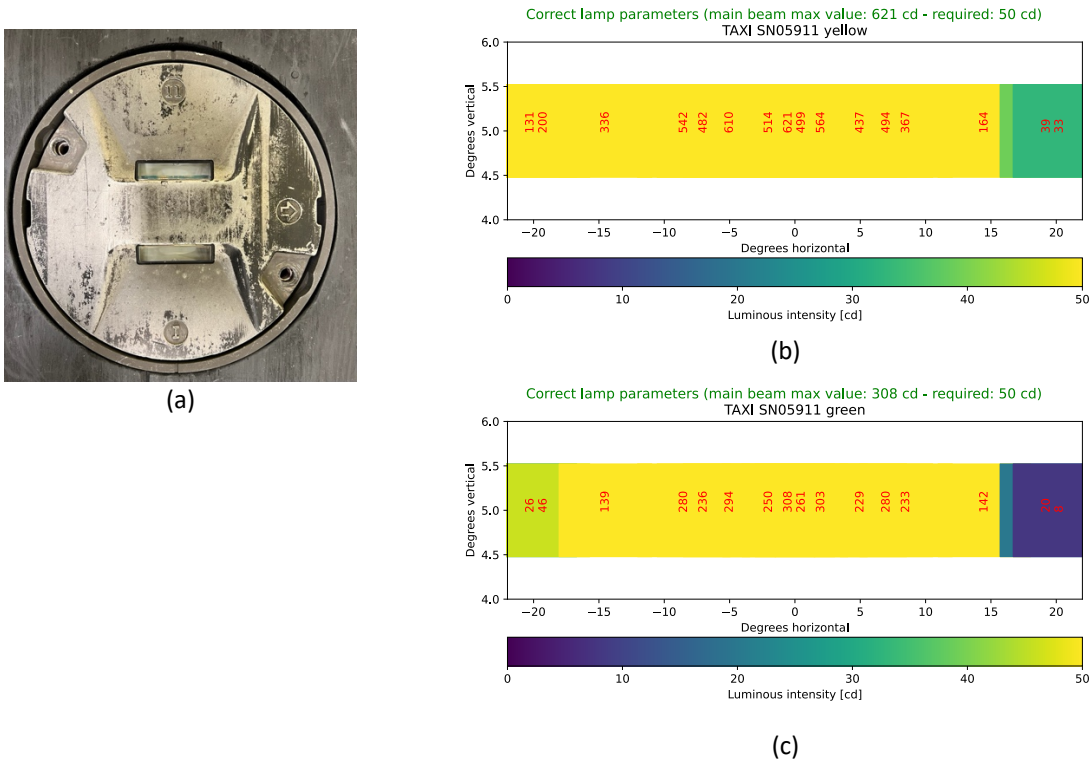


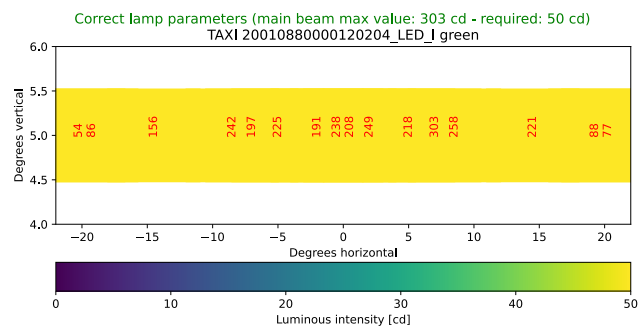
Figure 142 Measuring matrix inspection of TAXI G/Y lamp (a), luminous intensity heatmap (b, c)

Current trends promote the replacement of halogen light sources due to their durability and energy consumption. Also in the aviation industry, including AGL, manufacturers are offering more and more LED lamps. Their advantage is lower energy consumption and the life of the LEDs themselves. However, they also have disadvantages in the form of problems with the electronics controlling the diodes, the life of which is shorter, differences in the emitted color of light depending on the time of use of the lamp, and in addition, luminaires of this type require much more work to replace the light source.

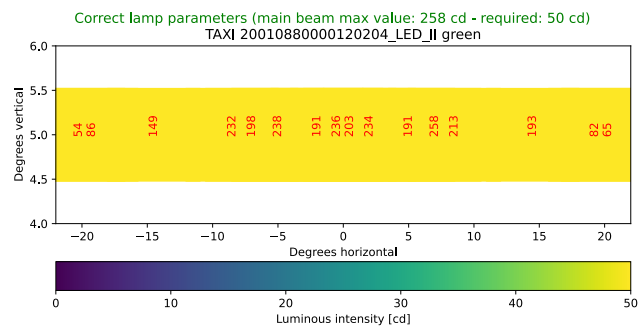
The SL-TC-I-8-B-W-S-FF-2C lamp is a new bidirectional green taxiway centerline luminaire (Figure 143a). Unlike all the previously described luminaires, the light source is of the LED type. The inspection showed that the lamp meets EASA requirements, with the difference that the horizontal beam distribution for both light sources (Figure 143b and c) is less visible due to the higher luminous intensity values.



(a)



(b)



(c)

Figure 143 Measuring matrix inspection of LED TAXI G/G lamp (a), luminous intensity heatmap (b, c)

An inspection was also carried out of the new SL-RX-I-8-U-S-S-Y-1C LED lamp, which comes from the taxiway rapid exit (Figure 144a). It emits yellow light. The inspection showed that the standards specified by EASA for this type of lamp were met. Unlike the LED taxiway centre line lamp, in this case the horizontal beam distribution is clearly visible (Figure 144b).

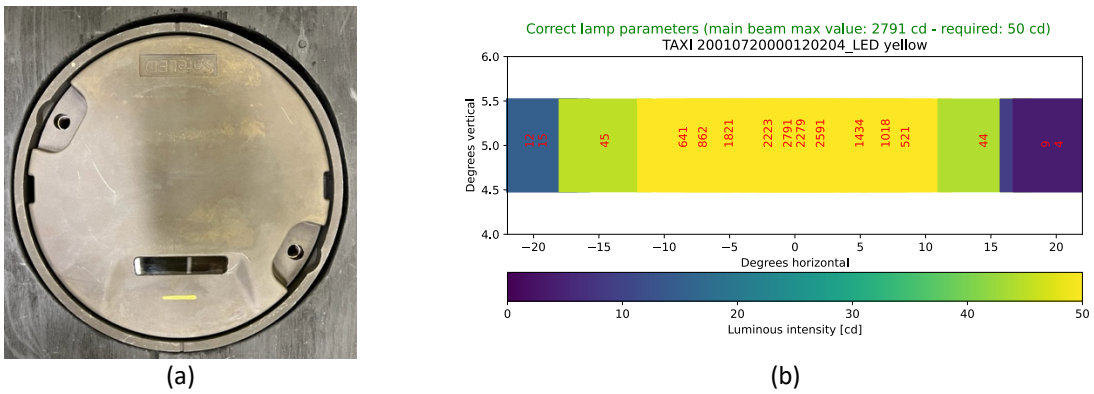


Figure 144 Measuring matrix inspection of taxiway rapid exit lamp (a), luminous intensity heatmap (b)

The next two lamps tested were damaged IDM5771 luminaires, which were destroyed during operation at the airport. Their common feature is one light source in the form of a 48W halogen bulb.

The taxiway rapid exit lamp with serial number SN07011 (Figure 145b) has an interesting damage to the prism in the form of a chip that caused a longitudinal crack in its surface (Figure 145c). Despite such extensive damage, the inspection found that it meets EASA standards regarding the luminous intensity value for yellow light, but the horizontal distribution of the beam is disturbed (Figure 145a).

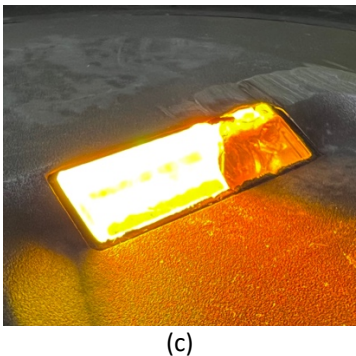
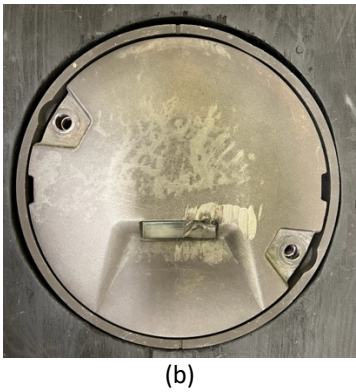
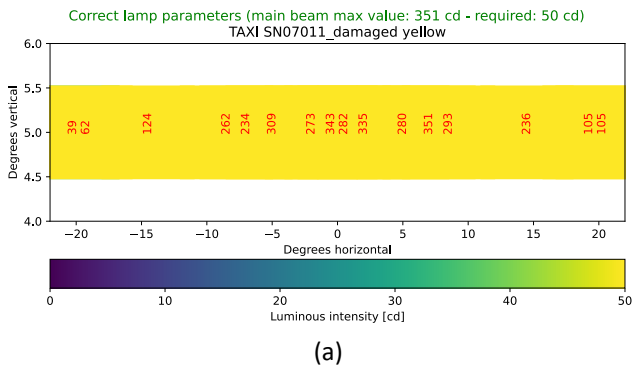
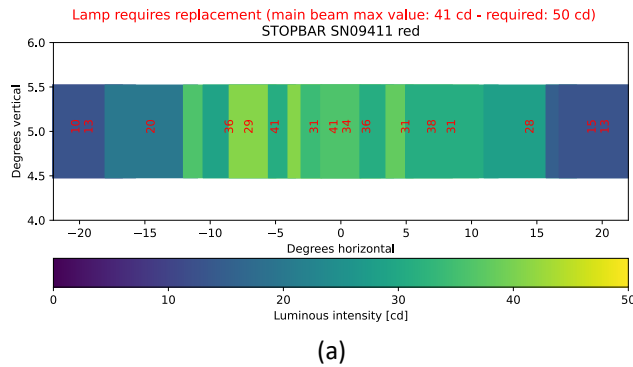


Figure 145 Measuring matrix inspection (a) of taxiway rapid exit lamp (b) with damaged prism (c)

The red stopbar lamp - serial number SN09411 (Figure 146b) was exposed to frequent operation of snow blowers during winter operations. Its prism was repeatedly scratched by their metal brushes, which led to its degradation and severe dulling (Figure 146c). As a result

of the inspection using a measuring matrix, it was proven that as a result of the damage, it does not meet EASA standards regarding the minimum luminous intensity value. However, the horizontal distribution of the beam is still visible (Figure 146a).



(b)



(c)

Figure 146 Measuring matrix inspection (a) of stopbar lamp (b) with damaged prism (c)

4.3.2 Comparison of proposed solution with reference measurements

Only some manufacturers of airport lamps provide information on the tested photometric parameters of the lamp type, not to mention the specific model. The HDK company decided to meet this trend and marks each lamp with an individual QR code under prism (Figure 147d), which, when scanned, allows to display information about the lamp and its operating instructions. This data also includes a graph of the lamp's luminous intensity distribution (Figure 147c) [245]. It can be a reference point for photometric measurements carried out using a measuring matrix. The ILA-TDZ(L)AP type touchdown zone lamp (Figure 147a) is a unidirectional luminaire emitting white light using an 18W LED light source. The inspection carried out using a measuring matrix showed similar photometric parameters to those in the manufacturer's measurements, i.e. taking into account a vertical angle of 5 degrees and the horizontal distribution of the light beam, the luminous intensity values are similar and there is a visible deviation of the main light beam slightly to the side from the 0 degree point (Figure 147a).

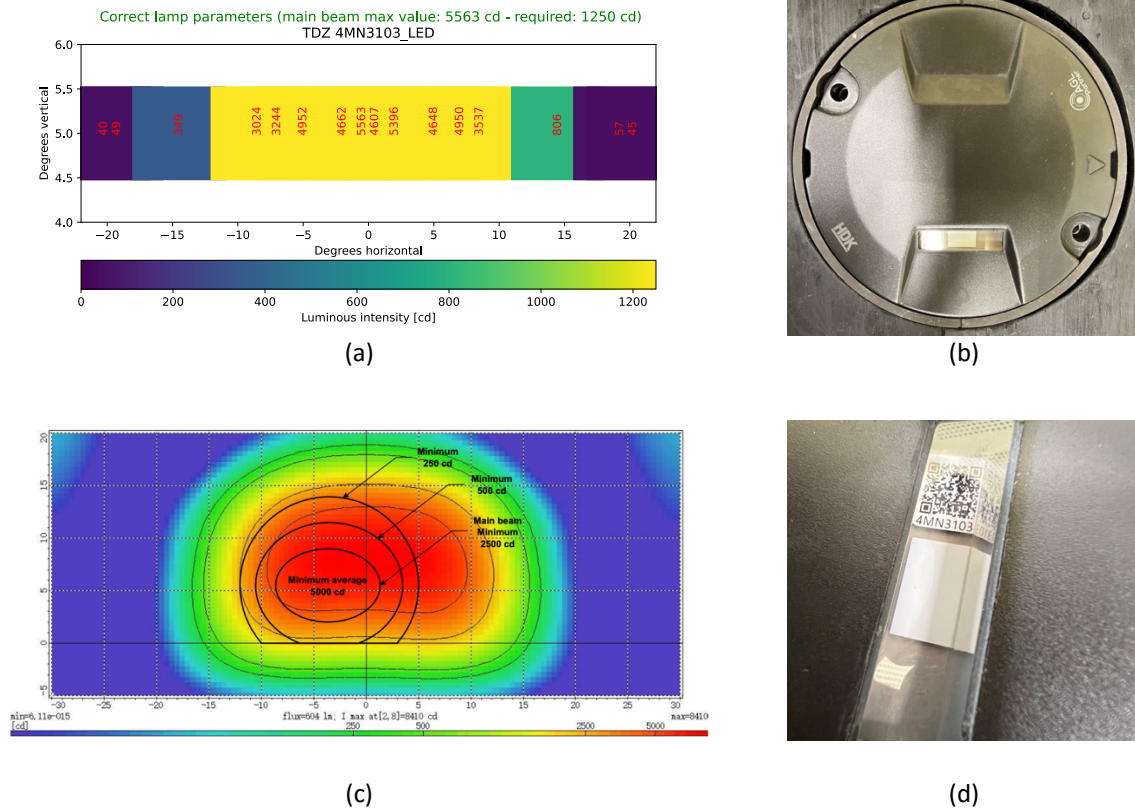


Figure 147 Measuring matrix inspection (a) of LED TDZ lamp (b) with comparison to the manufacturer's characteristic [245] (c) available under QR code placed behind the prism (d)

The experiments carried out using the proposed measuring matrix with irregular arrangement of sensors confirmed its suitability for carrying out the inspection of AGL. This specific arrangement allows determining not only the value of luminous intensity, but also the horizontal distribution of the beam. Thanks to the use of the measuring matrix, it is possible to check the correctness of photometric parameters of AGL in accordance with EASA standards.

4.4 Proposed AGL measurement platform with environment monitoring

The previously proposed techniques for improving the location determination of a mobile measuring device can be applied to the specifics of fast measurement of in-pavement AGL luminosity. In addition to the techniques studied, in this case, light multisensory integration was carried out in the form of an illuminance sensor array. The combination of these two proposals allows for the development of an advanced measurement system in the form of an improved version of the AGL measurement platform (Figure 148b).



Figure 148 Measuring platforms for AGL lamps testing: version 1 (a) and version 2 (b)

Its construction was possible thanks to the implementation of the Inkubator Innowacyjności 4.0 project. The device was developed based on special two-axle chassis, including a front steerable axle with a drawbar. The platform has a waterproof housing, inside which measurement control devices were placed. In order to minimize interference from neighboring lamps, rubber covers were mounted to the platform chassis. The construction of the device itself, as well as the method of measuring the quality of airport lamps, was submitted to the Patent Office [25] in order to establish legal protection for the proposed solution (Figure 150). The comparison of two proposed versions of measuring platforms for AGL lamps testing is listed in Table 34.

Table 34 Comparison of AGL measuring platforms main features

	AGL platform version 1	AGL platform version 2
Light sensors modules	2 modules BH1750 1 module VEML 7700	32 modules BH1750
Light color spectrum sensor	AS7262	AS7262
Main computer	Raspberry Pi 3 model B	Revolution Pi industrial computer
Localization sensors	GPS	GNSS LiDAR Camera Light sensors
User interface	Touchscreen Remote control panel	Touchscreen Remote control panel

The block diagram of internal structure of the measurement platform for testing the quality of AGL operation is shown in Figure 149. It consists of devices responsible for monitoring the environment of the measuring vehicle in the form of a GNSS module, LiDAR and a camera, the data of which are processed on Raspberry Pi 4 model B microcomputers. The measurement matrix consisting of sixteen BH1750 sensors, which transmit data via the I²C bus to the TCA9548A address translator, is managed by the ATmega328P microcontroller.

A separate microcontroller also has an AS7262 visible light spectrum sensor mounted in the measurement matrix. Data from the dedicated microcomputers and microcontrollers are processed by the Revolution Pi industrial computer powered by a battery. A touchscreen displaying the GUI is connected to it, as well as a router enabling remote use of the measurement platform control panel.

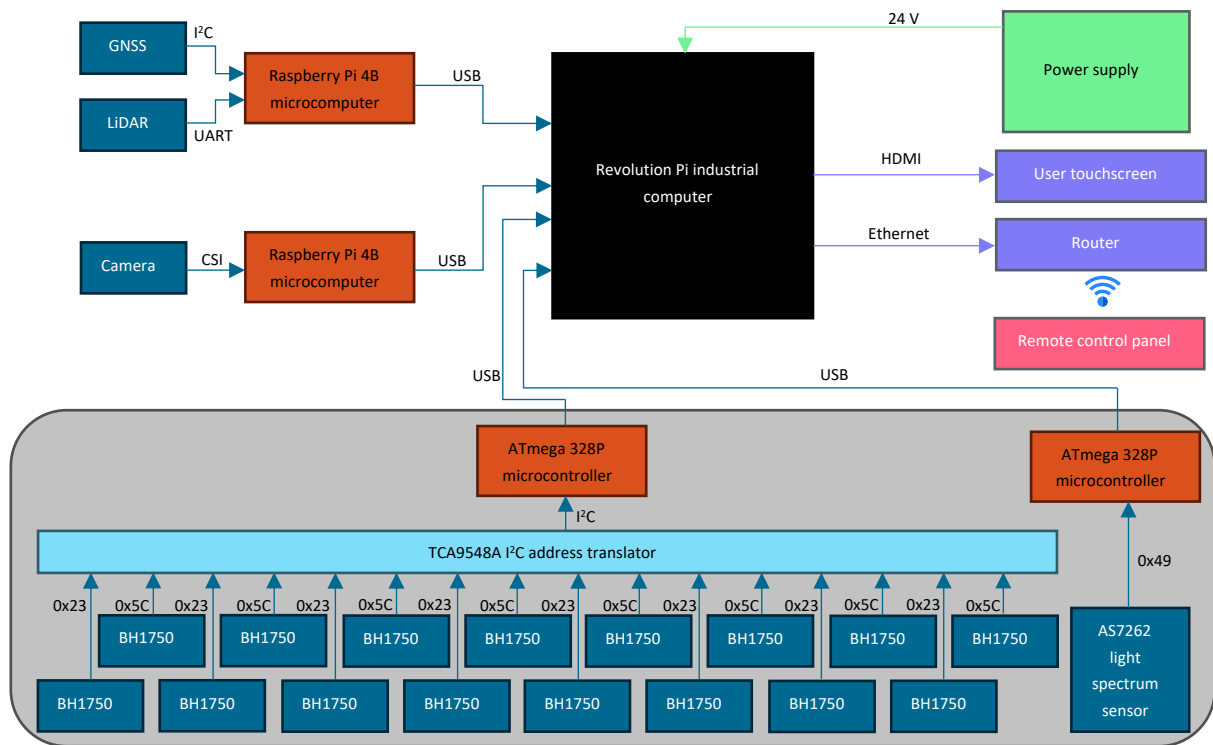



Figure 149 Measuring platform internal structure block diagram

The proposed solution for AGL testing using a measurement platform demonstrates the possibility of implementing the discussed methods of monitoring the environment in order to perform specialist measurements. The designed structure, system components and implemented data processing algorithms cover the scientific discipline of automation, electronics, electrical engineering and space technologies.



**URZĄD PATENTOWY
RZECZYPOSPOLITEJ POLSKIEJ**

al. Niepodległości 188/192
00-950 Warszawa, skr. poczt. 703
tel.: (+48) 22 579 05 55 | fax: (+48) 22 579 00 01
e-mail: kontakt@uprp.gov.pl | www.uprp.gov.pl

Kancelaria Ogólna

Warszawa, 2022-10-19

Nasz znak: POTWIERDZENIE/290118/P.442569
Wasz znak: JMP/10/22

POTWIERDZENIE

Urząd Patentowy RP stwierdza, że dnia 2022-10-19 przyjęto w formie elektronicznej wniosek o udzielenie patentu na wynalazek:

Sposób pomiaru jakości działania lamp lotniskowych oraz zestaw pomiarowy do badania jakości działania zagłębionych lamp lotniskowych

Zgłoszenie oznaczono numerem: **P.442569**
[WIPO ST 10/C PL442569]

Zgłaszający: **POLITECHNIKA POZNAŃSKA, POZNAŃ, Polska**

Dokument wystawiony automatycznie przez system teleinformatyczny UPRP.

Pouczenie:

1. Strony oraz ich przedstawiciele i pełnomocnicy mają obowiązek zawiadomić Urząd o każdej zmianie swojego adresu. W razie zaniedbania tego obowiązku doręczenie pisma pod dotychczasowym adresem ma skutek prawny (art. 41 kpa).
2. O zgłoszeniu wynalazku Urząd Patentowy dokonuje ogłoszenia niezwłocznie po upływie 18 miesięcy od daty pierwszeństwa do uzyskania patentu. Zgłaszający może w okresie 12 miesięcy od daty pierwszeństwa złożyć wniosek o dokonanie ogłoszenia w terminie wcześniejszym (art. 43 ustawy z dnia 30 czerwca 2000r. Prawo własności przemysłowej (Dz. U. z 2021 r. poz. 324).
3. W korespondencji należy powoływać się na nr P.442569.

Klauzula informacyjna:

Zgodnie z art. 13 ust. 1 i 2 Rozporządzenia Parlamentu Europejskiego i Rady (UE) 2016/679 z dnia 27 kwietnia 2016 r. w sprawie ochrony osób fizycznych w związku z przetwarzaniem danych osobowych i w sprawie swobodnego przepływu takich danych oraz uchylenia dyrektywy 95/46/WE (dalej RODO) Urząd Patentowy Rzeczypospolitej Polskiej informuje, że:

1. Administratorem Pani/Pana danych osobowych jest Urząd Patentowy Rzeczypospolitej Polskiej z siedzibą w Warszawie, adres: al. Niepodległości 188/192, 00-950 Warszawa, skrytka pocztowa 203;
2. Inspektor Ochrony Danych, dane kontaktowe: adres: al. Niepodległości 188/192, 00-950 Warszawa, tel. bezpośredni (022) 579 00 25, fax (022) 579 00 01, e-mail: iod@uprp.pl;

Figure 150 Confirmation of the patent application for the proposed solution for AGL testing

Chapter 5

Conclusions

To sum up the main achievements, own datasets were prepared, some of them in the unique conditions of the airport's restricted areas. These include a GNSS measurement dataset containing measurements from the runway and taxiways. A video dataset with a total size of 98 GB, includes recordings made at different times of day as well as in different weather conditions and seasons. The recorded materials show the view from the perspective of a car driver moving along different parts of the airport, including taxiways, runways and aprons, and the trajectory of the drive was also changed. The recordings show lit navigation lighting lamps. A dataset of measurements of photometric characteristics around navigation lighting lamps was also prepared. Their measurement was made after dismantling them from the airport as used lamps, and then they were re-measured after their maintenance. This is a unique dataset that can be used not only to determine the value of the main beam luminosity, but also the angular distribution of light. A dataset of measurement data from LiDAR in environments with a variety of arrangements was prepared in laboratory conditions.

Three different Teseo-LIV3F, NEO-6M and SIM28 modules were tested during the GNSS tests. It was verified that the localization results are better for devices using multiple satellite navigation systems, e.g. GPS and GLONASS, than for those using only one of them. The behavior of the modules in static and dynamic measurement was examined. An analysis of the size of measurement errors was carried out in relation to the number of visible satellites and the HDOP parameter. The error range before the proposed filtration was from 0 m to 80 m, and after data filtration from 0 m to 27 m, which means an improvement of 66.25%. It should be emphasized, however, that using a higher class GNSS module, the actual measurement error is about 4 m.

The LiDAR sensor module was tested in terms of its capabilities and limitations. Experimental tests were performed at different resolutions and object settings in the environment. Deliberations on the required resolution for the task of detecting edge lamps on the airport were also presented. As a result of the experiments, the RANSAC algorithm was selected using a square model, which allows for the detection of a larger number of inliers elements constituting the measurement background, in order to enable more effective detection of outliers elements being the sought edge lamps.

The proposed vision algorithm for detecting the light of navigation lamps built into airport surfaces is based on image binarization, double dilation and additional filtration based on histogram analysis. The tests were conducted in various lighting and atmospheric conditions. In the case of using standard methods for detecting light points in the image, the efficiency of correct detections was 0.83%, while false detections were 32.5%. The accuracy of the proposed algorithm was 86.09% for sunny conditions, 98.38% for cloudy conditions, 88.44% at night with the car lights on, and 91.04% without the car lights on.

An in-depth analysis of the correctness of the measurement process of photometric characteristics of AGL was carried out. In laboratory conditions, the aspect of the influence of the type of power supply of AC and DC airport lamps on the stability of light intensity measurements was examined. The measurement results obtained for the selected illuminance sensor were compared with the Sonopan L-200P luxmeter. A goniophotometer was prepared for testing the angular characteristics of airport lamps. During laboratory tests, measurements were taken for different levels of airport lamp operation and for different modes of operation of the BH1750 illuminance sensor. The measurement results were verified with the readings for the Sonopan L-200P luxmeter and a polynomial correction was proposed based on them, in order to bring the measurement results from the BH1750 module closer to the standard for different colors of light that differ in wavelength, due to its spectral characteristics. Using these converters, measurements were taken for about 500 lamps used at Poznań-Ławica airport and their re-testing after maintenance consisting in replacing bulbs and prisms.

During the research, the concept of a measuring matrix with illuminance sensors with a regular arrangement was proposed. Experiments were conducted using various I2C address translator modules in order to select the fastest solution. The final one allows for 297 measurements per second for 16 illuminance sensors. Photodiodes and illuminance sensors of various types were tested in terms of speed of operation and the concept of a proprietary sensor module based on the VTP1220FBH photodiode and ATmega328P microprocessor was proposed.

The conducted research works allow for design and construction of the measuring matrix with irregular arrangement of illuminance sensors. Their layout scheme was developed taking into account EASA and ICAO standards to cover the horizontal angular range of light of various types of AGL. A scheme was proposed and a PCB was designed. Then the matrix was built and lamp parameter tests were carried out, examining the luminous intensity of the main light beam and the horizontal light distribution for various types of built-in lamps, including new and damaged luminaires. The proposed solution was submitted to the patent office to protect intellectual property.

In summary, the solution to the problem of monitoring the environment of the measuring vehicle proposed in the doctoral thesis is an innovative contribution to the interdisciplinary issue of testing the quality of AGL in a manner supervised by operator support systems. The main conclusions from the implementation of the doctoral dissertation concern the successful realization of the research tasks. As a result of the conducted research, a multisensory system was developed that allows for effective performance of the task of conducting an accurate approach of the measuring platform over the tested lamp. Therefore, the scientific goals of this doctoral thesis have been achieved. The scientific thesis formulated in Section 1.2 has been proven.

Bibliography

- [1] A. Swief and M. El-Habrouk, "A survey of Automotive Driving Assistance Systems technologies," in *2018 International Conference on Artificial Intelligence and Data Processing (IDAP)*, 2018, pp. 1–12. doi: 10.1109/IDAP.2018.8620826.
- [2] F. Rosique, P. J. Navarro, C. Fernández, and A. Padilla, "A Systematic Review of Perception System and Simulators for Autonomous Vehicles Research," *Sensors*, vol. 19, no. 3, 2019, doi: 10.3390/s19030648.
- [3] M. Baïou, A. Mombelli, A. Quilliot, L. Adouane, and Z. Zhengze, "Algorithms for the Safe Management of Autonomous Vehicles," presented at the 2021 16th Conference on Computer Science and Intelligence Systems (FedCSIS), 2021. doi: 10.15439/2021F18.
- [4] J. Fayyad, M. A. Jaradat, D. Gruyer, and H. Najjaran, "Deep Learning Sensor Fusion for Autonomous Vehicle Perception and Localization: A Review," *Sensors*, vol. 20, no. 15, 2020, doi: 10.3390/s20154220.
- [5] D. L. Hall and J. Llinas, "An introduction to multisensor data fusion," *Proc. IEEE*, vol. 85, no. 1, pp. 6–23, 1997, doi: 10.1109/5.554205.
- [6] J. Kim, D. S. Han, and B. Senouci, "Radar and Vision Sensor Fusion for Object Detection in Autonomous Vehicle Surroundings," in *2018 Tenth International Conference on Ubiquitous and Future Networks (ICUFN)*, 2018, pp. 76–78. doi: 10.1109/ICUFN.2018.8436959.
- [7] D. J. Yeong, G. Velasco-Hernandez, J. Barry, and J. Walsh, "Sensor and Sensor Fusion Technology in Autonomous Vehicles: A Review," *Sensors*, vol. 21, no. 6, pp. 2140–2140–37, Mar. 2021, doi: <https://doi.org/10.3390/s21062140>.
- [8] S. Campbell *et al.*, "Sensor Technology in Autonomous Vehicles : A review," in *2018 29th Irish Signals and Systems Conference (ISSC)*, 2018, pp. 1–4. doi: 10.1109/ISSC.2018.8585340.
- [9] D. Jeon and H. Choi, "Multi-sensor fusion for vehicle localization in real environment," in *2015 15th International Conference on Control, Automation and Systems (ICCAS)*, 2015, pp. 411–415. doi: 10.1109/ICCAS.2015.7364949.
- [10] R. C. Luo, C.-C. Yih, and K. L. Su, "Multisensor fusion and integration: approaches, applications, and future research directions," *IEEE Sens. J.*, vol. 2, no. 2, pp. 107–119, 2002, doi: 10.1109/JSEN.2002.1000251.
- [11] V. Ankarao, V. Sowmya, and K. P. Soman, "Multi-sensor data fusion using NIHS transform and decomposition algorithms," *Multimed. Tools Appl.*, vol. 77, no. 23, pp. 30381–30402, Dec. 2018, doi: 10.1007/s11042-018-6114-2.
- [12] Z. Wang, Y. Wu, and Q. Niu, "Multi-Sensor Fusion in Automated Driving: A Survey," *IEEE Access*, vol. 8, pp. 2847–2868, Dec. 2019, doi: 10.1109/ACCESS.2019.2962554.
- [13] J. K. Hackett and M. Shah, "Multi-sensor fusion: a perspective," in *Proceedings., IEEE International Conference on Robotics and Automation*, 1990, pp. 1324–1330 vol.2. doi: 10.1109/ROBOT.1990.126184.
- [14] FB Technology, "MARC ONE Smart Robot For Airfield Maintenance." Accessed: Sep. 29, 2022. [Online]. Available: <https://www.fbtechnology.com/our-products-agl-photometric-maintenance/marc-one-agl-maintenance-robot/>
- [15] DeWiTec GmbH, "DALMAS AFL Analysis." Accessed: Sep. 29, 2022. [Online]. Available: <https://www.dewitec.de/en/airport-technology/dalmas-afl-analysis>
- [16] FB Technology, "PAC MATRIX AGL Photometric Tester (Airfield Ground Lighting)." Accessed: Sep. 29, 2022. [Online]. Available: <https://www.fbtechnology.com/our-products-agl-photometric-maintenance/agl-photometric-tester/>
- [17] J. Suder, P. Maciejewski, K. Podbucki, T. Marciniak, and A. Dąbrowski, "Platforma pomiarowa do badania jakości działania lamp lotniskowych," *Pomiary Autom. Robot. PAR*, vol. 23, no. 2/2019, pp. 5–13, 2019, doi: https://doi.org/10.14313/PAR_232/5.
- [18] J. Sun, P. Wang, Z. Qin, and H. Qiao, "Overview of camera calibration for computer vision," in *Proceeding of the 11th World Congress on Intelligent Control and Automation*, 2014, pp. 86–92. doi: 10.1109/WCICA.2014.7052692.
- [19] J. Oh, K.-S. Kim, M. Park, and S. Kim, "A Comparative Study on Camera-Radar Calibration Methods," in *2018 15th International Conference on Control, Automation, Robotics and Vision (ICARCV)*, 2018, pp. 1057–1062. doi: 10.1109/ICARCV.2018.8581329.
- [20] S. Sim, J. Sock, and K. Kwak, "Indirect Correspondence-Based Robust Extrinsic Calibration of LiDAR and Camera," *Sensors*, vol. 16, no. 6, 2016, doi: 10.3390/s16060933.
- [21] F. Castanedo, "A Review of Data Fusion Techniques," *Sci. World J.*, vol. 2013, no. 1, p. 704504, Jan. 2013, doi: 10.1155/2013/704504.

- [22] R. C. Luo and K. L. Su, "A review of high-level multisensor fusion: approaches and applications," in *Proceedings. 1999 IEEE/SICE/RSJ. International Conference on Multisensor Fusion and Integration for Intelligent Systems. MFI'99 (Cat. No.99TH8480)*, 1999, pp. 25–31. doi: 10.1109/MFI.1999.815960.
- [23] International Civil Aviation Organization, "Annex 14 to the Convention of International Civil Aviation." vol. I, Aerodrome Design and Operations, Jul. 2018.
- [24] European Union Aviation Safety Agency, "Artificial Intelligence Roadmap 2.0 Human-centric approach to AI in aviation." May 2023. Accessed: Jun. 26, 2024. [Online]. Available: <https://www.easa.europa.eu/en/downloads/137919/en>
- [25] A. Dąbrowski, T. Marciniak, K. Podbucki, and J. Suder, "Sposób pomiaru jakości działania lamp lotniskowych oraz zestaw pomiarowy do badania jakości działania zagłębionych lamp lotniskowych," P.442569, Oct. 19, 2022
- [26] K. Podbucki, T. Marciniak, and J. Suder, "Laboratory Assessment of In-Pavement Airport Lamp's Luminous Intensity Distribution," *Appl. Sci.*, vol. 13, no. 24, p. 13242, 2023, doi: <https://doi.org/10.3390/app132413242>.
- [27] K. Podbucki, J. Suder, T. Marciniak, W. Mańczak, and A. Dąbrowski, "Microprocessor-based photometric light intensity sensor for airport lamps quality testing," *Opto-Electron. Rev.*, vol. 30, no. 4, pp. e143396-1-e143396-7, 2022, doi: 10.24425/opelre.2022.143396.
- [28] K. Podbucki, "Możliwości i ograniczenia monitorowania otoczenia z wykorzystaniem czujnika LiDAR," *Przegląd Elektrotechniczny*, vol. 98, no. 1/2022, pp. 184–187, 2022, doi: 10.15199/48.2022.01.40.
- [29] K. Podbucki, J. Suder, T. Marciniak, and A. Dąbrowski, "Elektroniczna matryca pomiarowa do badania lamp lotniskowych," *Przegląd Elektrotechniczny*, vol. 97, no. 2, pp. 47–51, 2021, doi: 10.15199/48.2021.02.12.
- [30] K. Podbucki, J. Suder, T. Marciniak, and A. Dąbrowski, "Influence of power supply on airport navigation lamps photometric test accuracy," in *2023 Signal Processing: Algorithms, Architectures, Arrangements, and Applications (SPA)*, Poznan, Poland: IEEE, Sep. 2023, pp. 183–188. doi: 10.23919/SPA59660.2023.10274440.
- [31] K. Podbucki and T. Marciniak, "Camera-based light source localization for precise luminous intensity measurement of airport lamps," in *2024 Signal Processing: Algorithms, Architectures, Arrangements, and Applications (SPA)*, Poznan, Poland: IEEE, Sep. 2024, pp. 72–78. doi: 10.23919/SPA61993.2024.10715614.
- [32] J. Suder, K. Podbucki, and T. Marciniak, "Raport z pomiarów fotometrycznych zagłębionych lamp oświetlenia nawigacyjnego drogi startowej Portu Lotniczego Poznań – Ławica," Politechnika Poznańska, Poznań, r3335_2022, Aug. 2022.
- [33] J. Suder, K. Podbucki, and T. Marciniak, "Power Requirements Evaluation of Embedded Devices for Real-Time Video Line Detection," *Energies*, vol. 16, no. 18, p. 6677, Sep. 2023, doi: 10.3390/en16186677.
- [34] J. Suder, K. Podbucki, and T. Marciniak, "Chromaticity measurement of airport navigation lighting using integrated colour sensor," *Opto-Electron. Rev.*, vol. 31, no. 4, pp. e147040-1-e147040-9, 2023, doi: 10.24425/opelre.2023.147040.
- [35] T. Marciniak, K. Podbucki, and J. Suder, "Application of the Nucleo STM32 module in teaching microprocessor techniques in automatic control," *Przegląd Elektrotechniczny*, vol. 98, no. 10, pp. 245–248, Oct. 2022, doi: 10.15199/48.2022.10.55.
- [36] J. Suder, K. Podbucki, T. Marciniak, and A. Dąbrowski, "Low Complexity Lane Detection Methods for Light Photometry System," *Electronics*, vol. 10, no. 14, pp. 1665-1-1665-22, Jul. 2021, doi: 10.3390/electronics10141665.
- [37] J. Suder, K. Podbucki, T. Marciniak, and A. Dąbrowski, "Spectrum sensors for detecting type of airport lamps in a light photometry system. Opto-Electronics Review," *Opto-Electron. Rev.*, vol. 29, no. 4, pp. 133–140, 2021, doi: <https://doi.org/10.24425/opelre.2021.139383>.
- [38] K. Podbucki and T. Marciniak, "Aspects of autonomous drive control using NVIDIA Jetson Nano microcomputer," presented at the 17th Conference on Computer Science and Intelligence Systems, Sep. 2022, pp. 117–120. doi: 10.15439/2022F89.
- [39] K. Podbucki, J. Suder, T. Marciniak, and A. Dąbrowski, "Evaluation of Embedded Devices for Real-Time Video Lane Detection," in *2022 29th International Conference on Mixed Design of Integrated Circuits and System (MIXDES)*, Wrocław, Poland: IEEE, Jun. 2022, pp. 187–191. doi: 10.23919/MIXDES55591.2022.9838167.
- [40] J. Suder, K. Podbucki, T. Marciniak, and A. Dąbrowski, "Intelligent vision system for quality classification of airport lamp prisms," in *2022 Signal Processing: Algorithms, Architectures, Arrangements, and Applications (SPA)*, Poznan, Poland: IEEE, Sep. 2022, pp. 151–154. doi: 10.23919/SPA53010.2022.9927908.
- [41] J. Suder, T. Marciniak, K. Podbucki, and A. Dąbrowski, "Real-time density maps generation of moving

- objects using embedded systems,” in *2022 International Symposium ELMAR*, Zadar, Croatia: IEEE, Sep. 2022, pp. 179–184. doi: 10.1109/ELMAR55880.2022.9899807.
- [42] T. Marciniak, K. Podbucki, J. Suder, and A. Dąbrowski, “Analysis of Digital Filtering with the Use of STM32 Family Microcontrollers,” in *Advanced, Contemporary Control*, vol. 1196, A. Bartoszewicz, J. Kabziński, and J. Kacprzyk, Eds., in *Proceedings of KKA 2020 - The 20th Polish Control Conference*, Łódź, Poland, 2020, vol. 1196, Cham: Springer International Publishing, 2020, pp. 287–295. doi: 10.1007/978-3-030-50936-1_25.
- [43] K. Podbucki, J. Suder, T. Marciniak, and A. Dąbrowski, “CCTV based system for detection of anti-virus masks,” in *2020 Signal Processing: Algorithms, Architectures, Arrangements, and Applications (SPA)*, Poznan, Poland: IEEE, Sep. 2020, pp. 87–91. doi: 10.23919/SPA50552.2020.9241303.
- [44] M. L. Fung, M. Z. Q. Chen, and Y. H. Chen, “Sensor fusion: A review of methods and applications,” presented at the 29th Chinese Control And Decision Conference (CCDC), Chongqing, China, 2017, pp. 3853–3860. doi: 10.1109/CCDC.2017.7979175.
- [45] D. Lahat, T. Adali, and C. Jutten, “Multimodal Data Fusion: An Overview of Methods, Challenges, and Prospects,” *Proc. IEEE*, vol. 103, no. 9, pp. 1449–1477, 2015, doi: 10.1109/JPROC.2015.2460697.
- [46] D. L. Hall and S. A. H. McMullen, *Mathematical Techniques in Multisensor Data Fusion*. USA: Atrech House, 2004.
- [47] M. E. Liggins, D. L. Hall, and J. Llinas, *Handbook of Multisensor Data Fusion Theory and Practice*, Second Edition. in *The Electrical Engineering and Applied Signal Processing Series*. CRC Press, 2009.
- [48] S. Saponara, “Sensing and Connection Systems for Assisted and Autonomous Driving and Unmanned Vehicles,” *Sensors*, vol. 18, no. 7, p. 1999, 2018, doi: <https://doi.org/10.3390/s18071999>.
- [49] X. Jia, Z. Hu, and H. Guan, “A new multi-sensor platform for adaptive driving assistance system (ADAS),” presented at the 9th World Congress on Intelligent Control and Automation, Taipei, Taiwan, 2011, pp. 1224–1230. doi: 10.1109/WCICA.2011.5970711.
- [50] H. Carvalho, A. Vale, R. Marques, R. Ventura, Y. Brouwer, and B. Gonçalves, “Remote inspection with multi-copters, radiological sensors and SLAM techniques,” presented at the EPJ Web Conf., Uppsala, Sweden, 2018, p. 7014.
- [51] M. Nakagawa *et al.*, “SEAMLESS NAVIGATION USING VARIOUS SENSORS: AN OVERVIEW OF THE SEAMLESS NAVIGATION CAMPAIGN,” *Int. Arch. Photogramm. Remote Sens. Spat. Inf. Sci.*, vol. XXXIX-B4, pp. 35–38, 2012, doi: 10.5194/isprsarchives-XXXIX-B4-35-2012.
- [52] Y. Xia, “Sensor Fusion: The Source of AI’s Foresight,” *ElectronicDesign*. Accessed: Jul. 01, 2024. [Online]. Available: <https://www.electronicdesign.com/markets/robotics/article/55056786/amd-how-sensor-fusion-mimics-the-human-brain-to-make-robotics-safer>
- [53] Y. Chen and Q. Zhao, “A Novel Square-Root Cubature Information Weighted Consensus Filter Algorithm for Multi-Target Tracking in Distributed Camera Networks,” *Sensors*, vol. 15, no. 5, pp. 10526–10546, 2015, doi: 10.3390/s150510526.
- [54] G. Hernández-Peñaloza, A. Belmonte-Hernández, M. Quintana, and F. Álvarez, “A Multi-Sensor Fusion Scheme to Increase Life Autonomy of Elderly People With Cognitive Problems,” *IEEE Access*, vol. 6, pp. 12775–12789, 2018, doi: 10.1109/ACCESS.2017.2735809.
- [55] X. Mao, W. Li, C. Lei, J. Jin, F. Duan, and S. Chen, “A Brain–Robot Interaction System by Fusing Human and Machine Intelligence,” *IEEE Trans. Neural Syst. Rehabil. Eng.*, vol. 27, no. 3, pp. 533–542, 2019, doi: 10.1109/TNSRE.2019.2897323.
- [56] J. Ma, P. Huang, and X. Xu, “A coordinated control strategy for rotating motion of the Hub-Spoke Tethered Space Robot Formation System,” in *The 26th Chinese Control and Decision Conference (2014 CCDC)*, 2014, pp. 4628–4633. doi: 10.1109/CCDC.2014.6852999.
- [57] L. Song and R. Yan, “Bearing fault diagnosis based on Cluster-contraction Stage-wise Orthogonal-Matching-Pursuit,” *Measurement*, vol. 140, pp. 240–253, 2019, doi: <https://doi.org/10.1016/j.measurement.2019.03.061>.
- [58] S. Siachalou, G. Mallinis, and M. Tsakiri-Strati, “A Hidden Markov Models Approach for Crop Classification: Linking Crop Phenology to Time Series of Multi-Sensor Remote Sensing Data,” *Remote Sens.*, vol. 7, no. 4, pp. 3633–3650, 2015, doi: 10.3390/rs70403633.
- [59] J.-P. Giacalone, L. Bourgeois, and A. Ancora, “Challenges in aggregation of heterogeneous sensors for Autonomous Driving Systems,” in *2019 IEEE Sensors Applications Symposium (SAS)*, 2019, pp. 1–5. doi: 10.1109/SAS.2019.8706005.
- [60] S. Shafer, A. Stentz, and C. Thorpe, “An architecture for sensor fusion in a mobile robot,” in *Proceedings. 1986 IEEE International Conference on Robotics and Automation*, 1986, pp. 2002–2011. doi: 10.1109/ROBOT.1986.1087440.
- [61] “Multiple Sensor Fusion for Detection, Classification and Tracking of Moving Objects in Driving

- Environments," Université de Grenoble, Grenoble, France, 2014.
- [62] J. Vargas, S. Alsweiss, O. Toker, R. Razdan, and J. Santos, "An Overview of Autonomous Vehicles Sensors and Their Vulnerability to Weather Conditions," *Sensors*, vol. 21, no. 16, p. 5397, Aug. 2021, doi: 10.3390/s21165397.
 - [63] B. S. Jahromi, T. Tulabandhula, and S. Cetin, "Real-Time Hybrid Multi-Sensor Fusion Framework for Perception in Autonomous Vehicles," *Sensors*, vol. 19, no. 20, pp. 4357-1-4357-23, Oct. 2019, doi: <https://doi.org/10.3390/s19204357>.
 - [64] K. Sozański, *Digital Signal Processing in Power Electronics Control Circuits*, 2nd ed. in Power Systems Ser. London: Springer London, Limited, 2017.
 - [65] P. Kolar, P. Benavidez, and M. Jamshidi, "Survey of Datafusion Techniques for Laser and Vision Based Sensor Integration for Autonomous Navigation," *Sensors*, vol. 20, no. 8, 2020, doi: 10.3390/s20082180.
 - [66] R. B. Langley, P. J. G. Teunissen, and O. Montenbruck, "Introduction to GNSS," in *Springer Handbook of Global Navigation Satellite Systems*, P. J. G. Teunissen and O. Montenbruck, Eds., Cham: Springer International Publishing, 2017, pp. 3–23. doi: 10.1007/978-3-319-42928-1_1.
 - [67] S. Royo and M. Ballesta-Garcia, "An Overview of Lidar Imaging Systems for Autonomous Vehicles," *Appl. Sci.*, vol. 9, no. 19, pp. 4093-1-4093-37, Sep. 2019, doi: <https://doi.org/10.3390/app9194093>.
 - [68] A. Eitel, J. T. Springenberg, L. Spinello, M. A. Riedmiller, and W. Burgard, "Multimodal deep learning for robust RGB-D object recognition," *2015 IEEE/RSJ Int. Conf. Intell. Robots Syst. IROS*, pp. 681–687, 2015.
 - [69] L. Xiao, R. Wang, B. Dai, Y. Fang, D. Liu, and T. Wu, "Hybrid conditional random field based camera-LIDAR fusion for road detection," *Inf. Sci.*, vol. 432, pp. 543–558, 2018, doi: <https://doi.org/10.1016/j.ins.2017.04.048>.
 - [70] L. Xiao, B. Dai, D. Liu, T. Hu, and T. Wu, "CRF based road detection with multi-sensor fusion," in *2015 IEEE Intelligent Vehicles Symposium (IV)*, 2015, pp. 192–198. doi: 10.1109/IVS.2015.7225685.
 - [71] A. Broggi, "Robust real-time lane and road detection in critical shadow conditions," in *Proceedings of International Symposium on Computer Vision - ISCV*, 1995, pp. 353–358. doi: 10.1109/ISCV.1995.477027.
 - [72] M. Teichmann, M. Weber, M. Zöllner, R. Cipolla, and R. Urtasun, "MultiNet: Real-time Joint Semantic Reasoning for Autonomous Driving," in *2018 IEEE Intelligent Vehicles Symposium (IV)*, 2018, pp. 1013–1020. doi: 10.1109/IVS.2018.8500504.
 - [73] V. John *et al.*, "Sensor Fusion of Intensity and Depth Cues using the ChiNet for Semantic Segmentation of Road Scenes," in *2018 IEEE Intelligent Vehicles Symposium (IV)*, 2018, pp. 585–590. doi: 10.1109/IVS.2018.8500476.
 - [74] N. S. V. R. R. Brooks and S. S. Iyengar, "Resolution of Contradictory Sensor Data," *Intell. Autom. Soft Comput.*, vol. 3, no. 3, pp. 287–299, 1997, doi: 10.1080/10798587.1997.10750709.
 - [75] K. Banerjee, D. Notz, J. Windelen, S. Gavarraju, and M. He, "Online Camera LiDAR Fusion and Object Detection on Hybrid Data for Autonomous Driving," in *2018 IEEE Intelligent Vehicles Symposium (IV)*, 2018, pp. 1632–1638. doi: 10.1109/IVS.2018.8500699.
 - [76] J. Elfring, R. Appeldoorn, S. Van den Dries, and M. Kwakkernaat, "Effective World Modeling: Multisensor Data Fusion Methodology for Automated Driving," *Sensors*, vol. 16, no. 10, 2016, doi: 10.3390/s16101668.
 - [77] N. Floudas, A. Polychronopoulos, O. Aycard, J. Burlet, and M. Ahrholdt, "High Level Sensor Data Fusion Approaches For Object Recognition In Road Environment," in *2007 IEEE Intelligent Vehicles Symposium*, 2007, pp. 136–141. doi: 10.1109/IVS.2007.4290104.
 - [78] S. Kim, W.-J. Song, and S.-H. Kim, "Double Weight-Based SAR and Infrared Sensor Fusion for Automatic Ground Target Recognition with Deep Learning," *Remote Sens.*, vol. 10, no. 1, 2018, doi: 10.3390/rs10010072.
 - [79] D. Roggen, G. Tröster, and A. Bulling, "Signal processing technologies for activity-aware smart textiles," in *Multidisciplinary Know-How for Smart-Textiles Developers*, T. Kirstein, Ed., in Woodhead Publishing Series in Textiles, Woodhead Publishing, 2013, pp. 329–365. doi: <https://doi.org/10.1533/9780857093530.2.329>.
 - [80] P. H. Foo and G.-W. Ng, "High-level information fusion: An overview," *J. Adv. Inf. Fusion*, vol. 8, pp. 33–72, Jun. 2013.
 - [81] E. Waltz and J. Llinas, *Multisensor Data Fusion*, vol. 685. Boston, MA, USA: Artech House, 1990.
 - [82] P. Grossmann, "Multisensor data fusion," *GEC J. Technol.*, vol. 15, no. 1, pp. 27–37, 1998.
 - [83] E. Bosse, J. Roy, and D. Grenier, "Data fusion concepts applied to a suite of dissimilar sensors," in *Proceedings of 1996 Canadian Conference on Electrical and Computer Engineering*, 1996, pp. 692–695 vol.2. doi: 10.1109/CCECE.1996.548247.
 - [84] S. Cording, "Guide to Sensor Fusion Approaches and How to Use Them." Mouser Electronics White Paper.
 - [85] F. Castanedo, J. Garcia, M. A. Patricio, and J. M. Molina, "Analysis of distributed fusion alternatives in

- coordinated vision agents,” in *2008 11th International Conference on Information Fusion*, 2008, pp. 1–6.
- [86] B. V. Dasarathy, “Sensor fusion potential exploitation-innovative architectures and illustrative applications,” *Proc. IEEE*, vol. 85, no. 1, pp. 24–38, 1997, doi: 10.1109/5.554206.
- [87] R. Brena, A. Aguilera, L. Trejo, E. Molino-Minero-Re, and O. Mayora, “Choosing the Best Sensor Fusion Method: A Machine-Learning Approach,” *Sensors*, vol. 20, no. 8, pp. 2350–1–2350–22, 2020, doi: <https://doi.org/10.3390/s20082350>.
- [88] X. Liu and O. Baiocchi, “A comparison of the definitions for smart sensors, smart objects and Things in IoT,” in *2016 IEEE 7th Annual Information Technology, Electronics and Mobile Communication Conference (IEMCON)*, 2016, pp. 1–4. doi: 10.1109/IEMCON.2016.7746311.
- [89] G. Hope, “Volkswagen promises hands-free vans on the road by 2025.” Accessed: May 24, 2021. [Online]. Available: https://aibusiness.com/document.asp?doc_id=769485&utm_source=infront&utm_medium=newsletter&utm_campaign=vw&utm_term=44330&utm_content=TAI2256&tracker_id=TAI2256&fbclid=IwAR1hlb8K42etZKXkpwozo3cJFNclnDFvJmC8zal3uonyt0etHRooSn9HSUQ
- [90] T. Shimizu and K. Kobayashi, “Development of a Person-Searching Algorithm Using an Omnidirectional Camera and LiDAR for the Tsukuba Challenge,” in *2018 57th Annual Conference of the Society of Instrument and Control Engineers of Japan (SICE)*, 2018, pp. 810–815. doi: 10.23919/SICE.2018.8492678.
- [91] G. Reina, A. Milella, and R. Rouveure, “Traversability analysis for off-road vehicles using stereo and radar data,” in *2015 IEEE International Conference on Industrial Technology (ICIT)*, 2015, pp. 540–546. doi: 10.1109/ICIT.2015.7125155.
- [92] J. Steinbaeck, C. Steger, G. Holweg, and N. Druml, “Design of a Low-Level Radar and Time-of-Flight Sensor Fusion Framework,” in *2018 21st Euromicro Conference on Digital System Design (DSD)*, 2018, pp. 268–275. doi: 10.1109/DSD.2018.00056.
- [93] P. Rotter, M. Klemiato, and P. Skruch, “Automatic Calibration of a LiDAR–Camera System Based on Instance Segmentation,” *Remote Sens.*, vol. 14, no. 11, p. 2531, May 2022, doi: 10.3390/rs14112531.
- [94] M. Caputo, K. Denker, B. Dums, G. Umlauf, H. Konstanz, and Germany, “3D Hand Gesture Recognition Based on Sensor Fusion of Commodity Hardware,” *Mensch Comput*, vol. 2012, Jan. 2012.
- [95] D. De Silva, J. Roche, and A. Kondo, “Fusion of LiDAR and Camera Sensor Data for Environment Sensing in Driverless Vehicles,” Oct. 2017.
- [96] N. Rao, “A Fusion Method That Performs Better Than Best Sensor,” Aug. 1999.
- [97] A. Rövid and V. Remeli, “Towards Raw Sensor Fusion in 3D Object Detection,” in *2019 IEEE 17th World Symposium on Applied Machine Intelligence and Informatics (SAMII)*, 2019, pp. 293–298. doi: 10.1109/SAMII.2019.8782779.
- [98] M. Pollach, F. Schiegg, and A. Knoll, “Low Latency And Low-Level Sensor Fusion For Automotive Use-Cases,” presented at the 2020 IEEE International Conference on Robotics and Automation (ICRA), Paris, France: IEEE, Sep. 2020, pp. 6780–6786. doi: 10.1109/ICRA40945.2020.9196717.
- [99] Y. K. Abdelmohsen, “Camera - LIDAR Detection Fusion,” Bachelor thesis, German University in Cairo, Egypt, 2020. Accessed: Jan. 24, 2024. [Online]. Available: https://www.researchgate.net/publication/339630757_Camera-LIDAR_Detection_Fusion
- [100] S. Thrun, “Particle Filters in Robotics,” presented at the Proceedings of the 17th Annual Conference on Uncertainty in AI (UAI), Edmonton, AB, Canada, Oct. 2002.
- [101] B. Wu and R. Nevatia, “Detection of multiple, partially occluded humans in a single image by Bayesian combination of edgelet part detectors,” in *Tenth IEEE International Conference on Computer Vision (ICCV’05) Volume 1*, 2005, pp. 90–97 Vol. 1. doi: 10.1109/ICCV.2005.74.
- [102] J. Borenstein and Y. Koren, “Obstacle avoidance with ultrasonic sensors,” *IEEE J. Robot. Autom.*, vol. 4, no. 2, pp. 213–218, 1988, doi: 10.1109/56.2085.
- [103] P. F. Felzenszwalb, R. B. Girshick, D. McAllester, and D. Ramanan, “Object Detection with Discriminatively Trained Part-Based Models,” *IEEE Trans. Pattern Anal. Mach. Intell.*, vol. 32, no. 9, pp. 1627–1645, 2010, doi: 10.1109/TPAMI.2009.167.
- [104] W. Klembowski, A. Kawalec, and W. Wizner, “Critical views on present passive radars performance as compared with that of active radars,” in *2013 14th International Radar Symposium (IRS)*, 2013, pp. 131–135.
- [105] International Civil Aviation Organization, “Annex 10 to the Convention of International Civil Aviation.” vol. I, Radio Navigation Aids, Jul. 17, 2007.
- [106] P. Groves, *Principles of GNSS, Inertial, and Multisensor Integrated Navigation Systems, Second Edition*, Second Edition. Artech House, 2013.
- [107] A. Dorsey, W. Marquis, P. Fyfe, E. Kaplan, and L. Wiederholt, “GPS system segments,” *Underst. GPS-Princ. Appl.*, Jan. 2006.

- [108] G. Wübbena, M. Schmitz, and A. Bagge, "PPP-RTK: Precise Point Positioning Using State-Space Representation in RTK Networks," Sep. 2005.
- [109] L. Chen, G. Zhou, G. Chen, W. Sun, and L. Pan, "Signal-in-Space and Positioning Performance of BDS Open Augmentation Service," *Math. Probl. Eng.*, vol. 2022, pp. 1–11, Apr. 2022, doi: 10.1155/2022/1112646.
- [110] D. Odijk and L. Wanninger, "Differential Positioning," in *Springer Handbook of Global Navigation Satellite Systems*, P. J. G. Teunissen and O. Montenbruck, Eds., Cham: Springer International Publishing, 2017, pp. 753–780. doi: 10.1007/978-3-319-42928-1_26.
- [111] D. Weng, S. Ji, Y. Lu, W. Chen, and Z. Li, "Improving DGNSS Performance through the Use of Network RTK Corrections," *Remote Sens.*, vol. 13, no. 9, 2021, doi: 10.3390/rs13091621.
- [112] L. Chen, F. Zheng, X. Gong, and X. Jiang, "GNSS High-Precision Augmentation for Autonomous Vehicles: Requirements, Solution, and Technical Challenges," *Remote Sens.*, vol. 15, no. 6, 2023, doi: 10.3390/rs15061623.
- [113] H. Liu, H. Darabi, P. Banerjee, and J. Liu, "Survey of Wireless Indoor Positioning Techniques and Systems," *IEEE Trans. Syst. Man Cybern. Part C Appl. Rev.*, vol. 37, no. 6, pp. 1067–1080, 2007, doi: 10.1109/TSMCC.2007.905750.
- [114] A. Santra et al., "Augmentation of GNSS utility by IRNSS/NavIC constellation over the Indian region," *Adv. Space Res.*, vol. 63, no. 9, pp. 2995–3008, 2019, doi: <https://doi.org/10.1016/j.asr.2018.04.020>.
- [115] N. Joubert, T. G. R. Reid, and F. Noble, "Developments in Modern GNSS and Its Impact on Autonomous Vehicle Architectures," in *2020 IEEE Intelligent Vehicles Symposium (IV)*, 2020, pp. 2029–2036. doi: 10.1109/IV47402.2020.9304840.
- [116] M. Chen, S. Yang, X. Yi, and D. Wu, "Real-time 3D mapping using a 2D laser scanner and IMU-aided visual SLAM," in *2017 IEEE International Conference on Real-time Computing and Robotics (RCAR)*, 2017, pp. 297–302. doi: 10.1109/RCAR.2017.8311877.
- [117] S. B. Hong, C. M. Kang, S.-H. Lee, and C. C. Chung, "Multi-rate vehicle side slip angle estimation using low-cost GPS/IMU," in *2017 17th International Conference on Control, Automation and Systems (ICCAS)*, 2017, pp. 35–40. doi: 10.23919/ICCAS.2017.8204419.
- [118] Wahyudi, M. S. Listiyana, Sudjadi, and Ngatelan, "Tracking Object based on GPS and IMU Sensor," in *2018 5th International Conference on Information Technology, Computer, and Electrical Engineering (ICITACEE)*, 2018, pp. 214–218. doi: 10.1109/ICITACEE.2018.8576928.
- [119] Z. Zhang, H. Wang, and W. Chen, "A real-time visual-inertial mapping and localization method by fusing unstable GPS," in *2018 13th World Congress on Intelligent Control and Automation (WCICA)*, 2018, pp. 1397–1402. doi: 10.1109/WCICA.2018.8630513.
- [120] T. Frey, "Driverless Highways: Creating Cars That Talk to the Roads," *J. Environ. Health*, vol. 75, no. 5, pp. 38–40, 2012.
- [121] F. O. Flemisch, K. Bengler, H. Bubb, H. Winner, and R. Bruder, "Towards cooperative guidance and control of highly automated vehicles: H-Mode and Conduct-by-Wire," *Ergonomics*, vol. 57, no. 3, pp. 343–360, Mar. 2014, doi: 10.1080/00140139.2013.869355.
- [122] J. Zidan, E. I. Adegoke, E. Kampert, S. A. Birrell, C. R. Ford, and M. D. Higgins, "GNSS Vulnerabilities and Existing Solutions: A Review of the Literature," *IEEE Access*, vol. 9, pp. 153960–153976, 2021, doi: 10.1109/ACCESS.2020.2973759.
- [123] U. Lee, J. Jung, S. Jung, and D. H. Shim, "Development of a self-driving car that can handle the adverse weather," *Int. J. Automot. Technol.*, vol. 19, no. 1, pp. 191–197, Feb. 2018, doi: 10.1007/s12239-018-0018-z.
- [124] A. Mukhtar, L. Xia, and T. B. Tang, "Vehicle Detection Techniques for Collision Avoidance Systems: A Review," *IEEE Trans. Intell. Transp. Syst.*, vol. 16, no. 5, pp. 2318–2338, 2015, doi: 10.1109/TITS.2015.2409109.
- [125] J. Marais, J. Beugin, and M. Berbineau, "A Survey of GNSS-Based Research and Developments for the European Railway Signaling," *IEEE Trans. Intell. Transp. Syst.*, vol. 18, no. 10, pp. 2602–2618, 2017, doi: 10.1109/TITS.2017.2658179.
- [126] C. J. Hegarty and E. Chatre, "Evolution of the Global Navigation Satellite System (GNSS)," *Proc. IEEE*, vol. 96, no. 12, pp. 1902–1917, 2008, doi: 10.1109/JPROC.2008.2006090.
- [127] D. Salós, C. Macabiau, A. Martineau, B. Bonhoure, and D. Kubrak, "Analysis of GNSS integrity requirements for road user charging applications," in *2010 5th ESA Workshop on Satellite Navigation Technologies and European Workshop on GNSS Signals and Signal Processing (NAVITEC)*, 2010, pp. 1–8. doi: 10.1109/NAVITEC.2010.5708007.
- [128] P.-Y. Gilliéron, L. Ruotsalainen, F. Peyret, S. Feng, and J. Engdahl, "The SaPPART COST Action: Towards positioning integrity for road transport," in *2016 European Navigation Conference (ENC)*, 2016, pp. 1–6. doi: 10.1109/EURONAV.2016.7530570.

- [129] N. Zhu, J. Marais, D. Bétaille, and M. Berbineau, "GNSS Position Integrity in Urban Environments: A Review of Literature," *IEEE Trans. Intell. Transp. Syst.*, vol. 19, no. 9, pp. 2762–2778, 2018, doi: 10.1109/TITS.2017.2766768.
- [130] J. Rife, S. Pullen, S. Gleason, and D. Gebre-Egziabher, "Aviation applications," in *GNSS Applications and Methods*, Artech House Norwood, MA, 2009, pp. 245–268.
- [131] L. Heng, D. B. Work, and G. X. Gao, "GPS Signal Authentication From Cooperative Peers," *IEEE Trans. Intell. Transp. Syst.*, vol. 16, no. 4, pp. 1794–1805, 2015, doi: 10.1109/TITS.2014.2372000.
- [132] European Commission, "European Radio Navigation Plan." Accessed: Aug. 13, 2024. [Online]. Available: <https://ec.europa.eu/docsroom/documents/33024>
- [133] D. Margaria, E. Falletti, and T. Acarman, "The need for GNSS position integrity and authentication in ITS: Conceptual and practical limitations in urban contexts," in *2014 IEEE Intelligent Vehicles Symposium Proceedings*, 2014, pp. 1384–1389. doi: 10.1109/IVS.2014.6856485.
- [134] K. Kazmierski, "Performance of Absolute Real-Time Multi-GNSS Kinematic Positioning," *Artif. Satell.*, vol. 53, no. 2, pp. 75–88, Jun. 2018, doi: 10.2478/arsa-2018-0007.
- [135] K. Maciuk, "Współczynniki DOP w obserwacjach GNSS," *Bud. Archit.*, vol. 14, no. 1, pp. 65–72, 2015.
- [136] O. K. Isik, J. Hong, I. Petrunin, and A. Tsourdos, "Integrity Analysis for GPS-Based Navigation of UAVs in Urban Environment," *Robotics*, vol. 9, no. 3, p. 66, Aug. 2020, doi: 10.3390/robotics9030066.
- [137] O. Elmasry, M. Tamazin, H. Elghamarawy, M. Karaim, A. Noureldin, and M. Khedr, "Examining the benefits of multi-GNSS constellation for the positioning of high dynamics air platforms under jamming conditions," in *2018 11th International Symposium on Mechatronics and its Applications (ISMA)*, 2018, pp. 1–6. doi: 10.1109/ISMA.2018.8330133.
- [138] R. B. Langley, "Dilution of Precision," 1999. [Online]. Available: <https://api.semanticscholar.org/CorpusID:16850160>
- [139] P. Baranski, M. Polanczyk, and P. Strumillo, "Fusion of Data from Inertial Sensors, Raster Maps and GPS for Estimation of Pedestrian Geographic Location in Urban Terrain," *Metrol. Meas. Syst.*, vol. 18, no. 1, pp. 145–158, Jan. 2011, doi: 10.2478/v10178-011-0014-3.
- [140] STMicroelectronics, "Teseo-LIV3F Tiny GNSS module Datasheet - target specification." DS12152 Rev 8, Nov. 2023.
- [141] u-blox AG, "NEO-6 u-blox 6 GPS Modules Data Sheet." u-blox AG, 2011.
- [142] SIMCom, "SIM28 GPS Module." SIMCom, 2018.
- [143] STMicroelectronics, "X-NUCLEO-GNSS1A1 Data brief GNSS expansion board based on Teseo-LIV3F module for STM32 Nucleo." DB3458 - Rev 3, Jul. 2024.
- [144] H. Sarbolandi, M. Plack, and A. Kolb, "Pulse Based Time-of-Flight Range Sensing," *Sensors*, vol. 18, no. 6, pp. 1679–1–1679–22, May 2018, doi: <https://doi.org/10.3390/s18061679>.
- [145] A. Kolb, E. Barth, R. Koch, and R. Larsen, "Time-of-Flight Cameras in Computer Graphics," *Comput. Graph. Forum*, vol. 29, no. 1, pp. 141–159, Mar. 2010, doi: 10.1111/j.1467-8659.2009.01583.x.
- [146] J. Illade-Quinteiro, V. M. Brea, P. López, D. Cabello, and G. Domenech-Asensi, "Distance Measurement Error in Time-of-Flight Sensors Due to Shot Noise," *Sensors*, vol. 15, no. 3, pp. 4624–4642, Feb. 2015, doi: <https://doi.org/10.3390/s150304624>.
- [147] P. Pawłowski, M. Jeske, S. Kwiatkowski, and N. Kołodziejczyk, "Zrobotyzowane mapowanie przestrzeni z wykorzystaniem czujnika LIDAR," *Przegląd Elektrotechniczny*, vol. 97, no. 2, pp. 52–56, 2021, doi: 10.15199/48.2021.02.13.
- [148] R. Ji, L.-Y. Duan, J. Chen, T. Huang, and W. Gao, "Mining Compact Bag-of-Patterns for Low Bit Rate Mobile Visual Search," *IEEE Trans. Image Process.*, vol. 23, no. 7, pp. 3099–3113, 2014, doi: 10.1109/TIP.2014.2324291.
- [149] S. Zhao, L. Chen, H. Yao, Y. Zhang, and X. Sun, "Strategy for dynamic 3D depth data matching towards robust action retrieval," *Neurocomputing*, vol. 151, pp. 533–543, 2015, doi: <https://doi.org/10.1016/j.neucom.2014.03.092>.
- [150] S. Zhao, H. Yao, Y. Zhang, Y. Wang, and S. Liu, "View-based 3D object retrieval via multi-modal graph learning," *Signal Process.*, vol. 112, pp. 110–118, 2015, doi: <https://doi.org/10.1016/j.sigpro.2014.09.038>.
- [151] Yole Developpement, "The Automotive LiDAR Market." Accessed: Jul. 26, 2024. [Online]. Available: https://www.woodsdecap.com/wp-content/uploads/2018/04/Yole_WCP-LiDAR-Report_April-2018-FINAL.pdf
- [152] M. E. Warren, "Automotive LIDAR Technology," in *2019 Symposium on VLSI Circuits*, 2019, pp. C254–C255. doi: 10.23919/VLSIC.2019.8777993.
- [153] C. Goodin, D. Carruth, M. Doude, and C. Hudson, "Predicting the Influence of Rain on LIDAR in ADAS," *Electronics*, vol. 8, no. 1, 2019, doi: 10.3390/electronics8010089.

- [154] J. Wojtanowski, M. Zygmunt, M. Kaszczuk, Z. Mierczyk, and M. Muzal, "Comparison of 905 nm and 1550 nm semiconductor laser rangefinders' performance deterioration due to adverse environmental conditions," *Opto-Electron. Rev.*, vol. 22, no. 3, Jan. 2014, doi: 10.2478/s11772-014-0190-2.
- [155] M. Kutila, P. Pyykönen, W. Ritter, O. Sawade, and B. Schäufele, "Automotive LIDAR sensor development scenarios for harsh weather conditions," in *2016 IEEE 19th International Conference on Intelligent Transportation Systems (ITSC)*, 2016, pp. 265–270. doi: 10.1109/ITSC.2016.7795565.
- [156] M. Aldibaja, R. Yanase, T. H. Kim, A. Kuramoto, K. Yoneda, and N. Suganuma, "Accurate Elevation Maps based Graph-Slam Framework for Autonomous Driving," in *2019 IEEE Intelligent Vehicles Symposium (IV)*, 2019, pp. 1254–1261. doi: 10.1109/IVS.2019.8814007.
- [157] N. Baras, G. Nantzios, D. Ziouzos, and M. Dasygenis, "Autonomous Obstacle Avoidance Vehicle Using LIDAR and an Embedded System," in *2019 8th International Conference on Modern Circuits and Systems Technologies (MOCAST)*, 2019, pp. 1–4. doi: 10.1109/MOCAST.2019.8742065.
- [158] Shanghai Slamtec Co. Ltd, "RPLIDAR A1 Low Cost 360 Degree Laser Range Scanner Introduction and Datasheet Model: A1M8 rev.3.0." Oct. 15, 2020.
- [159] M. A. Fischler and R. C. Bolles, "Random sample consensus: a paradigm for model fitting with applications to image analysis and automated cartography," *Commun ACM*, vol. 24, no. 6, pp. 381–395, Jun. 1981, doi: 10.1145/358669.358692.
- [160] B. Leibe, E. Seemann, and B. Schiele, "Pedestrian detection in crowded scenes," in *2005 IEEE Computer Society Conference on Computer Vision and Pattern Recognition (CVPR'05)*, 2005, pp. 878–885 vol. 1. doi: 10.1109/CVPR.2005.272.
- [161] M. D. Breitenstein, F. Reichlin, B. Leibe, E. Koller-Meier, and L. Van Gool, "Online Multiperson Tracking-by-Detection from a Single, Uncalibrated Camera," *IEEE Trans. Pattern Anal. Mach. Intell.*, vol. 33, no. 9, pp. 1820–1833, 2011, doi: 10.1109/TPAMI.2010.232.
- [162] A. Joglekar, D. Joshi, R. Khemani, S. Nair, and S. Sahare, "Depth Estimation Using Monocular Camera," *Int. J. Comput. Sci. Inf. Technol.*, vol. 2, no. 4, pp. 1758–1763, 2011.
- [163] A. Bhoi, "Monocular Depth Estimation: A Survey," 2019, *arXiv*. doi: 10.48550/ARXIV.1901.09402.
- [164] R. Garg, N. Wadhwa, S. Ansari, and J. T. Barron, "Learning Single Camera Depth Estimation using Dual-Pixels," Aug. 14, 2019, *arXiv*: arXiv:1904.05822. Accessed: Aug. 07, 2024. [Online]. Available: <http://arxiv.org/abs/1904.05822>
- [165] V. De Silva, J. Roche, and A. Kondo, "Robust Fusion of LiDAR and Wide-Angle Camera Data for Autonomous Mobile Robots," *Sensors*, vol. 18, no. 8, 2018, doi: 10.3390/s18082730.
- [166] R. Myllylä, J. Marszalec, J. Kostamovaara, A. Mäntyniemi, and G.-J. Ulbrich, "Imaging distance measurements using TOF lidar," *J. Opt.*, vol. 29, no. 3, p. 188, Jun. 1998, doi: 10.1088/0150-536X/29/3/016.
- [167] R. Nair, F. Lenzen, S. Meister, H. Schäfer, C. Garbe, and D. Kondermann, "High Accuracy TOF and Stereo Sensor Fusion at Interactive Rates," in *Computer Vision – ECCV 2012. Workshops and Demonstrations*, A. Fusiello, V. Murino, and R. Cucchiara, Eds., Berlin, Heidelberg: Springer Berlin Heidelberg, 2012, pp. 1–11.
- [168] R. A. Hewitt and J. A. Marshall, "Towards intensity-augmented SLAM with LiDAR and ToF sensors," in *2015 IEEE/RSJ International Conference on Intelligent Robots and Systems (IROS)*, 2015, pp. 1956–1961. doi: 10.1109/IROS.2015.7353634.
- [169] B. Choi and J. Lee, "Sensor network based localization algorithm using fusion sensor-agent for indoor service robot," *IEEE Trans. Consum. Electron.*, vol. 56, no. 3, pp. 1457–1465, Aug. 2010, doi: 10.1109/TCE.2010.5606283.
- [170] V. John, Q. Long, Y. Xu, Z. Liu, and S. Mita, "Sensor Fusion and Registration of Lidar and Stereo Camera without Calibration Objects," *IEICE Trans. Fundam. Electron. Commun. Comput. Sci.*, vol. E100.A, no. 2, pp. 499–509, 2017, doi: 10.1587/transfun.E100.A.499.
- [171] H. Badino, D. Huber, and T. Kanade, "Integrating LIDAR into Stereo for Fast and Improved Disparity Computation," in *2011 International Conference on 3D Imaging, Modeling, Processing, Visualization and Transmission*, Hangzhou, TBD, China: IEEE, May 2011, pp. 405–412. doi: 10.1109/3DIMPVT.2011.58.
- [172] T. York and R. Jain, "Fundamentals of Image Sensor Performance." Accessed: Jun. 26, 2024. [Online]. Available: <https://www.cse.wustl.edu/~jain/cse567-11/ftp/imgsens/>
- [173] Z. Zhang, "A flexible new technique for camera calibration," *IEEE Trans. Pattern Anal. Mach. Intell.*, vol. 22, no. 11, pp. 1330–1334, 2000, doi: 10.1109/34.888718.
- [174] Y. Zhou, L. Zhang, C. Xing, P. Xie, and Y. Cao, "Target Three-Dimensional Reconstruction From the Multi-View Radar Image Sequence," *IEEE Access*, vol. 7, pp. 36722–36735, 2019, doi: 10.1109/ACCESS.2019.2905130.
- [175] P. Wei, L. Cagle, T. Reza, J. Ball, and J. Gafford, "LiDAR and Camera Detection Fusion in a Real-Time

- Industrial Multi-Sensor Collision Avoidance System," *Electronics*, vol. 7, no. 6, 2018, doi: 10.3390/electronics7060084.
- [176] Z. Han, J. Liang, and J. Li, "Design of Intelligent Road Recognition and Warning System for Vehicles Based on Binocular Vision," *IEEE Access*, vol. 6, pp. 62880–62889, 2018, doi: 10.1109/ACCESS.2018.2876702.
- [177] Z. Zhong, S. Liu, M. Mathew, and A. Dubey, "Camera Radar Fusion for Increased Reliability in ADAS Applications," *Electron. Imaging*, vol. 2018, pp. 1–4, Jan. 2018, doi: 10.2352/ISSN.2470-1173.2018.17.AVM-258.
- [178] C. Berger *et al.*, "Large-Scale Evaluation of an Active Safety Algorithm with EuroNCAP and US NCAP Scenarios in a Virtual Test Environment – An Industrial Case Study," in *2015 IEEE 18th International Conference on Intelligent Transportation Systems*, 2015, pp. 2280–2286. doi: 10.1109/ITSC.2015.368.
- [179] OpenCV team, "OpenCV computer vision library." Accessed: Sep. 12, 2024. [Online]. Available: <https://opencv.org>
- [180] MathWorks, "Image Processing Toolbox Perform image processing, visualization, and analysis." Accessed: Sep. 12, 2024. [Online]. Available: <https://www.mathworks.com/products/image-processing-processing.html>
- [181] R. Fisher, S. Perkins, A. Walker, and E. Wolfart, "Image Processing Learning Resources HIPR2 explore with JAVA." Accessed: Sep. 12, 2024. [Online]. Available: https://homepages.inf.ed.ac.uk/rbf/HIPR2/hipr_top.htm
- [182] R. C. Gonzalez and R. E. Woods, *Digital image processing*, Fourth edition, Global edition. New York, NY: Pearson, 2018.
- [183] S. Suzuki and K. be, "Topological structural analysis of digitized binary images by border following," *Comput. Vis. Graph. Image Process.*, vol. 30, no. 1, pp. 32–46, 1985, doi: [https://doi.org/10.1016/0734-189X\(85\)90016-7](https://doi.org/10.1016/0734-189X(85)90016-7).
- [184] FB Technology, "PAC2 V5 Photometric Airfield Calibration." Accessed: Sep. 29, 2022. [Online]. Available: <https://www.fbtechnology.com/our-products-agl-photometric-maintenance/airfield-lighting-photometric-measurement/>
- [185] S. Lin and M. Keo, "Detection of Light Sources and Shadow." Accessed: Jun. 02, 2024. [Online]. Available: <https://github.com/lexiddie/light-sources-and-shadow/blob/main/Detection%20of%20Light%20Sources%20and%20Shadow.pdf>
- [186] M. Laskowski, "Detection of light sources in digital photographs." Accessed: Jun. 02, 2024. [Online]. Available: <https://www.old.cescg.org/CESCG-2007/papers/Szczecin-Laskowski-Maciej.pdf>
- [187] R. de Charette and F. Nashashibi, "Real time visual traffic lights recognition based on Spot Light Detection and adaptive traffic lights templates," presented at the 2009 IEEE Intelligent Vehicles Symposium, Xi'an, China: IEEE, Jun. 2009, pp. 358–363. doi: 10.1109/IVS.2009.5164304.
- [188] J. Sierra, *Image analysis and mathematical morphology*, vol. 1. Academic Press, 1982.
- [189] F. Meyer, "Contrast Features Extraction," in *2nd European Symposium on Quantitative Analysis of Microstructures in Material Sciences, Biology and Medicine*, Caen, 1977, pp. 374–380.
- [190] R. de Charette and F. Nashashibi, "Traffic light recognition using image processing compared to learning processes," presented at the 2009 IEEE/RSJ International Conference on Intelligent Robots and Systems, St. Louis, MO, USA, 2009, pp. 333–338. doi: 10.1109/IROS.2009.5353941.
- [191] J. Balcerak, A. Konieczka, T. Marciniak, A. Dąbrowski, K. Maćkowiak, and K. Piniarski, "Automatic detection of traffic lights changes from red to green and car turn signals in order to improve urban traffic," presented at the 2014 Signal Processing: Algorithms, Architectures, Arrangements, and Applications (SPA), Poznan, Poland, 2014, pp. 110–115.
- [192] A. Rosebrock, "Detecting multiple bright spots in an image with Python and OpenCV." Accessed: Mar. 22, 2024. [Online]. Available: <https://pyimagesearch.com/2016/10/31/detecting-multiple-bright-spots-in-an-image-with-python-and-opencv/>
- [193] GoPro, "Hero8 Black - Regulatory Model Number SPJB1." 2019.
- [194] Sony Semiconductor Solutions Corporation, "IMX477-AACK Diagonal 7.857 mm (Type 1/2.3) 12.3Mega-Pixel CMOS Image Sensor with Square Pixel for Color Cameras." 2018.
- [195] ArduCam, "Arducam Complete High Quality Camera Bundle for Raspberry Pi." Accessed: Sep. 18, 2024. [Online]. Available: <https://www.arducam.com/product/b0241-arducam-imx477-hq-camera-6/>
- [196] T. Fawcett, "An introduction to ROC analysis," *Pattern Recognit. Lett.*, vol. 27, no. 8, pp. 861–874, 2006, doi: <https://doi.org/10.1016/j.patrec.2005.10.010>.
- [197] A. M. H. Wong and G. V. Eleftheriades, "Active Huygens' Box: Arbitrary Electromagnetic Wave Generation With an Electronically Controlled Metasurface," *IEEE Trans. Antennas Propag.*, vol. 69, no. 3, pp. 1455–1468, Mar. 2021, doi: 10.1109/TAP.2020.3017438.
- [198] U. Dey and J. Hesselbarth, "Millimeter-Wave Multi-Static Scattering for Sub-Wavelength Particle

- Characterization," *IEEE Trans. Microw. Theory Tech.*, vol. 70, no. 4, pp. 2351–2362, Apr. 2022, doi: 10.1109/TMTT.2022.3145014.
- [199] L. R. Luidolt, M. Wimmer, and K. Krosł, "Gaze-Dependent Simulation of Light Perception in Virtual Reality," *IEEE Trans. Vis. Comput. Graph.*, vol. 26, no. 12, pp. 3557–3567, Dec. 2020, doi: 10.1109/TVCG.2020.3023604.
- [200] L. Yu, H. Abuelła, M. Z. Islam, J. F. O'Hara, C. Crick, and S. Ekin, "Gesture Recognition Using Reflected Visible and Infrared Lightwave Signals," *IEEE Trans. Hum.-Mach. Syst.*, vol. 51, no. 1, pp. 44–55, Feb. 2021, doi: 10.1109/THMS.2020.3043302.
- [201] M. I. A. Shiddiq and S. Sunardi, "Performance Analysis of LDR, Photodiode, and BH1750 Sensors for Sunlight Intensity Measurement in Open Areas," *Signal Image Process. Lett.*, vol. 6, no. 1, pp. 11–26, 2024.
- [202] W. R. McCluney, *Introduction to radiometry and photometry*, 2nd ed. in Artech house applied photonics series. Boston: Artech house, 2014.
- [203] W. Żagan, *Podstawy techniki świetlnej*, Wydanie 3. Warszawa: Oficyna Wydawnicza Politechniki Warszawskiej, 2022.
- [204] ams-OSRAM AG, "BPW21TO39 Ambient Light Sensor Datasheet." 2022. [Online]. Available: https://dammedia.osram.info/media/resource/hires/osram-dam-5984961/BPW%2021_EN.pdf
- [205] Exelitas, "Ambient Light Sensors VTP1220FBH Product Description." 2022. [Online]. Available: <https://www.tme.eu/Document/99fa8b97bc9fac9fd65b9c88e771e8>
- [206] ROHM Semiconductor, "Ambient 16bit Serial Output Type Ambient Light Sensor IC BH1750FVI Rev.B." ROHM Co., Apr. 2009.
- [207] Sonopan, "Precision luxmeter L-200 with P-200 L-200P." [Online]. Available: <https://www.sonopan.com.pl/en/products/light/precision-illuminance-meter-l-200-with-p-200/>
- [208] GL OPTIC POLSKA SP. z o.o., "Technical Sheet GL SPECTIS 1.0 Touch." 2023. Accessed: Oct. 15, 2024. [Online]. Available: <https://gloptic.com/wp-content/uploads/2023/01/EN-Tech-Datasheet-GL-SPECTIS-1.0-Touch-1.pdf>
- [209] European Union Aviation Safety Agency, "Easy Access Rules for Aerodromes (Regulation (EU) No 139/2014)." Accessed: Jan. 11, 2023. [Online]. Available: <https://www.easa.europa.eu/en/downloads/98016/en>
- [210] L.-Y. Ma and N. Soin, "Recent Progress in Printed Physical Sensing Electronics for Wearable Health-Monitoring Devices: A Review," *IEEE Sens. J.*, vol. 22, no. 5, pp. 3844–3859, Mar. 2022, doi: 10.1109/JSEN.2022.3142328.
- [211] SENBA OPTOELECTRONIC, "LS06-S photodiode datasheet." Accessed: Nov. 15, 2024. [Online]. Available: https://seeedoc.github.io/Grove-Light_Sensor_v1.2/res/LS06-M05_datasheet.pdf
- [212] Vishay Semiconductors, "Accuracy Ambient Light Sensor with I2C Interface, VEML7700." 2016.
- [213] Sonopan, "Względny rozkład widmowy czułości głowicy fotometrycznej L-200 Nr 217." Dec. 2022.
- [214] P. Ptak, K. Górecki, and M. Gensikowski, "Porównanie właściwości dynamicznych wybranych czujników fotometrycznych," *Przegląd Elektrotechniczny*, vol. 96, no. 12, pp. 112–116, Dec. 2020, doi: 10.15199/48.2020.12.21.
- [215] E. Krac and K. Górecki, "Wpływ kąta padania światła na wartości natężenia oświetlenia zmierzone za pomocą czujników fotometrycznych," *Przegląd Elektrotechniczny*, vol. 97, no. 12, pp. 214–217, Dec. 2021, doi: 10.15199/48.2021.12.44.
- [216] D. S. D. Sitompul, F. E. Surya, F. P. Suhandi, and H. Zakaria, "Horizontal Scanning Method by Drone Mounted Photodiode Array for Runway Edge Light Photometry," presented at the 2019 International Seminar on Intelligent Technology and Its Applications (ISITIA), 2019, pp. 41–45. doi: 10.1109/ISITIA.2019.8937211.
- [217] D. S. D. Sitompul, F. E. Surya, F. P. Suhandi, and H. Zakaria, "Runway Edge Light photometry system by using drone-mounted instrument," presented at the 019 International Symposium on Electronics and Smart Devices (ISESD), 2019, pp. 1–5. doi: 10.1109/isesd.2019.8909498.
- [218] J. Gao, J. Luo, A. Xu, and J. Yu, "Light intensity itelligent control system research and design based on automobile sun visor of BH1750," presented at the 2017 29th Chinese Control And Decision Conference (CCDC), 2017. doi: 10.1109/CCDC.2017.7979192.
- [219] Seeed Development Limited, "Grove – Light Sensor v1.2." 2016. [Online]. Available: https://seeedoc.github.io/Grove-Light_Sensor_v1.2/
- [220] NXP Semiconductors, "UM10204 I2C-bus specification and user manual." Oct. 01, 2021.
- [221] Safegate Group, "Airfield Lighting Manual IDM 5581 Bidirectional runway centerline with two lamps-48W." Oct. 2012.
- [222] Safegate Group, "Airfield Lighting Manual 8" Inset Lights – IDM 4671, IDM 4581, IDM 4582 – Touchdown

- Zone." Aug. 2010.
- [223] European Union Aviation Safety Agency, "Certification Specifications and Guidance Material for Aerodrome Design (CS-ADR-DSN)." [Online]. Available: <https://www.easa.europa.eu/en/downloads/136283/en>
 - [224] International Civil Aviation Organization, "Doc 9157 Aerodrome Design Manual Fifth Edition, 2021 Part 4 — Visual Aids." International Civil Aviation Organization, 2021.
 - [225] OSRAM GmbH, "64319 Z/C 45-15." Accessed: Sep. 25, 2022. [Online]. Available: [https://www.osram.com/ecat/Halogen%20lamps,%20current-controlled%20with%20PK30d%20base-Halogen%20lamps,%20current-controlled%20\(Airfield\)-Halogen%20lamps-Industry-Specialty%20Lighting/com/en/GPS01_1028540/ZMP_56198/](https://www.osram.com/ecat/Halogen%20lamps,%20current-controlled%20with%20PK30d%20base-Halogen%20lamps,%20current-controlled%20(Airfield)-Halogen%20lamps-Industry-Specialty%20Lighting/com/en/GPS01_1028540/ZMP_56198/)
 - [226] T. Novak, J. Dudek, V. Kolar, K. Sokansky, and R. Baleja, "Solution of problems with short lifetime of airfield halogen lamps," presented at the 2017 18th International Scientific Conference on Electric Power Engineering (EPE), Kouty nad Desnou, Czech Republic, 2017, pp. 1–5. doi: 10.1109/EPE.2017.7967298.
 - [227] KIKUSUI Electronics Corp., "User's Manual PCR-MA Series AC Power Supply PCR 1000MA." KIKUSUI Electronics Corp., 2018.
 - [228] Polish Air Navigation Services Agency, "Polityka bezpieczeństwa." Accessed: Sep. 28, 2022. [Online]. Available: <https://www.pansa.pl/wp-content/uploads/2022/02/Polityka-bezpieczenstwa-PAZP.pdf>
 - [229] Airsafe Airport Equipment Co., Ltd., "Elevated lamp digital calibrator (unidirectional)." Accessed: Sep. 29, 2022. [Online]. Available: <http://www.airsafe.com.cn/index.php?m=content&c=index&a=show&catid=155&id=52>
 - [230] FB Technology, "PAC LAB II Workshop Photometry Controller." Accessed: Sep. 29, 2022. [Online]. Available: <https://www.fbtechnology.com/our-products-agl-photometric-maintenance/worskshop-photometry-controller/>
 - [231] S. Wichmann, "Verfahren und Vorrichtung zur Überprüfung von Leuchtmitteln und Lichtsignalen," EP1366989B1, May 27, 2002
 - [232] MALMS, "MALMS Mobile Measuring AGL performance." Accessed: May 31, 2024. [Online]. Available: <https://www.malms.aero/malms-mobile/>
 - [233] STMicroelectronics, "Navigation & Multimedia System & Architecture ST GNSS NMEA specification and commands." ST Automotive Product Group Automotive Infotainment Division, May 16, 2013.
 - [234] P. Kaniewski, "System nawigacji satelitarnej GPS, część 9 Komunikacja z odbiornikiem GPS," *Elektron. Prakt.*, no. 10, pp. 103–105, 2006.
 - [235] OSRAM SYLVANIA Inc., "Specialty Halogen - 6.6A Current Controlled." [Online]. Available: https://www.osram.us/pia/products/halogen-and-incandescent/p001_pia_product_detail_20.jsp
 - [236] M. Śliwicki and D. Wawrzyniak, "System for testing the lighting intensity of airport lamps," B. Sc. Thesis, Poznan University of Technology, 2019.
 - [237] DFROBOT, "TB6600 Stepper Motor Driver User Guide Version: V1.2." Sep. 2022.
 - [238] MathWorks, "Matlab Curve Fitter App." Accessed: Oct. 19, 2023. [Online]. Available: <https://uk.mathworks.com/help/curvefit/curvefitter-app.html>
 - [239] Linear Technology Corporation, "LTC4317 Dual I2C/SMBus Address Translator." 2015.
 - [240] Texas Instruments Incorporated, "TCA9548A Low-Voltage 8-Channel I2C Switch With Reset." May 2012.
 - [241] W. Raes, S. Bastiaens, D. Plets, and N. Stevens, "Assessment of the Influence of Photodiode Size on RSS-Based Visible Light Positioning Precision," presented at the 2019 IEEE SENSORS, 2020. doi: 10.1109/SENSORS43011.2019.8956543.
 - [242] A. Hudzikowski, "Luksomierz kit 2974 AVT," *Elektron. Dla Wszystkich*, vol. 03/11, pp. 56–58, 2011.
 - [243] W. Mańczak, "Development of a microprocessor matrix to measure the lightning intensity of airport lamps," B. Sc. Thesis, Poznan University of Technology, 2022.
 - [244] F. Alferink, "Fast Lux-meter: Electronic Measurements," Meettechnik.info. [Online]. Available: <https://meettechnik.info/diy-instruments/lux-meter.html>
 - [245] HDK, "8" LED Inset Light-Stingray Series TOUCHDOWN ZONE ILA-TDZ (L)." Hangdakang Mechanical & Electrical Technology (Wuhan) Co., Ltd.

List of Figures

FIGURE 1 SCIENTIFIC RESEARCH IN ASPECTS OF PHD APPLICATION AREA.....	1
FIGURE 2 EXAMPLE AREAS OF VEHICLE ENVIRONMENT MONITORING	2
FIGURE 3 STAGES OF DATA PROCESSING IN VEHICLE INTEGRATED MONITORING	3
FIGURE 4 VIEW OF THE RUNWAY WITH AGL LAMPS TURNED ON AT POZNAŃ – ŁAWICA AIRPORT RUNWAY 28.....	4
FIGURE 5 INVESTIGATED RESEARCH ASPECTS	5
FIGURE 6 MEASUREMENT PLATFORM FOR TESTING IN-PAVEMENT AGL WITH ENVIRONMENT MONITORING SYSTEM	6
FIGURE 7 FINAL PROPOSED ALGORITHM OF MEASURING DEVICE ENVIRONMENT MONITORING.....	7
FIGURE 8 R&D COOPERATION BETWEEN POZNAŃ – ŁAWICA AIRPORT AND POZNAN UNIVERSITY OF TECHNOLOGY	9
FIGURE 9 GENERAL SCHEME OF MULTI-SENSORY VEHICLE ENVIRONMENT MONITORING	19
FIGURE 10 MULTI-SENSOR SYSTEM DATA COLLECTION SCENARIO	23
FIGURE 11 DIVISION OF ENVIRONMENT MONITORING DEVICES WITH EXAMPLES	25
FIGURE 12 GLOBAL NAVIGATION SATELLITE SYSTEM ARCHITECTURE	28
FIGURE 13 X-NUCLEO-GNSS1A1 EXPANSION BOARD BASED ON TESEO-LIV3F FOR STM32 NUCLEO.....	33
FIGURE 14 SCHEME OF THE DISTANCE MEASUREMENT PRINCIPLE IN A LiDAR SENSOR BASED ON PULSED MODULATION OF THE LASER BEAM [28]	35
FIGURE 15 SLAMTEC RPLIDAR A1M8 LASER SCANNER MODULE [28]	38
FIGURE 16 LiDAR DATA PROCESSING PIPELINE	39
FIGURE 17 RANSAC ALGORITHM BLOCK SCHEME.....	40
FIGURE 18 RANSAC ALGORITHM DATA CLASSIFICATION	40
FIGURE 19 CAMERA PROCESSING PIPELINE	43
FIGURE 20 GEOMETRIC IMAGE TRANSFORMATIONS: ORIGINAL IMAGE (A), SCALING (B), ROTATION (C), REFLECTION (D), TRANSLATION (E), AFFINE TRANSFORMATION (F)	45
FIGURE 21 MORPHOLOGICAL IMAGE TRANSFORMATIONS: ORIGINAL IMAGE (A), EROSION (B), DILATION (C), OPENING (D), CLOSING (E)	47
FIGURE 22 HISTOGRAM GRAPH (A) OF MONOCHROME IMAGE (B)	48
FIGURE 23 EXAMPLE OF SPOT LIGHT DETECTION ALGORITHM [187]	49
FIGURE 24 ARDUCAM B0241 CAMERA WITH IMX477 MODULE	51
FIGURE 25 CONFUSION MATRIX	51
FIGURE 26 SPECTRAL SENSITIVITY CURVE $V(\lambda)$ ACCORDING TO CIE 1931.....	53
FIGURE 27 ISOCANDELA DIAGRAM FOR RUNWAY EDGE LIGHT WHERE WIDTH OF RUNWAY IS 60 M (WHITE LIGHT) [209].....	54
FIGURE 28 TOUCHDOWN ZONE LAMP HEATMAP LUMINOUS INTENSITY CHART	54
FIGURE 29 SPECTRAL SENSITIVITY OF: BPW21 PHOTODIODE [204] (A), VTP1220FBH PHOTODIODE [205] (B), BH1750 SENSOR [206] (C), LS06-S PHOTORESISTOR FROM GROVE LIGHT SENSOR V1.2 [211] (D), VEML7700 SENSOR [212] (E), SONOPAN L-200P LUXMETER WITH NO. 217 PHOTOMETRIC HEAD [213] (F)	55
FIGURE 30 SONOPAN L-200P LUXMETER (A), GL SPECTIS 1.0 TOUCH + FLICKER (B)	58
FIGURE 31 AIRPORT LAMPS: IN-PAVEMENT LAMP (A), ELEVATED LAMP (B)	59
FIGURE 32 LIGHT DISTRIBUTION REQUIRED FOR AIRPORT TOUCHDOWN ZONE LUMINAIRES [209]	61
FIGURE 33 LIGHT DISTRIBUTION REQUIRED FOR AIRPORT RUNWAY CENTRE LINE LUMINAIRES (WHITE LIGHT) [209].....	61
FIGURE 34 LIGHT DISTRIBUTION REQUIRED FOR AIRPORT TAXIWAY CENTRE LINE AND STOP BAR LUMINAIRES [209]	61
FIGURE 35 LIGHT DISTRIBUTION REQUIRED FOR AIRPORT APPROACH LUMINAIRES (WHITE LIGHT) [209].....	62
FIGURE 36 LIGHT DISTRIBUTION REQUIRED FOR AIRPORT END OF RUNWAY LUMINAIRES [209].....	62
FIGURE 37 RUNWAY CENTERLINE LAMP (IDM5582): (A) NEW, (B) DAMAGED, (C) COVERED WITH RUBBER FROM PLANE'S TIRES.....	63

FIGURE 38 WIRE BRUSHES ON PLOWS CLEARING SNOW FROM AIRPORT SURFACES [29]	64
FIGURE 39 FB TECHNOLOGY PAC MATRIX [16]	66
FIGURE 40 FB TECHNOLOGY PAC LAB II [230]	67
FIGURE 41 AIRSAFE PTS-200 [229]	67
FIGURE 42 DeWiTEC AIRFIELD LIGHT MOBILE ANALYZING SYSTEM (DALMAS) [15]	68
FIGURE 43 FB TECHNOLOGY PAC ² V5 MEASUREMENT MATRIX	69
FIGURE 44 MALMS MOBILE PHOTOMETRIC TEST SYSTEM	69
FIGURE 45 FIRST VERSION OF PROPOSED MEASURING PLATFORM FOR QUALITY TESTING OF AIRPORT LAMPS [29]	70
FIGURE 46 ILLUSTRATION OF CONCEPT ELEMENTS FOR AIRPORT ENVIRONMENT MONITORING SYSTEM: GNSS AND LIDAR TASKS (A), LIDAR AND CAMERA OBJECTS (B), LIGHT SENSORS MEASUREMENT HEATMAP (C)	71
FIGURE 47 EXAMPLE GNSS DATA FRAME FROM TESEO-LIV3F MODULE	73
FIGURE 48 MAP OF GNSS MODULES RAW MEASUREMENTS: REFERENCE POINT (BLACK), TESEO-LIV3F (BLUE), NEO-6M (GREEN), SIM28 (RED)	78
FIGURE 49 TESEO-LIV3F, NEO-6M AND SIM28 GNSS MODULES RAW POSITIONING DATA ERRORS BOXPLOT	79
FIGURE 50 ERROR HISTOGRAMS OF TESEO-LIV3F (A), NEO-6M (B) AND SIM28 (C) GNSS MODULES - RAW POSITIONING	80
FIGURE 51 TESEO-LIV3F, NEO-6M AND SIM28 GNSS RAW POSITIONING DATA ERRORS OVER TIME CHART	80
FIGURE 52 NUMBER OF SATELLITES OBSERVED BY TESEO-LIV3F, NEO-6M AND SIM28 GNSS MODULES FOR RAW DATA	81
FIGURE 53 HDOP PARAMETER VALUE FOR RAW DATA OF TESEO-LIV3F, NEO-6M AND SIM28 GNSS	81
FIGURE 54 POSITION ERROR IN COMPARISON TO NUMBER OF SATELLITES VISIBLE BY TESEO-LIV3F, NEO-6M AND SIM28 GNSS RAW DATA	82
FIGURE 55 POSITION ERROR IN COMPARISON TO HDOP VALUE OF TESEO-LIV3F, NEO-6M AND SIM28 GNSS RAW DATA	82
FIGURE 56 PROPOSED SOLUTION FOR REDUCING GNSS POSITIONING DATA ERROR	83
FIGURE 57 MAP OF GNSS MODULES FILTERED MEASUREMENTS: REFERENCE POINT (BLACK), TESEO-LIV3F (BLUE), NEO-6M (GREEN), SIM28 (RED)	84
FIGURE 58 TESEO-LIV3F, NEO-6M AND SIM28 GNSS MODULES FILTERED POSITIONING DATA ERRORS BOXPLOT	84
FIGURE 59 ERROR HISTOGRAMS OF TESEO-LIV3F (A), NEO-6M (B) AND SIM28 (C) GNSS MODULES - FILTERED POSITIONING	85
FIGURE 60 NUMBER OF SATELLITES OBSERVED BY TESEO-LIV3F, NEO-6M AND SIM28 GNSS MODULES DURING MOVEMENT TEST	86
FIGURE 61 HDOP PARAMETER VALUE OF TESEO-LIV3F, NEO-6M AND SIM28 GNSS DURING MOVEMENT TEST	87
FIGURE 62 MAP OF GNSS MODULES DURING MOVEMENT: TESEO-LIV3F (BLUE), NEO-6M (GREEN), SIM28 (RED)	87
FIGURE 63 MAP OF GNSS MODULES AT THE BEGINNING OF THE MEASUREMENT: TESEO-LIV3F (BLUE), NEO-6M (GREEN), SIM28 (RED)	88
FIGURE 64 MAP OF GNSS MODULES AT THE END OF THE MEASUREMENT: TESEO-LIV3F (BLUE), NEO-6M (GREEN), SIM28 (RED)	88
FIGURE 65 NEO-6M AND SIM28 GNSS W.R.T TESEO-LIV3F POSITIONING DATA ERRORS OVER TIME CHART	89
FIGURE 66 ERROR HISTOGRAMS OF NEO-6M (A) AND SIM28 (B) W.R.T. TESEO-LIV3F MEASUREMENT	90
FIGURE 67 TEST STAND OF ARRANGED ENVIRONMENT MODEL (A) AND ITS LIDAR MAP [28]	91
FIGURE 68 LIDAR AMBIENT SCAN WITH TWO CLOSELY PLACED OBSTACLES [28]	92
FIGURE 69 PLACEMENT AND DISTANCES BETWEEN DIFFERENT TYPES OF AERONAUTICAL GROUND LIGHTS [209]	94
FIGURE 70 RUNWAY (A) AND TAXIWAY (B) EDGE ELEVATED LAMP	94
FIGURE 71 SCHEMATIC OF LIDAR MEASUREMENT OF ELEVATED RUNWAY EDGE LAMP	95
FIGURE 72 LIDAR SCAN WITH FLAT SURFACE OBSTACLE IN OVERALL VIEW (A) AND DETAIL VIEW (B)	96
FIGURE 73 ANALYZED DATA POINT CLOUD DATA STATISTICAL BOX PLOT	96
FIGURE 74 COMPARISON OF LINEAR, QUADRATIC AND CUBIC RANSAC MODEL ESTIMATION	97
FIGURE 75 DATA SCATTER OF RAW LIDAR DATA AND LINEAR, QUADRATIC AND CUBIC RANSAC MODEL ESTIMATORS	98
FIGURE 76 RUNWAY VIEW WITH LIGHTING AND LINE MARKINGS (A) AND IN-PAVEMENT AIRPORT LAMP (B) [31]	99

FIGURE 77 CONCEPT OF THE MOVING LUMINOUS INTENSITY MEASUREMENT SYSTEM [31]	99
FIGURE 78 ANALYSIS OF AGL LIGHT SPOT SIZE OF THE VIDEO SEQUENCE FRAME	100
FIGURE 79 ENERGETICS DEPARTMENT OF POZNAŃ—ŁAWICA AIRPORT CAR EQUIPPED WITH CAMERA	101
FIGURE 80 PROPOSED ALGORITHM FOR THE DETECTION OF AIRPORT LAMPS IN A VIDEO SEQUENCE [31]	101
FIGURE 81 COMPARISON OF THE EFFECTIVENESS OF THE TESTED ALGORITHM [31]	103
FIGURE 82 OUTPUT FRAMES FROM ALGORITHM USING: EROSION (A), SINGLE STAGE DILATION (B), DOUBLE STAGE DILATION (C), HISTOGRAM FILTRATION (D) [31]	104
FIGURE 83 EXAMPLE FRAME OF HISTOGRAM FILTRATION [31]	105
FIGURE 84 YELLOW LINE LUMINANCE HISTOGRAM (A), RGB HISTOGRAM (B), WHITE LINE LUMINANCE HISTOGRAM (C), RGB HISTOGRAM (D), 1 ST LAMP LUMINANCE HISTOGRAM (E), RGB HISTOGRAM (F), 2 ND LAMP LUMINANCE HISTOGRAM (G), RGB HISTOGRAM (H) [31]	106
FIGURE 85 OVERALL DETECTION STATISTICS FOR DIFFERENT CONDITIONS [31]	107
FIGURE 86 EXAMPLE OUTPUT FRAME FOR CLOUDY CONDITIONS [31]	108
FIGURE 87 EXAMPLE OUTPUT FRAME FOR NIGHT CONDITIONS WITH HEADLIGHTS ON [31]	108
FIGURE 88 EXAMPLE OUTPUT FRAME FOR NIGHT CONDITIONS WITH HEADLIGHTS OFF [31]	109
FIGURE 89 ALGORITHM ACCURACY METRIC FOR DIFFERENT CONDITIONS [31]	109
FIGURE 90 EXPERIMENT ENVIRONMENT SCHEME [30]	112
FIGURE 91 APPROACH SYSTEM LAMP ILLUMINANCE MEASUREMENTS [30]	113
FIGURE 92 RUNWAY CENTRE LINE LAMP ILLUMINANCE MEASUREMENTS [30]	114
FIGURE 93 TOUCHDOWN ZONE LAMP ILLUMINANCE MEASUREMENTS [30]	114
FIGURE 94 GENERAL CONCEPT OF MEASURING DEVICE [26]	116
FIGURE 95 VIEW OF THE DEVICE WITH MARKED KEY ELEMENTS [26]	117
FIGURE 96 MEASUREMENTS OF ILLUMINANCE IN THE 2.8A POWER MODE: (A) LINEAR CHART; (B) BOX PLOT [26]	118
FIGURE 97 MEASUREMENTS OF ILLUMINANCE IN THE 3.4A POWER MODE: (A) LINEAR CHART; (B) BOX PLOT [26]	118
FIGURE 98 MEASUREMENTS OF ILLUMINANCE IN THE 4.1A POWER MODE: (A) LINEAR CHART; (B) BOX PLOT [26]	118
FIGURE 99 MEASUREMENTS OF ILLUMINANCE IN THE 5.2A POWER MODE: (A) LINEAR CHART; (B) BOX PLOT [26]	118
FIGURE 100 MEASUREMENTS OF ILLUMINANCE IN THE 6.6A POWER MODE: (A) LINEAR CHART; (B) BOX PLOT [26]	119
FIGURE 101 SPECTRAL CHARACTERISTIC OF BH1750 SENSOR AND SONOPAN L-200P LUXMETER [26]	120
FIGURE 102 BH1750 CORRECTION FOR TOUCHDOWN ZONE LAMP TDZ [26]	123
FIGURE 103 BH1750 CORRECTION FOR RUNWAY CENTERLINE CLEAR LAMP (RCL CLEAR) [26]	124
FIGURE 104 BH1750 CORRECTION FOR RUNWAY CENTERLINE RED LAMP (RCL RED) [26]	124
FIGURE 105 BH1750 CORRECTION FOR TAXIWAY GREEN LAMP (TAXI GREEN) [26]	124
FIGURE 106 BH1750 CORRECTION FOR TAXIWAY YELLOW LAMP (TAXI YELLOW) [26]	125
FIGURE 107 LUMINOUS INTENSITY MEASUREMENTS OF TDZ LAMP: (A) SONOPAN L-200P; (B) BH1750 [26]	125
FIGURE 108 LUMINOUS INTENSITY MEASUREMENTS OF RCL CLEAR LAMP: (A) SONOPAN L-200P; (B) BH1750 [26]	126
FIGURE 109 LUMINOUS INTENSITY MEASUREMENTS OF RCL RED LAMP: (A) SONOPAN L-200P; (B) BH1750 [26]	126
FIGURE 110 LUMINOUS INTENSITY MEASUREMENTS OF TAXI GREEN LAMP: (A) SONOPAN L-200P; (B) BH1750 [26]	126
FIGURE 111 LUMINOUS INTENSITY MEASUREMENTS OF TAXI YELLOW LAMP: (A) SONOPAN L-200P; (B) BH1750 [26]	127
FIGURE 112 LUMINOUS INTENSITY MEASUREMENTS OF USED RCL CLEAR LAMP: (A) HEATMAP CHART; (B) LAMP VIEW [26]	128
FIGURE 113 LUMINOUS INTENSITY MEASUREMENTS OF USED RCL RED LAMP: (A) HEATMAP CHART; (B) LAMP VIEW [26]	128
FIGURE 114 LUMINOUS INTENSITY MEASUREMENTS OF USED TDZ LAMP: (A) HEATMAP CHART; (B) LAMP VIEW [26]	129
FIGURE 115 LUMINOUS INTENSITY MEASUREMENTS OF REFURBISHED RCL CLEAR LAMP: (A) HEATMAP CHART; (B) LAMP VIEW [26]	129
FIGURE 116 LUMINOUS INTENSITY MEASUREMENTS OF REFURBISHED RCL RED LAMP: (A) HEATMAP CHART; (B) LAMP VIEW [26] ..	130
FIGURE 117 LUMINOUS INTENSITY MEASUREMENTS OF REFURBISHED TDZ LAMP: (A) HEATMAP CHART; (B) LAMP VIEW [26]	130

FIGURE 118 CONCEPTUAL DIAGRAM OF THE MEASUREMENT MATRIX CONNECTIONS [29]	131
FIGURE 119 READING THE LIGHT INTENSITY VALUE FOR THE BH1750 SENSOR AT AN LED FREQUENCY OF 20 Hz [29]	133
FIGURE 120 LTC4317 I ² C ADDRESS TRANSLATORS CIRCUIT DIAGRAM [239]	134
FIGURE 121 TCA9548A I ² C ADDRESS TRANSLATORS CIRCUIT DIAGRAM [240]	135
FIGURE 122 COMPARISON OF OPERATION TIMES IN VARIOUS MEASUREMENT MATRIX SYSTEMS USING THE BH1750 SYSTEM AND: (A) THE TCA9548A TRANSLATOR AND (B) THE LTC4317 TRANSLATOR [29]	136
FIGURE 123 GROVE LIGHT SENSOR V1.2 VOLTAGE OUTPUT SIGNAL FOR A 100 HZ SQUARE PWM SIGNAL [27]	137
FIGURE 124 GROVE LIGHT SENSOR V1.2 VOLTAGE OUTPUT SIGNAL FOR A 1000 HZ SQUARE PWM SIGNAL [27]	137
FIGURE 125 BPW21 CURRENT RESPONSE FOR A 1000 HZ SQUARE PWM SIGNAL [27]	139
FIGURE 126 VTP1220FBH CURRENT RESPONSE FOR A 1000 HZ SQUARE PWM SIGNAL [27]	140
FIGURE 127 OVERALL CONCEPT BLOCK SCHEME [27]	141
FIGURE 128 EXAMPLE OF AN I ² C FRAME MEASUREMENT TAKEN WITHOUT LIGHT SOURCE [27]	142
FIGURE 129 EXAMPLE OF AN I ² C FRAME MEASUREMENT TAKEN WITH LIGHT SOURCE [27]	142
FIGURE 130 CIRCUIT DIAGRAM [27]	143
FIGURE 131 PCB REALIZATION OF THE LIGHT-INTENSITY SENSOR WITH A PHOTODIODE [27]	144
FIGURE 132 MEASURING MATRICES PRINCIPLE OF OPERATION BLOCK SCHEME [25]	145
FIGURE 133 PLACEMENT OF THE MEASURING MATRIX UNDER THE MEASURING PLATFORM [25]	146
FIGURE 134 ANGULAR DEPENDENCIES OF M2 IRREGULAR ARRANGEMENT MATRIX ILLUMINANCE SENSORS [25]	146
FIGURE 135 DISTANCE DEPENDENCIES OF ILLUMINANCE SENSORS FOR M1 AND M2 MATRICES [25]	147
FIGURE 136 AIRPORT LAMPS MEASURING MATRIX CIRCUIT SCHEMATIC	148
FIGURE 137 AIRPORT LAMPS MEASURING MATRIX WITH IRREGULAR ALIGNMENT OF ILLUMINANCE SENSORS – DESIGNED BY AUTHOR	149
FIGURE 138 LABORATORY EXPERIMENTS USING MEASURING MATRIX	149
FIGURE 139 MEASURING MATRIX INSPECTION OF TDZ LAMP (A), LUMINOUS INTENSITY HEATMAP (B)	150
FIGURE 140 MEASURING MATRIX INSPECTION OF RCL CC LAMP (A), LUMINOUS INTENSITY HEATMAP (B, C)	150
FIGURE 141 MEASURING MATRIX INSPECTION OF RCL CR LAMP (A), LUMINOUS INTENSITY HEATMAP (B, C)	151
FIGURE 142 MEASURING MATRIX INSPECTION OF TAXI G/Y LAMP (A), LUMINOUS INTENSITY HEATMAP (B, C)	151
FIGURE 143 MEASURING MATRIX INSPECTION OF LED TAXI G/G LAMP (A), LUMINOUS INTENSITY HEATMAP (B, C)	152
FIGURE 144 MEASURING MATRIX INSPECTION OF TAXIWAY RAPID EXIT LAMP (A), LUMINOUS INTENSITY HEATMAP (B)	153
FIGURE 145 MEASURING MATRIX INSPECTION (A) OF TAXIWAY RAPID EXIT LAMP (B) WITH DAMAGED PRISM (C)	153
FIGURE 146 MEASURING MATRIX INSPECTION (A) OF STOPBAR LAMP (B) WITH DAMAGED PRISM (C)	154
FIGURE 147 MEASURING MATRIX INSPECTION (A) OF LED TDZ LAMP (B) WITH COMPARISON TO THE MANUFACTURER'S CHARACTERISTIC [245] (C) AVAILABLE UNDER QR CODE PLACED BEHIND THE PRISM (D)	155
FIGURE 148 MEASURING PLATFORMS FOR AGL LAMPS TESTING: VERSION 1 (A) AND VERSION 2 (B)	156
FIGURE 149 MEASURING PLATFORM INTERNAL STRUCTURE BLOCK DIAGRAM	157
FIGURE 150 CONFIRMATION OF THE PATENT APPLICATION FOR THE PROPOSED SOLUTION FOR AGL TESTING	158

List of Tables

TABLE 1 LIST OF AUTHORED AND CO-AUTHORED PUBLICATIONS DIRECTLY RELATED TO THE TOPIC OF PHD DISSERTATION.....	11
TABLE 2 LIST OF AUTHORED AND CO-AUTHORED PUBLICATIONS PARTLY RELATED TO THE TOPIC OF PHD DISSERTATION	12
TABLE 3 LIST OF CONCEPT SYSTEMS AND SOLUTIONS DIRECTLY RELATED TO THE TOPIC OF PHD DISSERTATION	15
TABLE 4 FEATURES COMPARISON OF DIFFERENT TYPES OF SENSORS	20
TABLE 5 ADVANTAGES AND DISADVANTAGES OF SENSOR FUSION APPROACHES	22
TABLE 6 VISION AND ACOUSTIC SENSORS DATA TYPES AND CHARACTERISTICS.....	26
TABLE 7 CAMERA, LIDAR AND RADAR PERFORMANCE ASSESSMENT IN DIFFERENT CONDITIONS VS THEIR FUSION.....	27
TABLE 8 GLOBAL GNSS SATELLITE NAVIGATION SYSTEMS	29
TABLE 9 DILUTION OF PRECISION (DOP) VALUES CATEGORIES	32
TABLE 10 COMPARISON OF DIFFERENT GNSS RECEIVER MODULES	33
TABLE 11 SLAMTEC RPLIDAR A1M8 TECHNICAL PARAMETERS [28]	38
TABLE 12 GoPro HERO 8 AND ARDUCAM B0241 CAMERAS TECHNICAL PARAMETERS.....	50
TABLE 13 BH1750 MEASUREMENT MODES [206]	56
TABLE 14 AIRPORT LAMPS MAIN BEAM ILLUMINANCE REQUIREMENTS	63
TABLE 15 DESCRIPTION OF THE DATA CONTAINED IN RMC SENTENCE	73
TABLE 16 DESCRIPTION OF THE DATA CONTAINED IN GGA SENTENCE	74
TABLE 17 DESCRIPTION OF THE DATA CONTAINED IN VTG SENTENCE	75
TABLE 18 DESCRIPTION OF THE DATA CONTAINED IN GSA SENTENCE	75
TABLE 19 DESCRIPTION OF THE DATA CONTAINED IN GSV SENTENCE	76
TABLE 20 DESCRIPTION OF THE DATA CONTAINED IN GLL SENTENCE.....	77
TABLE 21 DESCRIPTION OF THE DATA CONTAINED IN PSTMCPU SENTENCE.....	77
TABLE 22 RANSAC ESTIMATOR MODEL RESULTS.....	97
TABLE 23 METRICS DEPENDING ON WEATHER CONDITIONS [31].....	109
TABLE 24 POWER SUPPLY PARAMETERS [30]	113
TABLE 25 ILLUMINANCE DIFFERENCES DEPENDING ON POWER SOURCE TYPE [30].....	115
TABLE 26 RESULTS OF THE BH1750 EXPERIMENT [26]	119
TABLE 27 RESULTS OF THE BH1750 AND SONOPAN L-200P MEASUREMENT [26]	121
TABLE 28 GOODNESS OF FIT PARAMETERS FOR THE CALCULATED POLYNOMIAL CONVERSION EQUATIONS [26]	123
TABLE 29 DEPENDENCE OF THE THEORETICAL DRIVING SPEED OF THE MATRIX ON THE GENERATED FREQUENCY [29]	132
TABLE 30 COMPARISON OF DATA ACQUISITION TIME IN VARIOUS SENSOR CONFIGURATIONS IN THE MATRIX [29]	135
TABLE 31 MAXIMUM RANGES OF LIGHT INTENSITY MEASUREMENT BY SENSORS MEASURED AT A DISTANCE OF 1 M [27].....	138
TABLE 32 ESTIMATED PLATFORM SPEEDS ASSUMING 4 MEASUREMENTS AT A DISTANCE OF 20 CM [27]	139
TABLE 33 ESTIMATED PLATFORM SPEED ASSUMING 4 MEASUREMENTS AT A DISTANCE OF 4 CM [27].....	140
TABLE 34 COMPARISON OF AGL MEASURING PLATFORMS MAIN FEATURES.....	156

